THE ASTROPHYSICAL JOURNAL

AN INTERNATIONAL REVIEW OF SPECTROSCOPY AND ASTRONOMICAL PHYSICS

JULY 1951

THE SPECTROSCOPICALLY VARIABLE STAR HD 125248 1

THE SPECTRUM OF XX OPHIUCHI IN 1949 AND 1950 37

THE SECULAR CHANGES OF VV CEPHEI OUTSIDE ECLIPSE 47

THE ATMOSPHERES OF A-TYPE SUBDWARFS AND 31 LEONIS 53

SPECTROPHOTOMETRY OF EARLY A-TYPE STARS 73

EMISSION BY HYDROGEN REGIONS IN PLANETARY NEBULAE 79

ABSORPTION BY HYDROGEN IONS IN PLANETARY NEBULAE 105

THE THEORY OF THE FLUCTUATIONS IN BRIGHTNESS OF THE 109

AN INVESTIGATION OF GALACTIC STRUCTURE IN THE DIRECTION OF 123

AN EXPLORATION OF THE MILKY WAY IN PERSEUS 132

PHOTOELECTRIC STUDIES. VIII. POSITIONAL EFFECT IN ..... AND SOME REVISED MAGNITUDES IN THE NORTH POLAR ..... REGION Cr2 147

THE STRUCTURE OF THE SOLAR ATMOSPHERE AS INFERRED ..... FROM RADIO MEASURES 153

A DIFFERENTIAL ANALYSIS OF THE γ-SYSTEM OF THE 167

NOTES 179

THE UNIVERSITY OF CHICAGO PRESS
CHICAGO, ILLINOIS, U.S.A.

July 1951 Vol. 114, No. 1

THE ASTROPHYSICAL JOURNAL

AN INTERNATIONAL REVIEW OF SPECTROSCOPY AND ASTRONOMICAL PHYSICS

Edited by

W. W. MORGAN
Managing Editor
Yerkes Observatory of the University of Chicago

S. CHANDRASEKHAR

PAUL W. MERRILL
Mount Wilson Observatory of the Carnegie Institution of Washington

HARLOW SHAPLEY
Harvard College Observatory
Cambridge, Massachusetts

N. U. MAYALL
Lick Observatory
University of California

With the Collaboration of the American Astronomical Society

Collaborating Editors:

1949-51

W. BAADE
Mount Wilson Observatory

LEO GOLDBERG
Observatory of the University of Michigan

G. HERZBERG
National Research Council, Ottawa

1950-52

LYMAN SPITZER, JR.
Princeton University Observatory

A. N. VYSSOTSKY
Leander McCormick Observatory

ALBERT E. WHITFORD
Washburn Observatory

CECILIA [illegible]-PAYNE-GAPOSCHKIN
[illegible] Observatory

[illegible]

[illegible] AR
[illegible] National Observatory, Tonantzintla

The Astrophysical Journal is published bimonthly by the University of Chicago at the University of Chicago Press, 5750 Ellis Avenue, Chicago 37, Illinois, during July, September, November, January, March, and May. ¶Two volumes are published per year, one beginning with the January issue and the other beginning with the July issue. The subscription price is $6.00 per volume or $12.00 per year; the price of single copies is $3.00. (Orders for service of less than a volume will be charged at the single copy rate.) ¶Postage is prepaid by the publishers on all orders from the United States and its possessions. No extra charge is made for postage to countries in the Pan American Postal Union. ¶Postage is charged extra as follows: for Canada, 2c cents per volume, 40 cents per year (total $6.50 per volume, $12.40 per year); on single copies 5 cents (total $3.05); for all other countries in the Postal Union, 50 cents per volume, $1.00 per year (total $6.50 per volume, $13.00 per year), on single copies 10 cents (total $3.10). Subscriptions are payable in advance. Please make all remittances payable to The University of Chicago Press, in United States currency or its equivalent by postal or express money orders or bank drafts.

The following is an authorized agent:

For the British Empire, except North America and Australasia: The Cambridge University Press, Bentley House, 200 Euston Road, London, N.W. 1, England. Prices of yearly subscriptions and of single copies may be had on application.

Claims for missing numbers should be made within the month following the regular month of publication. The publishers expect to supply missing numbers free only when losses have been sustained in transit, and when the reserve stock will permit.

Business correspondence should be addressed to The University of Chicago Press, Chicago 37, Illinois.

Communications for the editors and manuscripts should be addressed to: W. W. Morgan, Editor of THE ASTROPHYSICAL JOURNAL, Yerkes Observatory, Williams Bay, Wisconsin.

Line drawings and photographs should be made by the author, and all marginal notes such as co-ordinates, wave lengths, etc., should be included in the cuts. It will not be possible to set any such material in type.

One copy of the corrected galley proof should be returned as soon as possible to the editor, Yerkes Observatory, Williams Bay, Wisconsin. Authors should take notice that this proof may not be sent to them with the proof.

The cable address is "Observatory, Williamsbay, Wisconsin."

The articles in this journal are indexed in the *International Index to Periodicals*, New York, N.Y.

Applications for permission to quote from this journal should be addressed to the University of Chicago Press, and will be freely granted.

Microfilms of complete journal volumes are available to regular subscribers, and may be obtained at the end of the year. Orders and inquiries should be addressed to University Microfilms, 313 North First Street, Ann Arbor, Michigan.

Notice to subscribers: If you change your address, please notify us and give both addresses immediately.

Entered as second-class matter, July 20, 1900, at the Post-Office at Chicago, Ill., under the Act of March 3, 1879.
Acceptance for mailing at special rate of postage provided for in United States Postal Act of February 28, 1925, embodied February 28, 1925.

[PRINTED IN U.S.A.]

THE ASTROPHYSICAL JOURNAL

AN INTERNATIONAL REVIEW OF SPECTROSCOPY AND ASTRONOMICAL PHYSICS

VOLUME 114 JULY 1951 NUMBER 1

THE MAGNETICALLY VARIABLE STAR HD 125248

HORACE W. BABCOCK
MOUNT WILSON AND PALOMAR OBSERVATORIES
CARNEGIE INSTITUTION OF WASHINGTON
CALIFORNIA INSTITUTE OF TECHNOLOGY
Received December 26, 1950

ABSTRACT

The reversing magnetic field of the peculiar A-type star HD 125248 = BD − 18°3789 has been investigated on twenty-seven high-dispersion spectrograms made with the double analyzer for circularly polarized light. The magnetic-field intensity at the pole, H_p, as determined from the Zeeman effect on numerous Fraunhofer lines, has been tabulated for several elements at different phases in the 9.295-day period found by Deutsch for the variations in line intensity. The lines of *Fe* I, *Fe* II, and *Ti* II, which vary only slightly in intensity, indicate a field represented by $H_p = 2000 + 6600 \cos\theta - 1600 \cos 2\theta$ gauss.

The positive extreme (+7000 gauss) is reached near zero phase, when the lines of the rare earths are at maximum intensity and lines of *Cr* I and *Cr* II are at minimum. The negative extreme (−6200 gauss) is reached at mid-period when *Eu* II is weak and *Cr* is at maximum intensity. H_p determined from the *Cr* lines is "more negative" than that indicated by *Fe–Ti*, while, especially at the "cross-over" phases (0.35 and 0.7, when $H_p = 0$), *Eu* II gives a stronger positive field. If results from all elements are averaged, the extremes are close to +7600 and −7600 gauss.

Velocities in the line of sight are also tabulated for elements at various phases. Again, systematic differences are found between the *Fe–Ti* group, the rare-earth group, and *Cr*. Rather sudden decelerations occur just as H_p reaches maximum.

A "cross-over effect" on the profiles of Fraunhofer lines was discovered on plates made near phases 0.35 and 0.7. This is interpreted as a combination of differential velocity and temporary opposite magnetic polarity on two zones of the star; apparently, the magnetic field reverses in a rapid, progressive manner over the surface.

The rare earths and *Cr* seem to be concentrated in separate atmospheric zones, which vary in effective size or location; *Fe* and *Ti* are supposed to be rather uniformly distributed and to represent best the general magnetic field.

Two fundamentally different physical models are considered: the magnetic oscillator and the oblique rotator. The latter does not satisfactorily represent the observations. Consequently, it is concluded that HD 125248 is observed pole-on and that it is oscillating, perhaps in a manner suggested by Schwarzschild, for only by large-scale motions of the material of the star can rapid changes of the magnetic field be explained. In his solution (odd mode), specialized pulsations of the star are coupled with an oscillating dipole component of the field. The constant component (+2000 gauss) indicated by *Fe–Ti* can perhaps be interpreted most plausibly according to the Elsasser-Bullard theory, although the observations yield no data as to rate of axial rotation (or as to differential rotation). For lack of these data the electromotive forces in the atmosphere cannot be specified completely; however, the oscillating component of the electric field induced by the changing magnetic field is specified in Schwarzschild's solution (for a nonconducting atmosphere). This has an amplitude at the equator of 36 volts/cm.

To account for the varying equivalent widths of lines, it is assumed that the effective atmospheric *Eu* and *Cr* have become concentrated in zones, *Eu* near the poles, *Cr* in an equatorial belt, and that the extent of these zones varies as the star oscillates. As a tentative approach to this separation of elements, a mass-spectrograph effect is considered, depending upon the transient differential drift velocities of ions, as a function of charge/mass, in crossed electric and magnetic fields.

The star HD 125248=BD−18°3789 is of spectral type A0p and magnitude 5.74, according to the *Henry Draper Catalogue*. In 1928, W. W. Morgan discovered it to be an outstanding spectrum variable, in which the lines of *Eu* II and of *Cr* I and *Cr* II undergo large changes of intensity, the two elements varying in opposite phase.[1] Numerous lines of *Fe* I, *Fe* II, *Ti* II, and some other elements remain much more nearly constant in strength. For a general description of the spectrum the reader is referred to Morgan's paper and to the later work of A. J. Deutsch,[2] who determined the elements of spectral variation to be

$$Eu\ \text{II maximum} = Cr\ \text{I, II minimum} = \text{JD}\ 2430143.07 + 9.295E\,. \qquad (1)$$

These elements continue to represent the observations well and have been used throughout this paper.

Morgan pointed out similarities in appearance and behavior of the spectrum between HD 125248 and α^2 Canum Venaticorum. Each of these peculiar A-type stars is a spectrum variable in which *Eu* II and *Cr* II alternate in attaining maximum intensity. The periods of the two stars are 9.3 and 5.5 days, respectively. In α^2 CVn the excitation is somewhat higher, and lines of *Fe* I are relatively weak; furthermore, with high dispersion, the lines are found to be generally broader and shallower. Lines of neutral or ionized metals are present, some of them with abnormal intensity, in the spectra of the peculiar stars and spectrum variables typified by the two objects mentioned, but these groups are to be distinguished from the "metallic-line" stars, also of type A. This distinction has been emphasized by the Yerkes observers.[3]

A summary of earlier work on the spectrum of HD 125248 shows that the lines may be classified according to three groups of elements, as follows:

Group A consists of lines of *Eu* II, notably λλ 3819, 3930, 4129, 4205, and 4435, that are very strong near zero phase and weak near mid-period. (On my plates of higher dispersion, lines of two other rare earths, *Ce* II and *Gd* II, are also found; they vary with *Eu* II.) Deutsch gives a plot of line intensity as a function of phase and suggests that the variations occur rather abruptly.

Group B is represented by numerous lines of *Cr* II of which λλ 4242, 4269, and 4558 are outstanding, as well as several strong lines of *Cr* I. As was pointed out by Morgan, the lines of *Cr* I and *Cr* II vary together from great strength to practically complete invisibility, being strongest when *Eu* II is weak, and this cannot be explained by any simple change of excitation. The line *Mg* II λ 4481 is also included in group B, although the variation is moderate.

Group C consists of lines which show comparatively little variation of intensity; included are numerous lines of *Fe* I and many strong lines of *Fe* II and *Ti* II. The *H* lines also belong here; they have rather prominent central cores and broad wings characteristic of main-sequence stars. The K line of *Ca* II is weak (as in most peculiar A-type stars), sharp, without wings, and of nearly constant intensity. The *Si* II pair of λ 4128 and λ 4131 is present but weak.

The first observation of the Zeeman effect in the spectrum of HD 125248 at the Mount Wilson Observatory in 1947 gave evidence of a general magnetic field with $H = +5500$ gauss at the pole; additional plates soon showed that H_p varies regularly with a semi-amplitude of about 7 kilogauss, being of positive (north-seeking) polarity when the *Eu* II lines are strong, and negative when the *Cr* II lines are most intense.[4] As the star is outstanding in the strength of its magnetic field and in the degree of variation of line intensities, plans were immediately made to obtain an extended series of observations with the highest practicable dispersion. It is particularly well suited to analysis of the

[1] *Ap. J.*, **74**, 24, 1931.

[2] Nancy G. Roman, W. W. Morgan, Olin J. Eggen, *Ap. J.*, **107**, 107, 1948.

[3] *Ap. J.*, **105**, 283, 1947.

[4] H. W. Babcock, *Pub. A.S.P.*, **59**, 260, 1947.

Zeeman effect because rotational broadening of the lines is very small, if not entirely absent, and because, for a star of its type, the spectrum is unusually rich in lines of the metals. The aim was to investigate the magnetic changes in as much detail as possible and, at the same time, to study further the varying line intensities and the radial velocities indicated by the lines of different elements. A detailed study of HD 125248 seems appropriate not only because of its own peculiarities but because it is a representative of the group of spectrum variables and peculiar stars that appear to be distinguished from the more normal stars of type A by strong, general magnetic fields.

OBSERVATIONS

The spectrograms were made with the coudé grating spectrograph of the 100-inch telescope, which is equipped with three Schmidt cameras. Most of the plates were taken in 1947, 1948, and 1949, with the intermediate dispersion of 4.54 A/mm and the Eastman 103-O emulsion. The plates were baked, usually for 3 days at 50° C, before use. The equivalent slit-width for most exposures was 0.12 A. The southerly position of the star

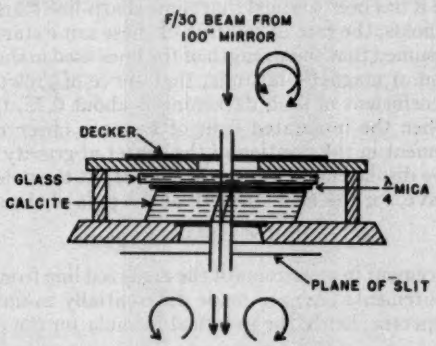

FIG. 1.—Double analyzer for circularly polarized light, used in front of slit of coudé spectrograph. Two adjacent images of the star, analyzed for polarization of opposite sign, are formed on the slit; these yield the double spectra of Figures 2, 3, and 4.

is not favorable, but under moderately good conditions plates of satisfactory density could be secured in 3–5 hours. The spectral range covered with intermediate dispersion was from the region of the K line to λ 4500, although on some plates the shortward region was weak. On two nights when conditions were exceptionally good, spectrograms were obtained with a dispersion of 2.9 A/mm. A number of supplementary plates were also made on the II*a*-O emulsion with a dispersion of 10.3 A/mm. Most of the observations were made with the aid of the photoelectric guider for holding the star on the slit.[5]

No extended photometric study of the present material has been made because, owing to the installation of a new grating early in 1950, superior spectra on fine-grain emulsions can now be obtained with reduced exposure time.

To analyze the spectral lines for polarization, the standard double circular analyzer[6] was employed, always in the same position. It is shown schematically in Figure 1. The calcite crystal forms two images of the star, side by side on the slit, 0.6 mm apart. Preceding the calcite, the mica quarter-wave plate, with its plane of fast vibration in an azimuth of 45° to the slit, converts any circularly polarized starlight into plane-polarized light, of which the electric vector is parallel to or perpendicular to the slit, depending on the sign of rotation of the incident light; the calcite then directs the plane-polarized light

[5] H. W. Babcock, *Ap. J.*, **107**, 73, 1948.

[6] H. W. Babcock, *Ap. J.*, **105**, 105, 1947.

into the right- or left-hand star image, depending on the plane of vibration. Light that is unpolarized or plane-polarized upon reaching the analyzer is divided equally between the two images.

The determination of magnetic polarity, according to which the *Eu* II maximum in HD 125248 occurs when the magnetic polarity is positive, depends upon the standardization of the analyzer, as mentioned in a preceding paper.[7] This was done with a magnet, a compass, and a spark source set up in front of the coudé spectrograph. The standardization was later checked by observing with the same analyzer the Zeeman effect in sunspots at the 150-foot solar tower and 75-foot spectrograph on Mount Wilson. The polarity thus determined agreed with the polarity indicated by the analyzers that have been used in routine magnetic observations of sunspots for many years.

In earlier papers on the magnetic fields of stars, it was assumed that such fields are associated with axial rotation, the magnetic moment being proportional to the rate of rotation for objects of about the same mass and radius[6] (or, more specifically, that the magnetic moment is proportional to the angular momentum[8]), and, further, that, by selecting sharp-line stars for observation, some pole-on objects with strong dipole fields might be found. While it has been verified that some sharp-line stars of type A do possess measurable magnetic fields, the rate of rotation of these same stars cannot be measured directly. It was also assumed that the strength of the lines used in the study of the Zeeman effect is not a function of magnetic latitude, that curve-of-growth effects can be neglected, and that the coefficient of limb darkening is about 0.45, typical of type A. On these assumptions, when the integrated light of a star is observed through a circular analyzer, the displacement in the position of the center of gravity of a blended Zeeman triplet is 0.31 times the displacement due to the field H_p at the pole. Rewriting equation (11) of Paper I, we have, for the field strength at the pole of the star,

$$H_p = 6.89 \times 10^{12} \lambda^{-2} \Delta\lambda \text{ gauss}, \tag{2}$$

where $\Delta\lambda$ is the displacement in angstroms of the analyzed line from the normal position. In practice, the measurements (Δs) are made differentially in units of 1μ between the right- and left-hand spectra; hence the practical formula for the polar field intensity is

$$H_p = 3.45 \times 10^9 F \lambda^{-2} \Delta s, \tag{3}$$

where F is the dispersion in A/mm. Reduced to λ 4500,

$$H_p = 170 F \Delta s. \tag{4}$$

These equations apply to a normal Zeeman triplet for which $Z = 1.00$.

The foregoing formula, with its implicit assumptions, has been applied in reducing the measurements in the spectrum of HD 125248. It becomes obvious in what follows, however, that some of these assumptions must be more or less seriously violated in this star, owing to the complex structure of its atmosphere. In particular, the distribution of elements must be nonuniform, either in depth or in position on the surface or both, and it is likely that the magnetic field is radically different from that of a dipole at certain phases of the variation. It may be inferred that an element showing strong absorption lines with relatively low central intensities is rather uniformly distributed over the visible hemisphere of the star; for such an element the numerical results may be fairly near the truth, except that saturation of the stronger components of the blended Zeeman pattern may reduce the observed effect. An element represented by weak lines, on the other hand, may be concentrated in a particular region as at the poles or near the equator; for such an element, the value of H_p obtained by applying equation (2) is, to a certain extent, only formal. It is possible that, having established the true polar field from lines of elements uniformly distributed, one can then infer the distribution of other ele-

[7] H. W. Babcock, *Ap. J.*, **108**, 191, 1948. [8] H. W. Babcock, *Pub. A.S.P.*, **59**, 112, 1947.

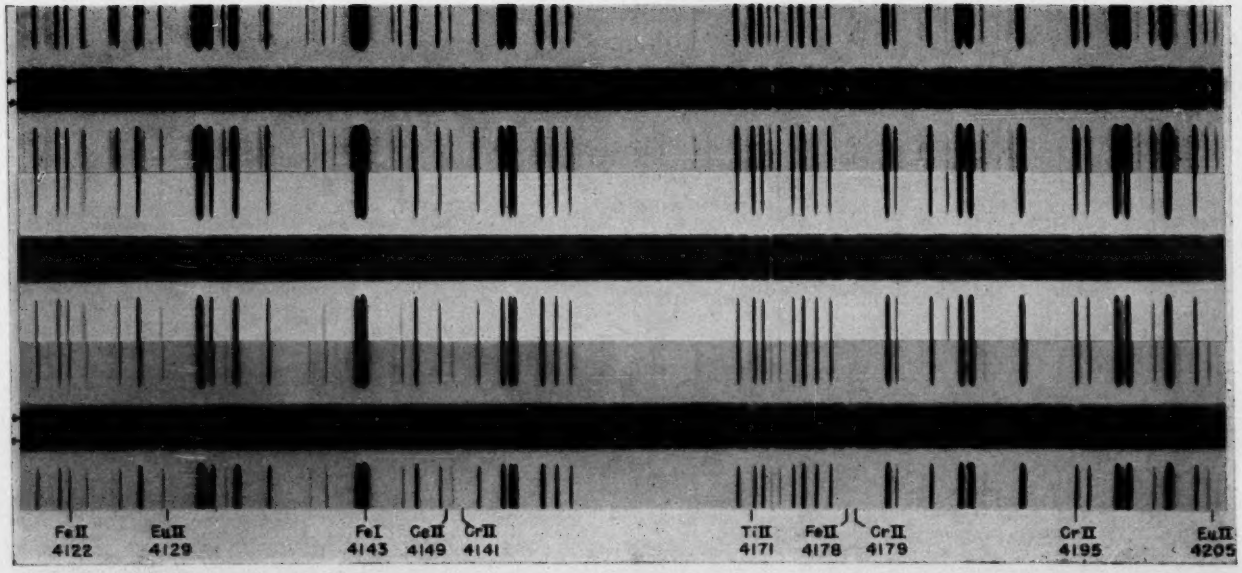

FIG. 2.—The spectrum of HD 125248, λλ 4120–4200, taken with the double analyzer at phases 0.11 (*top*), 0.77 (*middle*), and 0.55 (*bottom*). At phase 0.11 the lines in the upper part of the double spectrum are shifted slightly shortward with respect to the lower part, corresponding to positive magnetic polarity; at phase 0.55 the displacements are in the opposite sense. Shifts are small at phase 0.77, and the "cross-over effect" is visible in the profiles of many lines, which are broader and shallower in the upper than in the lower part of the double spectrum.

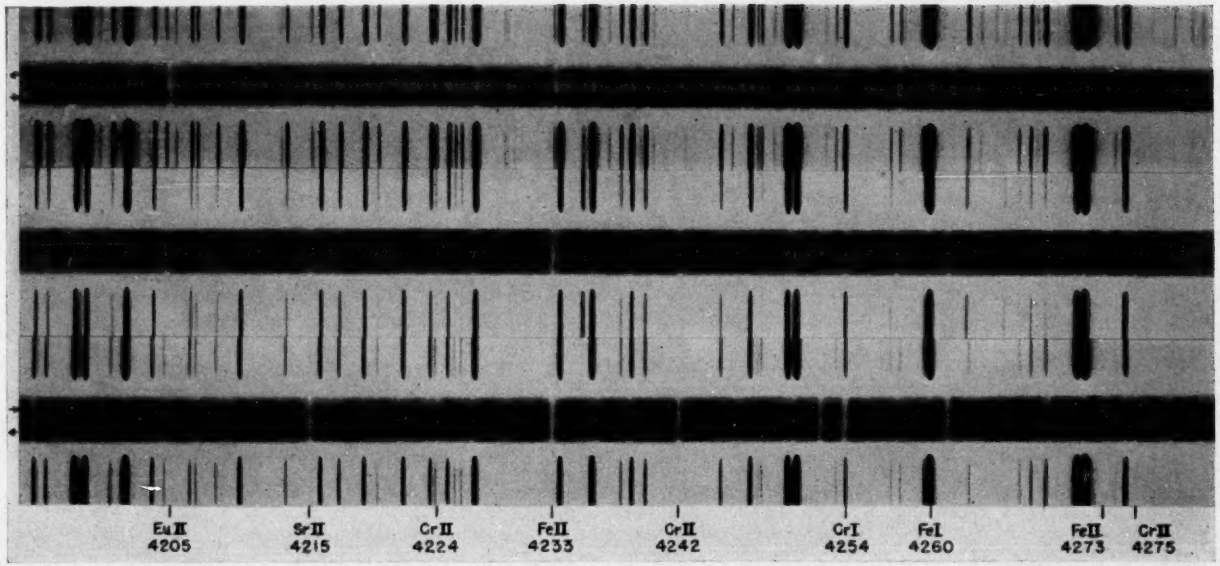

FIG. 3.—The spectrum of HD 125248, λλ 4200–4280, taken with the double polarizing analyzer at phases 0.11 (*top*), 0.77 (*middle*), and 0.55 (*bottom*)

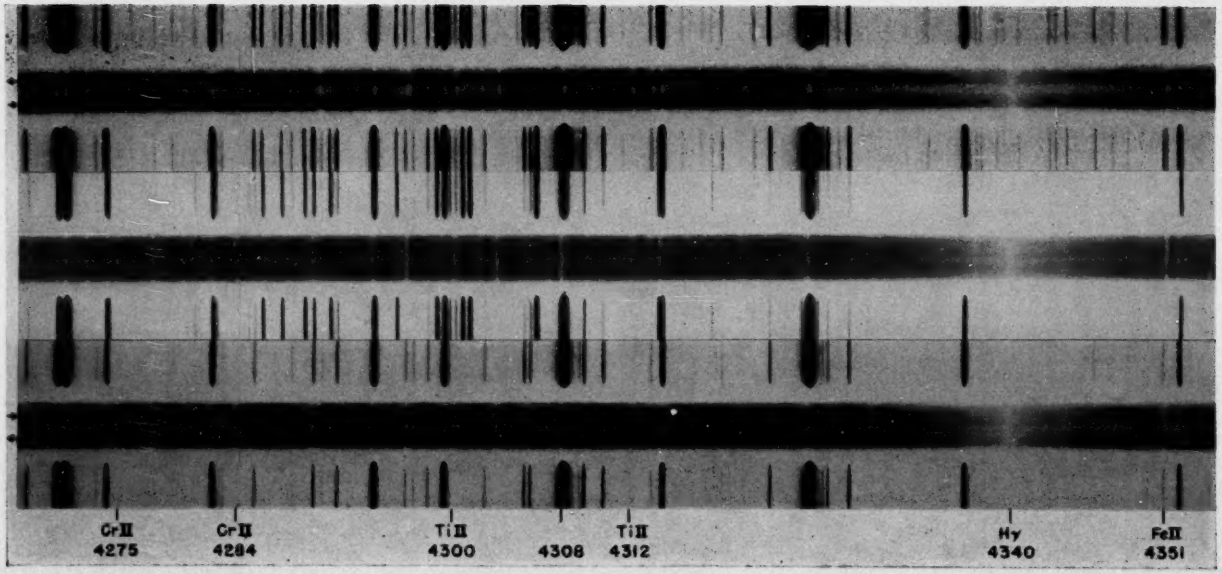

FIG. 4.—The spectrum of HD 125248, λλ 4270–4350, taken with the double polarizing analyzer at phases 0.11 (*top*), 0.77 (*middle*), and 0.55 (*bottom*)

ments from the field intensity indicated by their lines; but such an analysis will have to await the formulation of a satisfactory physical model of the star and its atmosphere.

In Figures 2, 3, and 4 are reproduced sections of double spectra of HD 125248 taken with the analyzer near the times of *Eu* II maximum, three-quarter phase, and *Cr* maximum (phases 0.11, 0.77, and 0.55, respectively). The striking changes in the intensities of lines of groups A and B, first noted by Morgan, are seen. Note particularly *Eu* II λ 4129 and λ 4205, *Cr* II λ 4242, and *Cr* I λ 4254. On the other hand, the intensity of *Fe* II λ 4233 and other lines of group C is nearly constant. At phases 0.11 and 0.55 the small Zeeman displacements for many of the lines between the upper and lower analyzed spectra are visible. Near *Eu* II maximum (0.11) the lines in the upper spectrum of the pair are slightly shifted shortward with respect to the lower (positive magnetic polarity), while at *Cr* maximum (0.55) the shifts are in the opposite direction. On the original spectrograms, many of these differential displacements lie between 10 and 20 μ—many times the probable error of measurement. On plates of the highest dispersion (2.9 A/mm) the shift of *Fe* I λ 4210 ($Z = 3.05$) near *Eu* II maximum is about 0.035 mm.

In Figures 5, 6, 7, and 8 are direct-intensity microphotometer tracings of spectra at phases 0.11, 0.73, and 0.50. The tracings are intended mainly to show changes with phase in total absorption and line depth for the variable lines of groups A and B. Tracings on a larger scale (Fig. 9) were made of short sections of a spectrogram (Ce 5164) taken at phase 0.98 near *Eu* II maximum. Profiles of a few typical lines were recorded, with continuous and dashed traces for the two types of polarization. The Zeeman displacements are visible, as is the approximate correlation of the displacements and of the profile widths with the respective widths of the individual Zeeman patterns, which are indicated for some of the lines. (The pattern widths were computed on the basis of a field of 7500 gauss, which was obtained from the measured displacements.) The Z-value, or mean displacement of the σ components of the pattern, is also given. The tracings of Figure 9 show that the weaker stellar lines with small Z-values such as *Fe* I λ 4178 ($Z =$ 0.80) have a recorded width (0.44A) only slightly greater than the recorded width of lines in the comparison spectrum of the iron arc. These widths are, of course, affected by instrumental broadening in the spectrograph and in the microphotometer. Doppler broadening due to axial rotation is therefore nearly absent. An upper limit of $v_e \sin i$ is perhaps 4 km/sec. It may be concluded that if the star is in rotation with an equatorial velocity v_e of the order of 100 km/sec, typical of type A0, the axis of rotation makes an angle i no larger than about 3° with the line of sight.

On some spectrograms obtained near *Eu* II maximum, the occurrence of a few weak emission lines was suspected; however, it was usually impossible to confirm these on other plates. An exception is a feature on the longward edge of λ 4212, which is shown on the tracings of Figures 6 and 9.

The original spectrograms were measured in both directions for Zeeman displacements and for radial velocity. For each line, several settings were made alternately on the upper and lower spectrum, the difference in microns being noted for the Zeeman shift, while the mean of the upper and lower settings was recorded for wave-length determination. The plates were turned end for end and also turned over for the reverse measurement, which was made through the glass; this procedure was designed to minimize personal error in the settings by reversing the apparent displacement of the upper spectrum with respect to the lower. Blends were avoided in so far as possible. Fifteen plates were measured by Miss Sylvia Burd and eleven by the writer; three other plates were measured by both. For one of the last (Ce 4704, phase 0.11) a correlation plot of Δs_c as found by the two measurers is given in Figure 10.

The Z-values, or relative displacements of the blended normal components of the Zeeman patterns of the lines as compared to a normal triplet, were computed or obtained from the tables of Kiess and Meggers,[9] except that an attempt was made to use

[9] *Bur. Standards Res. Paper No. 23* (Washington: Government Printing Office, 1928).

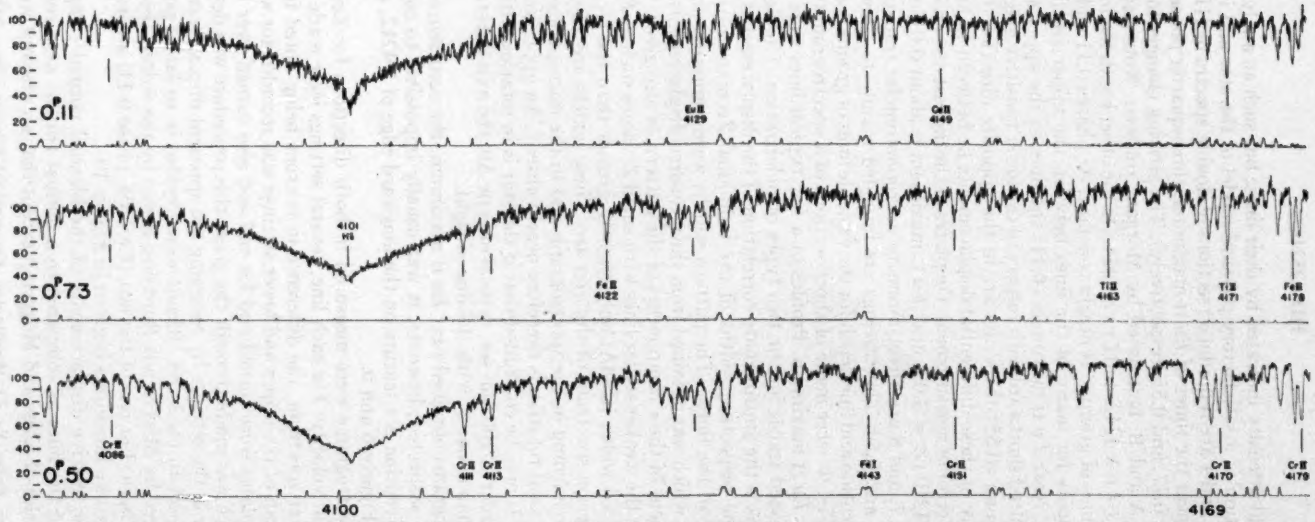

FIG. 5.—Direct-intensity tracings of the variable spectrum of HD 125248, λλ 4080–4180, at three phases corresponding approximately to *Eu* II maximum (*top*), cross-over (*middle*), and *Cr* maximum (*bottom*).

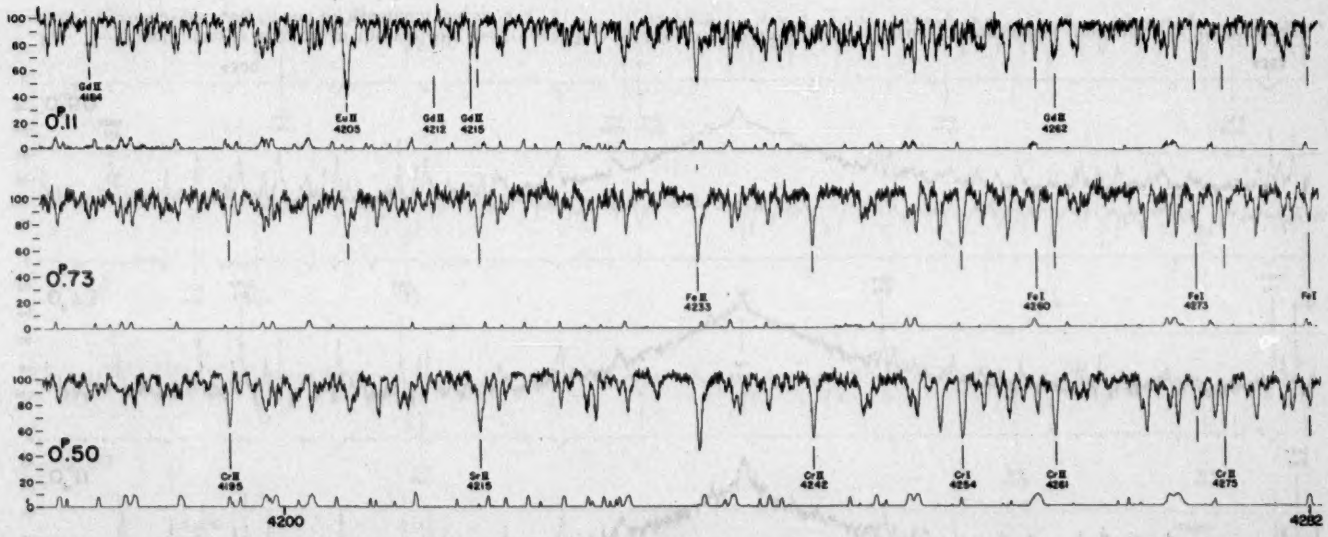

FIG. 6.—Direct-intensity tracings of the variable spectrum of HD 125248, λλ 4180–4280, at three phases corresponding approximately to *Eu* II maximum (*top*), cross-over (*middle*), and *Cr* maximum (*bottom*).

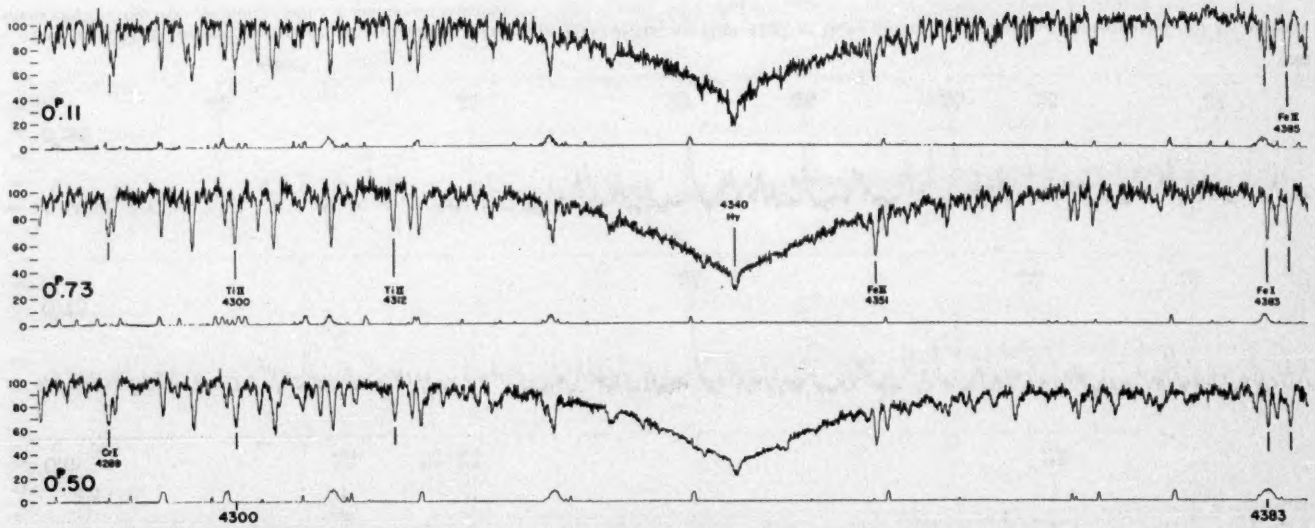

FIG. 7.—Direct-intensity tracings of the variable spectrum of HD 125248, λλ 4280–4380, at three phases corresponding approximately to *Eu* II maximum (*top*), cross-over (*middle*), and *Cr* maximum (*bottom*).

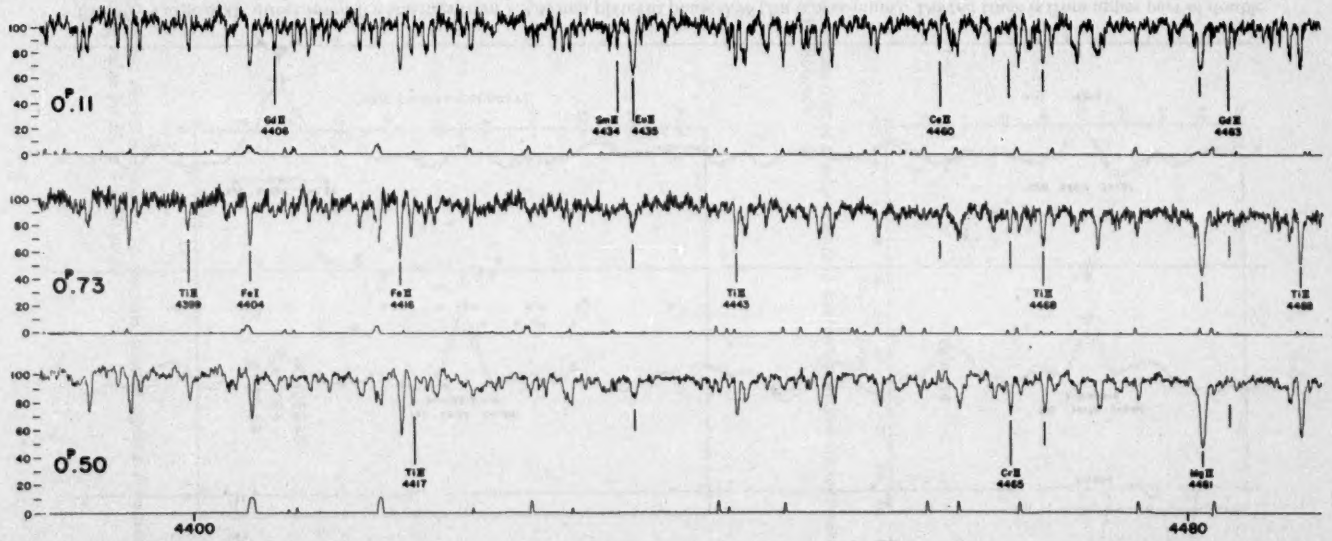

FIG. 8.—Direct-intensity tracings of the variable spectrum of HD 125248, λλ 4390–4490, at three phases corresponding approximately to *Eu* II maximum (*top*), cross-over (*middle*), and *Cr* maximum (*bottom*).

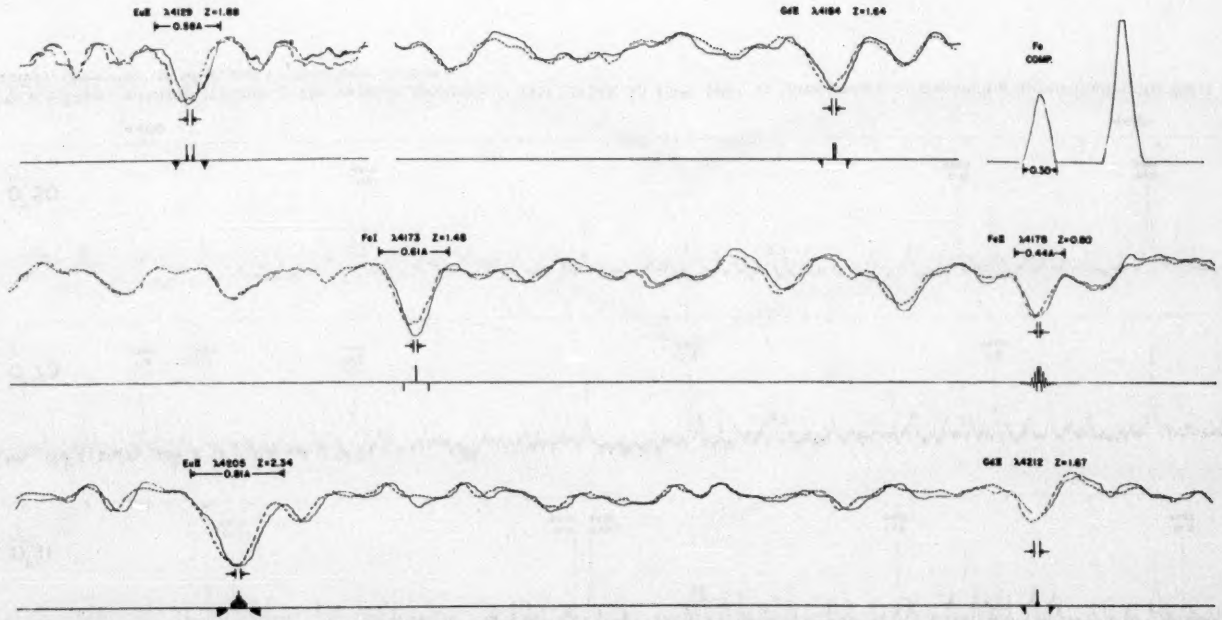

FIG. 9.—Large-scale direct-intensity tracings from 2.9 A/mm plates at phase 0.98 (*Eu* II maximum). Dotted trace is from upper part of double spectrum, continuous trace from lower part, to show displacements resulting from polarization in a stellar magnetic field with $H_p = 7500$ gauss. Zeeman patterns for the prominent lines are plotted to scale.

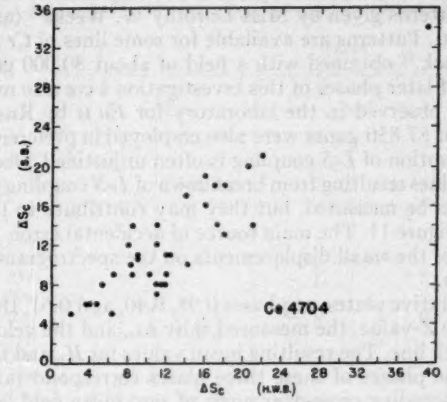

FIG. 10.—Correlation plot of displacements in microns measured for individual lines by Miss Sylvia Burd and by H. W. Babcock.

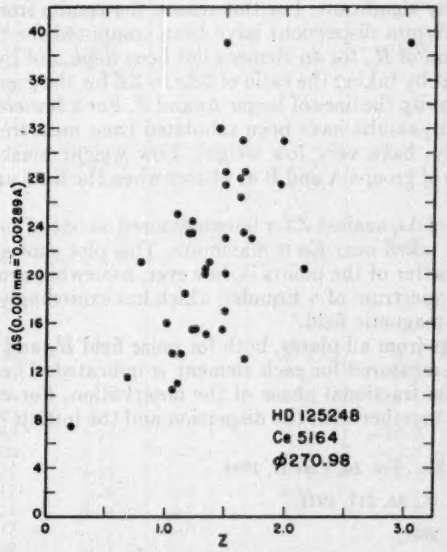

FIG. 11.—Measured displacements, Δs, in microns, plotted against Z-values for the lines at phase 0.98. The resulting value for H_p is +7600 gauss.

observed laboratory patterns when available. For many lines of *Fe* I the *Z*-values were obtained from the patterns given by Miss Dorothy W. Weeks[10] (as observed in a field of about 85,000 gauss). Patterns are available for some lines of *Cr* from the laboratory work of H. D. Babcock,[11] obtained with a field of about 30,000 gauss; additional but unpublished results of later phases of this investigation were also made available to the writer. The patterns observed in the laboratory for *Eu* II by Russell, Albertson, and Davis[12] with a field of 87,850 gauss were also employed in preference to computed patterns, since the assumption of *L-S* coupling is often unjustified. Occasional small errors in the computed *Z*-values resulting from breakdown of *L-S* coupling are not serious when many stellar lines can be measured, but they may contribute to the dispersion of the points as plotted in Figure 11. The main source of accidental error, however, is inherent in the measurement of the small displacements on the spectrograms, as affected by the grain of the emulsion.

For three representative plates, at phases 0.98, 0.40, and 0.61, the lines measured are listed in Table 1. The *Z*-value, the measured shift Δs_c, and the velocity (reduced to the sun) are given for each line. The resulting mean values for H_p and for velocity are given for each element. The phases of these three plates correspond rather closely to *Eu* II maximum, to the descending cross-over point of zero mean field, and to *Cr* maximum, respectively. Particularly on plates taken near the cross-over points, it is found that various elements yield different values of H_p. At phase 0.40, for example (Table 1), the indicated H_p in gauss for *Eu* II is +1900; *Fe* I, −1750; *Fe* II, +280; *Ti* II, −1560; *Cr* I, −3960; and *Cr* II, −4600. Where as many as ten lines are measured, the probable errors of the determinations are only a few hundred gauss, and the differences must therefore be physically significant. For this reason the results from most of the plates (except some of 10 A/mm dispersion) have been computed for the various elements separately. Calculation of H_p for an element has been done, not by taking the mean of $\Delta s/Z$ for the lines, but by taking the ratio of $\Sigma\Delta s$ to ΣZ for the group; this is equivalent to weighting more heavily the lines of larger Δs and Z. For a few elements, such as *Si* II, *Sr* II, *Ca* II, and *Mg* II, results have been tabulated from measures of only one or two lines; these, naturally, have very low weight. Low weight must also be assigned to measures of elements of groups A and B at phases when the lines are too weak for accurate measurement.

Figure 11 is a plot of Δs_c against Z for lines measured on one of the plates of dispersion 2.9 A/mm (Ce 5164) taken near *Eu* II maximum. This plot shows the general increase of Δs_c with Z. The scatter of the points is, however, somewhat greater than for similar measurements in the spectrum of γ Equulei, which has exceedingly sharp lines and, apparently, a constant magnetic field.[7]

Table 2 lists results from all plates, both for polar field H_p and for radial velocity v. The number of lines measured for each element is indicated. The results are listed in order according to the fractional phase of the observation. For each spectrogram the date (U.T.) is given, together with the dispersion and the initials of the measurer.

[10] *Trans. Amer. Phil. Soc.*, Vol. **34**, Part II, 1944.

[11] H. D. Babcock, *Ap. J.*, **33**, 217, 1911.

[12] *Phys. Rev.*, **60**, 641, 1941.

TABLE 1

TYPICAL MEASUREMENTS FOR ZEEMAN EFFECT AND VELOCITY

λ (I.A.)	z	Phase 0.98 Δs_c (μ)	0.98 v (Km/Sec)	0.40 Δs_c (μ)	0.40 v (Km/Sec)	0.61 Δs_c (μ)	0.61 v (Km/Sec)
Fe I							
3997.394	1.11w	.....	.....	.....	.....	−12	− 5.1
4005.246	1.72w	.....	.....	.....	.....	−18	− 9.1
4045.815	1.25w	.....	.....	− 1	− 7.8	− 7	− 7.5
4063.597	1.09w	.....	.....	.....	.....	− 7	−10.2
4071.740	0.69w	+12	−2.1	− 5	− 7.9	−12	− 7.4
4143.871	1.67w	+13	−2.6	.....	.....	− 8	− 9.0
4199.098	1.08w	.....	.....	.....	.....	− 3	− 9.5
4202.031	1.20w	.....	.....	.....	.....	−10	− 9.9
4203.987	1.45	+32	−1.6	.....	.....	.....	.....
4210.352	3.05w	+39	−5.9	.....	.....	.....	.....
4219.364	1.07w	.....	.....	.....	.....	− 9	− 7.9
4227.434	1.12w	.....	.....	.....	.....	− 9	−10.2
4235.942	1.65	.....	.....	.....	.....	+24	− 3.2
4238.816	1.22w	.....	.....	.....	.....	−21:	− 9.3
4243.786	1.22	.....	.....	.....	.....	+24	− 2.3
4250.790	0.96w	+25	−3.5	.....	.....	− 3	− 9.7
4260.479	1.62w	+26	−0.8	.....	.....	− 1:	− 6.1
4271.159	1.43w	.....	.....	.....	.....	− 9	− 8.4
4271.764	1.26w	+16	−0.1	− 5	− 6.0	− 6	− 5.9
4282.406	1.22	+16	−0.2	.....	.....	− 7	− 6.2
4294.128	1.20	+23	−1.3	.....	.....	.....	.....
4383.547	1.16w	+18	−3.9	− 6	− 7.9	−12	− 7.8
4404.752	1.17w	.....	.....	+ 5	− 7.3	− 8	− 8.4
H_p (gauss)	.....	+7600 ± 450	.....	−1750 ± 760	.....	−5680 ± 550	.....
v (km/sec)	.....	.....	−2.4 ±0.31	.....	− 7.4 ±0.28	.....	− 8.2 ±0.25
Fe II							
3935.942	1.00	.....	.....	.....	.....	− 4	− 7.0
3938.289	1.63	.....	.....	.....	.....	−13	− 7.7
3938.969	0.90	.....	.....	.....	.....	−17	− 7.4
4012.467	0.40	.....	.....	+ 1	− 8.9	−10	− 8.4
4024.552	1.20	.....	.....	− 3	− 8.3	−12	− 7.6
4044.01	0.86	.....	.....	.....	.....	− 6	− 8.4
4057.457	0.89	.....	.....	.....	.....	−12	− 9.2
4173.475	1.48	+16	−3.5	−10	−10.1	.....	.....
4178.855	0.80	+21	−2.1	− 6	− 9.9	− 9	− 7.2
4233.167	1.22	+24	−1.6	− 1	− 5.5	.....	.....
4273.317	2.17	+20	+1.2	+18	.....	.....	.....
4278.128	0.21	+ 8	+1.1	.....	.....	− 3	− 6.8
4303.166	1.47	.....	−0.5	.....	.....	− 7	− 8.4
4351.764	1.10	+11	−1.3	.....	.....	.....	.....
4357.574	.....	+28	−0.2	.....	.....	.....	.....
4361.249	.....	+24	+1.5	.....	.....	.....	.....
4385.381	1.33	.....	.....	+ 2	− 5.3	.....	.....
4416.817	0.83	.....	.....	− 6	− 7.4	− 8	− 9.1
4508.26	1.25	+22	−0.7	.....	.....	.....	.....
4515.337	1.03	+14	−0.7	.....	.....	.....	.....

TABLE 1—*Continued*

λ (I.A.)	Z	Phase 0.98 Δs_c (μ)	Phase 0.98 v (Km/Sec)	Phase 0.40 Δs_c (μ)	Phase 0.40 v (Km/Sec)	Phase 0.61 Δs_c (μ)	Phase 0.61 v (Km/Sec)
4520.225				+ 4	− 7.6		
4522.634	0.91			0	− 8.3		
4541.523	0.80	+14	−1.2				
H_p (gauss)		+7270 ± 960		+280 ±990		−7970 ± 980	
v (km/sec)			−0.7 ±0.28		−8.1 ±0.36		−7.9 ±0.20
Ti II							
4028.332	1.06					− 2	− 7.6
4163.644	1.07	+10	−3.5				
4290.222	1.10					− 9	− 6.8
4294.101	1.20	+24	−3.2	+ 1	− 7.8		
4300.052	1.22	+28	−2.2			− 8	−10.1
4301.934	0.84	+22	−3.5			−11	− 7.7
4307.900	1.47	+14	−3.5	+ 3	− 8.1		
4312.861	1.48	+21	−0.1			−11	− 4.9
4314.979	1.33	+20	−1.5			− 3	− 7.5
4337.916	0.80					− 6	− 9.2
4395.031	1.07	+14	−4.1	− 8	− 7.9	− 7	− 8.0
4395.848	1.22					−14	−10.6:
4399.767	1.40					− 6	− 8.3
4417.718	0.80					− 6	− 7.6
4443.802	0.90	+16	−3.6	− 1	− 9.9	− 4	− 8.7
4450.487	1.03					−14	−10.0
4468.493	1.05	+17	−3.4	− 7	− 8.2	−10	− 8.0
4501.270	0.93	+26	−3.0				
H_p (gauss)		+8250 ± 615		−1560 ± 985		−5600 ± 575	
v (km/sec)			−2.9 ±0.24		− 8.4 ± 0.26		− 8.2 ± 0.26
Eu II							
3930.50	1.96	+28					
4017.58	1.31					−10	−11.4
4129.737	1.88	+31	−4.2	+ 3:	− 8.5		
4205.046	2.34	+28	−3.9	+ 8:	− 7.7	−27	− 8.1
4435.58	1.88	+30	−4.2			−23	−11.6
H_p (gauss)		+7170 ± 330		+1900		−8250 ± 750	
v (km/sec)			−4.1 ±0.07		− 8.1 ± 0.3		−10.4 ± 0.77
Ce II							
4040.762	1.01	+16	−3.6				
4151.970	1.50	+17	−2.0				

TABLE 1—*Continued*

λ (I.A.)	z	Phase 0.98 Δs_c (μ)	Phase 0.98 v (Km/Sec)	Phase 0.40 Δs_c (μ)	Phase 0.40 v (Km/Sec)	Phase 0.61 Δs_c (μ)	Phase 0.61 v (Km/Sec)
4165.606	1.04	.....	.....	.....	.....	− 6	−10.4
4202.944	.....	+12	−1.3	.....	.....	.....	.....
H_p (gauss)	.....	+6500	.....	.....	.....	.....	.....
		.....	.....	.....	.....	.....	.....
v (km/sec)	.....	.....	−2.3	.....	.....	.....	.....
		.....	±0.46	.....	.....	.....	.....
Gd II							
4184.252	1.64	+31	−1.6	.....	.....	.....	.....
4212.001	1.67	+28	−4.9	.....	.....	.....	.....
4215.023	1.34	+15	−4.9	.....	.....	.....	.....
4238.782	.....	+32	−3.1	.....	.....	.....	.....
4251.733	1.72	+23	−1.0	.....	.....	.....	.....
4483.328	1.32	+26	−0.8	.....	.....	.....	.....
H_p (gauss)	.....	+7740	.....	.....	.....	.....	.....
		± 490	.....	.....	.....	.....	.....
v (km/sec)	.....	.....	−2.7	.....	.....	.....	.....
		.....	±0.51	.....	.....	.....	.....
Nd II							
4205.595	1.50	+28	−2.6	.....	.....	.....	.....
La II							
4296.05	1.50	+39	−2.9	.....	.....	.....	.....
Cr I							
3963.690	1.14	.....	.....	.....	.....	−16	− 8.8
3983.907	0.88	.....	.....	.....	.....	−13	− 7.2
3991.123	0.67	.....	.....	.....	.....	−10	− 8.8
3991.673	0.71	.....	.....	.....	.....	−18	− 5.6
4254.346	1.38	.....	.....	− 4	− 4.1	.....	.....
4274.803	1.96	.....	.....	0	− 8.8	.....	.....
4289.721	2.00	.....	.....	−16	− 8.4	.....	.....
4351.770	1.20	.....	.....	− 2	− 7.5	.....	.....
4391.753	2.00	.....	.....	−16	−10.0	−17	− 6.7
H_p (gauss)	.....	.....	.....	−3960	.....	−10600	.....
		.....	.....	±1000	.....	±1400	.....
v (km/sec)	.....	.....	.....	.....	.....	.....	.....
		.....	.....	.....	− 8.8	.....	− 7.4
Cr II							
3979.51	1.07	.....	.....	.....	.....	− 3	− 5.4
4003.33	0.94	.....	.....	.....	.....	− 8	−10.7
4017.96	1.80	.....	.....	.....	.....	−25	− 4.7
4022.36	1.03	.....	.....	− 1	− 8.8	−10	− 6.9
4038.03	1.04	.....	.....	−15	−14.6	−17	−11.4

TABLE 1—*Continued*

λ (I.A.)	z	Phase 0.98 Δs_c (μ)	0.98 v (Km/Sec)	0.40 Δs_c (μ)	0.40 v (Km/Sec)	0.61 Δs_c (μ)	0.61 v (Km/Sec)
4051.97	1.14	.....	.....	.....	.....	−10	− 7.7
4056.07	0.40	.....	.....	.....	.....	−10	− 6.2
4070.90	1.12b	.....	.....	− 4	−14.7	−11	−12.1
4072.56	0.83	.....	.....	− 5	− 9.6	−11	− 7.7
4082.30	1.11	.....	.....	.....	.....	− 8	− 7.7
4111.01	1.16	.....	.....	.....	.....	−12	− 9.8
4113.24	1.50	.....	.....	.....	.....	−17	− 9.8
4127.08	1.20	.....	.....	.....	.....	−12	− 8.4
4145.77	1.20	.....	.....	.....	.....	− 9	− 8.4
4151.00	1.07	.....	.....	.....	.....	− 8	− 6.9
4161.05	1.50	.....	.....	.....	.....	−19	− 6.9
4179.43	1.22	.....	.....	− 5	−11.4	−12	− 9.8
4195.41	1.40	.....	.....	− 2	− 9.1	−11	− 7.6
4207.35	1.48	.....	.....	−12	−12.2	−14	− 8.3
4209.02	1.50	.....	.....	.....	.....	−18	− 3.4
4217.07	0.84	.....	.....	.....	.....	−11	− 8.3
4222.02	0.60	.....	.....	.....	.....	− 5	− 5.5
4224.85	0.87	.....	.....	−16	− 8.5	−11	− 6.9
4229.81	1.90	.....	.....	.....	.....	−27	− 6.2
4242.38	1.17	.....	.....	− 5	−10.9	−10	− 9.0
4252.62	1.20	.....	.....	− 4	− 9.1	−13	− 6.9
4256.16	1.11	.....	.....	.....	.....	−12	− 9.7
4261.92	1.07	.....	.....	+ 2	− 8.9	− 7	− 8.3
4268.93	0.89	.....	.....	.....	.....	− 7	− 6.9
4269.28	0.80	.....	.....	.....	.....	− 4	− 7.6
4275.57	0.96b	.....	.....	− 2	−10.5	−10	− 8.3
4284.21	0.42b	.....	.....	−12	− 9.6	− 4	− 7.6
4362.93	0.90	.....	.....	.....	.....	−13	− 4.1
4465.78	1.04	.....	.....	.....	.....	−20	−10.2
H_p (gauss)	.....	.....	.....	−4600 ±1220	.....	−8260 ±1165	.....
v (km/sec)	.....	.....	.....	.....	−10.6	.....	− 7.8
Sr II							
4077.714	1.17	.....	.....	− 2	−15.1	.....	.....
4215.524	1.33	20	−2.0	.....	.....	− 7	− 5.6
Mg II							
4481.228	0.98	.....	.....	− 4	− 8.9	.....	.....
Ca II							
3933.644	1.17	.....	.....	+ 8	− 8.6	.....	−10.7
3968.470	.....	.....	.....	.....	.....	.....	−10.9

TABLE 2

MAGNETIC INTENSITY, H_p, AND RADIAL VELOCITY FOR ELEMENTS AT VARIOUS PHASES

Phase	H_p (Gauss)	No. of Lines	v (Km/Sec)
239.01	*Fe* I +9800	2	.....
Ce 4722	*Fe* II +7300	11	.....
1947 June 28.194	*Ti* II +6020	8	.....
10.3 A/mm.	*Cr* II +10000	1	.....
H.W.B.	*Co* I +9300	1	.....
	Lu II +4200	1	.....
	Eu II +5400	5	.....
	Ca II +7500	1	.....
341.04	*Fe* I, *Fe* II, *Ti* II +8300	16	.....
Ce 6109			
1950 Jan. 31.535			
10.2 A/mm	*Eu* II +7250	5	.....
H.W.B.	*Ca* II +5000	1	.....
343.08	*Fe* I +6500	22	−17.7±0.29
Ce 6139	*Fe* II +6700	23, 25	−16.6±0.21
1950 Feb. 19.50	*Ti* II +6400	14	−16.2±0.25
4.49 A/mm	*Eu* II +6720	5	−17.4±0.67
S.B.	*Ce* II +8080	14, 16	−16.6±0.45
	Gd II +6870	15	−16.4±0.30
	Sr II +7650	2	−18.5
	Ca II +4900	2	−16.8
236.11	*Fe* I +7850	17	−12.4±0.29
Ce 4704	*Fe* II +6580	24, 26	−12.2±0.32
1947 June 1.252	*Ti* II +7800	19, 20	−10.9±0.25
4.54	*Eu* II +5960	5	−12.8±1.10
S.B., H.W.B.	*Gd* II +7450	7	− 9.7±0.37
	Ca II +6600	1	−11.6
	Sr II +3000	1	−12.3
	H	3	−10.4
360.15	*Fe* I	21	−21.3±0.42
Ce 6374			
1950 July 28.146			
10.4			
S.B.			
230.21	*Fe* I +4780	6	.....
Ce 4641	*Fe* II +5500	10	.....
1947 April 7.391	*Ti* II +6060	2	.....
4.54	*Eu* II +4500	2	.....
H.W.B.			
239.23	*Fe* I +5250	8	.....
Ce 4728	*Fe* II +5600	11	.....
1947 June 30.231	*Ti* II +2920	4	.....
4.55	*Eu* II +4700:	2	.....
H.W.B.	*Mg* II +4000	1	.....
Weak $<\lambda$ 4250			
270.23	*Fe* I +5540±	43	− 5.1±0.20
Ce 5141	*Fe* II +4510±	30	− 5.4±0.16
1948 Apr. 13.356	*Ti* II +5270±	15	− 4.0±0.22
4.55	*Cr* II +3870	11	− 8.4±0.49
S.B.	*Eu* II +6800	5	− 5.4±0.39
	Gd II +4750	5	− 3.9±0.75
	Ce II +5200	14	− 4.2±0.20
	Sr II +5250	1	− 2.4

TABLE 2—*Continued*

Phase	H_p (Gauss)	No. of Lines	v (Km/Sec)
270.23—*Continued*.....	*Mn* I +6250	1	− 3.8
	Co I +7000	1	− 1.8
	Ca II +8600	1	.....
270.33.....	*Fe* I +4130	22	− 4.7±0.27
Ce 5144	*Fe* II +3100±370	26	− 4.0±0.21
1948 Apr. 14.333	*Ti* I +1800	1	− 9.9
4.55	*Cr* I + 400:	2	− 4.0
S.B.	*Cr* II +1590±490	21	− 7.0±0.31
	Eu II +5460±560	3	− 4.2±0.26
	Si II +10300	1	− 1.8
	Mg II +6200	1	− 2.7
	Al II.....	1	− 5.2
	H.....	1	− 1.7
341.36.....	*Fe* I −1370	14	−17.7±0.31
Ce 6121	*Fe* II − 850	24	−16.6±0.19
1950 Feb. 3.518	*Ti* II − 200	10	−16.3±0.31
4.5	*Cr* I −2710	3	−17.7±1.34
S.B.	*Cr* II −2270	21	−19.7±0.25
	Eu II +1000	1	−17.8
	Sr II 0	1	−13.6
	Mg II −3900	1	−17.8
	Ca II −2450	2	−17.2±0.20
312.40.....	*Fe* I −1750±750	5	− 7.4±0.28
Ce 5635	*Fe* II + 280±1000	10	− 8.1±0.36
1949 May 10.306	*Ti* II −1560±1000	5	− 8.4±0.26
4.54	*Cr* I −3960±1000	5	− 7.8±0.67
H.W.B.	*Cr* II −4600±1200	13	−10.6±0.39
	Eu II +1900	2	− 8.1±0.3
	Sr II −1650	1	−15.1
	Mg II −3200	1	− 8.9
	Ca II +5300	1	− 8.6
274.42.....	*Fe* I −3700	6	− 7.1±0.36
Ce 5185	*Fe* II −3450	13	− 6.3±0.08
1948 May 22.260	*Ti* II −3200	1	− 4.8
4.55	*Cr* I −5200	6	− 7.1±0.50
H.W.B.	*Cr* II −4600	17	− 8.5±0.24
	Eu II.....	2	− 6.3±0.3
	Si II +4650	1	− 4.1
	Mg II 0:	1	− 6.5
	Ca II −2000	1	− 8.2
	H.....	2	− 7.3
308.43.....	*Fe* I.....	30	− 5.2±0.23
Ce 5596	*Fe* II.....	13	− 5.3±0.46
1949 Apr. 3.462	*Ti* II.....	13	− 5.2±0.28
4.48	*Cr* I.....	7	− 7.3±0.26
No analyzer	*Cr* II.....	27	− 7.5±0.24
S.B.			
312.50.....	*Fe* I −5500	8	− 8.4±0.28
Ce 5638	*Fe* II −6380	12	− 8.2±0.13
1949 May 11.277	*Ti* II −5700	2	− 6.9
4.55	*Cr* I −6940	4	− 9.0±0.35
S.B.	*Cr* II −7250	29	− 9.7±0.19
	Eu II −5500	4	−12.8±0.90
	Ce II −9000	1	−10.6
	Sr II −3500	1	− 5.9
	Ca II.....	2	−10.7
	H.....	3	− 9.1

TABLE 2—*Continued*

Phase	H_p (Gauss)	No. of Lines	v (Km/Sec)
315.51	*Fe* I −6160	17	− 8.7±0.25
Ce 5655	*Fe* II −6030	21	− 8.2±0.22
1949 June 8.246	*Ti* II −5890	11	− 8.3±0.35
4.55	*Cr* I −6040	8	− 8.4±0.51
S.B.	*Cr* II −7195	32	− 9.8±0.20
	Eu II −6060	4	−10.7±0.99
270.55	*Fe* I −5000±400	7, 11	− 3.2±0.21
Ce 5149	*Fe* II −5100±500	14, 8	− 3.0±0.19
1948 Apr. 16.356	*Ti* I −4300	2, 1	− 1.3
4.55	*Ti* II −4750	11	− 3.0±0.49
S.B., H.W.B.	*Eu* II −4180	4	− 7.0±0.32
	Cr I −7340±300	6, 2	− 4.2±1.0
	Cr II −6850±550	23, 16	− 3.8±0.36
	Mg I −5000	1	.....
	Mg II −7000	1	.....
	Si II −6000	1	− 0.8
	Ca II −7300	1	− 8.3
	H	3	− 7.7±0.90
312.61	*Fe* I −5680±550	18	− 8.2±0.25
Ce 5642	*Fe* II −7970±980	12	− 7.7±0.20
1949 May 12.269	*Ti* I	1	− 8.8
4.55	*Ti* II −5600±570	14	− 8.2±0.26
S.B.	*Cr* I −10600±1400	5	− 7.4±0.42
	Cr II −8260±1160	34	− 7.8±0.23
	Eu II −8250±750	3	−10.4±0.77
	Ce II −4500	1	−10.4
	Mn II	1	− 9.8
	Sr II −4100	1	− 5.6
	Ca II	2	−10.8
	H	3	− 7.1
264.65	*Fe* I −3230	10	− 5.3±0.36
Ce 5099	*Fe* II −3280	20	− 5.1±0.24
1948 Feb. 21.501	*Ti* II −2950	11	− 5.3±0.30
4.55	*Cr* I −5320	4	− 3.2±0.78
S.B.	*Cr* II −4430	22	− 5.1±0.30
	Eu II −2750::	3	− 5.1±0.46
	Si II 0:	1	− 3.7
	Sr II −4100	1	− 1.5
	Mg II +2200	1	.....
	Ca II +2000	1	− 6.8
	H	3	− 4.9±2.4
270.66	*Fe* I −4300	18	− 5.6±0.18
Ce 5152	*Fe* II −3150	24	− 5.3±0.16
1948 Apr. 17.375	*Ti* I −2560	1	− 6.1
4.54	*Ti* II −3480	15	− 4.9±0.28
S.B.	*Cr* I −7810	5	− 3.4±0.63
	Cr II −5300	29	− 5.2±0.20
	Eu II −2720:	4	− 8.5±0.66
	Ce II −8200	1	− 4.3
	Mg II −2370	1	− 5.0
	Ca II	1	− 6.3
242.67	*Fe* I −3060	10	− 7.5±0.43
Ce 4764	*Fe* II −3090	27	− 8.5±0.22
1947 Aug. 1.169	*Ti* II −4510	10	− 8.8±0.32
10.3	*Cr* I −4020	6	− 7.2±0.69
S.B., H.W.B.	*Cr* II −4540	31	− 8.9±0.28
	Eu II −6930	3	−11.5±0.34
	Si II −6300	1	− 6.4

TABLE 2—*Continued*

Phase	H_p (Gauss)	No. of Lines	v (Km/Sec)
242.67—*Continued*	*Mg* II −5300	1	− 7.9
	Ca II −2100	2	−11.2
	H	3	−10.5±0.23
315.73.....	*Fe* I +4540±600	13	− 9.2±0.25
Ce 5665	*Fe* II +1830±220	18	− 9.2±0.17
1949 June 10.267	*Ti* II +2600	6	− 9.0±0.17
4.55	*Cr* I −8450±1500	3	− 3.6±0.45
IIa-O	*Cr* II −2810±560	15	− 7.1±0.30
H.W.B.	*Eu* II −1770:	3, 2	−12.8
	Ca II +5000	1	−11.5
242.77.....	*Fe* I +5280	5	.....
Ce 4774	*Fe* II +2530	17	.....
1947 Aug. 2.167	*Ti* II −4130	1	.....
10.3	*Eu* II +4800	2	.....
H.W.B.	*Cr* I −4100	2	.....
	Cr II −1660	6	.....
	Mg II −4200	1	.....
	Ca II +9000	1	.....
270.77.....	*Fe* I +4660	22	− 4.8±0.16
Ce 5154	*Fe* II +3850	27	− 4.4±0.12
1948 Apr. 18.354	*Ti* II +2930	13	− 4.3±0.29
4.54	*Cr* II +1780	26	− 3.1±0.22
S.B.	*Eu* II +5560	2	− 9.1
	Ce II +6550	5	− 6.5
	Ca II.....	1	− 6.9
	H	3	− 2.7
311.86.....	*Fe* I +6200	38	− 9.7±0.18
Ce 5623	*Fe* II +4940	33	− 9.2±0.13
1949 May 5.323	*Ti* I +10500	1	− 5.9
4.55	*Ti* II +6230	18	− 9.8±0.29
S.B.	*Cr* II +2660	11	− 8.7±0.30
	Eu II +7600	4	−13.9±0.86
	Ce II +8070	23	− 9.9±0.24
	Gd II +5140	13	−11.8±0.38
	V II +8200	2	−12.9
	Sr II +2900	1	−11.1
	Ca II +4630	1, 2	−11.1
	H	3	− 7.1
270.88.....	*Fe* I +6950±340	10, 13	− 5.2±0.23
Ce 5160	*Fe* II +5660±450	11, 15	− 4.6±0.34
1948 Apr. 19.365	*Ti* II +5860±310	4	− 5.2±0.38
2.89	*Cr* I −5900:	1	+ 5.5
H.W.B.	*Eu* II +6470±1000	3	− 9.7±0.82
	Ce II.....	4	− 8.4±0.74
	Gd II.....	2	−11.3±0.3
	H	1	−10.4
233.97.....	*Fe* I, II +5850	5	.....
Ce 4692	*Eu* II +5750	5	.....
1947 May 12.276	*Ca* II +2400	1	.....
10.3			
H.W.B.			
311.97.....	*Fe* I +5120	22	− 8.7±0.28
Ce 5627	*Fe* II +5290	22	− 8.4±0.19
1949 May 6.312	*Ti* II +6650	14	− 9.5±0.23
4.55	*Cr* II +6050	3	− 8.3±0.59
S.B.	*Eu* II +4700	5	−11.1±0.49

TABLE 2—*Continued*

Phase		H_p (Gauss)	No. of Lines	v (Km/Sec)
311.97—*Continued*	*Gd* II	+6250	14	−10.6±0.24
	Ce II	+7160	14	− 9.8±0.39
	Sm II	.....	1	−10.0
	V II	+5200	1	− 9.7
	Co I	+1200:	1	− 9.7
	Sr II	+6400	1	− 8.4
	Mg II	+10000:	1	−13.2
	Ca II	+7300	1	− 9.0
	H	.....	1	− 9.3
342.97	*Fe* I	+5980	22	−16.5±0.36
Ce 6130	*Fe* II	+6100	27	−16.2±0.18
1950 Feb. 18	*Ti* II	+7100	9	−18.2±0.28
4.49	*Co* I	+8050	1	−18.7
S.B.	*V* II	+9650	1	−16.1
	Eu II	+4930	4	−18.5±0.47
	Ce II	+7580	7	−17.6±0.42
	Gd II	+7500	5	−18.2±0.56
	Sr II	+5750	1	−19.3
	Ca II	+5510	2	−17.2
270.98	*Fe* I	+7600±440	13	− 2.4±0.31
Ce 5164	*Fe* II	+7270±700	9, 12	− 0.7±0.28
1948 Apr. 20.356	*Ti* I	+3800	1	− 3.5
2.89	*Ti* II	+8250±615	11	− 2.9±0.24
H.W.B.	*Co* I	+6100	1	− 0.2
	Sr II	+7600	1	− 2.0
	Eu II	+7170±330	4, 3	− 4.1±0.07
	Ce II	+6500	2, 3	− 2.3±0.46
	Gd II	+7740±490	5, 6	− 2.7±0.51
	Nd II	+9400	1	− 2.6
	La II	+12800	1	− 2.9
	H	.....	1	− 4.3

MAGNETIC VARIATIONS

Probably the most significant result to be obtained from the data of Table 2 is the curve showing the variation of the magnetic field H_p with time throughout the 9-day cycle. This curve is plotted in Figure 12, *a*, where each point represents the mean value of H_p obtained from equally weighted lines of *Fe* I, *Fe* II, and *Ti* II on a given plate. These elements of group C have been selected because they are fairly concordant and because they are believed to be the most uniformly distributed over the surface of the star; they should therefore give the most realistic representation of the general magnetic field. The tendency toward uniform distribution is inferred from the fact that, while many of the lines of these elements are comparatively strong, their total intensity remains nearly constant. In spite of the difficulties of measurement, some of the deviations from a smooth curve are probably real, and it does not seem possible to improve matters by revising the mean period. There is a suggestion of a slight irregularity in the timing of the magnetic cycle, which is reminiscent of the aperiodic nature of the solar cycle. The deviations from a smooth curve near phases 0.97 and 0.55 suggest either that there are real notches in the magnetic curve near the maxima or that the respective maxima in different cycles are nonuniform in amplitude. Evidence from the velocity-curve may tend to substantiate the notches.

Some real differences in behavior may occur among the elements *Fe* I, *Fe* II, and *Ti* II.

Values of H_p for these elements are plotted individually in Figure 12, *b*. At times of most rapid change of the field, *Fe* I tends to precede *Fe* II, while, near the positive maximum, *Fe* I usually indicates a slightly stronger field than does *Fe* II.

If the minor irregularities near the extremes of the magnetic curve (Figure 12, *b*) are neglected, the smoothed maximum and minimum are close to +7000 gauss and −6200 gauss, respectively, while the curve remains above the zero axis for about 0.65

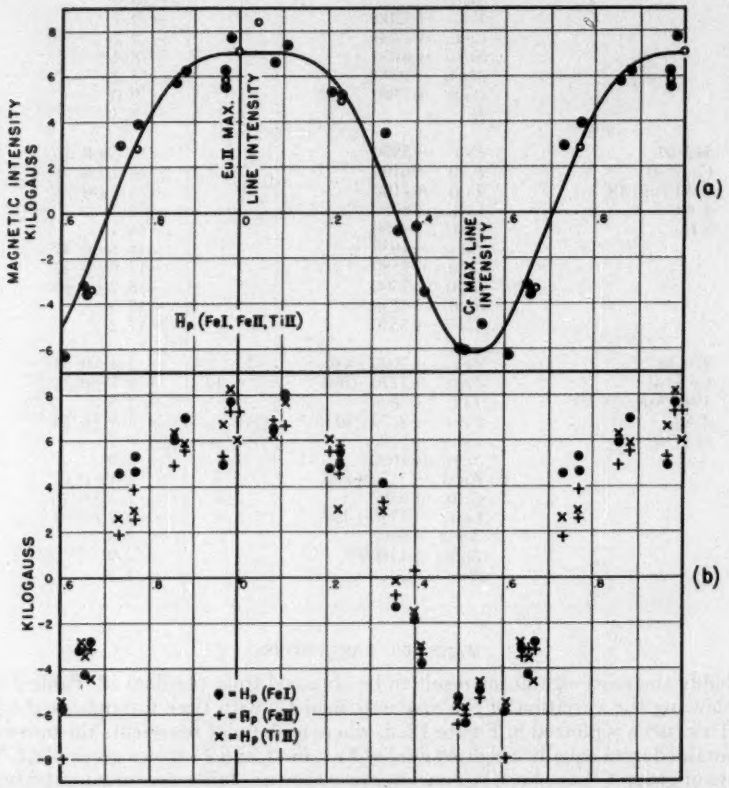

FIG. 12, *a*.—Magnetic field intensity at the pole, H_p, in kilogauss, plotted according to phase in the period of 9.295 days determined by Deutsch from the line-intensity variation (eq. [1]). The points are mean values from *Fe* I, *Fe* II, and *Ti* II. The smooth curve is represented by equation (5). Fig. 12, *b*.—Similar results for the individual elements *Fe* I, *Fe* II, and *Ti* II.

of the period. The positive loop of the curve, corresponding to *Eu* II maximum, appears to be centered about phase 0.03; it seems premature, however, to attempt a correction to the elements. A smooth curve represented by an equation with three disposable constants has been empirically fitted to the plotted points. Neglecting the small phase shift, the equation is

$$H_p = +2000 + 6600 \cos\theta - 1600 \cos 2\theta\,, \qquad (5)$$

where $\theta = 2\pi\nu_0 t$ and $\nu_0 = 1.25 \times 10^{-6}$ cycle/sec.

While the curve is a useful approximation to the data, it does not necessarily give the best possible representation, and the probability of real minor deviations should be recognized. The constant positive term and the first harmonic seem significant.

Magnetic results for the rare-earth elements *Eu* II, *Ce* II, and *Gd* II are plotted in Figure 13, *a*, where for comparison the curve of equation (5), representing the smoothed data for *Fe* I, *Fe* II, and *Ti* II, is also shown. For about half the period, while the magnetic field is positive, the total intensity of the *Eu* II lines is large, but only four or five of these lines are available on most of the plates. Lines of *Ce* II and *Gd* II are weaker, but near zero phase they are more numerous than those of *Eu* II. To a first approximation, the rare earths agree with the *Fe* group in showing a high maximum of magnetic intensity centered near zero phase, but the rare-earth maximum is perhaps broader. There are, in addition, suggestions of secondary variations, and probable differences among the three rare earths. *Ce* II seems to reach a high maximum (8000 gauss, phase 0.86) earlier than the others. For *Eu* II, as for the *Fe* group, there is some evidence for an abrupt fluctuation shortly before zero phase.

The large total absorption of the *Eu* II lines near maximum may be attributed provisionally to a combination of a temporary high effective abundance and magnetic intensification by Zeeman broadening. It has been shown that the observed lines of *Eu* II are particularly susceptible to the latter effect because of numerous components in their Zeeman patterns and because of the inherently narrow Doppler profiles of heavy elements.[18] If saturation of the blended components of these absorption lines occurs (curve-of-growth effect), as is highly probable, the Zeeman displacements as observed through the polarizing analyzer will be correspondingly reduced, with the result that a smaller H_p will be indicated for the affected lines.

The intensities of the *Eu* II lines are weak and probably about constant between phases 0.3 and 0.7, as Deutsch has pointed out. The profiles are shallow but remain rather broad. It was possible, however, to measure some of these lines for magnetic-field intensity in this interval near *Cr* maximum; the values of H_p, which are of relatively low weight for *Eu* II in this part of the cycle, agree roughly with the curve for the *Fe* group.

Figure 13, *b*, shows the magnetic data for *Cr* I and *Cr* II, where again the smooth curve for the *Fe* group is reproduced for comparison. As was discovered by Morgan, the intensities of the lines of the neutral and of the singly ionized element reached maximum together; those of *Cr* II in particular are numerous, moderately strong, and nicely measurable near mid-period. The actual minimum of visibility of *Cr* II lines seems to occur near phase 0.1; none was measured with certainty on plate Ce 4704. There are, however, four well-determined points for *Cr* II in the positive part of the cycle (phases 0.76, 0.86, 0.23, and 0.33). The extreme negative magnetic field is found at phase 0.61, when H_p is -8260 gauss from thirty-four lines of *Cr* II and $-10{,}600$ gauss from five lines of *Cr* I. The negative loop of the curve delineated by *Cr* is deeper and wider than that found from the *Fe* group. Put in another way, the negative values of H_p for *Cr* are about 2 kilogauss stronger than those for *Fe*. Particularly when the field is changing rapidly from negative to positive (phase 0.6–0.8), *Cr* I seems to lag behind *Cr* II.

Near *Cr* maximum, the lines of this element are as strong as those of *Fe* II and stronger than lines of *Fe* I. In this part of the cycle, then, *Cr* is perhaps as well distributed over the visible hemisphere of the star as are *Fe* and *Ti*. If, at phase 0.61, we take the mean H_p for *Fe* I, *Fe* II, *Ti* II, *Cr* I, and *Cr* II, giving equal weight to each, we obtain -7620 gauss for the extreme negative field. For comparison with the positive extreme, consider the results from the high-dispersion spectrogram Ce 5146 at phase 0.98. A simple mean of all elements represented by four or more measured lines—*Fe* I, *Fe* II, *Ti* II, *Eu* II, and

[18] H. W. Babcock, *Ap. J.*, **110**, 126, 1949.

Gd II—gives $H_p = +7605$ gauss. The results for the extremes are summarized in the accompanying tabulation. This comparison emphasizes the fact that there are rather

	Extreme Field (H_p)	
	Eu II Max.	*Cr* Max.
Fe I, *Fe* II, *Ti* II (smoothed curve)	+7000	−6200
Phase 0.98 (*Fe* I, *Fe* II, *Ti* II, *Eu* II, *Gd* II)	+7605	.....
Phase 0.61 (*Fe* I, *Fe* II, *Ti* II, *Cr* I, *Cr* II)	.....	−7620

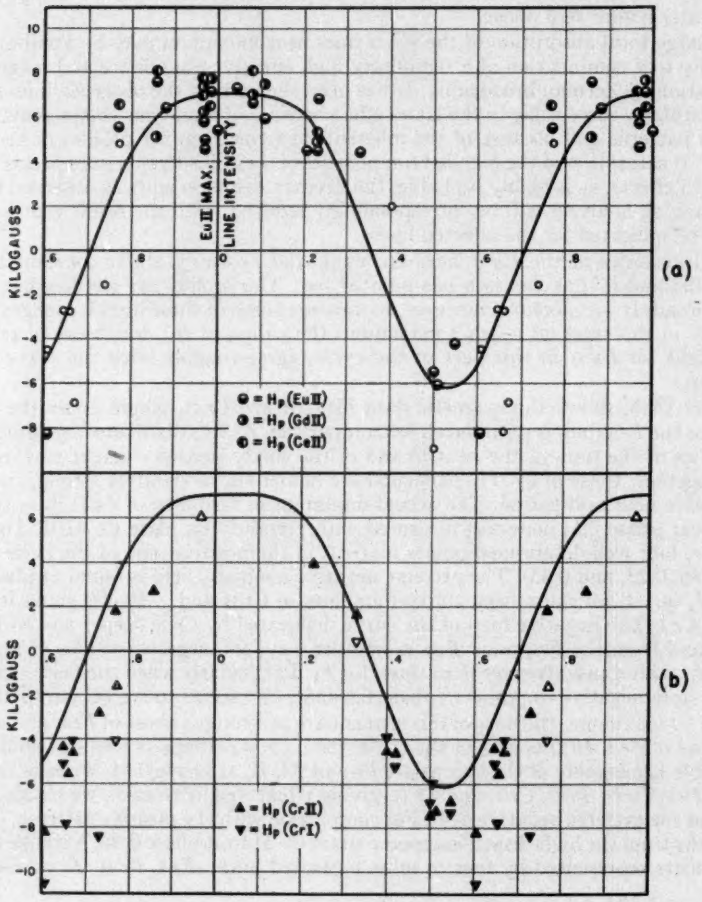

Fig. 13, *a*.—Magnetic field intensity, H_p, in kilogauss, for the rare earths, plotted against phase. Small open circles are of low weight. For comparison, the smooth curve for the *Fe-Ti* lines is also shown. Fig. 13, *b*.—Similar results for *Cr* I and *Cr* II.

complex selective effects on different elements and that equation (5), depending on only *Fe* I, *Fe* II, and *Ti* II, has distinct limitations. Particularly the value of the constant term (+2000 gauss) is in doubt if the results for *Cr* are taken into account.

RADIAL VELOCITIES

In 1923 Adams and Joy published a value of -9.5 ± 1.8 km/sec for the radial velocity of HD 125248; this was determined from five plates.[14] The velocity found by Morgan from the Yerkes plates was -8.2 km/sec.[1]

The observed velocity differences of a few kilometers per second between elements from the new data of Table 2 are, in general, significant, in view of the fact that the probable errors are usually between 0.2 and 0.4 km/sec if the element is represented by several lines. Plates taken in 1948, 1949, and 1950 at nearly the same phase in the 9-day period (0.98, 0.97, and 0.97) give for the velocity of *Fe* I reduced to the sun the values -2.4, -9.7, and -16.5 km/sec, respectively. Rather similar effects are found for other elements. These long-term differences in velocity may be ascribed to one of two causes: (*a*) a relatively long-period orbital motion about an unseen companion or (*b*) a general outflow, at a varying rate, of atmospheric constituents, presumably along the magnetic lines of force.

Within each 9-day period there are significant changes in velocity; these are best shown by a series of seven spectrograms made within one period, beginning on April 13, 1948. Velocity data from this series within one cycle ($E = 270$) are plotted in Figure 14, *a*, where there are gaps centered on phases 270.1 and 270.4. The first gap is tentatively filled by plates taken in 1950 at phases 342.97 and 343.08; the short section has been shifted vertically to match the main curve. Points have been plotted for *Fe* I, *Fe* II, and *Cr* II and for the rare earths (but not for *Ti* II, which follows *Fe* rather closely). The most striking feature is the sudden deceleration (decrease of outward velocity in the star's atmosphere), shown in largest measure by the rare earths, near phase 0.95. This deceleration precedes by only a brief interval the phase of maximum field intensity; further, it coincides with what may be a small-scale fluctuation or notch in the magnetic curve. It is noteworthy that even before this sudden change in velocity, the rare-earth lines have become strong and show a large positive field intensity. The data of Figure 14, *a*, also show that *Cr* II and the rare earths have significantly different velocity-curves from the *Fe* group and from each other. Before attaining maximum line intensity and maximum field strength, both *Cr* II and *Eu* II individually show a velocity of approach of 3 or 4 km/sec with respect to *Fe*.

In order to demonstrate to better advantage the velocity differences among the important groups of elements, the residual velocities, or differences between *Cr* II and *Fe* I, and those between the mean of the rare earths and *Fe* I, have been plotted for all measured phases in Figure 14, *b*. Certain regularities are again apparent, in that the rare earths show a relative velocity of approach of the order of 3 km/sec before zero phase, a velocity equal to that of *Fe* I at zero phase, and for nearly half a period thereafter a velocity of recession of slightly less than 1 km/sec. A rather similar behavior is found for *Cr* II, with a velocity equal to that of *Fe* I occurring near phase 0.58.

THE "CROSS-OVER EFFECT"

On certain spectrograms of HD 125248 made with the double polarizing analyzer, an unpredicted effect of considerable interest was discovered. This effect, which concerns the profiles of many of the absorption lines, occurred only on plates obtained rather near phases 0.35 and 0.7 (the cross-over points), at which times the mean observed magnetic field was relatively small. On spectrograms at other phases the profile of any given line was essentially identical in the two closely adjacent spectra characterized by circular polarization of opposite sign; near the cross-over point at phase 0.35, however, a system-

[14] *Ap. J.*, **57**, 149, 1923.

atic tendency was noted for a large number—perhaps a majority—of the lines in the left-hand (upper) spectrum to become sharper and deeper and for the corresponding lines in the right-hand spectrum to become wider and shallower. The total absorption seemed unchanged by the differences in profile, according to visual estimation, although the visibility of many of the lines in the lower spectrum was decreased by the width and shallowness of the profiles. Near the other cross-over point (phase 0.7) the effect was similar but of opposite sign, the lines in the right-hand or lower spectrum being sharper and deeper. So many of the lines were affected, and in such a systematic way, that there can be no doubt as to the reality of the observations.

The cross-over effect may be seen in many of the lines in the spectra reproduced in Figures 2, 3, and 4, for phase 0.77, although the actual cross-over is slightly earlier, at phase 0.70. Lines of group C, particularly those of *Fe* I, were most affected; other ele-

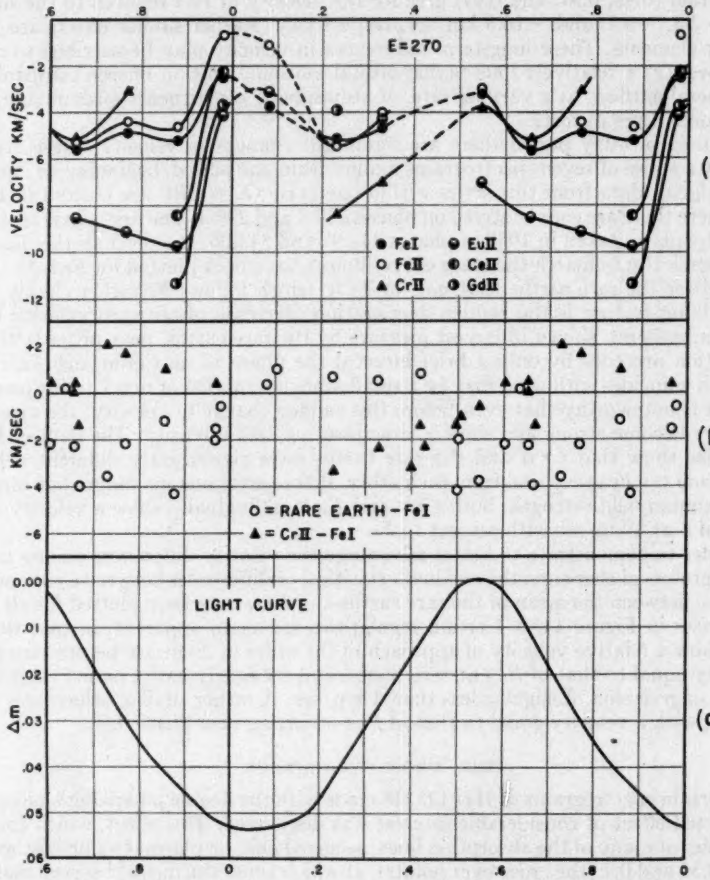

FIG. 14, *a*.—Velocities for various elements plotted according to phase in one cycle ($E = 270$). Note the sudden deceleration near phase 0.95, occurring just as the magnetic field attains maximum intensity. Probable errors are of the order of 0.2–0.5 km/sec. Fig. 14, *b*.—Residual velocities of the rare earths and of *Cr* II with respect to *Fe* I. Fig. 14, *c*.—Light-curve of HD 125248 determined by D. W. N. Stibbs (eq. [10]).

ments showing the effect to a smaller degree were *Cr* II, *Mg* II λ 4481, and *Ca* II (K). In lines of *Eu* II and *Cr* I the cross-over effect was not definitely seen. On plate Ce 5665 (phase 0.73), which was taken on a finer-grain emulsion than most, the cross-over effect is particularly striking; indeed, lines not rather plainly affected are in the minority. In Table 3 a few lines are listed for which the effect is present, together with *Z*-values of the lines. There is probably little to be gained at this time by listing visual estimates of the degree of the cross-over effect for a large number of lines. It should be investigated with the highest possible dispersion.

The cross-over effect can probably best be explained as a combination of Doppler effect and Zeeman effect as seen through the circular analyzer, if we suppose that there are temporarily two distinct areas characterized by magnetic fields of opposite polarity and by a small, but appreciable, difference in radial velocity. In the schematic diagram of Figure 15, *a*, for example, there are two areas, *P* and *Q*, equal in projection and of uniform surface brightness. It is assumed that they are affected by longitudinal magnetic

TABLE 3

PARTIAL LIST OF LINES SHOWING CROSS-OVER EFFECT

λ	Element	Z
4005.246	*Fe* I	1.72
4071.740	*Fe* I	0.69w
4122.638	*Fe* II	1.31
4250.125	*Fe* I	1.39w
4275.57	*Cr* II	0.96b(very slight)
4294.128	*Fe* I	1.20
4300.052	*Ti* II	1.22
4314.979	*Ti* II	1.33
4385.381	*Fe* II	1.33
4443.802	*Ti* II	0.90
4555.890	*Fe* II	1.24

fields of positive and negative polarity, respectively, and also that *P* has a differential velocity of approach, *v*, in the line of sight, with respect to *Q*. If, now, an absorption line of uniform equivalent width over both areas is observed through a double circular analyzer, the profile of the line in the right-hand spectrum will be sharper than in the left-hand spectrum, provided that *H* and *v* are suitably chosen as to order of magnitude. In Figure 15, *b*, the position of the absorption line is first shown unaffected by Doppler or Zeeman effect. It is understood that the small shifts to be considered are of the same order as the half-width of the line. In Figure 15, *c*, the line is split by Doppler shift alone in the integrated light of areas *P* and *Q*. In the next section of the figure (*d*), the longitudinal magnetic fields of opposite polarity in *P* and *Q* are also effective, splitting each line again into two σ components, circularly polarized in opposite senses. Finally, in *e*, the light of the combined areas *P* and *Q* is viewed through the analyzer, which produces two spectra of opposite polarization; here, in the upper or left-hand spectrum, only the two outer components are transmitted, while in the lower spectrum the two nearly central, relatively undisplaced, right-hand components are seen. If one introduces Doppler profiles of appropriate half-width, the blending will produce a wide, shallow profile in the upper spectrum and a sharp, deep profile below. Reversal of the sign of the differential velocity will, of course, interchange the profiles in the two spectra.

For any differential velocity *v*, the cross-over effect will be a maximum if the two inner-

most components coincide, i.e., if the Zeeman shift equals one-half the differential Doppler shift. These two displacements are, respectively,

$$\Delta\lambda_Z = 4.68 \times 10^{-13} \lambda^2 Z H \tag{6}$$

and

$$\Delta\lambda_D = \frac{\lambda v}{2c}. \tag{7}$$

The first of these is obtained from equation (2), with the condition that $H = 0.31\, H_p$, as the field here considered is purely longitudinal. Equating, one finds

$$H = 3.56 \times 10^6 \frac{v}{\lambda Z}, \tag{8}$$

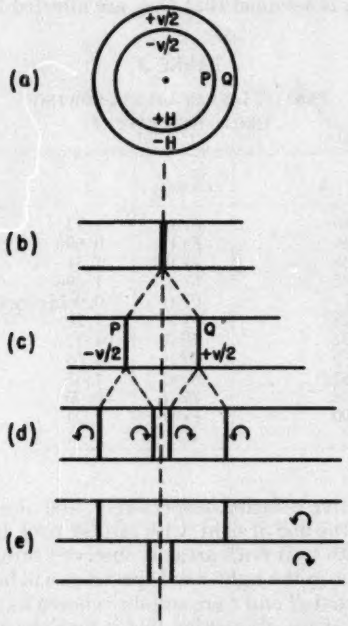

FIG. 15.—Proposed explanation of the cross-over effect in terms of two areas differing in velocity and in magnetic polarity. *a*, Projection of stellar hemisphere. *b*, Unaffected line. *c*, Line split by Doppler effect. *d*, Further splitting by Zeeman effect into polarized components. *e*, Observed through a double circular analyzer, profiles differ in left-handed and right-handed spectra.

where v is in km/sec, λ is in angstroms, and Z is the Zeeman shift relative to a normal triplet. If we choose a line near λ 4500 for which $Z = 1.00$, we find

$$H = 790\, v \text{ gauss}. \tag{9}$$

If the shift, $\Delta\lambda$, is as great as 0.05 A—of the order of the half-width of a typical absorption line—then a maximum cross-over effect would be obtained with $H = 5000$ gauss and $v = 6.5$ km/sec. While the actual differential velocity in HD 125248 may be somewhat less than 6 km/sec and while the model used is an idealized one, it seems that

the observed magnetic field strength and velocity are in such a range that the effect should be readily observable; this leads to confidence in the proposed explanation. It may be pointed out that, in the model of Figure 15, the surface need not be normal to the line of sight; furthermore, if the velocity and field vectors, remaining parallel to each other, become inclined at an angle γ to the line of sight, their effective values are $v \cos \gamma$ and $H \cos \gamma$. (The fact that the effective displacement of the blended components of a Zeeman triplet is proportional to $H \cos \gamma$ was shown by F. H. Seares.)[15] Therefore, the cross-over effect may be observed even from a surface element having a rather large γ, provided that v and H are sufficiently large and in a suitable ratio.

The sign of the cross-over effect in HD 125248 is such that near the descending node of the magnetic curve (phase 0.35) the portion of the stellar surface characterized by positive magnetic polarity has, relative to the rest of the surface, a positive velocity in the line of sight (inward with respect to the star); conditions are reversed at the ascending cross-over point.

THE LIGHT-CURVE

D. W. N. Stibbs, of the Commonwealth Observatory, Australia, has obtained photoelectrically a well-defined light-curve for HD 125248.[16] This light-curve, which has an amplitude of 0.053 mag., is reproduced in Figure 14, *c*. Stibbs's elements are:

$$\text{Light maximum} = \text{JD } 2433103.95 + 9.295E\,. \qquad (10)$$

In terms of Deutsch's elements for line-intensity variations (eq. [1]), light-maximum occurs at phase 0.545, coinciding very nearly with maximum intensity of the chromium lines. I am greatly indebted to Dr. Stibbs for making his results available to me before publication.

INTERPRETATION

The principal magnetic effects observed in HD 125248 are best explained in terms of a dipolar field that is a property of the star as a whole. While spots, similar to sunspots, may occur, it is highly improbable that they could produce the observed effects. The arguments adduced by F. H. Seares in regard to the general magnetic field of the sun apply here.[17] Sunspots tend to occur in pairs of opposite polarity; if star spots did the same, little or no outstanding polarization would be observed, but only a broadening of the lines affected by the spot fields. Also, spots are so dark compared to the photosphere that only the marginal spot fields extending with greatly weakened intensity over the adjacent photosphere could observably influence the absorption lines in the spectrum of the integrated light. Sunspots avoid latitudes higher than about 35°; spots below 35° on a star observed pole-on would have little effect compared to the polar region.

That observed stellar magnetic fields are essentially dipolar is a conclusion based on three independent types of evidence.

1. The coronal streamers of the sun, which are particularly in evidence during sunspot minimum, have long been thought to delineate the lines of force of a dipole magnetic field. Also observations of the Zeeman effect of the sun's general field by G. E. Hale and collaborators,[18] by H. D. Babcock,[19] and by G. Thiessen[20] agree that, when a field is detected at all, it has opposite polarity in the northern and southern hemispheres.

[15] *Ap. J.*, **38**, 99, esp. eq. (21), 1913.

[16] *Nature*, **165**, 195, 1950.

[17] *Observatory*, **43**, 310, 1920.

[18] Hale, Seares, van Maanen, and Ellerman, *Ap. J.*, **47**, 206, 1918.

[19] *Pub. A.S.P.*, **53**, 237, 1941.

[20] *Observatory*, **69**, 228, 1949.

2. Of more than twenty stars in which the Zeeman effect has been found, the majority seem to show magnetic fields of varying amplitude, yet without reversal of polarity. Among these stars showing nonreversing fields, those of positive and those of negative polarity are about equal in number. This is to be expected if pole-on dipolar stars are selected at random. If stellar quadrupole fields prevailed, the same polarity would presumably be observed in all nonreversing pole-on stars, provided that the fields are all generated by the same process.

3. Martin Schwarzschild has derived formulas for the integrated Zeeman effect of a stellar dipole and of a stellar quadrupole, for any angle of obliquity i between the magnetic axis and the line of sight.[21] These derivations were made on the assumption that neither the intrinsic surface brightness nor the intensity of the lines used is a function of magnetic latitude. Where the coefficient of darkening is u, the formulas for the "effective" field strength, H_e, are:

$$\text{Stellar dipole}: \quad H_e = \frac{15+u}{15-5u} \cdot \frac{H_p}{4} \cdot \cos i \; ; \tag{11}$$

$$\text{Stellar quadrupole}: \quad H_e = \frac{u}{3-u} \cdot \frac{H_p}{4} \cdot \frac{1+3\cos 2i}{4} . \tag{12}$$

I am indebted to Dr. Schwarzschild for placing these derivations at my disposal. From equation (11) we find $H_e = \pm 0.303\, H_p \cos i$ for the integrated effect of a stellar dipole if $u = 0.45$, typical of an A0 star. The result obtained earlier by the writer for a pole-on stellar dipole is in good agreement with this.[22] On the other hand, for a stellar quadrupole the integrated effect is zero for all orientations if there is no limb darkening, while, if $u = 0.5$, the integrated effect is $+(1/20)\, H_p$ if the star is viewed from either pole and $-(1/40)\, H_p$ if viewed from the equatorial plane. Thus, to explain a given observed effect, a stellar quadrupole must possess a polar field about ten times as strong as a stellar dipole.

The fact that the magnetic field of HD 125248 varies may be accounted for in a superficial way by either one of two physical models, which we may term the "magnetic oscillator" and the "oblique rotator." Because of the fundamental differences between these models, it is desirable to investigate them on the basis of the data now available. In the next section the theory of the oblique rotator will be discussed and will be shown to disagree with the observations. Subsequently, the interpretation of HD 125248 as a magnetic oscillator will be undertaken.

THE OBLIQUE ROTATOR

It is assumed that the star rotates about an axis having an obliquity i to the line of sight; that the magnetic dipole axis makes an angle i' with the axis of rotation; and that different elements have become concentrated, through some unspecified process, near the two opposite magnetic poles. The period of spectrum variation is then identical with the period of rotation. In the oblique rotator the field is fixed with respect to the material of the star, and the magnetic moment remains constant (except as the rotation of the star changes its direction in space).

On the oblique-rotator theory we should expect to represent the variations of the observed field of any magnetically variable star by a suitable choice of the angles i and i'. For example, γ Equulei has an apparently constant field of about -1900 gauss and no spectrum variation. It can be represented by a model with $i = 0$ and $i' = \cos^{-1}(-1900/H_p)$. The absence of rotational broadening in the spectrum of γ Equ is compatible with this interpretation. An intermediate example is HD 188041, for which several observations over a 4-year interval always show a field of positive polarity but of varying intensity such that the effective component of H_p lies between the approximate

[21] *Ap. J.*, **112**, 222, 1950. [22] *Ap. J.*, **105**, 105, 1947.

limits +4800 and +1500 gauss. An oblique rotator with $i + i'$ somewhat less than 90° might represent this star. Finally, the curve of magnetic variation for HD 125248 (Fig. 12, *a*) would seem to call for values of i and i' near 90°. This we may consider with the aid of Figure 16, where H is the magnetic vector that rotates uniformly about the axis OP in a 9-day period. The line of sight is the z-axis; hence the observed field is zero at those times when H lies in the x-y plane (these phases correspond to the cross-over points). The extreme values of the field are $H \cos (i + i')$ and $H \cos (i - i')$; from equation (5) we take these extremes to be +7000 and −6200 gauss, respectively. Their ratio ρ is −1.13. The fractional part of the period during which the observed field is positive is designated by f. Now, by simple geometry, we have

$$\cos f\pi = \frac{1+\rho}{1-\rho}. \tag{13}$$

From this equation we find that, according to the oblique-rotator theory, $f = 0.52$; yet, in fact (from Fig. 12, *a*) $f = 0.65$. Applying equation (13) in another way, we take the

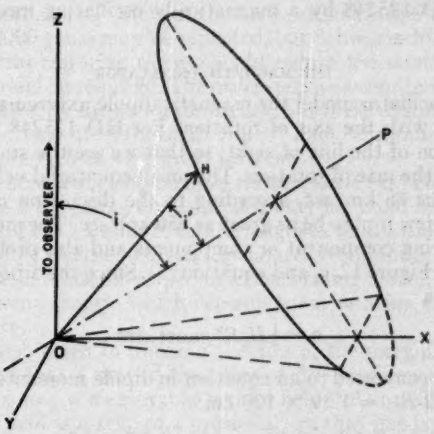

FIG. 16.—Geometry of the oblique rotator. *OP* is the axis of rotation; *OH* is the magnetic dipole axis, which rotates with the star at a uniform rate.

observed facts that the positive extreme of H is 7000 gauss and that $f = 0.65$, whence the calculated ratio ρ is −2.66, and on this model the negative extreme is only −2630 gauss, instead of the observed −6200. Therefore, we conclude that the oblique rotator does not represent the observations of HD 125248.

Another objection to this theory is the peculiar way in which the elements *Eu* and *Cr* would have to be concentrated according to magnetic polarity on opposite sides of a rotating star. No physical theory is known that would account for such a separation, which would seem to imply the existence of free magnetic poles. If, in fact, a separation does occur on this basis, we should expect the process to be a specific one, so that *Eu* and *Cr* would be associated with positive and negative magnetic polarity, respectively, in all magnetically reversing spectrum variables without exception, just as in HD 125248. Observations show that this is not so, however, for in α^2 CVn the maximum intensity of lines of *Eu* II (and of *Eu* III, as well) occurs when the polarity is negative.

Apart from the evidence of the magnetic results, we may consider the representation of the observed radial-velocity-curves by the oblique rotator. For simplicity it is assumed that $i = i' = 90°$ and that the star has a radius twice that of the sun, with a rotation period of 9 days. Hence the equatorial velocity will be about 11.2 km/sec. It is

further assumed that limb darkening is zero and that opposite magnetic hemispheres give rise to spectra of *Eu* and *Cr*, respectively, the line intensities over each hemisphere being independent of magnetic latitude. At the cross-over phases the centers of gravity of the two hemispheres are distant from the center of the disk by 0.425 of the radius; therefore, the differential velocities of *Eu* and of *Cr* will be represented by harmonic curves with amplitudes of 4.76 km/sec. Limb darkening will decrease this amplitude, while greater concentration toward the magnetic poles will increase it. A comparison shows that the velocity-curves of Figure 14, *a* and *b*, are not well represented, being asymmetric and of too low amplitude. But perhaps the most convincing evidence from the sight-line velocities is the sudden acceleration near phase 0.85, as shown in Figure 14, *a*. This cannot be explained on the oblique-rotator theory alone.

It may also be noted that an equatorial velocity of 11 km/sec for the oblique rotator would lead to a greater degree of rotational line broadening than is observed. Earlier in this paper it was pointed out that in HD 125248 an upper limit of $v_e \sin i$ is about 4 km/sec.

As several types of evidence seem to be in conflict with the oblique-rotator theory, the representation of HD 125248 by a magnetically oscillating model will be considered in the next section.

THE MAGNETIC OSCILLATOR

In the magnetic-oscillator model the magnetic dipole axis remains essentially fixed in direction, coinciding with the axis of rotation. For HD 125248 the axis probably lies nearly in the direction of the line of sight, so that we see the star pole-on. There is no direct evidence as to the rate of rotation. The mean equatorial velocity for stars of type A0 is, however, about 88 km/sec, according to the discussion of Chandrasekhar and Münch,[23] while for a few it may be as great as 250 km/sec. The magnetic moment of the star has a large varying component or components and also probably a constant component, as shown by Figure 12, *a*, and equation (5). Since the dipole moment a is related to H_p by the formula

$$a = \tfrac{1}{2} H_p R^3 \text{ gauss cm}^3 , \tag{14}$$

equation (5) may be converted to an equation in dipole moments as follows, on the assumption that $R = 2\,R_\odot = 1.39 \times 10^{11}$ cm:

$$10^{-36} a = 2.69 + 8.88 \cos\theta - 2.15 \cos 2\theta \text{ gauss cm}^3 . \tag{15}$$

Quadrupole moments may also be present, as, according to Schwarzschild's result (eq. [12]), such components would scarcely be detectable. From the velocity-curves of Figure 14, *a* and *b*, we conclude that the varying magnetic field of the star is coupled with large-scale motions in the atmosphere. On this model, separation of elements may be supposed to occur as a function of latitude but not of magnetic polarity; thus certain elements may be concentrated in the polar regions and others in zones at lower latitudes, but conditions are presumably symmetrical with respect to the equatorial plane. The periodic variations in line intensities must be considered in connection with the velocities of the elements and their integrals, in addition to the effects of magnetic intensification resulting from Zeeman broadening.

The oscillating magnetic field of HD 125248 is represented, according to equations (5) and (15), by a constant term, a large harmonically varying term, and a second harmonic. The second harmonic is omitted from further consideration here, although it may well be significant in the development of the theory of stellar oscillations. The large harmonically varying component of the field of HD 125248 (6600 cos θ gauss) can be interpreted according to the theory of Schwarzschild on magnetic oscillations of a highly idealized star.[24] He has considered oscillations of the whole star in which the motions,

[23] *Ap. J.*, 111, 142, 1950.

[24] *Ann. d'ap.*, 12, 148, 1949.

in the presence of a strong, uniform, internal magnetic field, are governed by electromagnetic laws in combination with the hydrodynamic equations. This is an application of the theory of magneto-hydrodynamic waves advanced by H. Alfvén.[25] Schwarzschild's formulation involved several simplifying assumptions; his equations were solved for two principal modes of oscillation. The solution for the *odd* mode is the one that corresponds most nearly to the observations of HD 125248. In this solution a periodically reversing dipolar magnetic field is superposed on a constant uniform internal field; coupled with the oscillatory field are oscillatory motions of the star that are symmetrical about the equatorial plane. In the oscillatory stream motion an inward flow of both polar regions of the star is coupled with a radial expansion of the equatorial zone. Half a period later the motions are reversed. The extremes of the oscillating field are reached at the phase of zero velocity. Schwarzschild's theory seems to explain the oscillating field observed in HD 125248, but it should be remembered that, to facilitate the solution, serious physical simplifications were used. Among the assumptions made were the following: the star does not rotate, and there exists a permanent, homogeneous, internal magnetic field. According to Schwarzschild, this internal field may be as great as 2,000,000 gauss for an oscillator with a 9-day period. If this is taken to represent the field strength deep in the interior of an actual star, values at the surface much larger than the observed constant component of 2000 gauss may be expected, but Schwarzschild points out that consideration of dynamical restoring forces should reduce the strength of the permanent magnetic field that would be required. The observed variations in velocity are more complex than those predicted by the oscillator theory, but these complex atmospheric effects involving relative motions of "rare-earth zones" and "chromium zones" may be regarded as secondary, though of very great interest.

With regard to the constant component of the magnetic field observed in HD 125248, amounting to perhaps 2 kilogauss, one approach may be found in the theory developed by W. Elsasser[26] and by E. C. Bullard[27] for the magnetic field within the earth. It is, however, highly questionable whether one can legitimately combine in a single star Schwarzschild's specialized oscillations, developed in a nonrotating model, and the Elsasser-Bullard self-exciting dynamo theory, which depends upon rotation and upon thermal convection within the core.

T. G. Cowling has objected to dynamo theories of the foregoing type as applied to the sun, on the ground that a time of the order of 10^{18} years would be required for the sun to build up in this way a measurable surface field.[28] As an alternative, he has suggested that the sun's field is a relic of a prestellar era that has persisted because of the very long relaxation time of such a field in a conducting medium.

ELECTRIC FIELDS

The varying magnetic field of an oscillating star, such as HD 125248, will induce an electromotive force around the star, everywhere perpendicular to meridian planes. Schwarzschild's equation (32) expresses the electric field outside the star in his nonrotating oscillator (odd mode):

$$E = d\,(d^2 + z^2)^{-3/2} h_o \frac{2\pi R}{\Pi} \sin \tau\,. \qquad (16)$$

Here d and z are the distances from the axis and from the equatorial plane, respectively, expressed in units of the star's radius R. The period of oscillation is Π, and h_0 is the amplitude of the variable magnetic field at the equator. The conductivity of the atmosphere is neglected. According to this equation, the amplitude of the electric-field intensity at

[25] *Nature*, **150**, 405, 1942.

[26] *Rev. Mod. Phys.*, **22**, 1, 1950, and *Phys. Rev.*, **60**, 876, 1941; **69**, 106, 1946; **70**, 202, 1946.

[27] *M.N., Geophys. Suppl.*, **5**, 24, 1948; *Proc. R. Soc. London, A*, **197**, 433, 1949; *Phys. Today*, **2**, 6, 1949.

[28] *M.N.*, **105**, 166, 1945.

the equator, where it is a maximum, is 36 volts/cm. It is assumed that $R = 2R_\odot = 1.39 \times 10^{11}$ cm.

A similar result is obtained directly by applying Faraday's law of electromagnetic induction. The electric potential around a fixed circle at the equator of the star is equal to the rate at which the magnetic lines of force are cutting this circle. From Figure 12, *a*, it is seen that H_p varies almost uniformly from -5000 gauss to $+5000$ gauss in 0.22 of the period or 1.77×10^5 sec, whence the potential, $\mathfrak{E}$, around the equator is 3.4×10^{21} e.m.u. or 3.4×10^{13} volts. The amplitude of the electric-field intensity is $E = \mathfrak{E}/2\pi R = 39$ volts/cm, in good agreement with the foregoing result.

With respect to the atmosphere of a real star, the actual electric field will be weaker than that just calculated, as a result of the finite conductivity and of material motions, which depend in an important way upon H. In the absence of a magnetic field, the conductivity is probably about the same as that of the solar atmosphere, namely, 10^{-8} e.m.u.;[29] but, when H becomes stronger than a few hundred gauss, the conductivity perpendicular to the direction of H is lowered by many orders of magnitude.

The electric field E of equation (16), induced by the oscillation of the magnetic dipole, is only one component of the total electric field surrounding the star. Another component arises from the rotation, and particularly the differential rotation, of the star in its own magnetic field. This rotation produces a quadrupole electric field represented by vectors which lie in meridian planes. Unfortunately, as has already been pointed out, the observations yield no direct information regarding rotational speed or differential rotation in HD 125248. The electric field of the sun engendered by rotation in its magnetic field has been discussed recently by V. C. A. Ferraro and H. W. Unthank,[30] with emphasis on the law of equirotation, according to which the angular velocity in the atmosphere should be uniform over the equipotential surfaces of revolution obtained by rotating the magnetic lines of force around the axis.

VARYING LINE INTENSITIES

The complex problem of the large variations in equivalent width of certain groups of lines can hardly be solved on the basis of data obtained from one star alone. As Morgan and Deutsch have shown, there is a wide variety among spectrum variable stars of type A as to period and as to the particular elements that undergo line-intensity changes, and it is now becoming apparent that the underlying magnetic and velocity effects are likewise diverse. In a varying magnetic field, corresponding changes in equivalent width of saturated absorption lines must be expected because of Zeeman broadening. This effect (magnetic intensification) is particularly pronounced for some of the lines of *Eu* II; however, the fact that the rare earths and chromium vary in opposite phase in HD 125248 and in some other stars implies that some additional process—the "varying effective abundance" of Morgan—is not only also active but probably predominant.

The physical conditions in the atmosphere of HD 125248, together with the inferred existence of europium zones and chromium zones, suggest that a clue to anomalous abundance effects and to spectrum variability may be found in the differential velocity of drift of ions in crossed electric and magnetic fields. We may theorize that a kind of mass-spectrograph effect occurs in the atmosphere of a magnetically oscillating star or even that a "bunching" of ions with certain ratios of charge to mass may result from a resonance between the period of magnetic oscillation of the star and the travel time between atmospheric zones or levels for these ions.

That electric and magnetic fields, such as occur in the atmosphere of HD 125248, lead to significant drift velocities of ions and electrons is indicated by the free-path theory. R. G. Giovanelli has applied this theory to the solar atmosphere in the vicinity of sunspots, where local magnetic and electric fields are not vastly dissimilar in magni-

[29] T. G. Cowling, *Proc. R. Soc. London, A*, **183**, 453, 1945.

[30] *M.N.*, **109**, 462, 1949.

tude to the general fields in HD 125248.[31] The drift velocity of a charged particle in crossed electric and magnetic fields has two components—a direct velocity,

$$w = \frac{E\omega\tau}{H(1+\omega^2\tau^2)}, \tag{17}$$

in the direction of E and a transverse velocity,

$$v = \frac{E\omega^2\tau^2}{H(1+\omega^2\tau^2)}, \tag{18}$$

in a direction perpendicular both to E and to H.[32] The gyro-frequency, ω, is equal to eH/m (e and m being the charge and mass of the particle in e.m.u. and in grams, respectively), and τ is the mean time between collisions of the particles with particles of other types.

The transverse velocity, which constitutes the Hall current, is in the same direction for charged particles of both signs; it is greatest when H is rather small but E is large and when $\omega\tau \approx 1$, i.e., when the mean free path is of the same order as the radius of gyration. As the transverse velocity v is perpendicular both to H and to E, it has, in general, a vertical and a horizontal meridian component in the atmosphere. According to Alfvén, the dependence of v upon e/m is transient, occurring for a limited time after a field is applied or while H and E are changing; if a stationary state is reached, all charged particles move with the same velocity, having imparted this velocity to all neutral particles as well.[33] We recall that near the cross-over phases in HD 125248 the variable lines are changing most rapidly and that near these phases the transverse drift velocities should be largest because the induced electric field is near maximum, while H, passing rapidly through zero, is small. A reversal of the direction of v occurs with a reversal of H; yet, in spite of this reversal, a preferential drift of an ion toward higher or lower latitudes may still take place because of the vertical component of drift. If the vertical component causes the ion to descend, the drift may be abruptly terminated, owing to changes in ionization and mean free path when the ion "strikes the photosphere." An upward component of velocity, however, may permit a much longer excursion and a correspondingly greater horizontal displacement.

The dependence of the transverse drift velocity v upon e/m for a number of singly ionized atoms is shown in a qualitative way by the curves of Figure 17, which have been computed from equation (18). The value of τ is taken to be 2.22×10^{-5} sec and E is assumed to be 2×10^9 e.m.u. It is noteworthy that an appreciable velocity difference, persisting up to values of H as large as 2 kilogauss, is indicated between the heavy ions, such as *Eu* II, and most lighter ions. The relative ordinates of the curves would be altered if differences in ionization potential were properly taken into account, but, nevertheless, it remains difficult to explain the marked difference in behavior between *Cr* and *Fe*. The curves of Figure 17 are invalid for $H < 1000$ gauss, where the conductivity reduces E.

That an unbounded ionized gas should exhibit diamagnetism is a proposition advanced by Alfvén.[34] In an inhomogeneous magnetic field a diamagnetic body experiences a force in the direction of weaker field strength. Since in the atmosphere of a magnetically oscillating star the field is not only inhomogeneous but is changing rapidly with time, the possible relationship between diamagnetism and the observed velocities in HD 125248 should be investigated.

It has been inferred that the spectroscopically effective *Eu* in the reversing layer of

[31] *Australian J. Sci. Res.*, *A*, 2, 39, 1949.

[32] J. S. Townsend, *Proc. R. Soc., London*, *A*, 86, 571, 1912.

[33] *Cosmical Electrodynamics* (Oxford: Clarendon Press, 1950), p. 47.

[34] *Ibid.*, p. 57.

HD 125248 has become concentrated near the two opposite poles and that the effective *Cr* is located in an equatorial zone or belt, which varies greatly in width as the star oscillates. A partial interpretation of these zonal effects, which does not appear to be in disagreement with the observations, may be had by referring again to Figure 15, *a* (which corresponds to phase 0.7), where the observer sees the star pole-on. The polar axis is elongated when the equator is contracted, and vice versa. The velocity data and Stibbs's light-curve (on the assumption of constant surface brightness) suggest that at zero phase (*Eu* II maximum) the polar elongation is at a maximum and that the equatorial expansion reaches a maximum near mid-period (phase 0.55), coinciding with maximum light. On this model, there is some *Eu* in evidence near the poles, even at *Cr* maximum; this explains the observation of weak lines of *Eu* II at mid-period. On the other hand, the fact that the lines of *Cr* II and *Cr* I are practically invisible at *Eu* II maximum may be

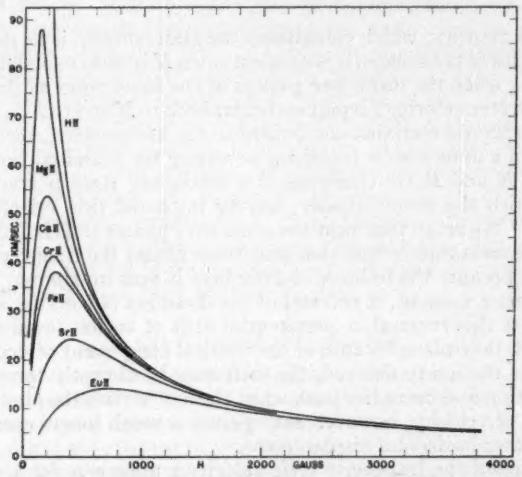

FIG. 17.—The transverse component of the drift velocity, v, at right angles to the magnetic and electric fields, for various singly ionized elements, is plotted as a function of H. E is taken to be 20 volt/cm.

accounted for by the recession of the effective zone of *Cr* to low latitudes, where it is suppressed by a combination of limb darkening and small effective area.

It is suggested that near the cross-over phases the reversal of magnetic polarity does not occur instantaneously over the whole star but rather with a rapid progression in latitude. From phase 0.3 to phase 0.4 the ϕ_0 boundaries, at which $H = 0$, move toward high latitudes in their respective hemispheres; between phases 0.65 and 0.75 these boundaries are again defined and move toward low latitudes. The cross-over effect is attributed to the opposite magnetic polarities as observed in the latitude zones of a pole-on star, coupled with two velocity effects: (*a*) the approach of the polar region with respect to the equator on Schwarzschild's theory (phase 0.7), and (*b*) ionic drift velocities in opposite directions on the two sides of the magnetic boundary.

It is a pleasure to thank Miss Sylvia Burd for carrying out a major share of the measuring and reduction of the plates. I have had stimulating discussions with Dr. Schwarzschild and Dr. Deutsch, and I am particularly grateful to Professor Sydney Chapman for reading the manuscript.

THE SPECTRUM OF XX OPHIUCHI IN 1949 AND 1950

PAUL W. MERRILL
MOUNT WILSON AND PALOMAR OBSERVATORIES
CARNEGIE INSTITUTION OF WASHINGTON
CALIFORNIA INSTITUTE OF TECHNOLOGY
Received February 12, 1951

ABSTRACT

During 1949 and 1950 the spectrum of XX Ophiuchi, then in the bright-line state, was photographed from λ 3600 to *Hβ* with a dispersion of 10 A/mm; from *Hβ* to *Hα* with 15 A/mm. Of the emission lines listed in Table 2, 29 are of *H*, 14 of *He* I, 72 of neutral metals, 441 of ionized metals, 11 miscellaneous, and 10 unidentified. The total number, 577, is possibly the greatest yet measured in any stellar spectrum. Lines of *Fe* II dominate the spectrum; certain multiplets are observed more completely than in the laboratory. The D lines of sodium are conspicuous in emission—a rare occurrence in stellar spectra.

The velocities from the bright lines have not changed markedly since 1921; in 1949 weak absorption components on the shortward edges of bright metallic lines had but a slight effect. *H* and [*O* I] lines yield the same velocities as metallic lines.

In 1949 the H and K lines of *Ca* II had well-defined, greatly displaced absorption components something like those in the spectrum of HD 190073. In XX Ophiuchi these lines are subject to large variations.

The bright metallic lines are stronger than in other Be stars exhibiting the same range of atomic excitation. This indicates a larger emitting atmosphere.

Bright hydrogen lines in the spectrum of XX Ophiuchi,[1] a variable star of the R Coronae type, were discovered in 1907 at the Harvard College Observatory.[2] The object was later nicknamed "the iron star"[3] because in 1921–1923 the most noteworthy features of its spectrum were numerous bright lines of ionized iron. In 1925 an extraordinary change was noted;[4] in that year the lines were predominantly in absorption, with large negative displacements, the lines of ionized titanium being stronger and more numerous than those of iron. In later years, however, bright iron lines have again dominated the spectrum. Spectrograms taken at Mount Wilson from 1921 to 1931 were described by P. W. Merrill in *Mount Wilson Contribution*, No. 444.[5]

Additional low-dispersion spectrograms taken in 1941 and 1945 showed dark lines, with even larger negative displacements than those previously observed.[6] A spectrogram taken with the 40-inch refractor at Yerkes Observatory on June 3, 1944, was reproduced in a note by Morgan and Sharpless.[7]

The present article is based on four spectrograms of the photographic region, 10 A/mm, and two of the visual region, 15 A/mm, taken with the 100-inch telescope in 1949 and 1950 (see Table 1). During these two years the spectrum was in the bright-line stage. Dark components were relatively weak and, excepting the lines of *Ca* II, had only moderate negative displacements. The spectrum from λ 3600 to λ 6600 is reproduced from the strongest exposures of the various regions in Figures 1–4.

The light-curve based on observations made by Dr. Sergei Gaposchkin at the Harvard Observatory had a flat maximum of magnitude 9.4 (photographic) in 1948, followed by a decline reaching 10.4 in August, 1950. I am grateful to Dr. Gaposchkin for sending me his results.

[1] HD 161114, MWC 269; 1900 R.A. 17^h38^m6; Dec. $-6°14'$; mag. 10 variable; Spec. Pec.

[2] Mrs. W. P. Fleming, *Harvard Circ.*, No. 143, 1908.

[3] P. W. Merrill, *Pub. A.S.P.*, **36**, 225, 1924.

[4] *Ibid.*, **38**, 45, 1926.

[5] *Ap. J.*, **75**, 133, 1932.

[6] Merrill, Burwell, and Miller, *Pub. A.S.P.*, **58**, 302, 1946.

[7] *Ap. J.*, **103**, 249, 1946.

METALLIC LINES

In 1949 and especially in 1950, during a period when the spectrum was relatively free from the wide, greatly displaced absorption lines sometimes present, numerous bright metallic lines stood out clearly from the continuous background. These lines are fairly narrow, and, because of the higher dispersion, more were measured than ever before. The total number of emission lines, 577 (Table 2), is possibly the greatest yet measured in any stellar spectrum. The bright lines showed more contrast with the continuous spectrum on plate Ce 6434 than on previous plates of the same region, although the total light of the star was somewhat fainter. Evidently the excitation of the bright lines is not proportional to the intensity of the continuous radiation in the region photographed. The bright lines probably depend on radiation far shortward from the observable limit.

Lines of most *neutral metals* are weak or absent. The elements represented are *Na* I, *Mg* I, *Al* I, *Si* I, and *Fe* I; the numbers of lines measured are shown in Table 3. The yellow sodium lines D1 and D2 are conspicuous in emission; with the exception of novae, this is a very rare occurrence in stellar spectra. These bright lines, which yield the same velocities as do other metallic lines, are bordered on their longward edges by strong dark

TABLE 1

SPECTROGRAMS OF XX OPHIUCHI

Plate Ce	Date	Mag.	Emuls.	Exp. (Min.)	Seeing
5687.....	1949 June 13	9.7	103-O	168	4
5751.....	July 13	9.7	IIa-O	300	3
6234.....	1950 May 23	10.1	IIa-O	250	1–2
6238.....	May 24	10.1	103a-E	192	2–3
6434.....	Aug. 5	10.4	IIa-O	300	2–3
6438.....	Aug. 6	10.4	103a-D	266	4

lines, possibly interstellar, while weak diffuse absorption extends shortward for about 2 A (see Figs. 4 and 5).

Emission lines of *ionized metals* dominate the spectrum (see Figs. 1–4). On the 1949 plates many of them, especially lines of *Ti* II, have weak, narrow absorption components on their shortward edges; in 1950 the bright lines were stronger, the dark lines practically absent. The data in Tables 4 and 5 show that in 1949 the dark components displaced the bright lines longward by the equivalent of a few kilometers per second. The numbers of emission lines measured are in Table 3. It is remarkable that in this faint star certain multiplets of *Fe* II have been observed more completely than in the laboratory. This is doubtless due to the great volume of the stellar atmosphere.

Forbidden lines of [*Fe* II] vary in intensity from plate to plate but are never very strong; they yield the same velocity as the permitted lines. Lines of [*S* II], λ 4068 and λ 4076, were seen on one or two plates.

The velocities derived from metallic lines (Table 4) appear to have been substantially constant for nearly twenty years. Small and variable displacements longward are introduced at various times by the effect of dark components. Measurements of lines of [*Fe* II] on the earlier plates have low weight. Various elements yield closely accordant velocities, as shown by the residuals in Table 5. Velocities derived from the dark components of metallic lines on two plates are shown in Table 6.

On the two plates taken in 1949 the H and K lines of *Ca* II exhibit several strong, sharply bounded absorption components having large negative displacements (see Fig. 1). The general appearance of these anomalous lines is similar to that of the remark-

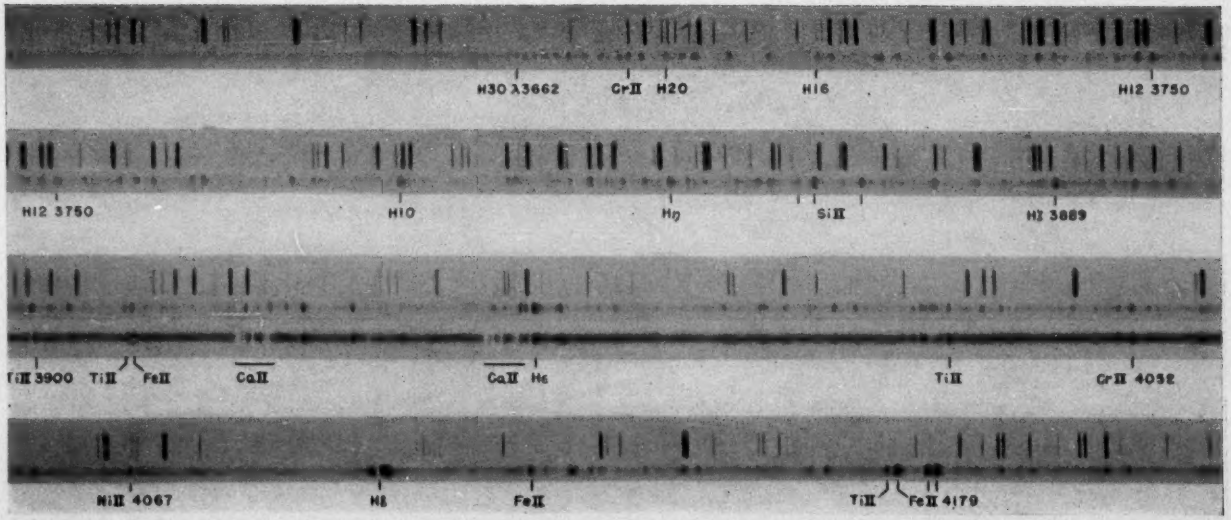

FIG. 1.—The spectrum of XX Ophiuchi, λλ 3600–4200. Ce 6434; the lower spectrum in the third strip is from Ce 5751

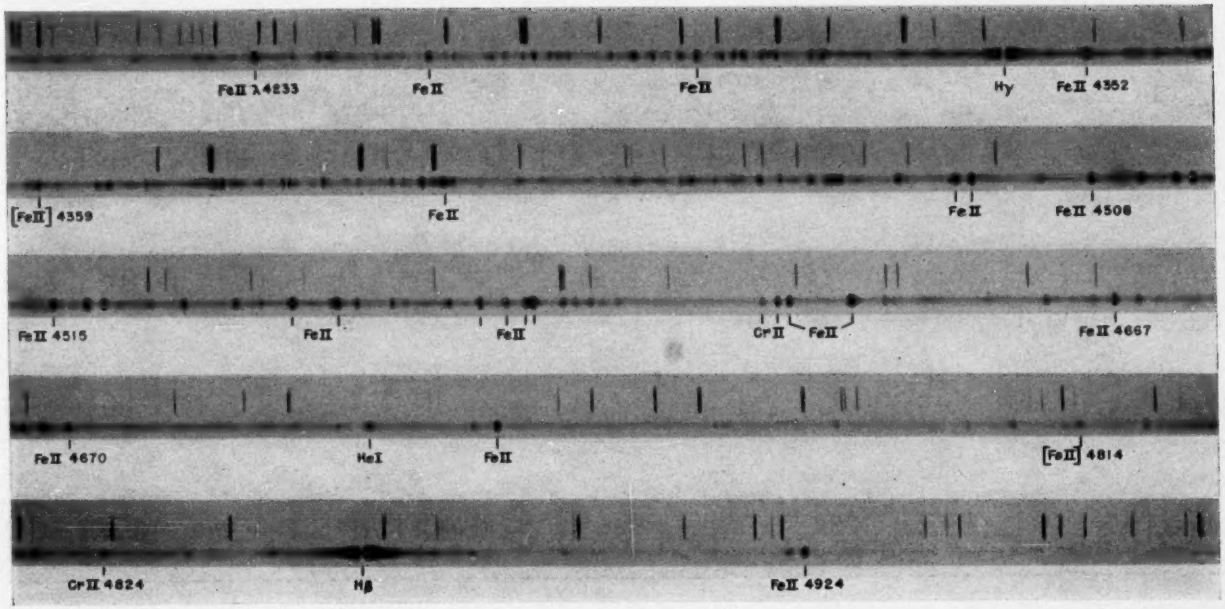

FIG. 2.—The spectrum of XX Ophiuchi, λλ 4200–5000. Ce 6434

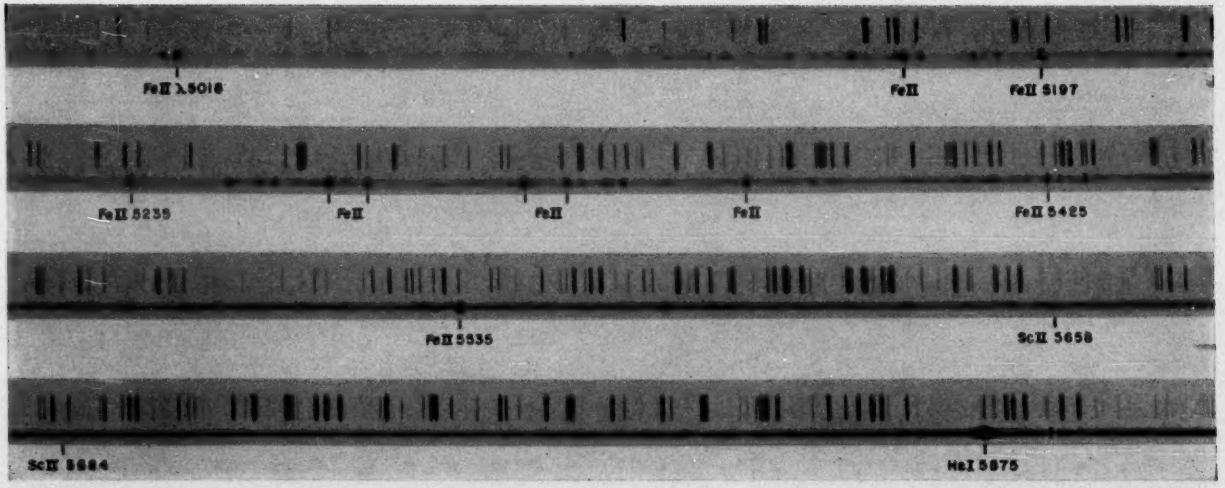

FIG. 3.—The spectrum of XX Ophiuchi, λλ 5000–5900. Ce 6438. The star spectrum is in the second order, the iron comparison spectrum in the third order.

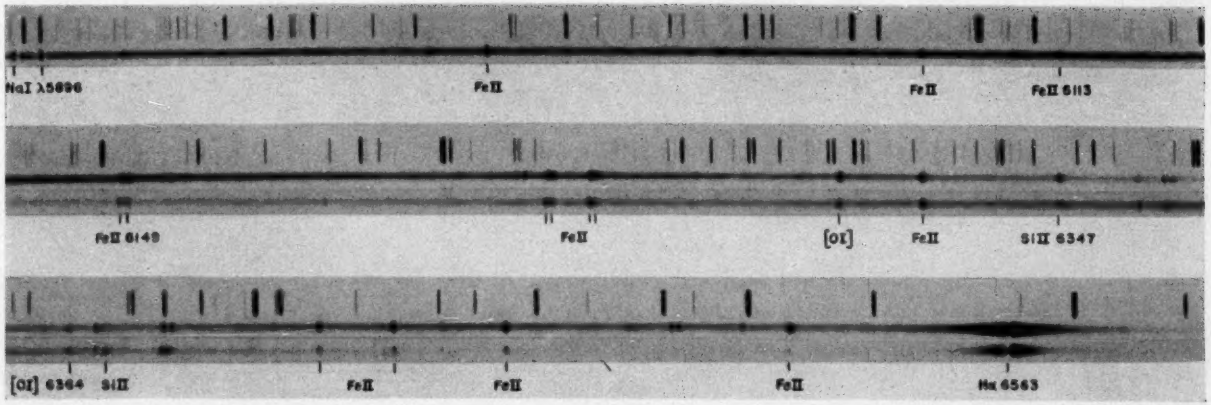

FIG. 4.—The spectrum of XX Ophiuchi, λλ 5900–6600. Ce 6438; the lower spectrum in the second strip and the upper spectrum in the third strip are from Ce 6238. The star spectrum is in the second order, the iron comparison spectrum in the third order.

TABLE 2

EMISSION LINES IN THE SPECTRUM OF XX OPHIUCHI

I.A.	Int.	Element	Mult.	I.A.	Int.	Element	Mult.
3661.22	tr	H 31	---	3835.39	12	Hη	---
3662.26	1	H 30	---	3838.29	4	Mg I	3
3663.41	1	H 29	---	3845.18 P	3	Fe II	127
3664.68	1	H 28	---	3848.24	4 n	Mg II	5
3666.10	1	H 27	---	3849.58	3	Ni II	11
3667.68	2	H 26	---	3850.40	1 n	Mg II	5
3669.47	2	H 25	---	3853.66	4	Si II	1
3671.48	2	H 24	---	3856.02	11	Si II	1
3673.76	2	H 23	---	3859.91	1	Fe I	4
3676.36	2	H 22	---	3862.59	5	Si II	1
3677.69	3	Cr II	12	3863.95	tr	Fe II	127,152
.86	--	Cr II	12	3865.59	1	Cr II	167*
.93	--	Cr II	12	6.01	--	Cr II	130
3679.36	3	H 21	---	3866.54	1	Cr II	130
3682.81	3	H 20	---	3872.76 P	3	Fe II	29
3684.25	1	Cr II	145	3878.02	1	Fe I	20
3685.19	2	Ti II	14	3878.58	2	Fe I	4
3686.83	4	H 19	---	.72	--	V II	33*
3691.56	4	H 18	---	3882.28	3	Ti II	34
3697.15	4	H 17	---	3886.28	1	Fe I	4
3700.34	tr	V II	116	3889.05	14	Hζ	---
3703.86	4	H 16	---	3896.11 P	2	Fe II	23
3706.03	4	Ca II	3*	.16	--	V II	10
.22	--	Ti II	73	3900.55	7	Ti II	34
3711.97	4	H 15	---	3903.27	1	V II	11
3712.97	6	Cr II	12	3905.53	3	Si I	3
3.04	--	Cr II	12	3906.04	1	Fe II	173
3715.19	4	Cr II	20	3913.46	2	Ti II	34
.45	--	Cr II	145	3914.48	8	Fe II	3
.48	--	V II	15	3916.42	1	V II	10
3719.94	2	Fe I	5	3918.68	tr n	---	---
3721.94	5	H 14	---	3920.26	tr	Fe I	4
3727.04 P	2	Fe II	192	3922.91	tr	Fe I	4
.35	--	V II	21	3927.92	tr	Fe I	4
3732.76	tr	V II	15	3930.31	6	Fe II	3
3734.37	6	H 13	---	3932.01	1	Ti II	34
3736.90	4	Ca II	3*	3933.66	6	Ca II	1
7.13	--	Fe I	5	3935.94	3	Fe II	173
3738.38	1	Cr II	20	3938.29	8	Fe II	3
3741.63	3	Ti II	72	3938.97	1	Fe II	190
3745.56	2	Fe I	5	3945.21 P	5	Fe II	3
.81	--	V II	15	3951.97	2	V II	10
3746.56 P	1	Fe II	14	3960.90	1	Fe II	212
3748.49	4	Fe II	154*	3961.52	1	Al I	1
.68	--	Cr II	11	3964.73	5 n	He I	5
3750.15	6	H 12	---	3966.43 P	1	Fe II	3
3754.59	1	Cr II	20	3968.47	7	Ca II	1
3755.56	tr	Fe II	154	3970.07	18	Hε	---
3757.68	1	Ti II	72	3973.64	tr	V II	9
3759.29	3	Ti II	13	3974.16	6	Fe II	29
.46	--	Fe II	154	3977.73	1	V II	10
3761.32	2	Ti II	13	3979.51	1	Cr II	183
3761.69	2	Cr II	11	3981.61 P	2	Fe II	3
.90	--	Cr II	11*	3982.00	1	Ti II	11
3762.89	tr	Fe II	192	3987.63 P	2	Ti II	11
3764.09	4	Fe II	29	3997.13	2	V II	9
3765.62	1	Cr II	20	4002.07	3	Fe II	29
3769.46	5	Ni II	4	4002.55	1	Fe II	190
3770.63	7	H 11	---	4002.94	1	V II	9
3774.65	1	Ti II	12	4005.71	2	V II	32
3776.06	1	Ti II	72	4009.27	1 n	He I	55
3779.58 P	2	Fe II	23	4012.37	6	Ti II	11
3781.51	tr	Fe II	130	.47	--	Fe II	126
3783.35	6	Fe II	14	.50	--	Cr II	183
3786.33 P	2	Ti II	12	4014.49	tr	Sc II	8
.37 P	--	Fe II	15	4015.50	2	Ni II	12
3787.24	1	V II	100	4023.39	1	V II	32
3797.90	9	H 10	---	4024.55	3	Fe II	127
3813.39	2	Ti II	12	4025.14	2	Ti II	11
3814.12	2	Fe II	153	4026.19	4 n	He I	18
3814.58	2	Ti II	12	4028.33	4	Ti II	87
3819.61	1 n	He I	22	4030.76	1	Mn I	2
3821.92 P	2	Fe II	14	4032.95	3	Fe II	126
3824.91	6	Fe II	29	4035.54 P	2	Fe II	22
3827.08	1	Fe II	153	.63	--	V II	32*
3827.67 P	1	Fe II	128	4036.78	1	V II	9
.82	--	Fe I	45	4044.01 P	tr	Fe II	172
3829.36	3	Mg I	3	4045.82	2	Fe I	43
3832.30	4	Mg I	3	4048.83	1	Fe II	172
3833.02 P	tr	Fe II	23	4051.21 P	tr	Fe II	172

TABLE 2 (Cont'd)

I.A.	Int.	Element	Mult.	I.A.	Int.	Element	Mult.
4051.97	3	Cr II	19	4282.41	1	Fe I	71
4053.81	2	Ti II	87	4284.21	3	Cr II	31
4054.11	2	Cr II	19	4287.40	12	Fe II	7 F
4056.21	2	Ti II	11	4287.89	3	Ti II	20
4057.46	1	Fe II	212	4290.22	8	Ti II	41
4063.60	2	Fe I	43	4292.25	tr	Mn II	6
4067.05	7	Ni II	11	4294.10	7	Ti II	20
4068.62	2	S II	1 F	.13	--	Fe I	41
4070.03 P	1	Fe II	22	4296.57	16	Fe II	28
4071.74	1	Fe I	43	4300.05	8	Ti II	41
4072.56	tr	Cr II	26	4301.93	6	Ti II	41
4076.22	?	S II	1 F	4303.17	12	Fe II	27
4077.50	1	Cr II	19	4305.72	2	Sc II	15
.71	--	Sr II	1	.90	--	Fe II	21 F*
4087.27 P	2	Fe II	28	4307.90	7	Ti II	41
4088.75 P	1	Fe II	39	.91	--	Fe I	42
4101.74	25	H δ	---	4312.86	8	Ti II	41
4102.93	4	Si I	2	4314.08	10	Sc II	15
4111.01	2	Cr II	18,26	.29	--	Fe II	32
4119.53 P	2	Fe II	21	4314.98	4	Ti II	41
4120.81	1 n	He I	16	4316.81	3	Ti II	94
4122.64	10	Fe II	28	4319.62	3	Fe II	21 F
4124.79	3	Fe II	22	4320.74	5	Sc II	15
4128.05	6	Si II	3	.96	--	Ti II	41
4128.74	4	Fe II	27	4325.01	2	Sc II	15
4130.88	3	Si II	3	4325.76	4	Fe I	42
4132.06	2	Fe I	43	4326.58	1	---	---
4134.68	1	Fe I	357	4330.26	2	Ti II	94
4138.21 P	3	Fe II	150	4330.71	4	Ti II	41
.40 P	--	Fe II	39*	4337.33	tr	Ti II	94
4143.76	6 n	He I	53	4337.92	2	Ti II	20
4145.77	3	Cr II	162	4338.70 P	tr	Fe II	32
4160.62 P	1	Fe II	39	4340.47	50	Hγ	---
4161.52	3	Ti II	21	4344.29	2	Ti II	20
4163.64	7	Ti II	105	4346.85	1	Fe II	21 F
4167.27	tr	Mg I	15	4350.83	1	Ti II	94
4171.90	5	Ti II	105	4351.76	18	Fe II	27
4173.45	15	Fe II	27*	4352.78	1	Fe II	21 F
.54	--	Ti II	21	4354.61	tr	Sc II	14
4174.09	2	Ti II	105	4357.57	3	Fe II	---
4177.70 P	9	Fe II	21	4358.37	4	Fe II	21 F
4178.86	18	Fe II	28	4359.34	8	Fe II	7 F
4179.43	1	Cr II	26	4361.25	tr	Fe II	---
4181.76	1	Fe I	354	4362.10	3	Ni II	9
4183.20 P	2	Fe II	21	4367.66	3	Ti II	104
.44	--	V II	37	4368.26	tr	Fe II	---
4184.33	4	Ti II	21	4369.40	7	Fe II	28
4187.81	5	---	---	4372.43	2 n	Fe II	21 F
4190.29	2	Ti II	21	4374.46	2	Sc II	14
4192.07	2	Ni II	10	4374.82	2	Ti II	93
4195.41	1	Cr II	161	4375.93	3	Fe I	2
4202.03	4	Fe I	42*	4383.55	1	Fe I	41
.35	--	V II	25	4384.21	10	Fe II	36 F
4205.08	2	V II	37	.33 P	--	Fe II	32
4205.48 P	2	Fe II	22	4385.38	11	Fe II	27
4211.80 P	tr	Fe II	21	4386.86	3	Ti II	104
4215.52	1	Sr II	1	4387.93	4 n	He I	51
4216.19	2	Fe I	3	4390.58	1	Mg II	10
4224.85	1	Cr II	162	4390.98	3	Ti II	61
4225.23	1	V II	37	4394.06	5	Ti II	51
4226.73	1	Ca I	2	4395.03	5	Ti II	19
4227.43	3	Fe I	693	4395.85	4	Ti II	61
4233.17	25	Fe II	27	4398.31	1	Ti II	61
4238.82	3	Fe I	693	4399.77	7	Ti II	51
4242.38	7	Cr II	31	4400.36	1	Sc II	14
4243.98	7	Fe II	21 F	.63 P	--	Ti II	93
4244.80	3	Ni II	9	4402.88	1	Fe II	---
.81	--	Fe II	21 F	4404.68	4	V II	30
4246.83	1	Sc II	7	.75	--	Fe I	41
4250.79	1	Fe I	42	4407.68	1	Ti II	51
4252.62	2	Cr II	31	.71	--	Fe I	68
4254.41	tr	V II	18	4408.42	1	Fe I	68
4258.16	12	Fe II	28	4409.22	3	Ti II	61
4261.92	4	Cr II	31	4409.52	2	Ti II	61
4267.02	5	C II	6	4411.08	3	Ti II	115
.27	--	C II	6	4411.94	tr	Ti II	61
4269.28	2	Cr II	31	4413.60	9	Fe II	32
4271.76	3	Fe I	42	.78	--	Fe II	7 F
4273.32	10	Fe II	27	4415.12	1	Fe I	41
4275.57	4	Cr II	31	4415.56	tr	Sc II	14
4276.83	4	Fe II	21 F	4416.27	1	Fe II	6 F
4278.13	6	Fe II	32	4416.82	7	Fe II	27

TABLE 2 (Cont'd)

I.A.	Int.	Element	Mult.	I.A.	Int.	Element	Mult.
4417.72	2	Ti II	40	4600.19	1	V II	56
4418.34	3	Ti II	51	.28 P	--	Ti II	60
4421.95	2	Ti II	93	4601.34 P	1	Fe II	43
4427.31	2	Fe I	2	4602.94	1	Fe I	39
4428.00	tr	Mg II	9	4616.64	4	Cr II	44
4430.62	tr	Fe I	68	4618.83	7	Cr II	44
4431.37	tr	Sc II	14	4620.51	14	Fe II	38
4433.99	1 n	Mg II	9	4625.91	tr	Fe II	186
4437.55	tr n	He I	50	4629.34	25	Fe II	37
4441.73 P	4	Ti II	40	4634.11	4	Cr II	44
4442.34	tr	Fe I	68	4635.33	2	Fe II	186
4443.80	5	Ti II	19	4636.34	tr	Ti II	38
4444.56	2	Ti II	31	4648.93	2	Fe II	25
.56	--	Fe II	201	4656.97	8	Fe II	43
4447.13	tr	Fe I	69	4663.70	3	Fe II	44
4447.72	1	Fe I	68	4666.75	10	Fe II	37
4450.49	6	Ti II	19	4670.17	5	Fe II	25
4451.54	5	Fe II	---	4702.98	1	Mg I	11
4452.11	7	Fe II	7 F	4708.66	1	Ti II	49
4455.26	tr	Fe II	---	4713.14	8 n	He I	12
4456.65	tr	Ti II	115	4728.07	2	Fe II	4 F
4457.95	3	Fe II	6 F	4731.44	10	Fe II	43
4459.12	1	Fe I	68	4762.77	1	Ti II	17
4461.43 P	8	Fe II	26	4763.84 P	1	Ti II	48
.65	--	Fe I	2	4764.54	1	Ti II	48
4464.46	4	Ti II	40	4774.74	tr	Fe II	20 F
4466.55	1	Fe I	350*	4779.99	3	Ti II	92
.57	--	Fe I	2	4798.54	2	Ti II	17
4468.49	7	Ti II	31	4805.10	4	Ti II	92
4469.16	2	Ti II	18	4812.35	1	Cr II	30
4470.86	1	Ti II	40	4814.55	4	Fe II	20 F
4471.48	12 n	He I	14	4824.13	6	Cr II	30
4472.92	10	Fe II	37	4825.71 P	1	Fe II	30
4474.91	tr	Fe II	7 F	4833.21 P	2	Fe II	30
4476.02	tr	Fe I	350	4836.22	2	Cr II	30
4481.13	9	Mg II	4	4840.00 P	tr	Fe II	30
.33	--	Mg II	4	4848.24	3	Cr II	30
4482.17	1	Fe I	2	4861.33	100	H β	---
.26	--	Fe I	68	4864.32	tr	Cr II	30
4488.32	3	Ti II	115	4865.62	tr	Ti II	29
4489.18	15	Fe II	37	4871.27 P	2	Fe II	25
4491.40	17	Fe II	37	4874.02	1	Ti II	114
4493.53	1	Ti II	18	4876.41	3	Cr II	30
4494.57	1	Fe I	68	4884.57	tr	Cr II	30
4501.27	5	Ti II	31	4889.63	2	Fe II	4 F
4508.28	17	Fe II	38	.70	--	Fe II	3 F
4515.34	20	Fe II	37	4893.78	1	Fe II	36
4518.30 P	1	Ti II	18	4905.35	1	Fe II	20 F
4520.22	17	Fe II	37	4911.20	1	Ti II	114
4522.63	13	Fe II	38	4921.93	3 n	He I	48
4528.51	2	V II	56	4923.92	12	Fe II	42
.62	--	Fe I	68*	4991.11 P	1	Fe II	25
4529.46	5	Ti II	82	4993.36	4	Fe II	36
4533.97	13	Ti II	50	5000.73 P	2	Fe II	25
4.17	--	Fe II	37	5005.14	1	N II	19,64
4539.62	tr	Cr II	39	5013.71	1	Ti II	71
4541.52	10	Fe II	38	5015.68	7 n	He I	4
4544.01	1	Ti II	60	5018.43	15	Fe II	42
4545.14	3	Ti II	30	5031.02	tr	Sc II	23
4549.47	25	Fe II	38*	5041.06	1	Si II	5
.62	--	Ti II	82	5047.74	1 n	He I	47
4552.25 P	1	Ti II	30	5056.02	1	Si II	5
4555.02	3	Cr II	44	5072.40	tr	Fe II	19 F
4555.89	20	Fe II	37	5100.66 P	2	Fe II	35
4558.66	6	Cr II	44	.70	--	Fe II	---
4563.76	4	Ti II	50	.84	--	Fe II	185
4564.59	tr	V II	56	5120.34 P	tr	Fe II	35
4565.78	2	Cr II	39	5129.14	2	Ti II	86
4568.31	1	Ti II	60	5132.67 P	3	Fe II	35
4571.10	3	Mg I	1	5136.79	tr	Fe II	35
4571.97	6	Ti II	82	5146.12 P	2	Fe II	35
4576.33	10	Fe II	38	5154.06	2	Ti II	70
4579.52	tr	Fe II	---	.40 P	--	Fe II	35
4580.06	5	Fe II	26	5158.81	3	Fe II	19 F
4582.84	8	Fe II	37	5167.32	3	Mg I	2
4583.83	18	Fe II	38	.49	--	Fe I	37
4588.22	5	Cr II	44	5169.03	12	Fe II	42
4589.89	4	Cr II	44	5171.62 P	1	Fe II	35
.96	--	Ti II	50	5172.68	3	Mg I	2
4592.09	4	Cr II	44	5183.60	4	Mg I	2
4593.83	1	---	---	5185.90	1	Ti II	86
4595.95	3	---	---	5188.70	2	Ti II	70

TABLE 2 (Cont'd)

I.A.	Int.	Element	Mult.	I.A.	Int.	Element	Mult.
5197.57	16	Fe II	49	5711.09	tr	Mg I	8
5211.54	tr	Ti II	103	5712.15	tr	Fe I	686
5226.53	2	Ti II	70	5732.72 P	tr	Fe II	57
5227.19	2	Fe I	37	5746.96	1	Fe II	34 F
5234.62	16	Fe II	49	5747.88 P	tr	Fe II	164
5237.34	2	Cr II	43	5754.8	2	N II	3 F
5254.92 P	6	Fe II	49	5813.67	tr	Fe II	163
5256.89 P	2	Fe II	41	5875.63	80 n	He I	11
5261.61	2	Fe II	19 F	5889.95	10	Na I	1
5262.10	1	Ti II	70	5895.92	8	Na I	1
5264.80	5	Fe II	48	5913.87	1	Cr II	---
5268.88	1	Fe II	18 F	5952.55 P	1	Fe II	182
5269.54	1	Fe I	15	5957.61	1 n	Si II	4
5272.41	1	Fe II	185	5978.97	5 n	Si II	4
5273.38	3	Fe II	18 F	5991.38	20	Fe II	46
5274.99	1	Cr II	43	6040.4	2	---	---
5275.99	16	Fe II	49	6046.2	1	---	---
5279.92	2	Cr II	43	6053.48	tr	Cr II	105
80.08	--	Cr II	43	6084.11	8	Fe II	46
5284.09	9	Fe II	41	6103.54	2	Fe II	200
5305.85	2	Cr II	24	6113.33	4	Fe II	46
5308.44	1	Cr II	43	6116.04 P	1	Fe II	46
5313.59	2	Cr II	43	6122.44	1	Mn II	13
5316.61	27	Fe II	49*	6124.85	tr	Si I	30
.78	--	Fe II	48	5.03	--	Si I	30
5325.56	5	Fe II	49	6125.86	tr	Mn II	13
5328.04	1	Fe I	15	6128.72	tr	Mn II	13*
5328.53	1	Fe I	37	9.02	--	Mn II	13
5333.65	3	Fe II	19 F	6129.71 P	tr	Fe II	46
5334.88	2	Cr II	43	6130.79	tr	Mn II	13
5336.81	2	Ti II	69	6131.92	tr	Mn II	13
5337.71	4	Fe II	48	6147.74	12	Fe II	74
5346.56 P	2	Fe II	49	6149.24	10	Fe II	74
5362.86	12	Fe II	48	6155.99	1 n	O I	10
5376.47	3	Fe II	19 F	6.78	--	O I	10
5381.02	1	Ti II	69	6158.19	2	O I	10
5396.3	1	Ti II	80	6160.75 P	tr	Fe II	161
5396.59 P	1	Ti II	102	6172.6	2	---	---
5407.62	1	Cr II	23	6175.16	1	Fe II	200
5408.84	3	Fe II	184	6179.38	tr	Fe II	163
5412.64	1	Fe II	17 F	6191.56	2	Fe I	169
5414.09	6	Fe II	48	6199.16	tr	Fe II	162
5418.80	1	Ti II	69	6229.34 P	2	Fe II	34
5420.90	3	Cr II	23	6230.73	tr	Fe I	207
5425.27	12	Fe II	49	6233.52	2	Fe II	---
5427.83	2	Fe II	---	6238.38	10	Fe II	74
5429.70	1	Fe I	15	6239.36 P	2	Fe II	34
5432.98 P	8	Fe II	55	6239.95 P	2	Fe II	74
5478.35	2	Cr II	50	6247.56	14	Fe II	74
5502.05	2	Cr II	50	6248.92	6	Fe II	---
5503.18	2	Cr II	50	6252.56	tr	Fe I	169
5506.78	1	Fe I	15	6269.94	3	---	---
5508.60	1	Cr II	50	6291.8	2 n	---	---
5510.68	2	Cr II	23	6300.30	20	O I	1 F
5525.14 P	4	Fe II	56	6317.98	30	Fe II	---
5526.81	1	Sc II	31	6331.97	1	Fe II	199
5527.33	2	Fe II	17 F	6347.09	10	Si II	2
5529.94 P	1	Ti II	68	6363.85	4	O I	1 F
.94	--	Fe II	224*	6369.45	7	Fe II	40
5534.86	30	Fe II	55	6371.36	4	Si II	2
5567.82	1	Fe II	---	6383.75	11	Fe II	---
5572.85	tr	Fe I	686	6385.47	5	Fe II	---
5577.35	3	O I	3 F	6407.30	2	Fe II	74
5586.76	2	Fe I	686	6416.90	12	Fe II	74
5591.38 P	2	Fe II	55	6432.65	18	Fe II	40
5615.65	tr	Fe I	686	6442.97	3	Fe II	---
5627.49 P	2	Fe II	57	6456.38	16	Fe II	74
5640.97	1	Sc II	29	6482.07	2	N II	8
5657.87	5	Sc II	29*	6491.28	4	Fe II	---
.92 P	--	Fe II	57	6493.05	5	Fe II	---
5667.16	1	Sc II	29	6506.33	1	Fe II	---
5669.03	tr	Sc II	29	6516.05	16	Fe II	40
5684.19	1	Sc II	29	6517.01	1	Fe II	---
5709.38	1	Fe I	686	6562.82	500	H α	---

NOTES

*Probably the stronger contributor.

λ4461.5 This line appears too strong to be due wholly to the two lines indicated.

λλ6347.09, 6371.36 On Ce 6238 the emission is divided by a strong absorption core.

able displaced *Ca* II lines in the spectrum of HD 190073.[8] But the detailed patterns of the numerous components in the two stars are quite different; in fact, the two strongest components in HD 190073 have no corresponding lines in XX Ophiuchi but lie squarely between pairs of well-marked lines (see Table 6). The apparent correspondence in displacement of four components may or may not be significant (note discrepancies in relative intensity).

TABLE 3

EMISSION LINES MEASURED IN THE SPECTRUM OF XX OPHIUCHI

Element	No.	Element	No.	Element	No.	Element	No.
H	29	*Mg* I	9	*Sc* II	15	[*Fe* II]	30
He I	14	*Mg* II	6	*Ti* II	103	*Ni* II	6
C II	1	*Al* I	1	*V* II	22	*Sr* II	2
N II	2	*Si* I	3	*Cr* II	58	Unident.	10
[*N* II]	1	*Si* II	9	*Mn* I	1		
O I	2	[*S* II]	2	*Mn* II	6	Total	577
[*O* I]	3	*Ca* I	1	*Fe* I	55		
Na I	2	*Ca* II	4	*Fe* II	180		

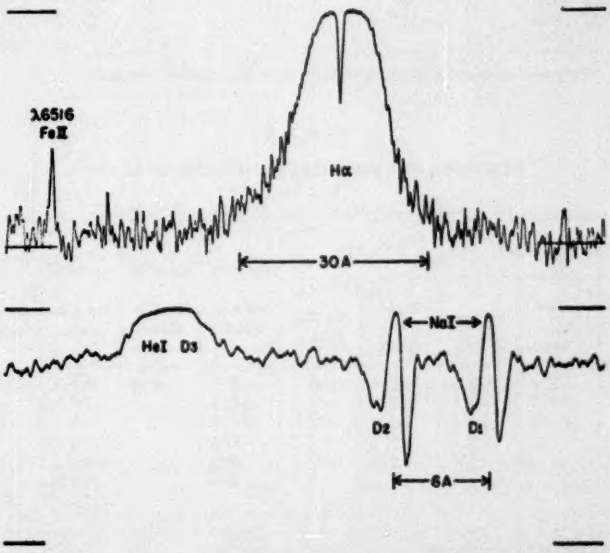

FIG. 5.—Tracings of lines in the spectrum of XX Ophiuchi. Ce 6438

On the 1950 plates the continuous spectrum is underexposed in the region of H and K. On the first plate, Ce 6234, however, there are several components having nearly the same displacements as in 1949 but with different relative intensities. On the second plate, Ce 6434, the similarity seems decidedly less, but the comparison is unsatisfactory be-

[8] *Mt. W. and P. Reprints*, No. 30; *Ap. J.*, 113, 55, 1951.

cause of underexposure and of interference by emission lines. Displaced H and K lines can be detected in the underexposed continuous spectrum of a few of the earlier low-dispersion spectrograms. It seems certain that these lines are not stabilized but are subject to large variations in intensity, if not in pattern.

Hydrogen lines.—The Balmer lines of hydrogen are complex, unsymmetrical, and subject to large variations. In 1949 both bright and dark components were relatively

TABLE 4

DISPLACEMENTS OF EMISSION LINES
(Km/Sec)

PLATE CE	*M* II (*Fe, Ti, Cr, V, Ni*)		[*Fe* II]
	With Abs. Comp.	No Abs. Comp.	
5687	−33.5 34	−37.6 121	−44.1 10
5751	−38.8 74	−42.3 115	−45.1 8
6234	.....	−38.8 164	−41.8 8
6238	.....	−41.8 28	.....
6434	.....	−43.5 229	−42.0 16
6438	.....	−42.6 86	−40.9 10
1921–1931	−34*	.....	−37
1941–1946	−35*	.....	−27

* Mean of all bright metallic lines with and without dark components.

TABLE 5

RESIDUALS OF VELOCITIES FROM EMISSION LINES
(Km/Sec)

ELEMENT	CE 5687		CE 5751		CE 6234	CE 6238	CE 6434	CE 6438	MEAN
	With* Abs. Comp.	No Abs. Comp.	With* Abs. Comp.	No Abs. Comp.	No Abs. Comp.	No Abs. Comp.	No Abs. Comp.	No Abs. Comp.	No Abs.† Comp.
Fe II	+5.2	+0.3	+4.5	−0.1	−0.5	0.0	+0.3	−0.2	0.0
Ti II	+4.1	−0.1	+4.1	−0.5	+0.4	.....	+0.9	+1.6	+0.4
Cr II	+3.1	+0.6	+2.2	+2.0	+0.4	.....	−1.6	−0.2	0.0
V II	.....	−0.7	−0.1	−1.0	−0.6	.....	−2.0	.....	−1.4
Ni II	.....	−2.6	+1.0	−1.2	0.0	.....	−1.3	.....	−1.2
[*Fe* II]	.....	−6.5	.....	−2.8	−3.0	.....	+1.5	+1.7	−1.2
[*O* I]	.....	.....	.....	.....	.....	−1.9	.....	+1.0	−0.4

* With respect to lines of the same element having no absorption component.

† The mean residuals of the following elements do not exceed ±3 km/sec: *Na* I, *Mg* I, *Si* I, *Fe* I, *Mg* II, *Si* II, *Sc* II.

weak; in 1950 the bright lines were wider and stronger, the dark cores deeper. During both years the bright lines, each taken as a whole, probably occupied positions corresponding to the same velocity as that yielded by the bright metallic lines. Apparent discrepancies will, of course, be found if, as on some of the older plates, only one component of the emission is measured. The Balmer continuum is strong in emission and seems to suppress metallic lines.

Table 7 shows that the strong absorption cores of the *H* lines yield nearly the same displacements as do the weak dark components of the metallic lines. Progression in displacement from line to line is small except for plate Ce 6234, which shows a trend from −56 km/sec at *Hβ* to −43 km/sec at *H* 11.

The structure of the *Hα* line on Plate Ce 6438 is shown by the tracing in Figure 5. The width shown here is 38 A, but the outer wings brought out by the stronger exposure, Ce 6238, extend the total width to at least 50 A, which is probably too great to correspond to a velocity dispersion. On plate Ce 5751 the bright *Hβ* line is 16.6 A wide. A quantitative study of the profiles of the wide emission lines in this and other Be spectra would be valuable. For the stronger lines special sets of graded exposures would be desirable.

TABLE 6

DISPLACEMENTS OF ABSORPTION COMPONENTS OF *Ca* II
(Km/Sec)

XX OPHIUCHI		HD 190073		XX OPHIUCHI		HD 190073	
Displ.	Int.	Displ.	Int.	Displ.	Int.	Displ.	Int.
(+34)	2*	.....	.....	−203	3	(−200)	3
Em. ?	.....	0	2*	−296	4	(−296)	1
(−28)	3	.....	.....	.....	.....	−323	4
(−72)	2	.....	.....	−366	8	−358	3
−144	1	−147	1	.....	.....	(−396)	Tr
.....	.....	−181	5				

* The intensities vary from plate to plate.

TABLE 7

DISPLACEMENTS OF ABSORPTION COMPONENTS
(Km/Sec)

Plate Ce	*H*	*M* II	Plate Ce	*H*	*M* II
5687.....	−59	−64	6238.....	−61 *Hα*	.....
5751.....	−61	−70	6434.....	−61	.....
6234.....	−54	.....	6438.....	−68 *Hα*, *Hβ*	.....

Helium lines.—The blue and violet lines of *He* I are inconspicuous, probably because of insufficient excitation. On the 1949 plates no *He* I lines are seen with certainty. In 1950, λ 4471 and λ 4026 are present as diffuse emission lines, which are very weak on plate Ce 6234, fairly strong on Ce 6434. No lines of *He* II were recognized. On plates Ce 6238 and 6438 showing the yellow region, D3 λ 5876 is a broad, intense emission line.

The spectrum of XX Ophiuchi is a singular one, no close match for it being known. The excitation of the emitting atmosphere is obviously much lower than in BD+11°4673, whose spectrum at times shows a set of bright metallic lines weaker than those in XX Ophiuchi but rather similar in general pattern. The spectrum of HD 190073 is similar to that of XX Ophiuchi in having (1) bright sodium lines and (2) several strong absorption components of H and K with large negative displacements; but otherwise the two spectra differ greatly.

The bright metallic lines of XX Ophiuchi are much stronger relative to the continuous spectrum than in other Be stars exhibiting the same range of atomic excitation. This indicates a larger emitting atmosphere, but the cause of the greater extension is not known. The emitting strata seem relatively quiescent, as both permitted and forbidden lines of various elements and ions yield practically the same velocity; moreover, the velocity has shown but little change in nearly thirty years. The absorbing layers have been more active. It would be interesting to observe the spectrum with high dispersion at some future time when the displaced dark lines are strong.

I am indebted to Miss Sylvia Burd and Miss Louise Lowen for valuable assistance in identifying the lines and calculating the velocities.

THE SPECTRAL CHANGES OF VV CEPHEI OUTSIDE ECLIPSE

DEAN B. MCLAUGHLIN
Observatory, University of Michigan
Received March 3, 1951

ABSTRACT

Changes of the spectrum of VV Cephei during nearly a complete orbital period of 20.4 years are summarized. The spectrum is a composite of: (1) supergiant M absorption; (2) strong "violet" continuum; (3) wide hydrogen emission split by strong "shell" absorption; (4) narrow bright lines of *Fe* II and [*Fe* II]. Components 2 and 3 disappeared during the eclipse in 1936–1937, but 4 remained undiminished and is assigned to a nebula enveloping the binary.

Hydrogen emission shows V/R variation, but the longward component remains nearly always the weaker. Positively displaced hydrogen absorption lines appear suddenly at irregular intervals. Metallic "shell" absorption is occasionally observed at phases far from eclipse.

Weaker *Fe* II emission with width and structure like that of hydrogen has been identified. At times this component strengthens and apparently suppresses the narrow *Fe* II lines. The forbidden lines do not show this change but have undergone slow variations relative to the permitted lines.

INTRODUCTION

Observations at Ann Arbor of the spectrum of this giant eclipsing system now extend over nine-tenths of the orbital period of 20.4 years, with an interruption in 1944–1945, during which years only one plate was obtained. The total number of spectrograms exceeds 200. The M-type supergiant star is now near approaching nodal passage, and the next eclipse of the early-type companion will begin early in the summer of 1956. If the events of the preceding eclipse are repeated, interesting effects due to the passage of the hot star behind the atmosphere of the cool supergiant may be expected to begin in 1955. The results of a study of the spectrograms from 1932 through June, 1938, including the eclipse in 1936–1937, have been published by Goedicke.[1]

No absorption lines have been found that can be referred with confidence to the reversing layer of the early-type star. The extent of its violet continuum suggests that it probably belongs to a subdivision of class B. The strong emission lines of hydrogen are definitely associated with this component, for they disappeared during its total eclipse in 1936–1937, but their widths are too great and their structural changes too conspicuous to permit accurate measurement for radial velocity. The sharp absorption lines of hydrogen that split the emission lines are doubtless formed in an outer shell, and their positions fluctuate with the changes of emission structure in a manner similar to that observed in Be shell stars.

In addition to the M supergiant spectrum, the strong violet continuum, and the bright and dark hydrogen lines, there are narrow bright lines of *Fe* II and [*Fe* II] whose radial velocities, in the main, are close to that of the center of mass of the system. This circumstance, in conjunction with the persistence of these lines at full strength during the eclipse, indicates that they probably originate in a nebula that surrounds the whole system.

THE LIGHT-VARIATIONS

The writer has made a long series of visual estimates, which is fairly continuous from 1933 to 1950, except for an interruption during 1944. The light varies through a range of about 0.5 mag., with no evident regularity, though the intervals between maxima are always several months and may exceed a year. In 1942 and again in 1947 the range of variation was much reduced, and the star remained near its median brightness. In gen-

[1] *Pub. Obs. U. Michigan*, 8, 1, 1939.

eral, the minima are broad and flat, the maxima of much shorter duration, rarely more than a month. A few broad, low maxima have occurred, e.g., in 1939.

In spite of the visual range of 0.5 mag., the contrast of the class M spectrum has not been observed to change appreciably, except near the time of the eclipse. The spectrum of the M giant is dominant in the visual region and only begins to appear "washed out" in the region shortward of λ 4300. It is natural to attribute the light-variation to the class M star. In general, we should expect such a star to exhibit a greater range of brightness in the photographic than in the visual region. Spectrograms taken at maxima and minima of light have been compared directly in a search for changes of contrast, but the lines of the class M spectrum are no more "washed out" at minimum than at maximum. It does not help to attribute the variation to the hot companion, for that would require a change in the reverse direction, and the strength of the class M spectrum in the bluer region would then be difficult to account for. The evidence at least suggests the possibility that both stars vary in some closely linked fashion, however improbable such a condition may appear.

HYDROGEN EMISSION AND ABSORPTION

The hydrogen emission is usually unsymmetrical about the dividing absorption. The shortward component commonly exceeds the longward in strength by a factor of 2 or more. The higher members of the Balmer series only rarely show the longward component, so that the spectrum suggests a reversal of that of P Cygni. Occasionally the longward components of $H\gamma$ and $H\delta$ become slightly the stronger, but the longward component of $H\beta$ has been seen clearly to be the stronger on only two dates: September 8, 1944, and May 6, 1950.

The cycle of variation of the ratio V/R is irregular. Appreciable changes sometimes occur within a week or two but are usually slower. Observations during the four years previous to the eclipse in 1936–1937 showed several cycles in which the changes of V/R were correlated with the light-variations, in the sense that the shortward component tended to be strongest near the minima of light. In a crude way this relationship has continued to hold, but it is not so well defined as it appeared to be in the first four years' observations.

On some occasions when the violet emission components were strongest, that component at $H\delta$ has been abnormally wide. Sometimes this "flare" is of brief duration, a few weeks at the most. On other occasions, as in 1938, it has lasted several months. Throughout the interval from January, 1946, to July, 1950, only rare and slight widening occurred. This inactivity may be related to the reduced range of variation of light that was so noticeable in 1947. The flaring has not been distinctly correlated with the light-variations, but it has been most frequently noticed near the beginning of an increase of light. During 1949 the hydrogen lines declined a little in strength and have remained at their reduced intensity through 1950. This change coincided roughly with a decrease of the permitted *Fe* II emission, to be noted below. The central absorption lines that divide the hydrogen emission vary in strength, but no clear correlation has been found, either with the light-variations or with other spectral changes.

Strong absorption satellites with displacements of +100 to +200 km/sec relative to the normal central absorptions appear from time to time at $H\delta$ and the higher Balmer lines, as well as at H and K of *Ca* II. On one occasion in 1948, corresponding displaced lines were also seen at some lines of *Fe* II and *Ti* II. The hydrogen satellites at their strongest may equal or exceed the normal absorption. They are usually short-lived, lasting only a few weeks, and show no evident regularity. From 1932 to 1935 they were seen occasionally, but only rarely were they outstanding. From the end of the eclipse in 1937 until 1943, inclusive, they were extremely rare and never strong. From early 1946 through 1950, however, there have been several recurrences of very strong positively displaced satellites. They are not distinctly related to the light-variations or to other spec-

tral changes. They have been seen more often at light-maxima than at minima; yet a few of the most conspicuous occurrences have been during light-minima.

The record is not sufficiently continuous to show clearly the life-history of these longward satellites. However, a series of plates in the latter part of 1948 is suggestive in this respect. On October 12, no satellites were seen. On October 22, weak satellites appeared at $H\delta$ and $H\epsilon$, with velocity about +200 km/sec. On November 12, stronger satellites were located at about +150 km/sec. In addition to components at the hydrogen lines, positively displaced absorptions were seen at K *Ca* II; λ 3900 and λ 3913 *Ti* II; and λ 4233 and λ 4584 *Fe* II. The next good plate was obtained on December 23. Separate satellites were no longer visible, but the hydrogen lines appeared greatly strengthened, widened, and shifted somewhat in the positive direction, as if the satellites had merged with them. A trace of brightening in the K absorption suggested duplicity. The displaced *Fe* II absorptions were gone, but those of *Ti* II were faintly visible. Finally, on January 8, 1949, the hydrogen and *Ca* II absorptions appeared a little less strong, and the *Ti* II absorption had disappeared.

VARIATIONS OF IRON EMISSION LINES

On the earlier plates, from 1932 to 1937, the permitted lines of *Fe* II were decidedly weaker in emission than the forbidden lines. The ratio of λ 4233 *Fe* II to λ 4244 [*Fe* II] is the best index to the variations. Late in 1937, just after the end of eclipse, λ 4233 fluctuated and at times approached equality with λ 4244. Gradually, during 1938 and 1939, the permitted lines increased. From 1940 through 1948 they remained nearly constant, with λ 4233 appreciably stronger than λ 4244. During 1949 the permitted lines weakened until λ 4233 was somewhat weaker than λ 4244. No noticeable changes occurred during 1950. The structure of the emission at λ 4233 is complicated. In the first series of plates measured by the writer,[2] the line was narrow and gave velocities in good agreement with those of the forbidden lines. Goedicke,[3] however, found that λ 4233 sometimes gave very discordant velocities, usually with negative residuals. He attributed this to variable blending with a maximum in the continuous spectrum of the M star.

The writer confirms the discordances but not the suggested explanation. All the plates were studied on the Hartmann spectrocomparator in conjunction with an excellent spectrogram on which λ 4233 agreed in velocity with the forbidden lines. The variations of position are extremely conspicuous, and the discordances often exceed 50 km/sec. During the total phase of eclipse no discordances occurred. This is considered significant, in view of the association of the hydrogen emission with the eclipsed star and the known association of hydrogen and *Fe* II emission in Be spectra. From the end of the eclipse in 1937 until the end of 1946, the position of λ 4233 was always more or less disturbed, and it often appeared diffuse and occasionally double. During 1947 the discordances decreased, and from 1948 through 1950, the line at λ 4233 has been sharp and has agreed in velocity with λ 4244.

The cause of the disturbance is identifiable on a number of spectrograms taken since 1938. Briefly, in addition to the narrow λ 4233 emission line that probably originates in the same nebular region as λ 4244, there is a usually weaker λ 4233 emission with a width and structure similar to that of the hydrogen lines. On occasions this wider emission becomes stronger, and its shortward component equals or even exceeds the narrow "nebular" line. Sometimes the two are badly blended, but on other occasions they are separable. On a number of spectrograms the longward emission component is visible, and on a few the central sharp shell-absorption line has appeared distinctly.

The changes are not fully accounted for by a simple strengthening of the hydrogen-like λ 4233 emission. It is quite evident on some plates that the sharp "nebular" λ 4233 emis-

[2] *Ap. J.*, **79**, 380, 1934.

[3] *Op. cit.*, p. 33.

sion actually weakens when the broad emission increases. No corresponding change has been noted in the forbidden lines.

It is noteworthy that the cessation of disturbances at λ 4233 in 1947 was followed by an appreciable fading of the hydrogen bright lines and also of the permitted *Fe* II lines during 1949.

IONIZED CALCIUM LINES

The occurrence of longward absorption satellites at the *Ca* II lines coincidentally with those of hydrogen has already been mentioned. However, on many plates that do not show hydrogen satellites the K line is double or triple. The shortward member of the group is persistent, and its velocity does not disagree greatly with that of the main hydrogen absorption. It is probably in part interstellar. The other two components vary greatly in strength and appreciably in position. Approximate positions on a few typical plates are displaced roughly +110 and +270 km/sec relative to the main component. The H line shows the absorption at +270 km/sec, but the less displaced one is masked by *He* absorption and emission.

Strong emission occurs on the shortward edges of H and K. It varies greatly in strength. At the longward edge of the K group is a conspicuous emission line. It may be due entirely to λ 3938 [*Fe* II], but it appears to be variable and seems less sharp than the other forbidden lines, which raises a suspicion that it may be due in part to *Ca* II.

Although absorption satellites at the *Ca* II lines can be identified as corresponding to those of hydrogen, when present, the changes of the *Ca* II satellites in general have not been clearly related either to the light-variations or to any other spectral changes.

METALLIC SHELL-ABSORPTION LINES AND ASSOCIATED EMISSION

During 1946 strong, sharp shell-absorption lines of *Ti* II were present at λλ 3900, 3913, 4164, 4172, and, when the plates were strongly exposed, 3759 and 3761. The *Mg* I lines near *Hη* were also seen on some plates, and occasionally λ 4067 *Ni* II and λ 4078 *Sr* II appeared. The velocities of these features did not differ greatly from those of the hydrogen absorption lines. The chief component of K was dominant and, though longward satellites appeared, they were not outstanding.

In 1947 conspicuous narrow emission borders appeared to the shortward of the *Ti* II absorption lines. During the winter and spring of 1948 the *Ti* II absorption weakened considerably. In July it disappeared, and its position was occupied by somewhat wide, undisplaced emission, which remained until the last observation of the season, January 8, 1949. Occasional traces of fine central absorption were seen on these emission lines. It will be recalled that from October to December, 1948, positively displaced *Ti* II shell absorption was observed. In the summer of 1949 "undisplaced" *Ti* II absorption was again fairly conspicuous, and the emission was weak. During 1950 neither absorption nor emission has been prominent, but both have been noted occasionally.

CONCLUSION

The chief impression conveyed by the variable spectrum of VV Cephei is one of bewildering complexity. The long-continued reversed P Cygni structure is itself difficult to comprehend, and it may hold the key to the problem. The obvious, and perhaps naïve, interpretation in terms of continuous infall would appear fantastic if we did not have the well-known example of similar behavior of solar prominences. The positively displaced absorption satellites may be merely another aspect of the same phenomenon. On the other hand, they call to mind the gaseous currents that occur in a number of close binaries, for example, β Lyrae and UX Monocerotis.

The apparent suppression of the "nebular" *Fe* II lines when the "stellar" *Fe* II emission strengthens is suggestive of a withdrawal of excitation from the nebula. If the per-

mitted emissions originate through recombination, then it appears that the strengthening of the wide stellar emission may represent the formation of a denser shell in which most of the high-frequency radiation of the hot star is exhausted, leaving little for the excitation of the nebula. The forbidden lines, on the other hand, are not affected, possibly because the population of the metastable states is determined chiefly by collisions.

The presence of a metallic shell-absorption spectrum at phases near greatest elongation, and even at times when the class M giant is more distant from us than the companion, shows that extreme caution must be exercised in the interpretation of supposed eclipse absorption effects long before or long after the eclipse. The shell-absorption lines of hydrogen must originate along the line of sight to the bright hydrogen envelope of the hot star. The strength of these dark lines at all orbital phases outside eclipse shows that they have no close relationship to the M-type star. The *Ti* II, *Mg* I, and *Ca* II absorption probably originates in the same general region as the hydrogen lines. Whether that region is a very small volume close about the bright hydrogen envelope of the hot star, or a very long light-path through the nebula that is believed to envelop the system, cannot be decided at this time.

THE ATMOSPHERES OF A-TYPE SUBDWARFS AND 95 LEONIS*

JOSEPH W. CHAMBERLAIN AND LAWRENCE H. ALLER
Observatory, University of Michigan
Received February 14, 1951

ABSTRACT

Line profiles and equivalent widths have been measured in the spectra of two subdwarfs, HD 19445 and HD 140283, classified as A4sp and A5sp, and a main-sequence A4 star, 95 Leonis. The data are analyzed by conventional curve-of-growth procedures and by the method of model atmospheres and line profiles. The point of view adopted is that the structure of the atmosphere must correctly reproduce the profiles of the hydrogen lines. It is found that for 95 Leonis $T_{\text{eff}} = 8900°$ K and $\log g \simeq 3.90$ (which are normal for an A4 star), whereas for the subdwarfs $T_{\text{eff}} = 6300°$ K and $\log g \simeq 4.80$.

The assumption that the amount of hydrogen per gram of stellar material is the same as that in the sun is in harmony with the data; i.e., there is no evidence that the subdwarfs are deficient in hydrogen. The excitation temperatures are derived from curves of growth for *Fe* I, using King's laboratory *f*-values. A comparison of theoretical and observed line profiles and equivalent widths suggests that *Ca* is deficient in the subdwarf atmospheres. Low *Fe* abundances in these stars are indicated by curves of growth constructed with Greenstein's empirical line strengths for τ UMa and υ Sgr. The color temperatures and the Balmer discontinuities are predicted.

I. INTRODUCTION

The stars HD 19445 and HD 140283 are listed in the Mount Wilson Spectroscopic Parallax Catalogue[1] with absolute magnitudes intermediate between the main-sequence A stars and the conventional white dwarfs. These "intermediate white dwarfs" or "subdwarfs" possess a number of interesting spectral peculiarities. The spectral classification given in the *Henry Draper Catalogue*, which is based essentially on the Balmer lines, differs considerably from that listed by the Mount Wilson observers, who classified the spectra without regard to the appearance of the hydrogen lines. The presence of relatively sharp and weak hydrogen lines, in what otherwise might be classed as A-type spectra, is perhaps the most interesting observed feature of the subdwarfs.

95 Leonis (HD 103578) is apparently a normal A star lying slightly above the main sequence of the Hertzsprung-Russell diagram. Table 1 summarizes the available information on these stars.

An interpretation of the subdwarf spectra must necessarily predict either (1) a chemical composition similar to that of the sun, with the peculiarities explained in terms of the physical parameters of the star's atmosphere; (2) an actual surplus or deficiency of one or more elements; or (3) a combination of anomalous abundances *and* physical conditions. In turn, the hydrogen/metal ratio may be abnormal, or the metals may show relative abundances different from those of the solar atmosphere. Kuiper[2] has suggested that the subdwarfs and the high-velocity stars in general might have low hydrogen contents.

No quantitative analysis of the spectra of A-type subdwarfs has heretofore been attempted. The object of this paper is to show that these spectra may be explained in terms of atmospheres that have temperatures appropriate to F-type stars and that are not deficient in hydrogen. Certain metals do appear to have abnormally low abundances, however. We will also attempt to show that several features of the spectrum of 95 Leonis can be reproduced theoretically on the assumption of normal solar abundances and a model atmosphere representing a star that is slightly above the main sequence.

* This investigation was made possible by a co-operative arrangement between the University of Michigan and the Mount Wilson and Palomar Observatories.

[1] *Ap. J.*, **81**, 187, 1935. [2] *A.J.*, **53**, 194, 1948.

In Section III we discuss the determination of the excitation temperature with the aid of King's laboratory *f*-values and conclude that the temperatures for the subdwarfs are much lower than for ordinary A stars. Similarly, Verweij's theoretical hydrogen profiles, when compared with the observed profiles, indicate either extremely low surface gravities (which seems doubtful) or low temperatures. Preliminary values for the surface gravities and effective temperatures of these stars are derived in Section IV from curve-of-growth considerations. T_{eff} and g are then used to construct provisional model atmospheres, which, in turn, serve as the starting point for the calculation of theoretical line profiles for hydrogen (Sec. V) and for λ 3933 and λ 4227 of *Ca* (Sec. VI). The correct prediction of line profiles and equivalent widths is a necessary condition for acceptable model atmospheres. Thus, to obtain the final model atmospheres, we use the trial-and-error method of assuming T_{eff} and g, calculating a model atmosphere, and then predicting line profiles, which are compared with the observations. The adopted atmospheric structure not only should yield the correct profiles but also should predict the

TABLE 1

DATA FOR 95 LEONIS AND SUBDWARFS

Star	α (1900)	δ (1900)	Spectral Type		M_{vis} Mt. W.
			HD	Mt. W.	
95 Leonis (HD 103578)....	11^h50^m5	+16°12′	A2	A4s	+1.2
HD 19445.....	3 2.5	+25 59	F2	A4sp	+5.0
HD 140283.....	15 37.7	−10 36	F5	A5sp	+4.9

Star	m_{vis}	Rad. Vel.	μ_α	μ_δ
95 Leonis (HD 103578)....	5.49	(Var.) $v_0 = -21$ km	+0″010	−0″007
HD 19445.....	8.0	−143.	−0.222	− .796
HD 140283.....	7.26	−171.0	−1.666	−0.320

observed color temperature and Balmer discontinuity (Sec. VIII). In a word, it must explain all the observed data. Curves of growth for *Fe*, based on Wrubel's theoretical curve, are given in Section VII. Empirical line strengths obtained from stars other than the sun seem to be most satisfactory for our purposes. The curve-of-growth results, however, definitely seem to be less reliable than those obtained from line profiles.

II. OBSERVATIONAL DATA

One plate of each of the subdwarfs and two of 95 Leonis were made with the coudé grating spectrograph and 32-inch camera at the 100-inch telescope of the Mount Wilson Observatory. This combination gives a normal dispersion of about 10 A/mm. Tracings of the plates were made with the conventional transmission-type microphotometer in Pasadena, with a magnification of 60 × plate. Photometric calibration was supplied by a step-slit.

The coudé plates were supplemented with two exposures of 95 Leonis made with the 24-inch camera attached to the two-prism spectrograph of the 37½-inch reflector in Ann Arbor. The dispersion is 20 A/mm at $H\gamma$. The emulsion employed was Eastman IIa-O, and the plates were calibrated with a wedge-slit calibration spectrograph, which is de-

scribed elsewhere.[3] Tracings with a magnification of 49× were made of the hydrogen and H and K lines with the Moll microphotometer at Ann Arbor.

Figure 1 illustrates the discrepancy in the observed profiles as obtained from the grating and prism spectrographs. It seems reasonable to suppose that the difference is due primarily to scattering of light in the grating spectrograph. Assuming that the amount of light scattered by the prism instrument in the direction of the plate is negligible, we have compared the observed equivalent widths of $H\beta$, $H\gamma$, and $H\delta$ to obtain an estimate of the amount of grating scattering. A mean value of about 25 per cent was obtained, with good agreement among the separate determinations. Applying this correction to the hydrogen and K-line profiles obtained from the grating spectra, we obtained good fits with the prism profiles. This estimate of the scattering is in accordance with some previous determinations for this Mount Wilson grating.[4]

On the assumption that the amount of scattering is the same in all regions of the spectrum and in all the grating plates used, we have applied the above correction to all grating equivalent widths and profiles. A systematic error of a few per cent in this correction should make very little difference in the final results.

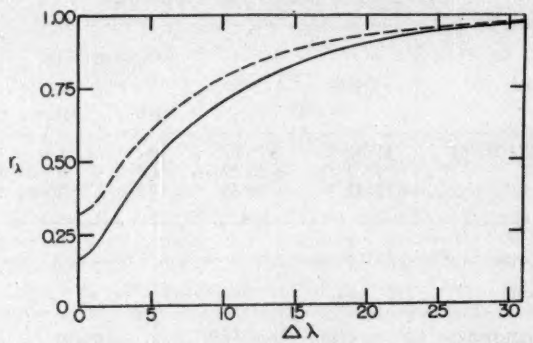

FIG. 1.—Effect of scattering produced by grating spectrograph. *Solid curve*, prism profile; *dashed curve*, uncorrected grating profile. Curves are for $H\gamma$ in 95 Leonis.

In general, there is good agreement between the equivalent widths obtained from the two grating plates of 95 Leonis. However, the central portions of the very strongest lines differ somewhat in the two cases. This is probably due to small errors in the toe of the characteristic curve, where a small change in plate density corresponds to a rather large factor on the intensity scale.

The measured grating intensities for the *Fe* I and *Fe* II lines are listed in Table 2, together with the wave length and excitation potential of the lower level for each line. As we will explain in Section VII, only lines in the λλ 4000–4800 region could be used in the final curve of growth. Lines falling in the wing of a hydrogen line were also omitted.

III. THE EXCITATION TEMPERATURE

For the determination of the excitation temperature of a star from equivalent widths, approximate values of the stellar temperature and of the damping constant for the lines utilized are necessary. Rough values of the damping constant can be determined if preliminary estimates of the effective temperature and surface gravity are available. From the spectral type of 95 Leonis we took $T_{\text{eff}} = 8900°$ K and $\log g = 4.30$, whereas the peculiarities of the subdwarf spectra make such estimates impracticable.

[3] R. C. Williams, *Pub. Obs. U. Michigan*, **7**, 93, 1938. [4] L. H. Aller, *Ap. J.*, **96**, 321, 1942.

TABLE 2

EQUIVALENT WIDTHS OF IRON ABSORPTION LINES
(Uncorrected Grating Intensities)

λ	IDENTIFICATION	W(mA)			E.P. (VOLTS)
		95 Leonis	HD 19445	HD 140283	
4063.61	*Fe* I	80	106	96	2.95
4067.99	I	22	23	8	1.80
4071.76	I	78	115	107	3.28
4122.64	II	42	.....	.....	2.57
4128.75	II	19	.....	.....	2.57
4132.04	I	52	68	68	1.60
4132.97	I	.....	15	23	2.82
4143.37	I	46	51	39	2.20
4143.87	I	68	78	68	2.67
4157.80	I	53	.....	37	1.90
4173.47	II	87	37	33	2.57
4175.60	I	36	39	71	1.85
4178.85	II	73	34	.....	2.57
4184.93	I	9	.....	.....	1.70
4187.02	I	52	56	35	2.40
4187.81	I	44	58	52	3.05
4210.31	I	35	.....	.....	2.07
4216.19	I	50	.....	.....	0.00
4219.41	I	33	.....	.....	3.56
4222.23	I	42	.....	.....	2.44
4227.41	I	58	58	35	3.32
4233.18	II	89	49	32	2.57
4233.61	I	42	33	38	2.47
4235.92	I	51	83	76	2.42
4247.41	I	25	.....	.....	3.35
4248.16	I	14	.....	.....	3.06
4250.10	I	45	43	.....	2.46
4250.78	I	50	89	.....	1.55
4260.46	I	60	72	72	2.39
4271.16	I	48	72	30	2.44
4271.76	I	60	110	50	1.48
4273.32	II	56	.....	19	2.69
4282.41	I	27	39	34	2.17
4296.56	II	44	.....	26	2.69
4303.16	II	62	.....	.....	2.69
4351.71	II	.....	104	.....	2.69
4369.41	II	39	.....	.....	2.77
4383.53	I	70	123	83	1.48
4385.38	II	77	.....	.....	2.77
4388.41	I	20	.....	.....	3.59
4404.74	I	68	98	63	1.55
4415.08	I	61	72	51	1.60
4416.80	II	64	.....	.....	2.77
4427.32	I	22	54	59	0.05
4430.62	I	19	.....	26	2.21
4442.35	I	26	41	.....	2.19
4447.71	I	49	.....	23	2.21
4466.55	I	42	51	17	2.82
4472.90	II	45	.....	.....	2.83
4476.09	I	41	33	24	2.83
4489.15	II	62	.....	.....	2.82
4491.36	II	62	.....	.....	2.84
4494.51	I	50	.....	.....	2.19
4508.26	II	68	50	.....	2.84
4515.31	II	70	.....	.....	2.83
4520.21	II	100	.....	.....	2.80
4522.59	II	88	47	.....	2.83
4541.50	II	42	.....	.....	2.84
4555.84	II	77	15	18	2.82
4576.25	II	35	.....	.....	2.83
4582.75	II	30	.....	.....	2.83
4583.79	II	59	28	.....	2.80
4620.48	II	60	.....	.....	2.82
4666.75	II	39	.....	.....	2.82
4731.50	II	30	.....	.....	2.88

The Verweij[5] theoretical line profiles may also be used to obtain these initial parameters (even though the negative hydrogen ion contributes about half the observed opacity longward of the Balmer limit for a main-sequence A star). They indicated that our initial assumptions were of the correct order of magnitude for 95 Leonis.

The observed hydrogen line profiles for the subdwarfs are much narrower than are the Verweij profiles for an A-type star, unless the latter are computed for a surface gravity of the order of 10 cm/sec^2. Such a low acceleration of gravity seems to be ruled out, however, since the resulting damping constant gives a theoretical curve of growth that deviates greatly from the observed points. Moreover, for a star with log $g = 1.0$ and $T_{\text{eff}} = 8900°$ K, a sizable Balmer discontinuity is predicted, whereas the observed points on the curve of growth indicate that the absorption coefficient should be nearly constant across the Balmer limit. An alternative interpretation of the subdwarf profiles is that they indicate temperatures much lower than those of main-sequence A stars.

Thus, with approximate starting values of T_{eff} and log g, we read an initial estimate of the electron pressure from previously calculated curves[6] relating P_e, T, and g for an optical depth of 0.6. The gas pressure follows from tables[7] of P_g as a function of P_e and T. Finally, the damping constant (cf. eqs. [15], [16], and [17]) or, more specifically, the constant a (cf. eq. [21]), which is required in order to employ the correct theoretical curve of growth, was computed.

Wrubel's[8] theoretical curve of growth, based on Chandrasekhar's exact solution for a line profile in the Milne-Eddington model, is used throughout this paper. It consists of a plot of log $(Wc/\lambda v)$, where $v = (2kT/M)^{1/2}$ is the most probable velocity, against log η_0, the ratio of the line-absorption coefficient for zero damping to the continuous absorption coefficient at the center of the line. That is,

$$\eta_0 = \frac{\pi e^2}{mc} f \frac{c}{v\nu\pi^{1/2}} N \frac{1}{\kappa_\nu}, \tag{1}$$

where κ_ν is the effective continuous absorption coefficient, f is the oscillator strength, and N is the number of atoms in the lower level of the transition per gram of stellar material.

We define, for a given line, the quantity

$$f' = \frac{f(2J+1)}{\varpi_t}, \tag{2}$$

where J is the inner quantum number of the lower level of the transition and ϖ_t is the statistical weight of the entire lower term. Then we may write equation (1) as

$$\eta_0 = \frac{\pi e^2}{mc} f' \frac{c}{v\nu\pi^{1/2}} N_t 10^{-\theta(\chi-\chi_0)} \frac{1}{\kappa_\nu}, \tag{3}$$

where $\theta = 5040/T$, N_t is the total number of atoms per gram of stellar material in the lower term, and χ_0 is an arbitrary excitation potential to which we refer N_t. When a single curve of growth is to be used over different regions of the spectrum, the η_0 of equation (3) must be corrected to allow for the fact that

$$\frac{B^{(0)}}{B^{(1)}} = \frac{8}{3} \frac{kT_0}{h\nu} \frac{\kappa_\nu}{\bar{\kappa}} \tag{4}$$

[5] *Pub. Astr. Inst. Amsterdam*, No. 5, 1936.

[6] L. H. Aller, *Astrophysics* (Philadelphia: Blakiston Co., 1951), chap. vii.

[7] *Ibid.*, chap. iv. The $P_g(P_e, T)$ relation naturally depends on a particular choice of the chemical composition.

[8] *Ap. J.*, 109, 66, 1949.

varies with wave length. The necessary correction to log η_0 is tabulated as a function of $B^{(0)}/B^{(1)}$ by Wrubel.

King[9] has published absolute laboratory f-values for lines originating from several terms of *Fe* I. In the stars considered there are a number of these lines arising from the three terms $3d^64s^2\ a^5D$, $3d^7(^4F)4s\ a^5F$, and $3d^7(^4F)4s\ a^3F$ which have lower excitation potentials of about 0.00, 1.00, and 1.50 volts, respectively. Thus from the curve of growth we may obtain the relative numbers of atoms in each of the three terms and then employ the Boltzmann equation to find the excitation temperature.

Neglecting the lines that fall on the short-wave-length side of the Balmer limit, we may assume the continuous absorption to be nearly constant. Then, for a given star, equation (3) becomes

$$\log \eta_0 = \log \lambda + \log N_i - \theta(\chi - \chi_0) + \log f' + \text{const}. \qquad (5)$$

From this expression we may obtain N_i.

Since $\chi - \chi_0$ is only a few hundredths of a volt for all the lines used, a small error in the value of θ will be insignificant. All the lines fall near the "flat" portion of the curve of growth, so slight uncertainties in the damping constant will not seriously affect the results, but the probable errors in the determination of θ_{exc} will be rather high. The excitation temperature turns out to be 5400° ± 900° K for both subdwarfs and 7500° ± 1100° K for 95 Leonis. The low excitation temperature of the subdwarfs suggests that their effective temperatures are lower than those for A stars, which is in agreement with our conclusions from the Verweij profiles. As we shall show later, the observed relative abundances of *Ca* II and *Ca* I, as determined from line profiles and equivalent widths, also indicate a temperature much lower than 8900° K. Thus a normal, high-surface-gravity, A-type atmosphere (either with a normal or with a low hydrogen content) seems to be an untenable assumption for the explanation of the subdwarf spectra.

IV. MODEL STELLAR ATMOSPHERES

For an accurate prediction of line profiles, a consideration of the variation with optical depth of temperature, electron pressure, gas pressure, and the mean absorption coefficient—i.e., a model atmosphere—is essential. The model atmosphere, however, is calculated for an assumed effective temperature and surface gravity, and the final model can be obtained only by a process of trial and error. That is, we assume values for the effective temperature and surface gravity and use the resulting model to predict the line profiles. Then a comparison between observed and computed profiles gives a clue as to the necessary modifications of our initial assumptions.

The structure of a model atmosphere depends on its assumed composition. In the cooler stars the hydrogen/metal ratio, A, is particularly important, since the metals supply the electrons. As long as the continuous absorption is primarily due to hydrogen, the value of A has little effect on the shapes of the hydrogen lines. The total intensities and the profiles of the metallic lines do depend on this ratio, however. We have tentatively adopted the hydrogen, helium, and metallic abundances as 1000, 200, and 0.44 by numbers of atoms. In Section VI we discuss the influence of the hydrogen/metal ratio upon the calcium-line profiles with the aid of a second subdwarf model atmosphere calculated for log $A = 4.2$.

We can obtain a reasonably accurate initial approximation for 95 Leonis from the observed spectral type and absolute magnitude. Unfortunately, such estimates appear to be less helpful for the subdwarfs. The curve-of-growth method provides the starting approximation for the subdwarfs and serves as a check on the spectral-type estimates for 95 Leonis. A value of the ratio of *Fe* II to *Fe* I can be obtained from the curve of growth by utilizing Greenstein's η_0's for τ UMa in a manner explained in Section VII. This

[9] *Ap. J.*, **87**, 24, 1938; cf. also *ibid.*, **95**, 78, 1942.

leads, by virtue of the Saha equation, to a relation between the temperature and electron pressure at a representative point in the stellar atmosphere, viz.,

$$\theta I + \log P_e = F(\theta). \tag{6}$$

Here I is the ionization potential of *Fe*, and F is nearly constant over a small range of θ. Another such relation could be obtained from similar considerations of another element, were the data of sufficient accuracy. In practice, however, as Greenstein[10] has pointed out, two such equations give straight lines so nearly parallel that the solution is essentially indeterminate.

In the wave-length region considered (λλ 4000–4800), κ_ν is very nearly constant. Therefore, in computing η_0 we may assign some arbitrary value to κ_ν so that the relation of the individual points on the empirical curve of growth will be nearly correct, although the zero point on the η_0-scale will be arbitrary. Now an assumption as to the abundance of *Fe* will give us the zero point (from a comparison of the observed and theoretical curves) and hence κ_ν. Greenstein[11] has tabulated $\kappa_\nu\,(H + H^-)$ as a function of θ and $\log P_e$ at λ 4300. Thus, with a value for κ_ν obtained from fixing the η_0 zero point, we

TABLE 3

PROVISIONAL MODEL ATMOSPHERES

τ	95 Leonis $T_{\rm eff} = 8900$, $\log g = 3.90$				Subdwarfs $T_{\rm eff} = 6300$, $\log g = 4.80$			
	T	$\log \bar{\kappa}$	$\log P_g$	$\log P_e$	T	$\log \bar{\kappa}$	$\log P_g$	$\log P_e$
0.05	7440	−0.08	+2.70	+1.26	5250	−0.70	+4.50	+0.90
0.10	7610	+0.05	+3.10	+1.60	5440	−0.61	+4.60	+1.07
0.20	7970	+0.38	+3.33	+1.93	5640	−0.48	+4.76	+1.27
0.40	8460	+0.69	+3.48	+2.30	6000	−0.28	+4.94	+1.59
0.60	8840	+0.90	+3.54	+2.47	6280	−0.10	+5.05	+1.87
0.80	9130	+1.08	+3.57	+2.60	6570	+0.07	+5.10	+2.14
1.00	9440	+1.25	+3.59	+2.72	6900	+0.20	+5.13	+2.30
2.00	10610	+1.45	+3.63	+3.08	7580	+0.55	+5.20	+2.70
3.00	11480	+1.40	+3.65	+3.20	8120	+0.80	+5.24	+3.00

can find another relation between θ and $\log P_e$ which may be solved simultaneously with equation (6). If we take the representative point for the formation of *Fe* lines to be $\tau = 0.25$, since iron becomes rapidly ionized with increasing optical depth, then approximately $\theta_{\rm eff} = \theta(0.6) = 0.90\,\theta(0.25)$ and, very roughly, $P_e(0.6) = 2.5\,P_e(0.25)$. The numerical values for $\theta_{\rm eff}$ and P_e (0.6) may then be utilized to predict the surface gravity.[8]

The method is admittedly crude: a small error in the empirical *Fe* II/*Fe* I abundance ratio will be rather serious. Also the resulting effective temperature and surface gravity will depend upon our assumption as to the total *Fe* abundance; hence the method is even less reliable when applied to the subdwarfs, where peculiar abundances might well prevail.

Nevertheless, the results did tend to substantiate the assumed effective temperature and surface gravity for 95 Leonis and sustained our suspicions of a low temperature and high surface gravity for the subdwarfs. But it must be emphasized that the trial-and-error approach by the method of model atmospheres was necessary for an accurate representation of line profiles. The final effective temperatures and surface gravities are given in Table 3 with the results of the numerical integrations for the respective models. The predicted surface gravities may well be in error by a factor of 2 or 3.

[10] *Ap. J.*, **107**, 151, 1948. [11] *Ibid.*, Table 10.

The variation of temperature with optical depth depends upon the physical process involved in the transfer of energy through the stellar atmosphere. We have assumed radiative equilibrium for our present calculations. B. Strömgren[12] has suggested that the temperature dependence for convective equilibrium is probably not greatly different from that for radiative equilibrium in an A dwarf atmosphere.

We start by assuming the atmosphere to be in hydrostatic equilibrium:

$$\frac{dP_g}{d\tau} = \frac{g_e}{\bar{\kappa}(P_e, T)}. \tag{7}$$

In equation (7) g_e is the effective surface gravity and for these stars should differ little from that calculated from the mass and radius, and $\bar{\kappa}$ is the Chandrasekhar mean absorption coefficient.[13] The temperature dependence upon optical depth is given by Chandrasekhar's exact solution of the equation of radiative transfer for a stellar atmosphere in radiative equilibrium.[14]

In the evaluation of $\bar{\kappa}$ we have made the simplifying assumption that the variation of flux distribution, F_ν/F, is so small throughout the relevant layers that it may be taken as constant with optical depth and equal to the value at $\tau = 0.6$. Thus we may use the values of the mean absorption coefficient per gram of hydrogen, $\bar{\kappa}(H + H^-)$, tabulated for various temperatures and electron pressures by Chandrasekhar and Münch.[15] The effects of electron scattering are negligible for A-type dwarfs within the limits of accuracy of our theory.

The calculation of the model atmosphere is executed in a straightforward fashion, the initial approximation being obtained in a manner similar to that described by Unsöld.[16] Once $P_g(\tau)$ is obtained, P_e may be found immediately from the afore-mentioned tables of $P_e(P_g, T)$.

Were the observational data of sufficient accuracy to merit the labor involved, the model atmospheres presented here could be refined by a calculation of the mean absorption coefficient that takes account of the variation of flux distribution with depth.

V. HYDROGEN-LINE PROFILES

We now wish to determine whether the narrow hydrogen lines in the two subdwarfs may be satisfactorily represented in terms of a normal hydrogen content and a temperature characteristic of an F-type (rather than an A-type) star.

Although the observed profiles of corresponding lines in the two subdwarfs differ somewhat from one another, the differences are no more than might be explained by observational error. In the subdwarfs we would expect greater residuals between observed and computed profiles, which are based on one plate for each star, than in 95 Leonis, for which profiles were obtained from two grating plus two prism plates. Consequently, the subdwarfs have been considered together, and their computed profiles are based on the same model atmosphere. In general, the data for HD 19445 are probably more reliable than those for HD 140283, since the coudé plate of the latter star was somewhat underexposed for spectrophotometric purposes in the region studied.

The principal source of line broadening for stellar hydrogen lines is the linear Stark effect. According to the Holtsmark theory of statistical broadening, at a point in the line well removed from the Doppler core, the line-absorption coefficient will be

$$l(\Delta\lambda) = N_2 a(\Delta\lambda) = N_2 3\,2\,1 C_{n_2} P_e T^{-1} (\Delta\lambda)^{-5/2}. \tag{8}$$

[12] Private communication.

[13] See S. Chandrasekhar, *Radiative Transfer* (Oxford: Clarendon Press, 1950), p. 298, eq. (46).

[14] *Ibid.*, p. 294, eq. (31); also *ibid.*, p. 80, Table X.

[15] *Ap. J.*, **104**, 446, 1946.

[16] *Physik der Sternatmosphären* (Berlin: J. Springer, 1938), p. 144.

Here C_n is a constant computed from the Stark-effect theory for each hydrogen line, and N_2 is the number of atoms in the second level of hydrogen per gram of stellar material.

The theory of line profiles on the basis of the Milne-Eddington model, where $\eta_\nu = l_\nu/\kappa_\nu$ is constant with the depth, has been given by A. S. Eddington,[17] B. Strömgren,[18] and by S. Chandrasekhar,[19] who has obtained an exact solution for $r_\nu = F_L(0)/F_c(0)$, the ratio of the flux at a point in the line to the continuous flux in the near-by continuum. When η_ν undergoes small variations, the residual intensity may be found by the mean-value method suggested by Strömgren and modified by M. Tuberg[20] to the problem of the center-limb variation of a number of lines of the solar spectrum.

In the model atmospheres presented in Table 3, η_ν for the hydrogen and calcium lines varies rapidly with optical depth, and approximate methods no longer suffice. Therefore, we have used a method proposed by Strömgren wherein the differential equation of transfer (with its boundary conditions) is replaced by an integral equation. The solution is obtained by an iteration procedure and in such a manner that the detailed variations of η_ν with depth are taken into account.

Theoretical line profiles depend upon the quantity ϵ, which is a measure of the relative importance of scattering and thermal absorption in the process of line formation. For monochromatic radiative equilibrium (pure scattering), $\epsilon = 0$; and for the limiting case of local thermodynamic equilibrium, $\epsilon = 1$. Since a complete theory of line formation is not yet available, it is necessary to use an empirical ϵ. Let us define

$$\mu_\nu = \frac{1}{1+\eta_\nu} \tag{9}$$

and

$$\Lambda_\nu = \frac{1+\epsilon\eta_\nu}{1+\eta_\nu}. \tag{10}$$

At the center of a line η_ν becomes large and $\Lambda \to \epsilon$. Hence, using the Milne-Eddington formula in Chandrasekhar's first approximation, viz.,

$$r_\nu = \frac{2}{(4/3)\sqrt{3} + (1/2)(x_0/n_\nu)} \frac{(4/3)\sqrt{(3\Lambda_\nu)} + (1/2)(x_0/n_\nu)\mu_\nu}{(1+\sqrt{\Lambda_\nu})}, \tag{11}$$

we find, for $\Delta\lambda = 0$,

$$r_0 = \frac{2}{(4/3)\sqrt{3} + (1/2)(x_0/n_\nu)} \frac{(4/3)\sqrt{(3\epsilon)}}{(1+\sqrt{\epsilon})}. \tag{12}$$

In equations (11) and (12)

$$n_\nu = \frac{\kappa_\nu}{\bar{\kappa}} \tag{13}$$

and

$$x_0 = \frac{h\nu}{kT_0}(1 - e^{-h\nu/kT_0})^{-1}, \tag{14}$$

where T_0 represents the boundary temperature.

[17] *M.N.*, **89**, 620, 1929.

[18] *Ap. J.*, **86**, 1, 1937; cf. also *Festschrift für Elis Strömgren* (Copenhagen: Einer Munksgaard, 1940), p. 218.

[19] *Ap. J.*, **106**, 145, 1947.

[20] *Ap. J.*, **103**, 145, 1946.

If we use the observed residual intensity at the center of the line, we can solve equation (12) for ϵ. This method is very sensitive, however, to errors in the boundary temperature and in η_ν, which must be taken near the top of the atmosphere. Also the empirical measures of the central intensity, r_0, have a fairly large probable error, for reasons explained in Section II. Therefore, we have computed profiles for 95 Leonis with various assumed values of ϵ and find that with the adopted model atmospheres a value of $\epsilon \sim 0.25$ gives a good representation of the three lines, $H\beta$, $H\gamma$, and $H\delta$. For the subdwarfs it turns out that the choice of ϵ is not so critical, and computations for $\epsilon = 0$ and $\epsilon = 1$ give very nearly the same profiles in the damping wings. From considerations of the process of line formation, it seems likely that $\epsilon \sim 1$ for hydrogen lines.

In Tables 4 and 5 and Figures 2–7 we compare the observed profiles with those com-

TABLE 4

HYDROGEN PROFILES FOR 95 LEONIS

$\Delta\lambda$ (A)	$H\beta$		$H\gamma$		$H\delta$	
	Obs. r_λ	Comp. r_λ	Obs. r_λ	Comp. r_λ	Obs. r_λ	Comp. r_λ
5.....	0.54	0.55	0.49	0.50	0.47	0.47
10.....	.72	.71	.70	.72	.67	.70
15.....	.82	.81	.83	.85	.81	.84
20.....	0.90	0.90	0.91	0.93	0.90	0.92

TABLE 5

HYDROGEN PROFILES FOR SUBDWARFS

$\Delta\lambda$ (A)	$H\beta$			$H\gamma$			$H\delta$		
	Obs. r_λ		Comp. r_λ	Obs. r_λ		Comp. r_λ	Obs. r_λ		Comp. r_λ
	HD 19445	HD 140283		HD 19445	HD 140283		HD 19445	HD 140283	
1.0.....	0.63	0.65	0.68	0.61	0.68	0.65	0.65	0.63	0.65
2.0.....	.78	.80	.81	.76	.81	.75	.79	.75	.78
3.0.....	.85	.86	.86	.84	.87	.83	.87	.83	.86
4.0.....	0.88	0.90	0.90	0.89	0.93	0.90	0.91	0.90	0.91

puted by Strömgren's iteration method. Values of r_ν were not computed near the line center, where the error arising from the uncertainty in ϵ enters to the fullest extent. In the wings the agreement appears to be satisfactory.

VI. THE CALCIUM ABUNDANCE

The determination of the abundances of the elements in a stellar atmosphere may proceed along two different lines. One is a comparison of theoretical and observed equivalent widths; the other is an analysis of the line profiles. An example of the first method is the curve-of-growth procedure, which makes possible the utilization of a large number of lines but which frequently involves the introduction of questionable assumptions; e.g., η_ν is assumed constant with depth. The strongest line arising from *Ca* I—λ 4227—is so narrow that only the instrumental profile is obtained. Therefore, the best alternative is

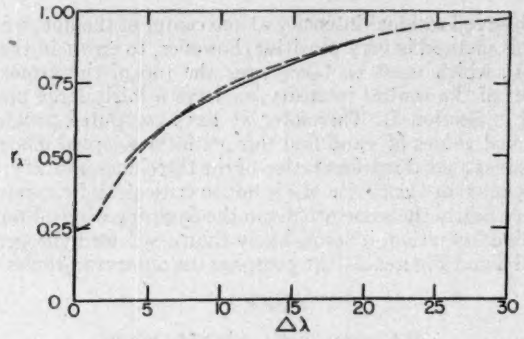

FIG. 2.—Profile of $H\beta$ in 95 Leonis. *Dashed curve*, observed; *solid curve*, computed

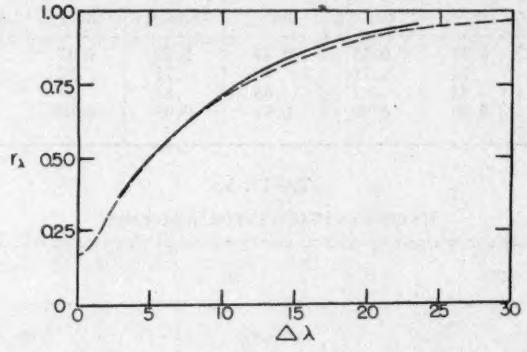

FIG. 3.—Profile of $H\gamma$ in 95 Leonis. *Dashed curve*, observed; *solid curve*, computed

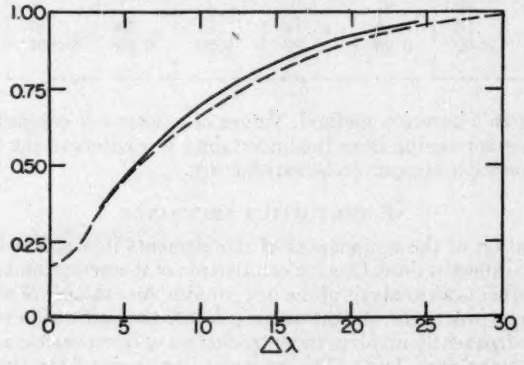

FIG. 4.—Profile of $H\delta$ in 95 Leonis. *Dashed curve*, observed; *solid curve*, computed

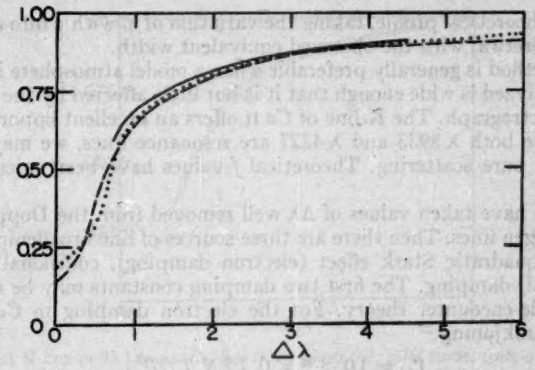

FIG. 5.—Profiles of $H\beta$ in subdwarfs. *Dashed curve*, observed in HD 19445; ***dotted curve***, observed in HD 140283; ***solid curve***, computed.

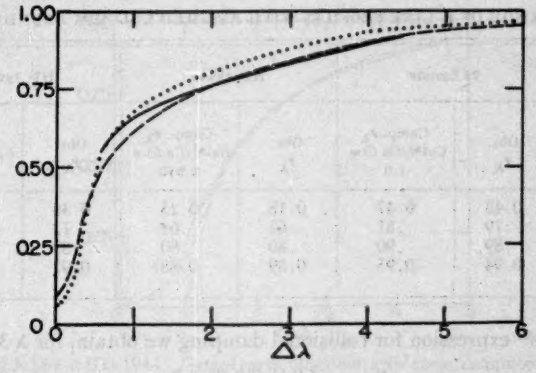

FIG. 6.—Profiles of $H\gamma$ in subdwarfs. *Dashed curve*, observed in HD 19445; ***dotted curve***, observed in HD 140283; ***solid curve***, computed.

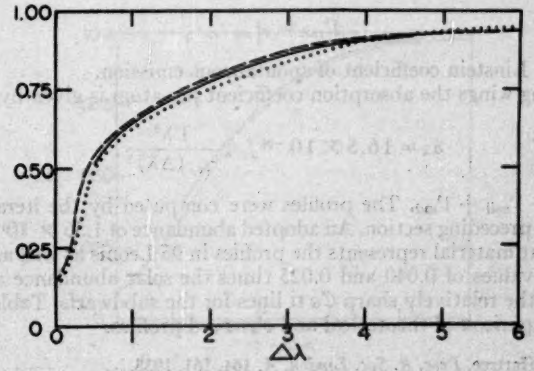

FIG. 7.—Profiles of $H\delta$ in subdwarfs. *Dashed curve*, observed in HD 19445; ***dotted curve***, observed in HD 140283; ***solid curve***, computed.

to calculate the theoretical profile, taking the variation of η_ν with τ into account, and to compare the theoretical with the observed equivalent width.

The second method is generally preferable when a model atmosphere is available and the line to be analyzed is wide enough that it is but little affected by the finite resolving power of the spectrograph. The K line of *Ca* II offers an excellent opportunity for such an analysis. Since both λ 3933 and λ 4227 are resonance lines, we may adopt $\epsilon = 0$, corresponding to pure scattering. Theoretical *f*-values have been calculated for both lines.[21]

For λ 3933 we have taken values of Δλ well removed from the Doppler core, as we did for the hydrogen lines. Then there are three sources of line broadening that must be considered: the quadratic Stark effect (electron damping), collisional damping, and radiation (natural) damping. The first two damping constants may be calculated from Weisskopf's single-encounter theory. For the electron damping in *Ca* II we use the formula of M. Rudkjøbing:[22]

$$\Gamma_{el} = 10^{-4.46} \times 0.72 N_e T^{-1/2} . \tag{15}$$

TABLE 6

COMPARISON OF K-LINE PROFILES WITH ASSUMED CALCIUM ABUNDANCES

Δλ (A)	95 Leonis		HD 19445		HD 140283	
	Obs. r_λ	Comp. r_λ $Ca^{(*)}/Ca\ \odot =$ 1.0	Obs. r_λ	Comp. r_λ $Ca^{(*)}/Ca\ \odot =$ 0.040	Obs. r_λ	Comp. r_λ $Ca^{(*)}/Ca\ \odot =$ 0.025
1.0.....	0.48	0.47	0.18	0.25	0.38	0.40
2.0.....	.79	.81	.62	.63	.72	.73
3.0.....	.89	.90	.80	.80	.89	.90
4.0.....	0.94	0.95	0.89	0.88	0.97	0.97

From Lindholm's[23] expression for collisional damping we obtain, for λ 3933,

$$\Gamma_{coll} = 10^{+6.92} P_g T^{-0.70} . \tag{16}$$

Formulae similar to equations (15) and (16) hold for λ 4227. Also for resonance lines we may write

$$\Gamma_{rad} = A_{nn'} , \tag{17}$$

where $A_{nn'}$ is the Einstein coefficient of spontaneous emission.

In the damping wings the absorption coefficient per atom is given by

$$a_\lambda = 16.5 \times 10^{-26} f_{n'n} \frac{\Gamma \lambda^2}{\gamma_{el} (\Delta\lambda)^2} , \tag{18}$$

where $\Gamma = \Gamma_{el} + \Gamma_{coll} + \Gamma_{rad}$. The profiles were computed by the iteration procedure mentioned in the preceding section. An adopted abundance of 1.36×10^{18} calcium atoms per gram of stellar material represents the profiles in 95 Leonis as well as in the sun. On the other hand, values of 0.040 and 0.025 times the solar abundance are necessary in order to explain the relatively sharp *Ca* II lines for the subdwarfs. Table 6 and Figures 8–10 show a comparison of theoretical and observed profiles.

[21] D. R. and W. Hartree, *Proc. R. Soc. London, A*, **164**, 161, 1938.

[22] *Ann. d'ap.*, **12**, 237, 1949.

[23] *Ark. f. Math., Astr., och Phys.*, Vol. **28**, No. 3, 1941.

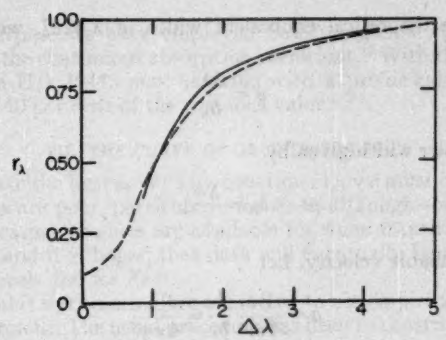

FIG. 8.—Profile of K line in 95 Leonis. *Dashed curve*, observed; *solid curve*, computed for solar abundance of *Ca*.

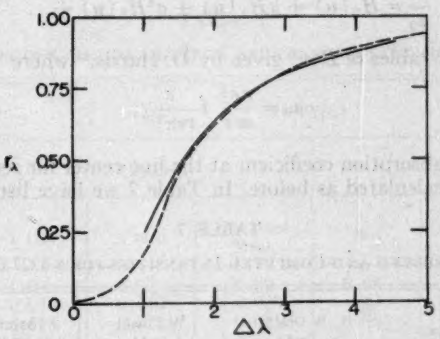

FIG. 9.—Profile of K line in HD 19445. *Dashed curve*, observed; *solid curve*, computed for 0.040 × solar abundance of *Ca*.

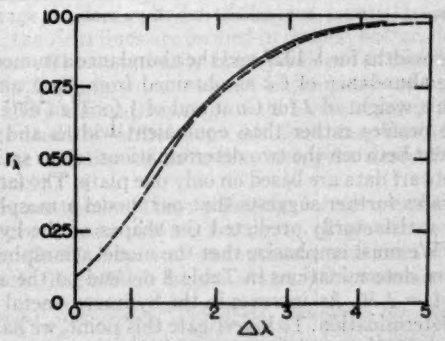

FIG. 10.—Profile of K line in HD 140283. *Dashed curve*, observed; *solid curve*, computed for 0.025 × solar abundance of *Ca*.

In calculating the theoretical equivalent width of λ 4227, we must consider the Doppler core. Define

$$u = \frac{\Delta\lambda}{b_\lambda}, \tag{19}$$

where b_λ is the Doppler width given by

$$b_\lambda = \frac{\lambda v}{c}, \tag{20}$$

and v is the most probable velocity. Let

$$a = \frac{\Gamma c}{4\pi\nu^2}\frac{1}{b_\lambda} = \frac{\Gamma\lambda}{4\pi v}, \tag{21}$$

so that by equations (19) and (21) we can calculate u and a for various points in the model atmosphere. Then

$$\frac{a_\nu}{a_0} = H_0(u) + aH_1(u) + a^2H_2(u) + \ldots \tag{22}$$

is computed from the tables of $H(u)$ given by D. Harris,[24] where

$$a_0 = \frac{\pi e^2}{m c} f \frac{c}{v\nu\pi^{1/2}}. \tag{23}$$

Physically, a_0 is the absorption coefficient at the line center for zero damping. The line profile may now be calculated as before. In Table 7 we have listed the observed and

TABLE 7

OBSERVED AND COMPUTED INTENSITIES FOR λ 4227 *Ca* I

Star	W Obs.* (mA)	W Comp. (mA)	Assumed $Ca(*)/Ca\ \odot$
95 Leonis.....	130	124	1.0
HD 19445.....	230	230	0.036
HD 140283....	154	154	0.013

* Observed equivalent widths corrected for grating scattering.

theoretical equivalent widths for λ 4227 and the abundance assumed for the calculations. Table 8 presents the abundance of *Ca* as obtained from *Ca* II and *Ca* I, with a mean value computed with a weight of 2 for *Ca* II and of 1 for *Ca* I determinations, since the former involved line profiles rather than equivalent widths and are considered more reliable. The agreement between the two determinations seems satisfactory, considering the fact that the subdwarf data are based on only one plate. The fact that the two values are similar in both cases further suggests that our model atmospheres, which were accepted because they satisfactorily predicted the shapes of the hydrogen lines, are approximately correct. We must emphasize that the model atmospheres (Table 3) and the subsequent abundance determinations in Table 8 depend on the assumed composition. $H/He = 5$, and $\log A = 3.36$. An increase in the hydrogen/metal ratio will modify the calcium abundance determination. To investigate this point, we have calculated a model atmosphere for $T_{\text{eff}} = 6300°$ K and $\log g = 4.80$ for the case of $\log A = 4.20$ and no

[24] *Ap. J.*, **108**, 112, 1948.

helium. For this purpose we have employed B. Strömgren's P_g, P_e tables[25] and the more recent data on the continuous absorption coefficient.[15] With this model atmosphere the K-line profile in HD 19445 may be fitted with a profile calculated for a calcium abundance of about 40 per cent of the previous value.

VII. THE CURVE OF GROWTH FOR IRON

In order to calculate the log (η_0/N)'s by equation (1), we must have reliable f-values. Theoretical strengths are poor, particularly for *Fe* II, although some progress has been made for *Fe* I. Laboratory f-values are available for some transitions arising from the lower terms in *Fe* I, and it is hoped that data will eventually be available for lines involving the higher levels and for *Fe* II.

Until such material is forthcoming, we are forced to use empirical data based on solar or stellar curves of growth. The usual procedure has been to construct an initial curve of growth with the aid of lines for which relative f-values are known, usually lines of *Fe* I, *Ti* I, etc. Then, using the observed equivalent widths, on the assumption that the same curve of growth holds for all atoms and ions, we read empirical relative f-values from the curve. This procedure is objectionable for a number of reasons, among which we

TABLE 8

SUMMARY OF CALCIUM AND IRON ABUNDANCE DETERMINATIONS

Star	$N(*)/N(\odot)$					
	Calcium			Iron		
	λ 4227	λ 3933	Weighted Mean	*Fe* I	*Fe* II	Weighted Mean
95 Leonis	1.0+	1.00	1.00	0.68	1.25	0.97
HD 19445	0.036	0.040	0.039	.13	0.30	.17
HD 140283	0.013	0.025	0.021	0.06	0.18	0.09

may enumerate the following: (1) Because of the differences in excitation, the effects of blending, and secondary effects such as interlocking, empirical f-values derived for the solar atmosphere are not necessarily valid for hotter stars. (2) Higher-excitation lines originate, on the average, in deeper layers of the star, where the collisional damping is greater. In particular, the *Fe* II lines are formed in deeper, hotter, denser layers than are the *Fe* I lines in the sun. Thus spuriously large f-values for transitions involving high levels may be found.[26] (3) Turbulence may not be properly taken into account in the construction of solar and stellar curves of growth. Furthermore, it may depend on the optical depth. On the basis of turbulence considerations, Unsöld and Struve[27] have recently questioned the validity of solar-line strengths derived with an excitation temperature as low as 4800° K.

Greenstein has overcome some of these difficulties by the use of empirical strengths in F stars.[10] His procedure was to construct a curve of growth for τ UMa with solar strengths and then to obtain empirical strengths for the lines in this star from the adopted curve of growth. The τ UMa empirical strengths were used in the construction

[25] "Tables of Model Stellar Atmospheres," *Pub. Medd. Københavns Obs.*, No. 138, Table 7, 1944.

[26] E.g., see A. K. Pierce and L. Goldberg, *Technical Report No. 2* (ONR Contract N6onr-232-V [1948]), pp. 7–14.

[27] *Ap. J.*, **110**, 455, 1949.

of curves of growth for other F stars. Although some of the obstacles noted under objection 1 above are circumvented by this procedure, complications introduced by stratification are not so easily avoided. Ultimately, Greenstein's η_0's for τ UMa[28] and his recently determined η_0's for υ Sgr, which we have used in the construction of the curves of growth for *Fe* I and *Fe* II, are based on the solar data.

The η_0's for υ Sgr (denoted here by η_0'') were reduced to the same system as those for τ UMa (which we represent by η_0') in the following manner: Writing equation (1) for a given line in each star and taking the ratio of the two equations, we have

$$\frac{\eta_0''}{\eta_0'} = \frac{v'B'(T)\,N_0''\,\kappa_\nu'}{v''B''(T)\,N_0'\,\kappa_\nu''}\,10^{-(\theta''-\theta')\chi}. \tag{24}$$

Here $B(T)$ represents the partition function and N_0 the number of atoms in the stage of ionization in question. Also in equation (24) we have made use of the Boltzmann equation,

$$N = \frac{N_0\varpi}{B(T)}\,10^{-\theta\chi}. \tag{25}$$

Since the continuous absorption coefficients are nearly constant in both stars over the wave-length region in which the η_0''s are listed by Greenstein ($\lambda\lambda$ 4000–4800), we may write equation (24), considering only lines with nearly the same value of χ,

$$\log \eta_0'' = \log \eta_0' + \text{const}. \tag{26}$$

For *Fe* II, 19 lines with $\chi \sim 2.75$ volts were found in common in τ UMa and υ Sgr; thus the constant in equation (26) could be determined. Then a few additional η_0'''s were converted to η_0''s. For *Fe* I all the η_0's were taken only from τ UMa. In general, the η_0's obtained from τ UMa were given more weight in fixing the η_0's for the stars considered in this paper.

The η_0'''s are related to the η_0's of 95 Leonis or of the subdwarfs by an equation similar to (24) in which we replace η_0'' by η_0. Similarly, we use unprimed symbols for the other quantities involved when they pertain to the star in question. Defining

$$z = \frac{N_0}{N_0'}, \tag{27}$$

we obtain

$$\frac{\eta_0}{z} = \eta_0'\,\frac{v'B'(T)\,\kappa_\nu'}{vB(T)\,\kappa_\nu}\,10^{-(\theta-\theta')\chi}. \tag{28}$$

The numerical values of the factors pertaining to τ UMa can be obtained from the data given by Greenstein. We evaluate the necessary data for 95 Leonis and the subdwarfs at an optical depth $\tau = 0.25$, and calculate $\log \eta_0/z$ for each line. The correct branch of Wrubel's[8] theoretical curve of growth is obtained from the value of $\log a$ given by equation (21). Thus the *Fe* I and *Fe* II curves of growth provide values of z^{I} and z^{II}, respectively.

Since τ UMa was found to have about the same iron abundance as the sun and since in all the stars involved *Fe* is almost entirely in the singly ionized stage,

$$z^{\text{II}} = \frac{N_0(Fe\ \text{II})}{N_0'(Fe\ \text{II})} = \frac{Fe}{Fe\,(\odot)} \tag{29}$$

[28] *Op. cit.*, Table 2.

gives directly a value of the abundance of iron in the star. In order to derive a value of the total *Fe* abundance from the *Fe* I curve of growth, we must obtain a relation between z^{I} and z^{II} by means of the Saha equation. On the basis of model-atmosphere considerations for a metal that becomes rapidly ionized with depth, we take $\theta_{ion} = \theta(\tau = 0.25)$. Furthermore, we use the value

$$\log \frac{Fe\,\text{I}(\odot)}{Fe\,(\odot)} = -1.04\,,$$

which is based on a temperature of 5675° K and log P_e = 1.51 dyne/cm² for the solar reversing layer.

The curves of growth for the three stars are given in Figures 11–13. The number of *Fe* II lines available in the subdwarfs was small. Consequently, in fixing the total abundance of *Fe*, we gave the abundance determinations from the *Fe* II curves of growth one-third the weight of the determinations based on *Fe* I (cf. Table 8).

Although for 95 Leonis the mean value of the *Fe* abundance turns out to be very nearly the solar value, the separate determinations for *Fe* I and *Fe* II differ by a factor of 2. In fact, for all three stars the abundance found from *Fe* II is consistently higher by a factor of from 2 to 3.

Attempts to determine the *Ca* abundance from the curve of growth gave discrepancies, similar to those of *Fe*, which were much higher than the differences found in the calculation of profiles. These discrepancies, although not larger than one usually encounters in the curve-of-growth type of analysis, still are undesirable. Perhaps the difficulty is inherent in the method, which forces us to represent atoms in two stages of ionization by the same effective optical depth. In spite of the large probable error in the subdwarf curves of growth, the observed *Fe* abundance appears to be smaller than in the sun, although this conclusion must be taken with caution.

VIII. PREDICTION OF COLOR TEMPERATURES AND BALMER DISCONTINUITIES

The color temperature of a star is obtained by fitting a Planckian curve to the intensity-curve of the star over a given wave-length region. That is, the average slope of the Planck black-body-curve for $T = T_c$ must be the same as that for the true energy distribution-curve in this interval. If F_1 and F_2 denote the emergent fluxes at wave lengths λ_1 and λ_2 and if we employ the Wien approximation to the Planck formula, the color temperature T_c is given by

$$T_c = \frac{c_2\,(\log_{10} e)\,(1/\lambda_2 - 1/\lambda_1)}{\log F_1/F_2 - 3\log \lambda_2/\lambda_1}\,, \tag{30}$$

where c_2 is the second Planck radiation constant.

The ratio F_1/F_2 may be calculated from the model atmosphere, since the Planck function, $B_\nu(T)$, is known for all optical depths, τ_ν. For a body that is not in thermodynamic equilibrium, the color temperature may differ greatly from the effective temperature. Also, for a star in which there are significant departures from gray-body energy distribution, the color temperature may vary considerably with the spectral region for which it is evaluated. Observations of color temperatures by the Greenwich observers[29] and by Barbier and Chalonge[30] have been made in regions of the spectrum above λ 4000. Accordingly, we have computed the color temperatures for these stars in the wave-length interval 4100–5500 A.

[29] Sir F. Dyson, *Observations of Color-Temperatures of Stars, 1926–1932* (London, 1932); also *M.N.*, **100**, 189, 1940.

[30] *Ann d'ap.*, **4**, 30, 1941.

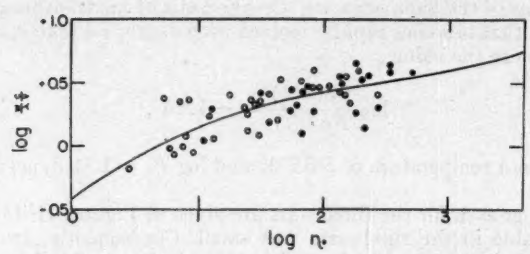

FIG. 11.—Curve of growth for 95 Leonis. *Open circles, Fe* I; *closed circles, Fe* II. The line is the theoretical curve.

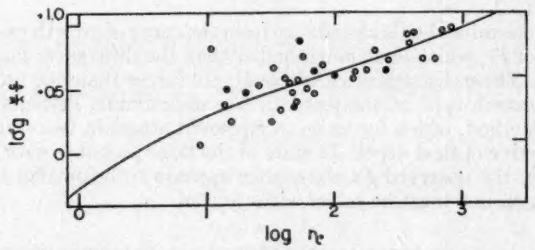

FIG. 12.—Curve of growth for HD 19445. *Open circles, Fe* I; *closed circles, Fe* II. The line is the theoretical curve.

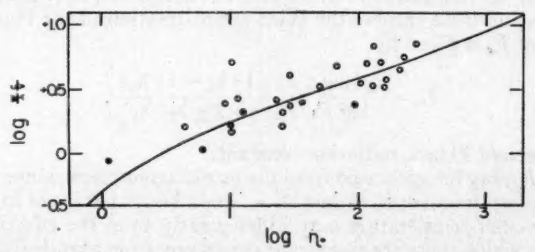

FIG. 13.—Curve of growth for HD 140283. *Open circles, Fe* I; *closed circles, Fe* II. The line is the theoretical curve.

The Balmer discontinuity is calculated directly from the defining equation,

$$D = \log \frac{F_{\lambda>3647}}{F_{\lambda<3647}} . \quad (31)$$

At present, no measures of T_c or D are available for these stars. The predicted values are tabulated in Table 9, along with our determinations of the excitation, ionization, and effective temperatures.

IX. CONCLUSION

95 Leonis appears to be a normal A-type star, whose spectrum may be satisfactorily interpreted by means of a model atmosphere for a star in radiative equilibrium and with normal abundances. On the other hand, our two so-called "A-type subdwarfs" may evidently be satisfactorily represented by an F-type subdwarf model atmosphere. Observational checks of the color temperatures and Balmer discontinuities presented in Table 9 are certainly to be desired, but, in the light of the present evidence, effective temperatures of around 6300° K seem probable.

The one possibly undesirable factor in our interpretation is the prediction of abnormally small amounts of *Ca* and *Fe*. Low apparent abundances of some elements are

TABLE 9

COMPARISON OF STELLAR TEMPERATURES AND BALMER DISCONTINUITY

Star	T_{eff}	T_{ion}	T_{exc}	T_c	D
95 Leonis.....	8900	8100	7500	16,000	+0.64
Subdwarfs.....	6300	5700	5400	8250	+0.16

not a new phenomenon for F stars. Greenstein[31] has recently found very large apparent deficiencies of *Ca* in the metallic-line stars. In fact, it was the abnormally sharp K line in these stars, combined with fairly wide hydrogen lines, that caused the metallic-line stars to be originally classified in spectral type A.

As Greenstein suggests, the observed deficiency of some elements could possibly be caused by *excess* second ionization—i.e., much higher ionization than that predicted by the Saha formula. For example, an unusually large amount of ultraviolet radiation of the right frequencies might not affect the first ionization of calcium but might place most of the atoms in the unobservable stage of *Ca* III, leaving the ratio of *Ca* II/*Ca* I unaffected. Rudkjøbing[32] has suggested that the apparent peculiar abundances in the metallic-line stars are a result of a difference in atmospheric structure between the metallic-line and the "normal" F stars. In the subdwarf model given in Table 3, convection would appear to set in[33] at about $\tau \sim 1$. According to Rudkjøbing, a large surface gravity will tend to suppress adiabatic equilibrium in the convection zone; this might have the effect of causing excess ionization. At any rate, the stars treated in the present paper are undoubtedly quite different from the metallic-line stars, and it may well be that superionization cannot explain the apparent peculiar abundances found in these subdwarfs.

The determination of the calcium abundance, based on the theoretical line profiles, is probably more accurate than the iron abundance, determined by the curve-of-growth method. Although many workers have previously suspected the subdwarfs of having a

[31] *Ap. J.*, **109**, 121, 1949. [32] *Ann. d'ap.*, **13**, 69, 1950. [33] See Unsöld, *op. cit.*, p. 381.

low hydrogen content, it appears that, with respect to *Ca* and *Fe* at least, the subdwarfs are *rich* in hydrogen! The extent and accuracy of our data did not suffice for the construction of curves of growth for elements other than *Fe*. The determinations of other metallic abundances in the subdwarfs would be most interesting. Also an analysis of subdwarfs of other spectral types would do much toward determining whether a large hydrogen/metal ratio exists in type II population objects in general.

A recent investigation of high- and low-velocity F dwarfs by M. and B. Schwarzschild[34] indicated that the *H/Fe* ratio might be somewhat larger in the high-velocity dwarfs than in the low-velocity dwarfs, although the results were rather uncertain. Miss N. Roman[35] has recently published a list of weak-lined F and G stars that are probably closely related to the subdwarfs considered here. If, indeed, this turns out to be the case, then Miss Roman's weak-lined stars may be classified systematically too early.

We are indebted to Dr. R. F. Sanford for making available to us his coudé plates of 95 Leonis and the two subdwarfs. Thanks are due to Dr. J. L. Greenstein, who supplied us with empirical line strengths from υ Sgr in advance of publication, and to Mrs. Chamberlain, who made the accompanying line drawings.

[34] *Ap. J.*, 112, 248, 1950.

[35] *Ap. J.*, 112, 554, 1950.

SPECTROPHOTOMETRY OF EARLY A-TYPE STARS*

WILLIAM BUSCOMBE
Princeton University Observatory
Received January 8, 1951

ABSTRACT

Coudé spectra of the main-sequence star γ Geminorum and of the supergiant α Cygni in the wavelength region 3300–4700 A have been traced with the direct-intensity microphotometer at Mount Wilson Observatory. Empirical line-absorption coefficients, derived by other workers from the spectra of stars of both higher- and lower-excitation temperatures, are used to construct separate curves of growth for the regions shortward and longward of the Balmer series limit. Analyzed with the theoretical curves of growth for resonance lines on the Milne-Eddington model, the measured equivalent widths of nearly four hundred absorption lines averaged from three plates of each of the two A stars indicate that their excitation temperatures are close to 10,000° K.

Mean electron pressures are derived from the ionization equilibria of several elements. Opacity differences between the blue and the ultraviolet are discussed, and the continuous absorption coefficient in the blue is compared with those for other stars. The very flat transitional portions of the curves of growth indicate damping constants smaller than the classical radiation value. No significant difference in turbulence is evident between the atmospheric layers giving rise to line absorption in the visible and ultraviolet.

A summary of the principal results follows:

Star and spectral class	γ Gem A1 V	α Cyg A2 I*a*
Electron pressure (dyne/cm^2)	5400	600
Increase in opacity across Balmer limit ($\Delta \log \kappa_\lambda$)	0.7	0.9
Turbulent velocity (km/sec)		
From line profiles	17	35
From curves of growth	4	13

I. INTRODUCTION

This investigation considers the intensities of absorption lines in A-type spectra as evidence of physical conditions in stellar atmospheres. Several recent studies have analyzed high-dispersion spectrograms of the sun and stars of adjacent spectral classes, with reference to theoretical discussions of the continuous opacity. Many lines for which empirical absorption coefficients have been derived from the solar curve of growth are present with reduced intensity in the spectra of A stars. Since little quantitative work has been done in the ultraviolet region of stellar spectra, it is of interest to extend the curve-of-growth technique to a study with higher dispersion of the influence of continuous Balmer absorption on the equivalent widths of metallic lines, an effect first pointed out by Struve and Sherman.[1]

Although the absorption by hydrogen atoms reaches a maximum at class A0, the metallic lines are then so weak that the effect can be more easily observed in later subclasses. Other considerations suggest the choice of at least two stars differing as much as possible in luminosity, but of almost the same spectral type, comparatively free from rotational broadening, and sufficiently bright to be photographed with high dispersion in reasonable exposure times even in the ultraviolet. Deneb (α Cygni, A2 I*a*) is the

* This investigation is based on plates taken by M. Schwarzschild and L. Spitzer, Jr., as guest investigators at the Mount Wilson and Palomar Observatories. The doctoral thesis was revised for publication at Mount Wilson during the author's tenure as a Fellow of the Carnegie Institution of Washington.

[1] *Ap. J.*, 91, 428, 1940.

brightest A-type supergiant; Alhena (γ Geminorum, A1 V) is a bright blue-dwarf,[2] which exhibits mildly the characteristics of a metallic-line star. Since an early spectroscopic binary orbit was withdrawn,[3] its small radial-velocity variations have not been definitely explained. Professor G. P. Kuiper has suggested informally that any suspected contamination of its spectrum by a late-type companion may be identified on infrared spectrograms.

The spectral regions were selected by reference to published lists of wave-length identification and the *Revised Multiplet Table*.[4] It appeared fairly easy to expose correctly on one plate suitable for photometry the interval λλ 3900–4700, which is rich in lines of many ions for which relative oscillator strengths are available. Immediately shortward of the Balmer series limit, the region λλ 3300–3646 selected for comparison contains enough unblended lines of *Ti* II, *Cr* II, and *Fe* II that curves of growth could be constructed if a system of oscillator strengths were available. Professor J. L. Greenstein, of the Mount Wilson and Palomar Observatories, very graciously extended his study of the spectrum of v Sagittarii, to make available in advance of publication a provisional list of

TABLE 1

JOURNAL OF OBSERVATIONS

Star	Slit-Width (Mm)	Wave Lengths	Date (No. of Plates)
γ Gem	0.03	3300–3646	1949 Nov. 11 (2), 12
		3900–4180, 4220–4700	1948 Dec. 9, 10
		3900–4520	1949 Aug. 18
α Cyg	.02	3300–3646	1949 Aug. 18 (2), Sept. 7
		3900–4500	1949 Aug. 18, Sept. 7 (2)
		4350–4700	1949 Sept. 8 (2)
Sun	.03	3300–4700	1948 Dec. 10
	0.02	3300–4500	1949 Sept. 8

empirical values of the line-absorption coefficient for over five hundred lines from the curve of growth for this star. Since its spectrum shows a hydrogen deficiency, its opacity is unchanged across the Balmer limit. Owing to its high level of ionization and excitation, the analysis of this star's curve of growth contributes oscillator strengths for many lines not present in the spectra of solar-type stars.

II. OBSERVATIONS AND PHOTOMETRIC TECHNIQUE

For the two stars coudé spectrograms were obtained with the 100-inch telescope on Mount Wilson. All together, twenty-three plates were taken; seven of these, however, could not be used because of over- or underexposure. The fourteen plates listed in Table 1 which showed a density appropriate for photometry cover each spectral region for each star three times, with the exceptions indicated. Also included, for comparison, are two plates of the sky in the zenith just before sunset. All plates were taken with the 114-inch camera of the coudé grating spectrograph, giving a dispersion of 2.85 A/mm.

[2] Spectral types from Morgan, Keenan, and Kellman, *An Atlas of Stellar Spectra* (Chicago: University of Chicago Press, 1943); color parallax from Eggen, *Ap. J.*, **112**, 141, 1950.

[3] W. E. Harper, *Pub. Dom. Ap. Obs., Victoria*, **6**, 207, 1935.

[4] C. E. Moore, *Contr. Princeton U. Obs.*, No. 20, 1945.

The spectra were widened by trailing to secure uniform density over a width of 1.0 mm on the plate. Eastman II*a*-O emulsion was used throughout. The exposure times of the calibration spectra were chosen sufficiently long that they differed by less than a factor of 3 from the effective exposure times of the stellar spectra (which, because of the trailing, were appreciably shorter than the total stellar exposure times). To reduce scattered light in the spectrograph (most serious in the ultraviolet), the half of the diffraction grating which appeared to contribute most of this effect was covered for all the ultraviolet exposures. Under average atmospheric conditions the ultraviolet spectra of γ Gem required 3–4 hours' exposure.

Photometric tracings of the spectra were prepared with the new direct-intensity photoelectric microphotometer[5] designed by Dr. Horace W. Babcock, who very kindly assisted in its adjustment and operation. Tests indicated that the photometer favored certain definite positions. In part this was caused by slightly faulty performance of the damping generator. This source was eliminated by using the minimum damping which would still maintain stability of response. A second cause of the preference for selected positions—the effect of grain in the photographic wedges—was largely overcome by using a large area of the wedge spectrogram. Instead of a sharply focused analyzing beam on the wedge, a spot of light 3 sq mm in area was produced, so that the grain effect on the wedge was averaged over an area much greater than that scanned on the stellar spectrogram. The plates were passed through the analyzing beam at 2 mm per minute. The paper drive was geared in most cases to give a linear dispersion on the tracing of fifty times that on the plate, or 1 mm = 0.057 A. The throw between clear plate and the continuum was usually adjusted close to 8 cm.

For use with the new microphotometer, photographic wedges were exposed with an auxiliary calibrating spectrograph on plates from the same package, developed simultaneously with the stellar spectrograms. Since, however, the wedge spectrograph was not yet in reliable operating condition, the usual calibration spectra of a lamp through a step-slit were exposed on the stellar spectrograms through nearly the same optical path as the starlight from the coudé focus of the 100-inch mirror. The basic calibration of each spectrogram is the tracing of these strips at the standard wave lengths λ 3450 in the ultraviolet and $\lambda\lambda$ 4000, 4300, and 4550 for the visible. Since the spectral intervals are comparatively short, each wedge was used only at one wave length near the center of the interval, where the wedge appeared freest from blemish. The strips were traced both immediately before and immediately after the stellar spectrum.

The intensity scale of each tracing was determined from a graph of the measured height of each step, expressed as a function of the relative intensity computed from the known shape of the step-slit. These graphs show a response very nearly linear over an intensity range of more than 1 mag., quite adequate for all absorption features in these A-type spectra except the very strong lines $H\gamma$, $H\delta$, $H\epsilon$, *Ca* II H and K, and *Mg* II λ 4481. A slight curvature appeared when the steps of very low intensity were included. The unfinished state of the calibrating spectrograph appears to contribute much of this nonlinearity in the intensity scale. The intercept of the best straight line, drawn through these points covering the intensity range observed in the stellar spectrum, was used as the origin of the intensity scale. An appreciable error may be introduced by using this method to determine the zero point for the weakly exposed section of the spectrogram at the extreme limit of the wave-length range. Any slight variation in the zero point between the step calibrations, registered before and after the stellar spectrum, was interpolated linearly along the tracing.

On tracings of high-dispersion spectrograms of A-type stars, the position of the continuum is seldom uncertain, except across the Balmer lines, whose wings are very broad because of the Stark effect. To maintain the continuity of slope, the line represent-

[5] Similar in principle to that of Williams and Hiltner, *Pub. Obs. U. Michigan*, **8**, 45, 1940.

ing the continuum was drawn even across those wide features, although no attempt was made to measure line intensities in the wings of the hydrogen lines. The possible error of the scale reading of the continuum, estimated to average 5 per cent, is due largely to the uncertainty of the zero point.

A serious deterrent to accurate photometry, especially in the ultraviolet, has been the uncertain error introduced by scattered light in grating spectrographs. An estimate of this effect can be obtained by comparing the tracings of coudé spectrograms of integrated sunlight, referred to in Table 1, with the higher-dispersion tracings for the center of the sun's disk, published in the Utrecht *Photometric Atlas of the Solar Spectrum*.[6] In the equivalent widths of several blended absorption features near λ 3650, a systematic difference of 1 ± 2 per cent was found between the two sets of tracings. This comparison was not extended to the farther ultraviolet, where the effect of scattered light has not been securely eliminated from the *Atlas*.

As a further test of the scattered light, the residual central intensities of several blended absorption features near λ 3900 in the coudé spectrograms were measured as 12–18 per cent (averaging slightly less than in the *Atlas*, where the origin of the intensity scale has been adjusted for grating ghosts). After correction for the finite resolving power of the coudé spectrograph, the true central intensities of these lines are from 3 to 5 per cent. As it is unlikely that these particular subordinate lines should have completely black centers, one may again conclude that the error in intensity measurements caused by scattered light does not exceed 3 per cent.

III. LINE PROFILES

The absorption features on the tracings were identified by reference to the *Revised Multiplet Table* and several papers describing the spectra of early-type stars.[7] When profiles were drawn at first only for unblended lines, which appeared to be due exclusively to a single ion, it was immediately evident that the profiles of lines absorbed by various ions are identical. Detailed profiles were measured for five lines, absorbed by different ions at different excitation potentials, selected to be free of blending and sufficiently weak so that complications from damping and from the problem of radiative transfer would be largely avoided. The central depths of these lines range from 5 to 20 per cent of the intensity of the adjacent continuum. The line depths were measured at millimeter intervals on each tracing independently, then normalized to the mean central depth of the three tracings of the particular line for each star, and averaged. In each case the mean profile is very well represented by a Gaussian formula. The velocity-dispersion parameters, corrected for instrumental broadening, are listed in Table 2. Since the shapes of all the lines agree very closely, a mean uncorrected profile for each star is shown in Figure 1, a semilogarithmic diagram.

In order to test the effect of the spectrograph on the line profiles, a tracing was made of a section of the comparison spectrum on a stellar spectrogram which had been exposed with a slit width of 0.03 mm. Since the focal lengths of both collimator and camera are 114 inches, the image of the slit on the plate is also 0.03 mm wide. The mean half-half-width of 10 faint iron-arc emission lines in the region near λ 4200 is 0.065 ± 0.001 A, corresponding to a velocity of 5.6 km/sec. The corresponding Gaussian profile is shown by a straight line in Figure 1, inverted for comparison with the profiles of stellar absorption lines. This instrumental profile is the relevant one for the spectrograms of γ Gem, taken with the slit-width 0.03 mm. For α Cyg, taken with slit-width 0.02 mm, the half-half-width of the instrumental profile is estimated as 4.0 km/sec. For both stars the instrumental profile is sufficiently narrow that the observed line profiles could be securely corrected for instrumental broadening.

[6] Minnaert, Mulders, and Houtgast (Amsterdam: D. Schnabel, 1940).

[7] The author is grateful for the opportunity of consulting Professor C. W. Curtis' unpublished list of laboratory wave lengths for *Mn* II, which indicated this ion's contribution to several blends.

Since the shapes appear, over the region covered, to be almost independent of wave length, atomic weight of the absorbing ion, or excitation potential, the profiles of blended lines were sketched with similar shapes. An exception was made to draw broader wings for the linear Stark effect of helium, as indicated on the tracings of α Cyg. Blends were divided in this way among the ions contributing most of the absorption, wherever the line centers are separated by more than 1.5 times the observed half-half-widths. In a few cases where adjacent lines differ in intensity by a large factor, the asymmetry of the blends was used to draw the profiles of even closer pairs.

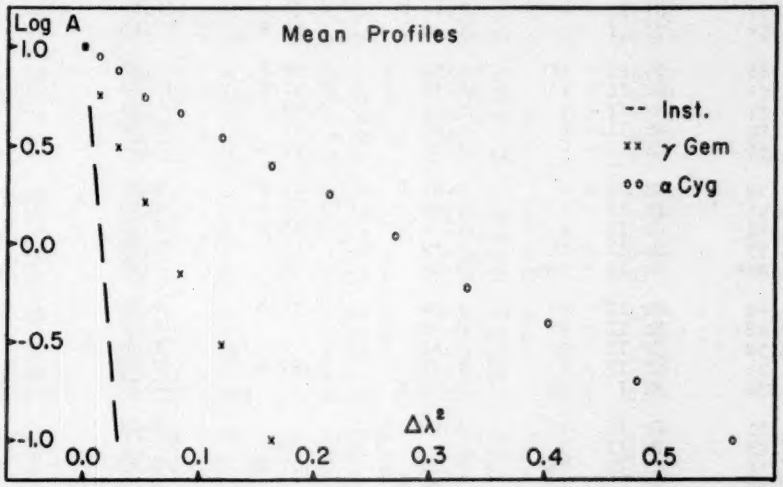

FIG. 1.—Mean profiles for lines listed in Table 2. Δλ, distance from center of line, in angstroms. *A*, absorption at distance Δλ, in per cent, for mean of the five lines, measured on three tracings for each star, normalized to central intensity 10 per cent. The plotted values are not corrected for instrumental profile. The dashed line represents the mean profile for several faint iron-arc comparison lines in emission, on spectrograms taken with the slit width 0.03 mm.

TABLE 2

LINE PROFILES

WAVE LENGTH	ION	E.P. (VOLTS)	HALF-HALF-WIDTH (KM/SEC)	
			γ Gem	α Cyg
3468.68	*Fe* II	4.0	12	27
3596.06	*Ti* II	0.6	13	30
3927.92	*Fe* I	0.1	17	31
4273.32	*Fe* II	2.7	14	29
4287.88	*Ti* II	1.1	15	27
Mean			14±1	29±1
Thermal velocity			1.4	1.4
Instrumental profile			5.6	4.0

TABLE 3. MEASURED EQUIVALENT WIDTHS

λ	Ident.	log 10^6 W/λ γ Gem	log 10^6 W/λ α Cyg	log η_o γ Gem	log η_o α Cyg
3308.81	Ti II - 7	1.26	1.28 B	1.00	0.12
14.57	Cr II - 150	1.14 b		0.72	
18.61	Fe II - 136	1.38	1.24 B	1.34	0.07
26.76	Ti II - 7	1.47	1.60	1.63	0.66
28.35	Cr II - 4	1.23 b	1.62	0.92	0.69
29.46	Ti II - 7	1.50 b	1.85 b	1.74	1.25
30.77*	Mn II	1.00 b	1.12	0.46	- 0.08
32.11	Ti II - 65	1.49 b	1.73	1.70	0.92
36.32	Cr II - 4	1.44 b	1.86 b	1.52	1.27
40.34	Ti II - 7	1.42 b	1.84 B	1.45	1.21
41.88	Ti II - 16	1.52	1.92 B	1.82	1.47
42.51	Cr II - 4	1.39	1.91 B	1.36	1.44
43.77	Ti II - 7	1.29	1.46	1.07	0.51
46.72	Ti II - 7	1.37	1.61	1.30	0.68
47.83	Cr II - 4	1.35	1.82 b	1.24	1.16
49.40	Ti II - 1	1.61 B	1.77 B	2.27	1.02
50.41	Ni II - 1	1.05	1.33 b	0.55	0.20
53.12	Cr II - 4	1.11	1.33 B	0.66	0.20
53.73	Sc II - 12	1.12		0.68	
56.26*	Fe II - 105	0.84	1.00	0.22	- 0.23
57.40	Cr II - 79	1.20	1.57 b	0.86	0.60
59.68	Sc II - 4	0.92		0.34	
60.30	Cr II - 21	1.43		1.49	
61.21	Ti II - 1	1.59	1.87 B	2.16	1.31
61.56	Ni I - 19	1.16 b		0.76	
63.71	Cr II - 3	1.08		0.61	
64.23	Fe II - 5		1.27		0.11
66.18	Ti II - 54	1.11	1.27 B	0.66	0.11
69.57	Ni I - 6	1.04 b		0.54	
72.80	Ti II - 1	1.58	2.07 B	2.00	2.06
73.98	Ni II - 1	1.15 b	1.41 B	0.75	0.32
74.35	Ti II - 54		1.35 B		0.23
78.34	Cr II - 21	1.20	1.64 b	0.86	0.73
79.37	Cr II - 21	1.24		0.95	
79.82	Cr II - 21	1.40 b		1.39	
80.28	Ti II - 1	1.48 b	1.88 B	1.67	1.40
80.57	Ni I - 20	0.99 B		0.45	
81.36	Fe II - 5	0.88	1.30 B	0.28	0.15
82.68	Cr II - 3	1.38	1.88 b	1.33	1.40
83.77	Ti II - 1	1.60	2.00 b	2.21	1.76
87.85	Ti II - 1	1.52	1.73 B	1.82	0.92
88.76	Ti II - 53	1.08	0.82 B	0.61	- 0.45
90.08	Fe II - 207	0.58	0.65	- 0.14	- 0.64
91.96	Zr II - 1	1.18	1.16 B	0.82	- 0.04
94.57	Ti II - 1	1.39	1.52 B	1.36	0.50
98.36	Fe II - 105	0.78	1.08	0.13	- 0.14
3399.54	Cr II - 100	0.94 b	0.99 b	0.37	- 0.24
3401.76	Ni II - 4	0.79	0.89 B	0.14	- 0.37
03.32	Cr II - 3	1.53	1.95 b	1.86	1.56
3404.96	Ti II - 63	0.67	0.67	- 0.02	- 0.61

TABLE 3.--Cont.

λ	Ident.	log 10^6 W/λ γ Gem	log 10^6 W/λ α Cyg	log η₀ γ Gem	log η₀ α Cyg
3407.20	Ti II - 1	1.19 b	1.36 B	0.83	0.24
07.30	Ni II - 4	1.05 B		0.55	
08.77	Cr II - 3	1.51	2.01	1.78	1.80
09.81	Ti II - 1	1.04	1.14	0.53	- 0.06
14.14	Fe II - 91		0.77		- 0.51
14.76	Ni I - 19	1.16	0.82	0.77	- 0.45
16.96	Ti II - 53	0.88	0.86	0.28	- 0.40
21.20	Cr II - 3	1.38	1.91 b	1.33	1.44
22.74	Cr II - 3	1.49	2.05	1.70	1.98
23.71	Ni I - 20	1.04	0.81 b	0.54	- 0.46
25.58	Fe II - 5	1.01 b	1.29	0.48	0.14
26.81	Fe II - 103	0.91 b	0.69	0.32	- 0.60
33.30	Cr II - 3	1.44	1.95 b	1.52	1.56
33.56	Ni I - 19	0.86 b		0.25	
36.11	Fe II - 91	0.94	1.30	0.37	0.15
37.28	Ni I - 3	0.83		0.20	
38.23	Zr II - 1	1.00	0.92 B	0.47	- 0.33
38.98	Mn II - 1	1.11	1.39	0.66	0.29
40.61	Fe I - 6	1.21 b	0.94 B	0.88	- 0.30
40.99	Fe I - 6	1.15 b	0.98 B	0.75	- 0.26
43.88	Fe I - 6	1.15 b	1.28 B	0.75	0.12
44.31	Ti II - 6	1.37 B	1.63 B	1.30	0.71
46.26	Ni I - 20	1.20	1.22	0.86	0.04
49.28	Cr II - 111	0.67	0.86	- 0.02	0.40
51.3 *	Fe II - 208	0.58	0.94	- 0.14	- 0.31
52.48	Ti II - 99	1.13 B	1.14	0.71	- 0.06
53.60	Fe II	0.91 B	0.94 B	0.32	- 0.31
54.17	Ni II - 1	1.06 B	1.38 B	0.57	0.27
54.98	Cr II - 136	0.92 B	1.19 b	0.34	0.00
56.40	Ti II - 99	1.18	1.29 B	0.82	0.14
57.62	Cr II - 135	0.95	1.22 B	0.39	0.04
58.47	Ni I - 19	1.02	0.85 B	0.50	- 0.41
59.29	Cr II - 136	0.74	1.00	0.08	- 0.23
60.31	Mn II - 3	1.44 b	1.94	1.52	1.54
61.50	Ti II - 6	1.49	1.61	1.70	0.68
62.73	Cr II - 2	0.88 B	0.71	0.28	- 0.57
64.50	Fe II - 114	0.92	1.12 B	0.34	- 0.09
67.50	Ni I - 3		0.74		- 0.54
68.68	Fe II - 114	1.21	1.64	0.88	0.73
69.49	Ni I - 8	0.50		- 0.24	
71.35	Ni II - 4	1.13	1.50 B	0.71	0.47
72.50	Ni I - 20	0.88		0.28	
76.70	Fe I - 6	0.95 B	1.36 B	0.39	0.24
77.18*	Ti II - 6	1.34 b	1.32 B	1.20	0.18
81.92	Fe II - 102	0.50 b	0.76 B	- 0.24	- 0.52
82.91	Mn II - 3	0.86 b		0.25	
87.99	Fe II - 4	0.76		0.10	
88.68	Mn II - 3	1.36	1.78 B	1.26	1.04
89.74	Ti II - 6	0.96	0.96 b	0.40	- 0.28
3490.58	Fe I - 6	1.06	1.35 B	0.57	0.23

TABLE 3.--Cont.

λ	Ident.	log 10^6 W/λ γ Gem	log 10^6 W/λ α Cyg	log η_0 γ Gem	log η_0 α Cyg
3491.05	Ti II - 6	1.25	1.11 B	0.97	- 0.10
92.96	Ni I - 18	1.06		0.57	
93.47	Fe II - 114	1.17		0.79	
3494.67	Fe II - 16	1.05	1.40 B	0.55	0.30
3500.34	Ti II - 6	0.96	0.99 B	0.40	- 0.25
00.85	Ni I - 6	0.68	0.63	- 0.01	- 0.66
01.73	Co II - 2	0.89	1.10	0.29	- 0.11
02.60	Ni I - 3	0.66		- 0.04	
04.43	V II - 6	0.78	0.84 B	0.13	- 0.42
04.89	Ti II - 88	1.30	1.66 b	1.10	0.78
05.45	Ti II - 6	0.71 b	0.69	0.03	- 0.60
07.39	Fe II - 16	0.90	1.22 b	0.31	0.04
08.21	Fe II - 4	0.76	1.11 b	0.10	- 0.10
09.85	Ti II - 88	0.87	0.78	0.26	- 0.50
10.34	Ni I - 18	0.96	0.61 B	0.40	- 0.68
10.85	Ti II - 88	1.29	1.60	1.07	0.66
11.84	Cr II - 2	1.16	1.42	0.77	0.34
13.03	Cr II - 107		0.99		- 0.24
15.07	Ni I - 19	1.08	0.81	0.61	- 0.46
15.82	Fe II - 208		0.50		- 0.80
17.30	V II - 6	1.11	1.32	0.66	0.18
20.25	Ti II - 98	1.13 b	1.33	0.71	0.20
21.26	Fe I - 24	0.93	0.86	0.35	- 0.40
23.44	Ni I - 16	0.68	0.81	- 0.01	- 0.46
27.98	Ni I - 6	0.71		- 0.04	
30.76	V II - 5	1.00	1.06	0.47	- 0.16
33.87	Ti II - 98		0.68		- 0.61
35.73	Sc II - 11	0.83 b		0.20	
45.19	V II - 5	1.00	1.21	0.46	0.03
51.94	Zr II - 1	0.76		0.10	
56.80	V II - 5	1.25 b	1.37 b	0.97	0.26
61.58	Ti II - 15	0.83	0.94 B	0.20	- 0.31
64.54	Fe II - 113	0.88	1.17 b	0.28	- 0.02
65.38	Fe I - 24	1.28	1.07	1.05	- 0.15
67.70	Sc II - 3	0.92	0.70	0.34	- 0.58
72.52	Sc II - 3	1.32	1.36	1.16	0.24
73.74	Ti II - 15	1.07	0.81	0.59	- 0.46
76.34	Sc II - 3	1.10 b	1.34 B	0.64	0.21
76.76	Ni II - 4	1.16		0.77	
80.93	Sc II - 3	0.95 B	1.02 B	0.39	- 0.21
81.20	Fe I - 23	1.38 b	1.25 B	1.33	0.08
83.55	Fe II - 101		0.65		- 0.64
87.93	Ni I - 16	0.62	0.70 b	- 0.08	- 0.58
89.74	V II - 4	1.23	1.25 B	0.93	0.08
92.01	V II - 4	1.01	1.19	0.48	0.00
96.05	Ti II - 15	1.15	1.19	0.75	0.00
3597.70	Ni I - 18	0.66	0.72	- 0.04	- 0.56
3600.74	Y II - 9	0.77	0.62	0.12	- 0.68
02.61	Fe II - 101	0.59 b	0.52 b	- 0.12	- 0.78
3603.8 *	Cr II - 13	1.40	1.60	1.39	0.66

TABLE 3.--Cont.

λ	Ident.	log 10^6 W/λ γ Gem	log 10^6 W/λ α Cyg	log η_o γ Gem	log η_o α Cyg
3606.68	Fe I - 294	0.95		0.38	
08.86	Fe I - 23	1.22	1.29	0.90	0.14
13.84	Sc II - 2	1.27	1.37 b	1.02	0.26
14.87	Fe II - 112	0.90 B	1.28 b	0.31	0.12
19.40	Ni I - 35	1.09 b	0.86 B	0.62	- 0.40
24.84	Ti II - 52	1.19	1.40 b	0.84	0.30
27.17	Fe II - 193		0.87 b		- 0.39
30.75	Sc II - 2	1.18	1.32 B	0.82	0.18
32.29	Fe II - 112	0.82	1.10 B	0.19	- 0.11
34.37	He I - 28		0.44		- 0.87
41.34	Ti II - 52	1.21	1.39 b	0.88	0.29
42.78	Sc II - 2	1.14	1.15 b	0.73	- 0.05
43.22	Cr II - 1	0.65 b	1.00 b	- 0.05	- 0.24
44.70	Cr II - 1	0.67	0.87 B	- 0.02	- 0.39
3645.31	Sc II - 2	0.97 b	0.96 b	0.41	- 0.24
3900.55	Ti II - 34		2.11		1.76
13.46	Ti II - 34	1.51	1.82 b	1.29	0.70
16.42	V II - 10	1.00	1.00	0.08	- 0.57
17.18	Fe I - 20		0.49 b		- 1.12
20.26	Fe I - 4	1.17 b		0.38	
22.91	Fe I - 4	1.19		0.42	
25.95	Fe I - 364	0.77 b		- 0.24	
27.92	Fe I - 4	1.31	0.93	0.68	- 0.65
29.73	V II - 10	0.45	0.66 b	- 0.63	- 0.94
30.30	Fe I - 4	1.29	1.50 b	0.63	0.09
32.01	Ti II - 34	1.31 B		0.68	
33.68*	Ca II - 1	2.49 b	2.38 b	4.10	2.96
35.94	Fe II - 173	1.29 B	1.50 b	0.63	0.09
38.29	Fe II - 3	1.26	1.67 b	0.56	0.38
38.97	Fe II - 190	0.87	1.40 B	- 0.11	- 0.07
44.01	Al I - 1	1.34	1.15	0.75	- 0.39
51.97	V II - 10		1.22 b		- 0.31
60.89	Fe II - 212		0.96 b		- 0.62
61.53	Al I - 1		1.23 b		- 0.29
3998.05	Fe I - 276	0.85 b		- 0.14	
4002.07	Fe II - 29	0.86 b		- 0.12	
05.25	Fe I - 43	1.19 b		0.42	
05.71	V II - 32	1.12 b		0.28	
09.71	Fe I - 72	0.72		- 0.30	
15.50	Ni II - 12	0.78	1.23	- 0.23	- 0.29
16.43	Fe I - 560	0.90		- 0.04	
17.16	Fe I - 527	0.35		- 0.74	
21.87	Fe I - 278	0.83		- 0.16	
23.39	V II - 32	0.93	1.16	- 0.02	- 0.38
24.55	Fe II - 127	1.20 b	1.47 B	0.44	0.04
25.14	Ti II - 11	1.05 b		0.16	
26.19	He I - 18		1.14 b		- 0.41
28.33	Ti II - 87	1.23	1.43	0.50	- 0.02
30.77	Mn I - 2	1.00 B		0.08	
4034.49	Mn I - 2	0.62	0.62	- 0.43	- 0.98

TABLE 3.--Cont.

λ	Ident.	log 10^6 W/λ γ Gem	log 10^6 W/λ α Cyg	log η_o γ Gem	log η_o α Cyg
4035.63	V II - 32	1.00 b	1.07	0.08	- 0.49
36.78	V II - 9	0.46	0.59	- 0.62	- 1.02
38.03	Cr II - 194	0.69	0.92	- 0.34	- 0.66
41.35	Mn I - 5	0.60 b		- 0.43	
44.01	Fe II - 172	0.72	0.98	- 0.30	- 0.59
44.61	Fe I - 359	0.35		- 0.74	
45.81	Fe I - 43	1.46	1.46	1.12	0.02
51.97	Cr II - 19	0.97	1.22	0.04	- 0.31
55.54	Mn I - 5	0.62		- 0.43	
57.46	Fe II - 212	1.09	0.94	0.23	- 0.64
62.50	Fe I - 359	0.65		- 0.39	
63.60	Fe I - 43	1.40	1.28 b	0.92	- 0.23
67.98	Fe I - 559	0.82 b		- 0.18	
71.74	Fe I - 43	1.37 b	1.18 b	0.83	- 0.36
4077.71	Sr II - 1		1.32		- 0.18
4120.81	He I - 16		0.77		- 0.83
22.64	Fe II - 28		1.62		0.28
24.79	Fe II - 22		1.08		- 0.48
28.05	Si II - 3		1.77 b		0.58
28.73	Fe II - 27		1.47 B		0.04
30.88	Si II - 3	1.50 b	1.82	1.25	0.70
32.06	Fe I - 43	1.25 B		0.54	
32.90	Fe I - 357	0.95 B		0.01	
34.68	Fe I - 357	0.99 b		0.07	
43.42	Fe I - 523	1.08 b	0.76 B	0.22	- 0.84
43.76	He I - 53		1.08 B.		- 0.48
43.87	Fe I - 43	1.29 b		0.63	
57.79	Fe I - 695	0.78 b		- 0.23	
63.64	Ti II - 105	1.32	1.54	0.70	0.15
67.27	Mg I - 15	1.18	0.70	0.40	- 0.90
71.90	Ti II - 105	1.32 b	1.47	0.70	0.04
73.45	Fe II - 27	1.47	1.88 b	1.15	0.87
75.64	Fe I - 354	0.83 b		- 0.16	
78.85	Fe II - 28	1.35 b	1.88 B	0.78	0.87
83.44	V II - 37	0.70	0.64	- 0.33	- 0.96
84.90	Fe I - 355	0.65		- 0.39	
87.04	Fe I - 152	1.00		0.08	
87.80	Fe I - 152	1.24	1.02	0.52	- 0.55
92.07	Ni II - 10	0.56	0.66	- 0.50	- 0.94
4199.10	Fe I - 522	1.13	0.72	0.30	- 0.88
4206.38	Mn II - 7		0.59		- 1.02
10.35	Fe I - 152	0.77		- 0.24	
15.52	Sr II - 1	1.20 b	1.24	0.44	- 0.28
22.22	Fe I - 152	0.88	0.58	- 0.09	- 1.03
24.18	Fe I - 689	0.77		- 0.24	
25.46	Fe I - 693	0.65 B		- 0.39	
26.73	Ca I - 2	1.29	0.64	0.63	- 0.96
33.17	Fe II - 27	1.50 b	2.12	1.25	1.82
33.61	Fe I - 152	0.87 b		- 0.11	
4235.94	Fe I - 152	1.12	0.69 b	0.28	- 0.91

TABLE 3.--Cont.

λ	Ident.	log 10^6 W/λ γ Gem	log 10^6 W/λ α Cyg	log η_o γ Gem	log η_o α Cyg
				- 0.59	
4238.03*	Fe I - 689	0.48			
38.82	Fe I - 693		0.69		- 0.91
42.38	Cr II - 31	1.26 b	0.65	0.56	- 0.95
44.82	Ni II - 9	0.51		- 0.56	
45.26	Fe I - 352	0.58 B		- 0.48	
46.83	Sc II - 7	1.30	1.51	0.65	0.11
47.43	Fe I - 693	0.91		- 0.07	
50.12	Fe I - 152	1.09	0.57 B	0.23	- 1.04
50.79	Fe I - 42	1.15	0.73 b	0.34	- 0.87
52.62	Cr II - 31	0.88	1.17	- 0.09	- 0.37
54.35	Cr I - 1	1.21	0.88	0.46	- 0.70
58.15	Fe II - 28	1.18	1.49	0.40	0.08
60.48	Fe I - 152	1.24 b	0.91	0.52	- 0.67
61.92	Cr II - 31	1.18	1.52	0.40	0.12
69.28	Cr II - 31	0.88 B		- 0.09	
71.16	Fe I - 152	1.10		0.25	
71.76	Fe I - 42	1.32	1.19 b	0.70	- 0.34
73.32	Fe II - 27	1.09	1.56	0.23	0.19
74.80	Cr I - 1	1.04		0.14	
75.57	Cr II - 31	1.09	1.42 b	0.23	- 0.04
82.41	Fe I - 71	1.01		0.10	
83.01	Ca I - 5	0.60		- 0.45	
84.21	Cr II - 31	0.96	1.32	0.02	- 0.18
87.89	Ti II - 20	1.08	1.21	0.22	- 0.32
90.23	Ti II - 41	1.37	1.65 b	0.83	0.34
92.25	Mn II - 6	0.35 b	0.30	- 0.74	- 1.32
96.57	Fe II - 28	1.27 b	1.73	0.58	0.50
4299.24	Fe I - 152	1.12	0.67 B	0.28	- 0.93
4300.05	Ti II - 41	1.47	1.81 b	1.15	0.68
01.93	Ti II - 41	1.28		0.60	
02.53	Ca I - 5	0.86		- 0.12	
03.17	Fe II - 27	1.34	1.91 b	0.75	0.96
16.81	Ti II - 94		0.72 B		- 0.88
19.72	Fe II - 220		0.67		- 0.93
25.01	Sc II - 15		0.92 B		- 0.66
25.76	Fe I - 42		1.41 B		- 0.05
26.76	Fe I - 413		0.78 b		- 0.82
30.26	Ti II - 94		0.67 B		- 0.93
30.71	Ti II - 41		0.88 B		- 0.71
31.93	Mg II - 27		0.48		- 1.13
51.76	Fe II - 27		2.00 b		1.26
54.36	Fe II - 213		0.94		- 0.64
57.57*	Fe II		1.15		- 0.39
61.25*	Fe II		0.86 b		- 0.73
62.10	Ni II - 9		1.02 b		- 0.55
62.93	Cr II - 179		0.59 b		- 1.02
67.66	Ti II - 104		1.11 B		- 0.44
69.10	Fe II - 28		1.31		- 0.19
74.44	Sc II - 14	1.07 B	0.98 B	0.19	- 0.59
4374.95	Y II - 13	1.13 B	0.89 B	0.30	- 0.69

TABLE 3.--Cont.

λ	Ident.	log 10^6 W/λ γ Gem	log 10^6 W/λ α Cyg	log η_o γ Gem	log η_o α Cyg
4383.55	Fe I - 41	1.43	1.43 B	1.01	- 0.02
84.64	Mg II - 10	1.05 B		0.16	
85.38	Fe II - 27	1.31	1.81 B	0.68	0.68
86.86	Ti II - 104		1.18 b		- 0.36
87.93	He I - 51		1.04		- 0.52
90.58	Mg II - 10	1.29	1.44 b	0.63	- 0.01
94.06	Ti II - 51	1.07	1.07 B	0.19	- 0.49
95.03	Ti II - 19	1.47	1.75 B	1.15	0.54
95.85	Ti II - 61	0.98		0.05	
4399.77	Ti II - 51	1.25	1.43 B	0.54	- 0.02
4400.35	Sc II - 14	0.90	0.98 B	- 0.07	- 0.60
04.75	Fe I - 41	1.31	1.19	0.68	- 0.34
07.68	Ti II - 51	0.68 b	0.59	- 0.36	- 1.02
09.3 *	Ti II - 61	0.66	0.87	- 0.38	- 0.72
11.08	Ti II - 115	1.05	1.09	0.16	- 0.47
11.94	Ti II - 61	0.64 b		- 0.40	
13.60	Fe II - 32	0.74	1.04	- 0.28	- 0.52
15.12	Fe I - 41	1.17 b		0.38	
15.56	Sc II - 14	0.82 B		- 0.18	
16.82	Fe II - 27	1.29	1.78 B	0.62	0.61
17.72	Ti II - 40	1.23	1.44 B	0.50	- 0.01
18.34	Ti II - 51	0.96	1.05 B	0.02	- 0.51
21.95	Ti II - 93	0.79	0.86	- 0.21	- 0.73
25.44	Ca I - 4	0.50		- 0.57	
27.31	Fe I - 2	0.56		- 0.50	
28.00	Mg II - 9	0.80	0.75	- 0.20	- 0.85
31.63	Fe II - 222		0.63		- 0.97
33.99	Mg II - 9	1.02	1.12	0.11	- 0.43
34.96	Ca I - 4	0.72		- 0.30	
35.69	Ca I - 4	0.53 b		- 0.54	
36.48	Mg II - 19		0.71		- 0.89
39.13	Fe II - 32	0.47 b		- 0.61	
41.72	Ti II - 40	0.63	0.75	- 0.42	- 0.85
42.35	Fe I - 68	0.79		- 0.22	
43.20	Fe I - 350	0.69		- 0.34	
43.80	Ti II - 19	1.42	1.68 B	0.98	0.40
44.56	Ti II - 31	0.84		- 0.15	
46.25	Fe II - 187		0.57		- 1.04
47.72	Fe I - 68	0.75		- 0.27	
49.66	Fe II - 222	0.42 b		- 0.66	
50.49	Ti II - 19	1.19	1.28 b	0.42	- 0.23
51.54*	Fe II	0.91	1.13	- 0.05	- 0.42
53.35	V II - 199	0.31	0.49	- 0.78	- 1.12
54.78	Ca I - 4	0.88 b		- 0.09	
55.26*	Fe II		1.12		- 0.43
55.89	Ca I - 4	0.47		- 0.61	
61.65	Fe I - 2	0.83 b	1.25	- 0.16	- 0.27
66.56*	Fe I - 350	0.81	0.60	- 0.19	- 1.01
68.49	Ti II - 31	1.31	1.67 B	0.67	0.38
4470.86	Ti II - 40	0.83	0.84 B	- 0.16	- 0.75

TABLE 3.-- Cont.

λ	Ident.	log 10^6 W/λ γ Gem	α Cyg	log η_o γ Gem	α Cyg
4471.5	He I - 14		1.33 B		- 0.16
72.92	Fe II - 37	0.93	1.39	- 0.02	- 0.08
76.02	Fe I - 350	0.78		- 0.23	
81.33*	Mg II - 4	1.95	2.16	2.50	1.93
82.17	Fe I - 2	0.75		- 0.26	
88.32	Ti II - 115	1.04	1.20 B	0.14	- 0.33
89.18	Fe II - 37	1.23	1.68 b	0.50	0.40
91.40	Fe II - 37	1.20	1.72	0.43	0.47
4494.57	Fe I - 68	0.92	0.52	- 0.04	- 1.09
4501.27	Ti II - 31	1.38	1.68	0.96	0.40
08.28	Fe II - 38	1.32	1.86	0.70	0.80
15.34	Fe II - 37	1.33	1.83	0.73	0.73
20.22	Fe II - 37	1.30	1.86	0.65	0.80
22.62	Fe II - 38	1.43	1.97	1.01	1.15
29.46	Ti II - 82	0.99	1.05	0.06	0.51
41.52	Fe II - 38	1.17	1.70	0.38	0.43
55.02	Cr II - 44	1.11	1.55 B	0.26	0.17
55.89	Fe II - 37	1.42	1.88 b	0.98	0.87
58.66*	Cr II - 44	1.39	1.88	0.89	0.87
63.77	Ti II - 50	1.40	1.74	0.92	0.52
65.78	Cr II - 39	0.98	1.03 B	0.05	- 0.44
71.97	Ti II - 82	1.43	1.77	1.01	0.59
76.33	Fe II - 38	1.21	1.65	0.46	0.34
82.83	Fe II - 37	1.17	1.62 B	0.38	0.29
83.83	Fe II - 38	1.46	2.01 b	1.12	1.30
88.22	Cr II - 44	1.37	1.82	0.83	0.70
4592.09	Cr II - 44	1.07	1.51	0.20	0.11
4616.64	Cr II - 44	1.02	1.48	0.11	0.06
18.83	Cr II - 44	1.22	1.68	0.48	0.40
20.51	Fe II - 38	1.07	1.48	0.20	0.06
29.34	Fe II - 37	1.37 b	1.87	0.83	0.84
34.11	Cr II - 44	1.17	1.64	0.38	0.32
35.33	Fe II - 186	1.01	1.46	0.10	0.02
66.75	Fe II - 37	1.11	1.53	0.27	0.14

NOTES

3330.77	E.P. = 4.67 volts (C. W. Curtis, unpublished analysis)
3356.26	Blend of 2 Fe II lines
3451.3	Blend of 3 Fe II lines
3477.18	Blend of 2 lines in same multiplet
3603.8	Blend of 3 lines in same multiplet
3933.68	log a = - 1.8 (γ Gem), - 2.2 (α Cyg)
4238.03	Blend of 2 Fe I lines
4357.57	E.P. = 6.06 volts (C. M. Sitterly, informal communication)
4361.25	E.P. = 6.11 volts
4409.3	Blend of 2 lines in same multiplet
4451.54	E.P. = 6.11 volts
4455.26	E.P. = 6.06 volts
4466.56	Blend of 2 Fe I lines
4481.33	log a = - 1.4 (γ Gem), - 1.8 (α Cyg)
4558.56	Blend of 2 lines in same multiplet

IV. EQUIVALENT WIDTHS

The total absorption of every line on each tracing was measured by guiding a sensitive rolling planimeter around the profile twice. The readings were reduced to equivalent widths with factors for the linear dispersion scale and the measured height of the continuum from the zero point of intensity. The logarithms of equivalent widths (in dimensionless units, 1 fraunhofer $= 10^{-6}$ λ A), averaged for the three plates covering each spectral region, are listed in Table 3. In addition to the wave length, the absorbing ion and *Revised Multiplet Table* multiplet number are given; asterisks refer to notes at the end of the table. The letters "b" and "B" (slight and severe blending, respectively) indicate that the line profile is extrapolated over about a quarter or half the line width. In the case of lines not listed in the *Revised Multiplet Table* the relevant details of excitation potential and multiplet designation have been furnished from manuscript tables, through the kindness of Professor C. W. Curtis, of Lehigh University, and Mrs. Charlotte Moore Sitterly, of the National Bureau of Standards. The choice of parameters for the

TABLE 4

SYSTEMATIC VARIATIONS FROM OTHER DETERMINATIONS OF EQUIVALENT WIDTH (Δ LOG *W*)

	Observer and Observatory				
	Aller (Greenstein) McDonald	Hiltner and Williams McDonald	Wright Victoria	Pannekoek Victoria	Struve and Elvey Yerkes
Dispersion (A/mm) ($H\gamma$)	3	3	4	12	12
Star	γ Gem	α Cyg	α Cyg	α Cyg	α Cyg
λ 4050	+0.20	0.00	0.00	.....	.....
λ 4200	+0.12	−0.05	−0.05	0.00	0.00
λ 4350	+0.05	−0.10	−0.12	+0.03	0.00
λ 4500	0.00	−0.20	−0.20	0.00	−0.12

theoretical curves of growth (Figs. 2–5) from which the values of log η_0 have been read, is discussed in a subsequent section.

Several comparisons of the equivalent widths of the absorption lines measured in the A stars with the photometric measures of other observers are possible, chiefly in the blue region. These are summarized in Table 4, by logarithmic deviations in the sense of Table 3 *minus* corresponding measures by other observers, averaged over groups of lines in short-wave-length intervals. The two spectrograms of γ Gem analyzed by Aller[8] were taken by Greenstein with the two-prism coudé spectrograph of the McDonald Observatory, which gives slightly higher dispersion than the Mount Wilson grating coudé in the region shortward of $H\gamma$. Aller's values are smaller at the shortward end but approach good agreement longward of $H\gamma$. On the other hand, the present author measured the intensities of all lines included in Table 3, on the published tracings of single McDonald coudé spectrograms of α Cyg in the *Photometric Atlas of Stellar Spectra*,[9] in order to compare equivalent widths. The ratios of equivalent widths between the Michigan *Atlas* and the Mount Wilson tracings average close to 1 for lines in the region λλ 4000–4300 but increase rapidly longward from λ 4300, where the tracing in the *Atlas* is from a spectrogram exposed under different conditions. The nearly constant difference of about 0.2

[8] *Ap. J.*, 96, 321, 1942.

[9] Hiltner and Williams (Ann Arbor: University of Michigan Press, 1946).

between the second and third columns of Table 4 seems rather puzzling, particularly since both columns are based on comparisons between McDonald spectra and the Mount Wilson plates taken for the present investigation.

Dr. K. O. Wright has kindly communicated preliminary results of recent measures in the spectrum of α Cyg with the Cassegrain spectrograph at Victoria, using six-prism dispersion (2 A/mm at K) and the third order of the Littrow grating (4.5 A/mm at $H\gamma$). His measures have been reduced to allow for grating ghosts. Comparison of the third and fourth columns in Table 4 shows that Wright's equivalent widths are in very close agreement with those from the Michigan *Atlas*. In an earlier investigation at Victoria, using the original three-prism spectrograph, Pannekoek[10] has tabulated the equivalent widths of sixty lines of the ionized metals in the spectrum of α Cyg. These agree more closely with the results in Table 3, except in a few cases where blends have been apportioned differently.

Finally, we consider two researches based on lower-dispersion spectrograms of α Cyg. Struve and Elvey[11] have discussed equivalent widths in the blue region, in the paper which first interpreted the form of the curve of growth in terms of turbulent motions in stellar atmospheres. The comparison with the present investigation is shown in the last column of Table 4. The only direct comparison possible in the ultraviolet is with the work of Struve and Sherman,[1] who used a two-prism quartz spectrograph at the Casse-

TABLE 5

PROBABLE ERRORS OF MEAN EQUIVALENT WIDTHS

$\log 10^6\, W/\lambda$	0.4	0.8	1.2	1.6	2.0
$\Delta \log W$					
Unblended	.07	.04	0.03	0.02	0.02
Blended	0.09	0.05	0.03	0.02	0.02

grain focus of the 82-inch reflector at McDonald Observatory, giving a dispersion of 25 A/mm. The equivalent widths of twenty-five *Ti* II lines show rather large individual variations due to a different division of blended features, with values in Table 3 averaging 0.06 less than the logarithms of those given by Struve and Sherman, throughout the wave-length interval.

For the ultraviolet region of γ Gem and the blue region of α Cyg, statistical analyses were made to determine the probable errors of the mean equivalent widths. In each spectrum the lines were divided into nine groups on the basis of intensity and the degree of blending apparent from the tracings. For each group the root-mean-square deviation of individual measures from the mean equivalent width for each line was computed and was expressed in the form of a mean relative probable error for all the lines of the group. Although the lines in the spectrum of γ Gem are intrinsically narrower than those in α Cyg, the relative errors are the same for corresponding groups in the spectra of the two stars. It is more surprising that the relative errors increase considerably between pure and slightly blended lines but show no further increase for the more heavily blended lines. The mean errors are indicated in Table 5 in logarithmic form for several typical equivalent widths, for lines in which respectively less or more than about one-tenth the measured profile departs from the microphotometer tracing because of blending.

Careful examination of the deviations of the individual measurements from the mean equivalent widths do not reveal any systematic variation of the line intensities between

[10] *Proc. Kon. Akad. Wetensch. Amsterdam*, 34, 755, 1931.

[11] *Ap. J.*, 79, 409, 1934.

the plates used, either in adjacent wave-length intervals or arising from the same ion or energy level. The sources of error in photographic spectrophotometry outlined by Wright[12] are, in the aggregate, more than sufficient to account for these internal variations. His experience with the solar-type spectra is confirmed by the foregoing discussion of the interobservatory comparison of photometric standards.

A disturbing effect is observed between well-exposed plates and the weaker ones, which were finally discarded because they do not uniformly cover the spectral range. As the intensity of the continuous spectrum fades, the equivalent widths of the lines on the weak plates decline rapidly to less than half the values measured on the stronger plates. Further reasons must be sought for this effect of the blackness of the continuum on the measured equivalent widths. It seems possible, however, that the equivalent widths may be systematically too small by as much as 10 per cent near the longward end of the blue spectral range, where the continuum is fainter on most plates than over the rest of the range. This suspicion is borne out by comparisons of equivalent widths in the solar spectrum, measured from the zenith-sky tracings and from the Utrecht *Atlas*.

V. SOURCES OF RELATIVE OSCILLATOR STRENGTHS

To construct curves of growth, one must have a consistent set of oscillator strengths for lines of the various ions in all spectral regions. Absolute oscillator strengths have been computed with confidence for many lines of the lighter ions, but for the heavier metals satisfactory results have not yet been obtained, owing to complex interlocking of the energy levels. The results of computations based on the exact theory for the simpler spectra are summarized by Bates and Damgaard.[13] They have also derived a set of tables facilitating the rapid calculation of line strengths for more complex spectra, based on the approximate assumption that the valence electron is moving in a Coulomb field of force. Professor Lawrence H. Aller, of the University of Michigan, has very kindly placed at the author's disposal unpublished oscillator strengths computed in this way for several transition arrays in *Ca* I, *Mg* II, and *Sc* II. A glance at the curves of growth (Figs. 2–5) shows that the observed line intensities fit these oscillator strengths quite well; the scatter from the theoretical curve in each case is somewhat smaller than for the heavier metals.

Laboratory determinations of empirical strengths for many low-excitation lines of neutral atoms have proved extremely useful in the analysis of the atmospheres of solar-type stars. Since little work has been done on the spectra of ionized atoms, the use of laboratory f-values is rather limited for this problem. The work of R. B. King[14] on *Ti* II and *Ni* I is the only material available for lines in the ultraviolet region of A-type spectra. Considerable use is also made of his results[15] for *Fe* I in the blue, and especially of a list of relative oscillator strengths recently determined by W. W. Carter[16] for higher-excitation lines, which Professor King very kindly made available in advance of publication.

Several recent investigators of the spectra of solar-type stars have discussed curves of growth based on empirical f-values derived from the theoretical curve of growth for the sun. Greenstein, applying this technique to the F stars,[17] has published a list of the values of log η_0 for lines in the blue region from the observational curve of growth for τ UMa. Since this star's excitation temperature is slightly higher than the sun's, stellar f-values are available for a few lines of higher-excitation potential not observed in the

[12] *Pub. Dom. Ap. Obs., Victoria*, **8**, 1, 1948.

[13] *Phil. Trans. R. Soc. London, A*, **242**, 101, 1949.

[14] *Ap. J.*, **94**, 27, 1941, and **108**, 87, 1948.

[15] *Ibid.*, **87**, 24, 1938.

[16] *Phys. Rev.*, **76**, 962, 1949.

[17] *Ap. J.*, **107**, 151, 1948.

solar spectrum. In two important respects Professor Greenstein is now extending this technique through the analysis of equivalent widths measured from coudé spectrograms of υ Sgr. From measures on at least two tracings of each part of the spectrum $\lambda\lambda$ 3300–4700, he has constructed a curve of growth, assuming an excitation temperature of 16,800° K. He has very kindly made available for this investigation a list of provisional values of log η_0, including more than half the lines measured in the A-type spectra. This is the first set of stellar line strengths covering lines in the ultraviolet as well as the blue and includes many lines of the ionized atoms arising from higher-energy levels. This system of stellar f-values for the heavier ions forms the basis for all curves of growth drawn in the present study.

Since the Balmer lines are unusually weak and no hydrogen or helium absorption edges are observed in the spectrum of υ Sgr, its continuous absorption must be due mainly to electron scattering and must be independent of wave length. The ratio of line to continuous absorption at the center of a line may be written as follows:

$$\eta_0 = \frac{\sigma_{\lambda 0}}{\kappa_\lambda} = \frac{\pi^{1/2} e^2 f \lambda N_{rs}}{m c v \kappa_\lambda}, \tag{1}$$

where N_{rs} is the number, per square centimeter column above optical depth 1, of absorbing atoms of an element in the energy level χ_s above the ground state of the rth state of ionization; f is the oscillator strength of the line; and v is the most probable resultant velocity in three dimensions of the atoms owing to thermal and turbulent motions in the atmosphere. In a Boltzmann distribution,

$$\log N_{rs} = \log N_r - \chi_s \theta + \log g_s - \log g_0 , \tag{2}$$

where N_r is the number of atoms of this element in the rth state of ionization, the g's are statistical weights, and $T = (5040/\theta)°$ K is the excitation temperature. To take account of the variation of opacity with the inverse cube of the frequency, observed in the cooler stars because of continuous hydrogen absorption, a wave-length dependence was introduced into the line-absorption coefficients by the relation

$$\log \eta'_0 = \log \eta_0 + 3 \log \frac{4300}{\lambda}. \tag{3}$$

For lines not resolved in υ Sgr, one may use empirical line strengths derived from other stellar curves of growth, adjusted to the abundance, opacity, temperature, and velocity for υ Sgr. The scale factors were empirically determined in the following way. The difference in values of the line-absorption coefficient for the same line, from curves of growth for any two stars, may be expressed as follows:

$$\Delta \log \sigma_{\lambda 0} = \Delta \log \eta_0 + \Delta \log \kappa_\lambda = \Delta \log N_r - \chi \Delta\theta - \Delta \log v . \tag{4}$$

Within a short spectral range the difference in opacity is nearly constant, so that the sum $\Delta \log \eta_0 + \chi\Delta\theta$ for a group of lines of the same ion in the two stars is constant. The mean values of this expression for each of several ions between υ Sgr, on the one hand, and τ UMa or the sun, on the other, were computed. For *Fe* I the scatter was rather large, but the probable errors of the means for *Ti* II, *Cr* II, and *Fe* II were each less than 0.05. The published values of log η_0 for τ UMa[17] and the sun[12] were adjusted by these factors for the individual ions to the scale of log η'_0 for υ Sgr, and averages were taken wherever possible as the definitive set of relative line strengths. A similar technique was employed to obtain mean values of log $\eta'_0 + 0.3\chi - \log gf$, so that the relative strengths determined in the laboratory [14,15,16] for *Ti* II and *Fe* I might augment those found from the curve of growth for υ Sgr.

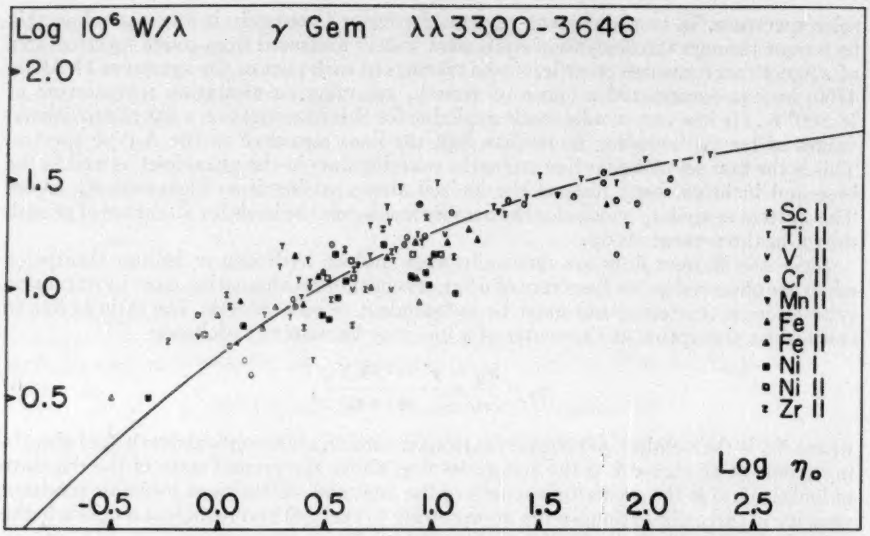

FIG. 2.—The curve of growth for γ Gem in the ultraviolet. The theoretical curve for $B^{(0)}/B^{(1)} = \frac{1.0}{3}$ and $\log a = -3.0$ is plotted.

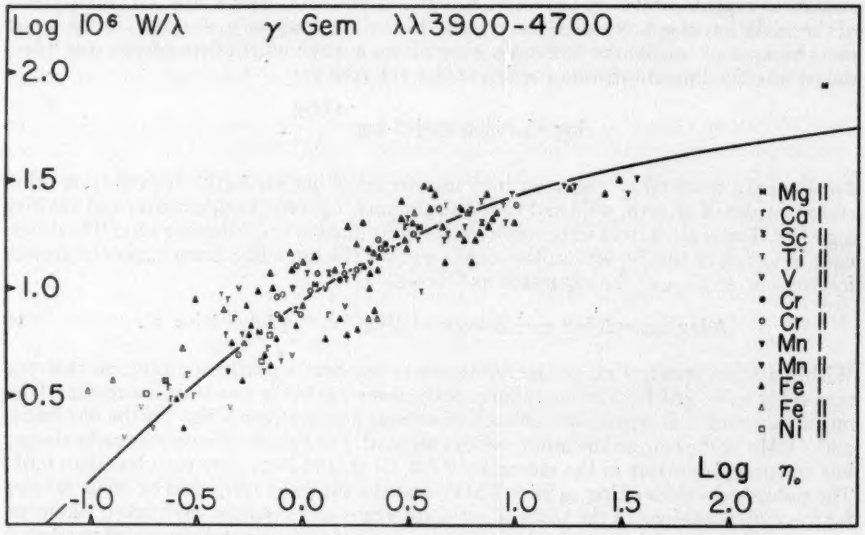

FIG. 3.—The curve of growth for γ Gem in the blue. The theoretical curve for $B^{(0)}/B^{(1)} = \frac{1}{3}$ and $\log a = -3.0$ is plotted.

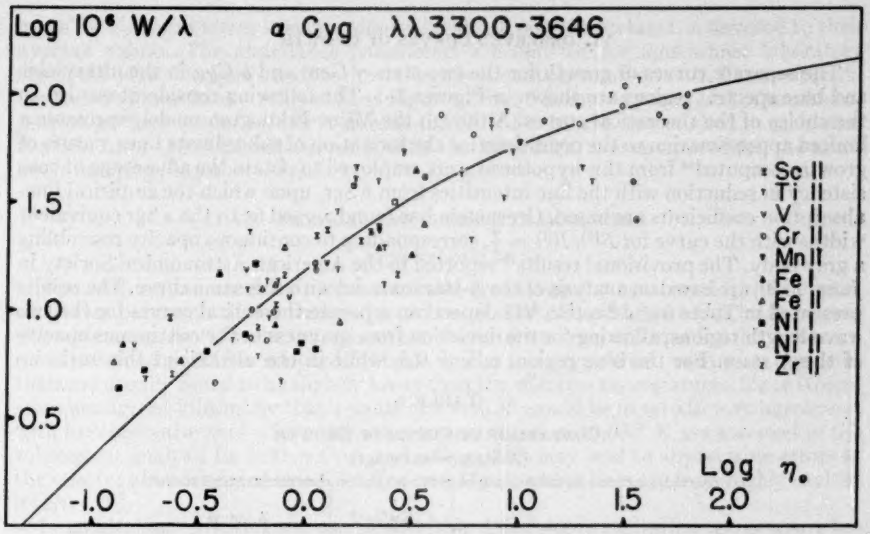

FIG. 4.—The curve of growth for α Cyg in the ultraviolet. The theoretical curve for $B^{(\infty)}/B^{(1)} = \frac{1}{3}$ and log $a = -3.0$ is plotted.

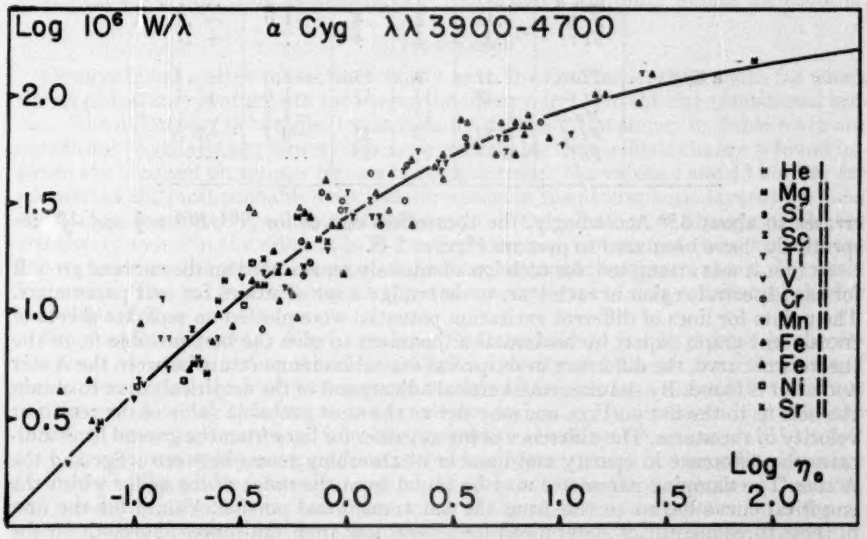

FIG. 5.—The curve of growth for α Cyg in the blue. The theoretical curve for $B^{(\infty)}/B^{(1)} = \frac{1}{3}$ and log $a = -3.0$ is plotted.

VI. OBSERVED CURVES OF GROWTH

The separate curves of growth for the two stars γ Gem and α Cyg in the ultraviolet and blue spectral regions are shown in Figures 2–5. The following considerations led to the choice of the theoretical curves. Although the Milne-Eddington model represents a limited approximation to the conditions for the formation of subordinate lines, curves of growth computed[18] from this hypothesis were employed to obtain the advantage of consistency in reduction with the line intensities from v Sgr, upon which the empirical line-absorption coefficients are based. Greenstein has found a good fit to the v Sgr equivalent widths with the curve for $B^{(0)}/B^{(1)} = \frac{2}{3}$, corresponding to continuous opacity resembling a gray body. The provisional results[19] reported to the American Astronomical Society in June, 1950, are based on analysis of the A-star material with this same curve. The results presented in Table 6 and Section VII depend on separate theoretical curves for the two wave-length regions, allowing for the deviation from grayness in the continuous opacity of the A stars. For the blue region, $\kappa_\lambda/\bar{\kappa} \approx 0.3$, while in the ultraviolet this ratio increases to about 3.[20] Accordingly, the theoretical curves for $B^{(0)}/B^{(1)} = \frac{1}{3}$ and $\frac{10}{3}$, respectively, have been used to prepare Figures 2–5.

TABLE 6

COMPARISON OF CURVES OF GROWTH
(A Stars *minus* v Sgr)

Star	Ion	$\Delta\theta$	v (Km/Sec)		$\Delta \log \eta_0$	
			U.V.	Blue	U.V.	Blue
γ Gem....	*Ti* II	0.18	6	3	−1.0	+0.6
	Cr II	.13	4	4	−1.0	+ .2
	Mn II	.....	3	.....	−1.2	.....
	Fe II	.12	2	4	−1.0	− .1
	Fe I	.3	2	4	.....	+ .7
α Cyg.....	*Ti* II	.12	8	13	−1.0	− .4
	Cr II	.18	13	13	−1.0	+ .1
	Mn II	.....	13	.....	−1.7	.....
	Fe II	0.12	3	13	−0.7	−0.5
	Fe I	0	.....	13	.....	.....

At first it was attempted, for each ion adequately represented on the curve of growth for each spectral region in each star, to determine a set of values for four parameters. The points for lines of different excitation potential were plotted on separate sheets of translucent graph paper; by horizontal adjustment to give the best possible fit to the theoretical curve, the difference in reciprocal excitation temperature between the A star and v Sgr is found. By simultaneous vertical adjustment of the empirical curve to obtain the best fit to the flat portion, one may derive the most probable value of the resultant velocity of the atoms. The difference of log η_0 values for lines from the ground level indicates the difference in opacity and number of absorbing atoms between v Sgr and the A star. The damping parameter may be found from the value of log η_0 for which the empirical curve begins to rise from the flat transitional portion. Values for the first of these three quantities, determined for several ions from the curves of growth for the two regions in each star's spectrum, are shown in Table 6. Since the temperature differ-

[18] M. Wrubel, *Ap. J.*, **109**, 66, 1949.

[19] *A.J.*, **55**, 166, 1950.

[20] Chandrasekhar and Münch, *Ap. J.*, **104**, 446, 1946.

ences for blue and ultraviolet are almost identical, only one column is devoted to their average values. The abundance parameters are omitted for ions whose laboratory strengths were principally used to draw the provisional curves of growth. The most striking feature immediately evident from Figures 3 and 5 is the very long, flat, transitional portion of these curves for the A stars in the blue. For all the ions studied in each star, the best fit of the empirical curves is with the theoretical one computed for the minimum damping, $\log a = -3.0$.

VII. PHYSICAL AND CHEMICAL PARAMETERS

a) TEMPERATURE

For each ion for which empirical curves of growth can be constructed, the range in excitation potentials of the lines is limited to, at most, 2 volts. Since this leads to considerable uncertainty in the determination of excitation temperatures for the A stars, a mean value $\Delta\theta = 0.15$ is adopted for each. In the solar-type stars, excitation temperatures are usually found to be slightly lower than the effective temperatures. Since Greenstein has agreed informally that a value of $\theta = 0.35$ would be in satisfactory agreement with his observations of υ Sgr, excitation temperatures of 10,080° K are assumed in the subsequent analysis for both γ Gem and α Cyg. This may lead to appreciable errors in the relative abundances of ions (like *He* I and *Mg* II) whose lines are from highly excited levels.

In an attempt to distinguish any appreciable difference in excitation temperature between the dwarf and the supergiant stars, differences of the values of $\log \eta_0$ (in Table 3) between γ Gem and α Cyg were plotted against excitation potential for each of the ions *Ti* II, *Cr* II, *Fe* I, and *Fe* II. Owing to the scatter for individual absorption lines arising from the same energy level, this insensitive method yielded no new information. It seems evident that the excitation temperatures of γ Gem and α Cyg differ by less than 500° K.

b) TURBULENCE

Observational scatter causes uncertainty as to the exact equivalent width for which the empirical curves of growth turn from the linear portion to the flat transitional section. The differences in turbulent velocities for different ions shown in Table 6 are not considered physically significant; it is more remarkable that so little change is found between the blue and ultraviolet regions of the spectrum. The values 4 and 13 km/sec are adopted as the most probable velocities for atoms in the atmospheric layers of γ Gem and α Cyg, respectively, which contribute most of the metallic-line absorption. As the velocity of sound in the mixture is 11 km/sec, one may conceive of these heavier ions being carried by the thermal motion of the more abundant hydrogen atoms. Professor Richard N. Thomas has informally suggested kinetic temperatures considerably higher than 10,000° K.

From an earlier study, Aller[8] concluded that turbulence is not present in the atmosphere of γ Gem, and he found for α Cyg[21] a velocity of 2 km/sec from the curve of growth for *Fe* II in the blue, as compared to over 10 km/sec for *Cr* II and *Ti* II. Struve and Elvey[11] adopted 2 km/sec as the turbulence for α Cyg. In corresponding units the turbulent velocities determined from line profiles are 17 km/sec for γ Gem and 35 km/sec for α Cyg. A reasonable interpretation is that much energy may be transported in large turbulent eddies whose dimensions exceed the scale height in the atmosphere. However, the possibility cannot be excluded that much of the observed line broadening is due to axial rotation of these stars. Schwarzschild[22] has shown that the line profile observed in η Aquilae at mid-descending branch of its light-curve (where the velocity parameters are similar to those found for γ Gem) is practically as well represented by a rotational

[21] *Ap. J.*, **95**, 73, 1942. [22] *Ap. J.*, **108**, 227, 1948.

velocity $v \sin i = 15$ km/sec, modified by instrumental broadening and the small turbulence found from the curve of growth, as by the Gaussian profile for pure turbulence.

c) DAMPING

The theoretical curves of growth drawn in Figures 2–5, from which the values of log η_0 in Table 3 were derived, represent the minimum value of the damping parameter for which Wrubel's tables[18] have been computed, which corresponds to 0.06 of the classical value for γ Gem, and to $\Gamma = 0.2\ \gamma_{el}$ for α Cyg, using the most probable velocities determined from the curves of growth. The Gaussian line profiles discussed in Section III indicate that the effect of damping is small. Professor Bengt Strömgren has expressed the opinion informally that damping wings dominate only those lines in these spectra whose equivalent widths exceed 0.5 A. The only lines in the spectral regions studied which are selected under this criterion are the Balmer lines, *Ca* II H and K and *Mg* II λ 4481. Discussion of the Stark-broadened hydrogen lines and of lines blended with their wings (e.g., H with $H\epsilon$) is beyond the scope of this investigation.

Blends with other strong metallic lines make it difficult to sketch the profile of the K line with confidence. A further complication in the spectrum of α Cyg is the presence of two interstellar components recognizable on the tracings only by the asymmetrical profile of the K line. At the suggestion of Dr. Isadore Epstein, an approximate equivalent width was obtained for this line by subtracting the combined width of the interstellar components from the measured total absorption.[23] For the *Ca* II resonance lines it is easily shown theoretically that the damping constant has exactly the classical radiation value, which is used in deriving the values of log η_0 in Table 3 for λ 3933. The separation of the theoretical curves of growth for different values of the damping parameter is here quite considerable, but no measures of fainter lines are available to facilitate the determination of the abundance of *Ca* II. For *Mg* II λ 4481, Mr. Allan F. Cook has computed, by the method of Unsöld's textbook,[24] that a value of at least three times the classical damping should be expected. This is uncertain because of the meager information available regarding the exact probabilities for higher transitions; the effect of collisions has not been considered. The abundances of *Mg* II derived from the linear portion of the empirical curves of growth for the A stars make it appear reasonable to use this value of the damping parameter in listing values of log η_0 for λ 4481.

From lines of the ionized metals in the spectrum of α Cyg, Pannekoek[10] found $\Gamma/\gamma_{el} = 19$; but Struve and Elvey[11] have questioned this result for a supergiant atmosphere in which collisions contribute very little to the damping. For the sun, values of this ratio near 10 have been reported by several investigators who used theoretical curves of growth based on the Schuster-Schwarzschild model. An intermediate model probably represents more exactly the variation of line and continuous absorption with height in a stellar atmosphere. Owing to the scarcity of strong lines in the regions considered in A-type spectra and the suspicion that some measured equivalent widths may be too small, one must conclude that the damping parameter is almost indeterminate in this study. Of the eight lines for which log η_0 is greater than 1.0 on Figures 3 and 5, six are in the region longward of λ 4400, where the scale of the tracings is uncertain.

d) ABUNDANCES

For lines of the lighter elements whose oscillator strengths are known, one may solve equation (1) for the number of absorbing ions. A value must be assumed for κ_λ, which for the early A stars depends almost entirely on the temperature and only very slightly on the electron pressure, as the opacity due to atomic hydrogen far exceeds that of the nega-

[23] Spitzer, Epstein, and Li Hen, *Ann. d'ap.*, 13, 147, 1950.

[24] *Physik der Sternatmosphären* (Berlin: J. Springer, 1938).

tive hydrogen ion.[25] For lines of the heavier elements the number of absorbing ions may be derived in terms of the corresponding abundance in the solar atmosphere[12] by the use of equation (4). The results of these computations are shown in Table 7. The number of lines of each ion for which separate determinations are averaged is included as an indication of the relative degree of confidence in the results. The determination of the total abundances of the elements in various stages of ionization depends on the values of the electron pressures, discussed in the following section.

e) ELECTRON PRESSURES

From the relative abundances of neutral and ionized atoms of the same element, the Saha equation,

$$\log P_e = \log \frac{2b_1}{b_0} + \tfrac{5}{2} \log T - \log \frac{N_1}{N_0} - \frac{5040}{T} \chi_0 - 0.48 , \qquad (5)$$

gives a relation between electron pressure and absolute temperature. The quantities b_0 and b_1 are the partition functions for neutral and ionized atoms at temperature T; N_0 and N_1 are the observed numbers of atoms, and χ_0 is the first ionization potential. Since

TABLE 7

NUMBERS OF ATOMS IN A-TYPE STELLAR ATMOSPHERES

ELEMENT	γ GEM					α CYG				
	log N_0	Wt.	log N_1	Wt.	log N	log N_0	Wt.	log N_1	Wt.	log N
He	.....	.....	.....	.....	.....	24.8	3	.....	.....	24.8
Mg	17.5	1	20.3	5	20.3	16.5	1	20.0	5	20.1
Al	15.6	1	.....	.....	18.7	14.9	1	.....	.....	19.0
Si	.....	.....	19.8	1	19.8	.....	.....	19.5	2	19.5
Ca	14.0	5	17.3	1	17.7	12.7	1	16.8	1	18.0
Sc	.....	.....	14.7	3	14.9	.....	.....	14.8	3	15.6
Ti	.....	.....	16.1	10	16.2	.....	.....	16.1	10	16.5
V	.....	.....	15.8	2	15.8	.....	.....	15.4	2	15.7
Cr	15.6	2	17.8	6	17.8	14.8	1	18.0	6	18.0
Mn	16.5	2	18.7	2	18.7	15.5	1	18.6	2	18.7
Fe	17.7	8	19.8	15	19.8	16.9	6	20.3	15	20.3
Co	.....	.....	17.6	1	17.6	.....	.....	17.7	1	17.7
Ni	16.4	5	18.7	3	18.7	15.9	2	18.7	3	18.7
Sr	.....	.....	14.2	1	14.9	.....	.....	13.5	2	15.1
Y	.....	.....	15.5	1	15.9	.....	.....	15.2	1	16.2
Zr	.....	.....	16.5	2	16.5	.....	.....	16.2	2	16.5

the level of ionization does not depend critically on the temperature, an ionization temperature of 10,000° K is assumed for the A stars. From the ionization equilibria of different elements, a mean electron pressure is adopted for each star. Approximate weights are assigned to the individual values, depending on the number of lines used and the scatter of observations from the empirical curves of growth for both neutral and ionized atoms of each element. The results are collected in Table 8. The mean level of ionization (11.5 volts for γ Gem, 13.5 volts for α Cyg) indicates readily the degree of ionization for any element. Where second ionization is appreciable, the number of doubly ionized atoms

[25] The author acknowledges the opportunity of consulting, in manuscript, Professor Bengt Strömgren's accurate opacity tables, computed for a close network of pressures and temperatures.

is computed from equation (5) with each subscript increased by unity. The total number of atoms above 1 sq cm at optical depth 1, $N = N_0 + N_1 + N_2$, is listed in Table 7 for each element observed in the spectra of the A stars. The electron pressure predicted[20] for a main-sequence A1 star is 5000 dyne/cm^2.

The values of log P_e for hydrogen, found by solving the Inglis-Teller formula,[26] differ considerably from the results of ionization equilibrium, although the ratio of pressures between dwarf and supergiant is unchanged. The highest members of the Balmer series of Stark-broadened absorption lines which can be resolved from the confluence of their wings are H_{23} for γ Gem and H_{32} for α Cyg. More accordant results have been obtained by applying this criterion of resolution to spectrograms of lower dispersion.[27] On the other hand, the cores of the hydrogen lines may be formed much higher in the stellar atmospheres, under greatly reduced pressure.

f) OPACITY

The variation, between visible and ultraviolet regions, of the preliminary values of $\Delta \log \eta_0$ (A stars *minus* υ Sgr), reported in Table 6, shows that the increase in opacity in the Balmer continuum can be determined by comparing curves of growth. Since the same

TABLE 8

ELECTRON PRESSURES

Element	log P_e		Weight	Element	log P_e		Weight
	γ Gem	α Cyg			γ Gem	α Cyg	
H	0.8	−0.3	0	*Fe*	3.8	2.5	3
Mg	3.2	2.5	2	*Ni*	3.7	3.2	1
Ca	3.5	2.7	1				
Cr	4.2	3.2	2	Mean	3.7±0.1	2.8±0.1	.....
Mn	3.9	3.0	1				

values of excitation temperature and turbulent velocity have now been adopted for all ions observed in each region of a particular star's spectrum, one may expect a more consistent determination of the difference in continuous absorption. For each ion the values of log $\eta_0 + \chi\theta$ were taken from Table 3, corresponding to the observed intensities of lines in each spectrum, for which the value of log η_0' from the curve of growth for υ Sgr is 1.0. The A-star curves of growth are constructed for spectral regions having mean wave lengths of λ 3500 and λ 4300. Over this interval the increase in continuous absorption at the Balmer limit is somewhat reduced by the gradual increase of the Paschen continuum toward the red. The results shown in Table 9 represent entirely the increase in opacity in the A stars, relative to υ Sgr, at the Balmer limit. Extra weight has been given to values found for *Cr* II and *Fe* II, represented by many lines in both spectral regions, whose equivalent widths have been measured in υ Sgr as well as in the A stars.

The theoretical values of $\Delta \log \kappa_\lambda$, listed for comparison, are from a table[25] of the continuous absorption coefficient due to *H* and H^-. The relative increase in opacity determined from the curves of growth depends on the integrated effect over a large range in optical depth and is smaller than the absolute effect at a representative point where the local temperature is 10,000° K and the electron pressure has the mean value adopted in the preceding section. The earlier work of Struve and Sherman,[1] limited to the comparison of equivalent widths of *Ti* II lines near the Balmer limit with their laboratory intensi-

[26] *Ap. J.*, **90**, 439, 1939.

[27] E. van Dien, *Ap. J.*, **109**, 452, 1949.

ties, indicated a tenfold increase in opacity in α Cyg and even a factor of 2 for υ Sgr. It would be rather important to verify this last factor, which could materially affect the present results. Barbier and Chalonge[28] found no measurable change in the intensity of the continuous background at λ 3646 for υ Sgr, while in the spectrum of γ Gem it is more than doubled and in α Cyg more than trebled.

Owing to the high level of ionization in the atmosphere of α Cyg, nearly half the hydrogen atoms must be ionized. Under these conditions electron scattering may be an important contributor to the continuous opacity. In an attempt to determine the wavelength variation of κ_λ, mean differences in $\log \eta_0 + \chi\theta$ between the A stars and υ Sgr (*not* adjusted for the λ^3 variation in the Paschen continuum) for groups of lines of the same ion in 50 A intervals were plotted against log λ. While the scatter is large, a relation intermediate between linear and quadratic is indicated. Possibly the effects of electron scattering and of the atomic helium continua are commensurate in this region of the spectrum of υ Sgr. A more detailed interpretation of these results may become possible when models are computed for the atmospheric structure of these early-type stars.

TABLE 9

INCREASE IN OPACITY ACROSS THE BALMER LIMIT

Ion	Δ log κ_λ		Ion	Δ log κ_λ	
	γ Gem	α Cyg		γ Gem	α Cyg
Sc II	0.4	0.5	*Fe* II	1.0	1.1
Ti II	.7	0.8	*Ni* II	1.0	1.2
V II	.4	0.7			
Cr II	.8	1.0	Mean value	0.7±0.1	0.9±0.1
Mn II	.6	0.9	Theoretical	1.0	1.2
Fe I	0.6	0.6			

After completion of this article, a paper of G. A. Shajn and P. F. Shajn[29] has come to my attention. Although chiefly devoted to discussions of displacements of lines of various elements in the spectra of α Cyg and β Ori, their work includes a section comparing line intensities in α Cyg and υ Sgr in the blue region. Their independent conclusions are in close agreement with those of Section VII above, especially with respect to abundances and electron pressures.

It is a pleasure to express my appreciation to Professors Lyman Spitzer, Jr., and Martin Schwarzschild for their stimulating advice and constant encouragement during this investigation. I am especially indebted to Professor Jesse Greenstein, who suggested the problem and contributed much to the analysis. Many useful ideas have come from detailed discussions with Professors Lawrence Aller, David Bates, Bengt Strömgren, and Otto Struve. I am grateful to Princeton University for support of this work on the Thaw Fellowship. Thanks are due to Professor Ira S. Bowen, director of the Mount Wilson and Palomar Observatories, for making this investigation possible.

[28] *Ann. d'ap.*, **4**, 30, 1941.

[29] *Comm. Crimean Ap. Obs.*, **4**, 49, 1949.

IONIZED HYDROGEN REGIONS IN PLANETARY NEBULAE

THORNTON PAGE AND JESSE L. GREENSTEIN
Yerkes Observatory
and
Mount Wilson and Palomar Observatories
Carnegie Institution of Washington
California Institute of Technology
Received March 9, 1951

ABSTRACT

A compilation of the best observational data for nine planetary nebulae, after adjustment for internal consistency, shows that the linear dimensions of the bright rings are approximately the same as the calculated radii of the *H* II regions around the central stars. The relative sizes of seventeen other nebulae, of all stages of excitation and ranging from 2″ to 70″ in apparent diameter, confirm this result. The masses, spectral characteristics, and forms of the planetary nebulae are re-examined in the light of this conclusion.

In Zanstra's theory,[1] which has been remarkably successful in determining self-consistent temperatures of the nuclei of the planetary nebulae, it is assumed that these nebulae are opaque to the Lyman continuum, $\lambda < 912$ A. Together with other approximations, this assumption was recognized by Zanstra to lead to a lower limit to T_*. Menzel and his co-workers[2] have carried through theoretical calculations with these and alternative assumptions, and Wurm[3] has recently suggested that planetary nebulae may differ in their opacity in the Lyman region.

If these nebulae do not absorb all the hydrogen-ionizing light from their central stars, their limits must be explained in terms of a discontinuity in some other parameter—most likely the density. However, since the nebular shells have velocities of expansion[4] as high as 20 km/sec and dimensions of the order of 2×10^{17} cm, this explanation would limit the ages of these objects to 10^{11} seconds, or only 3000 years. It thus seems likely, as assumed implicitly by several recent investigators (e.g., R. Minkowski[5] and O. C. Wilson[4]), that there is a change of ionization at the visible edge of a planetary nebula rather than a change in density. On this view the planetary nebulae are *H* II regions[6] in far larger masses of gas, which surround their central stars and have expanded through the *H* II boundary into an *H* I region.

In order to confirm this conclusion, we have compiled data for nine planetary nebulae, of which accurate observations have been made, and will show, first, that the absolute linear dimensions of these nebulae agree with the calculated radii of the *H* II regions associated with their central stars, within a factor of 2. Second, we will show from less complete data that seventeen other nebulae, with apparent diameters ranging from 2″ to 71″, have relative sizes in proportion to the calculated radii of their *H* II regions.

The radius of an *H* II region is given by[6]

$$r_0 = 0.67 \times 10^{-6} \bar{a}_u^{-1/3} T_e^{1/6} T_*^{1/3} 10^{-2280/T_*} R_*^{2/3} N^{-2/3}, \qquad (1)$$

where $\bar{a}_u$ is the effective absorption coefficient of hydrogen below λ 912, T_e is the electron temperature in the nebula, T_* is the black-body temperature of the exciting star, R_* is the radius of the exciting star in solar units, and N is the number of hydrogen atoms and

[1] *Pub. Dom. Ap. Obs. Victoria*, **4**, 209, 1931.

[2] *Ap. J.*, **85**, 330, 1937; **86**, 70, 1937; **88**, 52, 313, 422, 1938; **90**, 601, 1939.

[3] *Naturwiss.*, **9**, 273, 1949; **10**, 306, 1949.

[4] O. C. Wilson, *Ap. J.*, **111**, 284, 1950.

[5] *Pub. A.S.P.*, **61**, 151, 1949, and in private communications.

[6] B. Strömgren, *Ap. J.*, **89**, 531, 1939; **108**, 259, 1948. The effect of absorption by *He* I and *He* II, neglected by Strömgren and in this paper, will be to reduce the dimensions of *H* II regions slightly.

ions per cubic centimeter. The coefficient $\bar{a}_u$ is approximately the mean of $a_u(\lambda)$ weighted with $B_\lambda(T_s)$, the Planck function, over the region $0 < \lambda < 912$. It is a function of T_s and has been determined from graphical integration to vary from 0.61 $a_u(912)$ at 25,000° K to 0.155 $a_u(912)$ at 100,000° K.

We will determine R_s from T_s, the absolute magnitude M_s, and the bolometric correction Δm_B. Errors in the parallax, which are most serious in these data, will enter R_s and r_0 directly, but they enter the linear radius of the nebula R in the same way and therefore do not affect the comparison of r_0 with R. We assume that the nebulae are predominantly hydrogen, virtually 100 per cent ionized in the inner parts, so that $N \simeq N_e$, the electron density, which may, in turn, be determined from the "surface brightness" of a nebula in the Balmer continuum.[7]

The necessary data are listed in Table 1, together with data on the visual continuum and H^- emission for the accompanying paper.[8] An inconsistency was immediately noted; the observed emission-line surface brightnesses of the nebulae, S_L, in erg/cm²/sec, derived by Menzel and Aller,[7] are in five cases too large to satisfy the energy relation,

$$4\pi R^2 S_L < L_{SB} , \tag{2}$$

where L_{SB} is the bolometric luminosity of the nucleus derived from its observed photographic magnitude, its distance, and the bolometric correction for its Zanstra temperature. This inconsistency also is not affected by errors in the distance, which enter both sides of equation (2) in the same way. It appears, rather, to be due to the combination of spectrophotometric intensities into integrated magnitudes,[7] although the measured magnitudes themselves may also be at fault. The continua, V_c, Ba_c, Pa_c, etc., and unobservable emission lines are omitted from equation (2); including them would make the inconsistency even worse. Sources of the data in each column of Table 1 are listed below.

Column

2, 3. Total photographic magnitudes of the nebulae and photographic magnitudes of nuclear stars, from observations of Hubble, Vorontsov-Velyaminov, Parenago, and others; listed by Berman (*Lick. Obs. Bull.*, **18**, 73, 1937).

4. Angular radius of the brighter part of the nebula, in seconds of arc, listed by Menzel and Aller (*Ap. J.*, **93**, 199, 1941).

5. Distance in parsecs, derived from galactic rotation by Berman (*loc. cit.*) (distances derived by Vorontsov-Velyaminov, *A.J. Soviet Union*, **27**, 285, 1950, are about half as large).

6. Interstellar absorption in photographic magnitudes, derived from distances and line intensities by Berman (*M.N.*, **96**, 892, 1936).

7. Zanstra temperature of the nuclear star in ° K (derived from ratios of nebular emission lines to nuclear continuum), listed by Berman (*Lick. Obs. Bull.*, **18**, 73, 1937).

8. The derived absolute bolometric magnitude of the nuclear star, using bolometric corrections from Kuiper (*Ap. J.*, **88**, 438, 1938).

9. Log of the radius of the nuclear star in solar units, derived from columns 7 and 8.

10. Electron temperature of the brighter part of the nebula, derived from the ratio of intensities of the [*O* III] lines by Menzel and Aller (*Ap. J.*, **93**, 230, 1941) and confirmed by measures of the Balmer continuum (Page, *Ap. J.*, **96**, 78, 1942).

11. Log of the mean surface brightness of the brighter part of the nebula in the $H\beta$ emission line, in erg/cm²/sec, derived from m_n, A, and the ratio of $H\beta$ to the total photographic emission, by Menzel and Aller (*Ap. J.*, **93**, 200, 1941).

12. Log of the mean surface brightness in the Balmer continuum at λ 3645, in erg/cm²/sec per angstrom unit, derived from column 11 and the ratio of Balmer

[7] Menzel and Aller, *Ap. J.*, **93**, 200, 1941. The term "surface brightness" will be used in the same sense here, i.e., the flux in erg/cm²/sec at the outer boundary of the nebula.

[8] Greenstein and Page, *Ap. J.*, **114**, 106, 1951.

TABLE 1*

DATA FOR NINE PLANETARY NEBULAE

(1) NGC	(2) m_{pg} (Mag.)	(3) m_v (Mag.)	(4) A	(5) D (Psc)	(6) Δm_v (Mag.)	(7) T_e (° K)	(8) M_{BB} (Mag.)	(9) log R_e	(10) T_e (° K)	(11) log S_β	(12) log $S_B\Delta\lambda$	(13) N_e	(14) log $S_V\Delta\lambda$	(15) log $S_V(H^-)$	(16) log r_0	(17) log R	(18) log S_L	(19) $4\pi R^2 S_L/L_{BB}$
I 418.....	10.6	10.8	6*	1800	0.31	25,000	−3.2	+0.27	9700	−0.46	−2.64	8700	.....	−7.49	16.90	17.21	+0.42	0.17
	11.0	**10.4**	.....	.....	.....	**27,000**	**−3.8**	**+0.31**	.....	**−1.02**	**−3.20**	**4600**	.....	**−7.77**	**17.21**	.....	**−0.14**	**0.03**
6826.....	9.2	10.7	13	1050	0.43	30,000	−2.8	+0.04	8200	−0.65	−3.19	3500	−3.75	−7.99	17.22	17.31	+0.58	0.56
	9.6	**10.3**	.....	.....	.....	**33,000**	**−3.4**	**+0.08**	.....	**−1.21**	**−3.75**	**1800**	**−4.31**	**−8.27**	**17.53**	.....	**+0.02**	**0.09**
40.....	9.5	11.3	18	1220	0.50	35,000	−2.7	−0.11	(6000)	−0.84	−3.65	1400	−3.75	−8.72	17.47	17.52	+0.11	0.55
	9.9	**10.9**	.....	.....	.....	**38,000**	**−3.3**	**−0.07**	.....	**−1.40**	**−4.21**	**750**	**−4.31**	**−9.00**	**17.76**	.....	**−0.45**	**0.09**
1535.....	9.9	11.8	9	1720	0.18	35,000	−2.6	−0.13	10,000	−0.75	−2.88	5600	.....	−7.67	17.10	17.37	+0.47	0.69
	10.3	**11.4**	.....	.....	.....	**38,000**	**−3.2**	**−0.08**	.....	**−1.31**	**−3.44**	**2900**	.....	**−7.95**	**17.39**	.....	**−0.09**	**0.11**
6543.....	8.7	11.2	10	1080	0.22	35,000	−2.2	−0.21	6500	−0.14	−2.60	6300	−3.21	−7.93	16.97	17.21	+1.00	1.6
	9.1	**10.8**	.....	.....	.....	**38,000**	**−2.8**	**−0.16**	.....	**−0.70**	**−3.16**	**3600**	**−3.77**	**−8.21**	**17.26**	.....	**+0.44**	**0.25**
6572.....	9.2	12	7	1230	0.50	45,000	−2.6	−0.35	9000	−0.14	−2.75	8300	.....	−7.55	17.06	17.11	+1.15	1.1
	9.6	**11.6**	.....	.....	.....	**49,000**	**−3.2**	**−0.30**	.....	**−0.70**	**−3.31**	**4400**	.....	**−7.83**	**17.33**	.....	**+0.59**	**0.17**
7009.....	7.9	11.9	9	930	0.19	50,000	−2.0	−0.56	8900	+0.10	−2.36	13,000	−2.89	−7.37	16.86	17.10	+1.37	2.8
	8.3	**11.5**	.....	.....	.....	**54,000**	**−2.6**	**−0.51**	.....	**−0.46**	**−2.92**	**6800**	**−3.45**	**−7.65**	**17.12**	.....	**+0.81**	**0.44**
7662.....	8.7	12.7	8	1200	0.36	55,000	−2.1	−0.62	9900	+0.12	−2.64	9500	−2.93	−7.44	16.98	17.16	+1.62	5.9
	9.1	**12.3**	.....	.....	.....	**60,000**	**−2.7**	**−0.57**	.....	**−0.44**	**−3.20**	**5000**	**−3.49**	**−7.72**	**17.24**	.....	**+1.06**	**0.94**
7027.....	9.8	(15.6)	5	2130	0.92	80,000	−2.1	−0.95	9600	−0.20	−3.70	2600	−3.87	−8.03	17.40	17.20	+1.26	3.1
	10.2	**15.2**	.....	.....	.....	**87,000**	**−2.7**	**−0.90**	.....	**−0.76**	**−4.26**	**1350**	**−4.43**	**−8.31**	**17.66**	.....	**+0.70**	**0.49**
Est. error..	±1.	±1.	±20%	±100%	±100%	±20%	±1.8	±0.45	±1000	±0.50	±0.55	±100%	±0.55	±0.4	±0.4	±0.32	±0.55	.....
Dep.....	.....	.....	.....	D	(D)	T_e	$[D^2]$	$[DT_e^{-4}]$	.....	.....	.....	$D^{-1/2}$	.....	$[D]$	$[D(T_e)]$	$[D]$	.....	.....

* Adjusted values are given in boldface type.

continuum to $H\beta$, corrected for overlapping visual continuum and interstellar reddening, measured by Page (*loc. cit.*).

13. The mean electron density per cubic centimeter in the brighter part of the nebula, derived from $7.60 \times 10^{10}\, T_e^{3/4} R^{-1/2} S_B'^{1/2}$, following Menzel and Aller (*Ap. J.*, **93**, 195, 1941) (the constant has been revised to eliminate an error in calculation and is given here for S_B per angstrom unit).
14. Log of the mean surface brightness in the visual continuum at λ 3900, in erg/cm²/sec per angstrom unit, derived from column 11 and the ratio of V_c to $H\beta$ measured by Page (*loc. cit.*).
15. The computed log of $S_\nu(H^-)$ at λ 4000 from Greenstein and Page (*Ap. J.*, **114**, 106, 1951).
16. Log of the radius of the *H* II region in centimeters derived from equation (1).
17. Log of the radius of the brighter part of the nebula, in centimeters, derived from $R = 1.5 \times 10^{13}\, AD$.
18. Log of the mean surface brightness in all observed emission lines, in erg/cm²/sec, derived from the line intensities relative to $H\beta$ published by Aller (*Ap. J.*, **93**, 236, 1941).
19. The ratio of total flux in the nebular emission lines to the bolometric luminosity of the nuclear star.

Estimated errors are given below the last nebular entry in each column. Errors in columns 2–7 and the error in T_e, column 10, are assigned arbitrarily, and the others deduced therefrom. The last row of Table 1 gives the dependence of the values in certain columns on the two parameters D and T_e. In the case of r_0 the dependence on T_e is not linear.

The flux discrepancies, indicated by the upper (unadjusted) entries in column 19 of Table 1 which are greater than unity, are most likely due to systematic errors in the data. Hence adjustments should be made uniformly in all the data; that is, if the value of S_L for NGC 7662 must be reduced by the factor 6, values of S_L for the other nebulae (derived in the same manner from homogeneous observational data) should be reduced by approximately the same factor.

Excessive values of S_L may be attributed to three causes: (*a*) the plate-sensitivity factors used by Menzel and Aller[7] to convert line intensities into m_n might be too small; (*b*) the measured values of the nebular diameter in seconds of arc, A, might be too small; and (*c*) the measured values of the nebular magnitudes, m_n might be too large. The direct effect on equation (2) of a change in A is nil, since $R^2 S_L$ is independent of A, but a change in A does effect N_e and r_0. Note that, if S_L is decreased by a factor of 6, S_β, S_V, and S_B must also be reduced by the same factor, the last causing a reduction in N_e by a factor of $6^{1/2}$ and increasing r_0 by $6^{1/3}$. An increase in the values of r_0, the radius of the *H* II region, brings them close to equality with values of R, the radius of the brighter part of the nebula.

The flux discrepancies can also be eliminated by increasing L_{SB} by the factor 6, which, in turn, necessitates increasing R_s by the factor $6^{1/2}$ and increasing r_0 by the *same* factor ($6^{1/3}$) as before. In order to balance equation (2), therefore, values of r_0 must be increased by the factor $6^{1/3}$ regardless of which quantity is to be adjusted.

Insufficient values of L_{SB} may be attributed to two causes: (*a*) the observed values of m_s might be too large, and (*b*) the derived values of the bolometric correction—and therefore T_e—might be too small. It is to be expected that values of T_e are too small, as Zanstra's method[1] leads to a lower limit of T_e only, even if the absorption by hydrogen is complete.

Since adjustments are necessary either in the surface brightnesses or in the values of L_{SB} or in both, it remains to divide them equitably, keeping all changes within the estimated errors. The increase in T_e permits the rough equality of R and r_0 for a majority of

these nebulae. The uniform adjustments applied in Table 2 to yield the boldface entries are: 0.4-mag. decrease in m_s; 0.2-mag. decrease in bolometric correction—about 20 per cent increase in T_e; 0.4-mag. increase in m_n; no change in A, D, or Δm_a; and 0.56-mag. decrease in log S_L, log S_β, log S_γ, and log S_B, with associated changes in M_{SB}, R_s, r_0, and N_e. Although these are somewhat arbitrary in magnitude, they are intended to indicate the probable direction of systematic errors in the present data and are expected to yield the best possible values of r_0, S_γ, and N_e.

Unpublished values of m_s for IC 418, NGC 40, and NGC 1535, measured by G. P. Kuiper with a low-dispersion spectrograph and kindly made available by him, average 0.1 mag. lower than the values listed by Berman and thus tend to confirm the adjustment adopted here. Values of T_e obtained by other methods and summarized by one of us[9] tend also to confirm the 20 per cent increase in T_e.

Conclusions to be drawn from the adjusted data in Table 2 are briefly these:

a) The adjusted values of r_0, the radius of the ionized region, are very nearly equal to R, the radius of the brighter part of the nebula. The significance of individual differences between R and r_0 is questionable; however, such differences are not caused by errors in D, which enters the derivation of both these quantities to the first power.

b) The trend of decreasing R_s (or increasing M_{SB}) with increasing T_e reflects systematic errors in Berman's derivation of D, in the course of which he undercorrects all values of m_n to reduce them to a single T_e. This systematic undercorrection is well illustrated by a plot of M_{SB} versus $1/T_e$ for thirty-eight nebulae appearing in Berman's list. These data are represented by $M_{SB} = 1.37 - 0.40/T_e$, with a mean-square deviation of only ± 0.2 mag. in M_{SB}. The distances given by Vorontsov-Velyaminov[10] are also subject to this systematic error, with $M_{SB} = 3.7 - 1.7/T_e$ and a much larger disperson.

Such systematic errors in distances, however, do not affect our conclusions; they do not change the necessity for adjusting the data of Table 1, since D enters both sides of equation (2) in the same way; they do not affect the equality of R and r_0, since both these quantities are proportional to D; and they affect N_e and S_γ to a minor extent.

c) Because of the adjustment of values of S_B and also the allowance made for space reddening and for V_c overlapping the Ba_c, the electron densities listed in Table 1 are about half the values previously accepted.[7] Using $N_i = N_e$ and assuming hydrogen to be the predominant constituent, we find the material density in the planetaries to be between 1.2×10^{-21} and 1.1×10^{-20} gm/cm^3.

Confirmation of the equality between r_0 and R can be obtained from the apparent diameters of nebulae for which detailed observations are lacking. The ratio of Balmer continuum to $H\delta$ has been measured in twenty-four other nebulae,[11] for seventeen of which the mean photographic surface brightness H, the apparent diameter d, and the magnitude of the nuclear star m_s are listed by Vorontsov-Velyaminov.[10] From equation (1) and the expressions for N_e and R_s we obtain an expression independent of the distance:

$$\log A = -\tfrac{1}{2}\log \tilde{a}_u - \frac{3420}{T_e} - \tfrac{3}{2}\log T_e - \tfrac{1}{2}\log T_e - \tfrac{1}{2}\log \frac{H_c}{H\delta} - 0.2\,m_s - 0.2\Delta m_B + 0.2H + \text{const.}\,, \tag{3}$$

where $A = d/2$ is the apparent radius in seconds of arc, T_e is the electron temperature, $H_c/H\delta$ is the ratio of Balmer continuous emission to $H\delta$ per angstrom,[11] and Δm_B is the bolometric correction for T_e. In the constant term we assume that the ratio of $H\delta$ to other emission lines is the same for each of these nebulae. To be consistent with Table 1,

[9] Page, *Ap. J.* (in press).

[10] *Gaseous Nebulae and Novae* (Moscow: Academy of Sciences, U.S.S.R., 1948); see also *A.J. Soviet Union*, **11**, 40, 1934, for an earlier listing, and *ibid.*, **27**, 285, 1950.

[11] Page, *Ap. J.*, **96**, 78, 1942.

we have used Berman's values of T_e and m_v, which in some cases differ from those listed by Vorontsov-Velyaminov. However, the latter's data yield essentially the same results. The data are listed in Table 2.

In Figure 1 we plot log A from equation (3) versus log d observed. The straight line represents the expected relation log A = log d − log 2, with the constant in equation (3) determined as +1.1 from seven of the nebulae of Table 1 (which are plotted as circled crosses). The smallest nebulae, IC 4846, 4997, 5112, and NGC 6790 and 6833, are all designated "stellar" and listed with $d \simeq 2''$, the minimum given by Vorontsov-Velyaminov. The largest is NGC 6720, with a mean apparent diameter of 71″. Combining the errors assigned in Table 1, we find an expected error in the calculated values of log A of ±0.28 due to errors in T_e, T_e, $H_c/H\delta$, m_v, and H. Since the scatter is only ±0.18 in log A

TABLE 2

DATA FOR TWENTY-FOUR PLANETARY NEBULAE

NGC	FORM AND EXCIT.*	T_e† (°K)	T_e (°K)	m_v (MAG.)	d	H (MAG.)	log $H_c/H\delta$	N_e	CALC. LOG A	OBS. LOG d	R (A.U.)	D (PSC)
40...	Ring 1	35,000	6000	11.4	37*	9.1	−2.21	750‡	+1.24	1.57	45,000	1220
II 1747...	Ring 7	30,000	(7000)	14.9	13	9.8	(−2.0)	430	+0.91	1.11	55,500	4270
I 351...	Disk 5	40,000	8100	14.8	7	7.7	(−1.9)	2600	+0.68	0.85	38,500	5500
II 2003...	8	70,000	(8000)	(18.4)	5	7.2	(−2.0)	2100	+0.28	0.70	30,000	(6000)
6210...	Disk 3	30,000	7100	11.7	8	6.8	−1.78	4400	+0.84	0.90	14,000	1720
6543...	Ring 5	35,000	6500	11.2	19	6.3	−1.78	3600‡	+1.03	1.28	20,000	1080
6572...	Disk 2	45,000	9000	12	14	6.5	(−1.93)	4400‡	+0.87	1.15	17,000	1230
6720...	Ring 8p	70,000	7000	14.4	71	9.6	−2.02	410	+1.56	1.85	120,000	1640
6741...	6	80,000	6500	17.5	8	7.4	(−2.1)	1400	+0.69	0.90	31,000	3910
II 4846...	4	50,000	12,600	16.5	(2)	(5.3)	−1.9	12,000	−0.10	(0.30)	13,000	6610
6790...	4	80,000	8300	17.3	(2)	(4.2)	−1.75	22,000	−0.19	(0.30)	9300	4650
6807...	4	65,000	8300	18.8	2	6.4	−1.9	3400	−0.06	0.30	25,000	12,600
6818...	Ring 8	70,000	7000	15.0	18	7.3	−2.06	1400	+1.05	1.26	43,000	2380
6826...	3	30,000	8200	10.7	25	6.9	−1.82	1800‡	+1.08	1.40	26,000	1050
6833...	4	40,000	9000	16.5	(2)	(6.4)	−1.70	5900	−0.05	(0.30)	19,000	9680
6884...	Disk 6	95,000	7400	19	7.5	8.1	−1.9	1100	+0.52	0.88	52,000	6890
6879...	4	30,000	7400	(15.2)	5	6.7	(−1.7)	3200	+0.07	0.70	36,000	7180
6886...	Disk 7p	80,000	8200	18.1	7.5	7.2	−2.0	1600	+0.42	0.88	54,000	7240
II 4997...	4	30,000	27,000	11.7	(2)	(4.0)	−1.83	71,000	−0.03	(0.30)	4700	2340
7009...	Ring 6	50,000	8900	11.9	28	5.6	−1.86	6800‡	+0.94	1.45	20,000	930
7027...	7	80,000	9600	15.6	14	7.3	−2.61	1350	+1.21	1.15	30,000	2130
II 5117...	5	50,000	8200	17.1	(2)	5.9	(−1.4)	11,500	−0.24	0.30	14,000	7010
II 5217...	Disk 5	50,000	8200	15	6.8	7.9	−2.08	1700	+0.92	0.83	21,000	3060
7662...	Ring 7	55,000	9900	12.7	15	5.9	−2.17	5000‡	+1.03	1.18	18,000	1200

* Page, *Ap. J.*, **96**, 78, 1942.

† The values of T_e have not been adjusted as in Table 1.

‡ Values of N_e from Table 1; the remainder were calculated relative to these.

and not appreciably skew, we conclude that $r_0 = R$, from the smallest to the largest planetaries observed spectrophotometrically.

Among the consequences of this conclusion, which can now be stated with some certainty, are these:

a) The masses of the planetary nebulae are almost certainly larger than the sun's mass, possibly by a large factor, since the nebular material extends beyond the bright observable region. In fact, a density of 10^{-20} gm/cm^3, radius of 2×10^{17} cm, and expansion[4] of 20 km/sec would result in 10^{-4} ⊙ per year being ejected through the luminous edge to nonluminous obscurity. The masses of the bright parts are of the order of 0.1 ⊙; but, if the nebulae have existed as at present for 10^6 years or more, they must be surrounded by nonluminous masses of 10 ⊙ or more. This suggests that the planetary nebulae must be transitory.

b) Classification of the spectra of the planetary nebulae requires at least a two-dimensional array,[11] indicating that at least two parameters are involved, one of which is certainly T_e. Wurm[3] has suggested that the opacity of the nebulae in the Lyman continuum

may be the second parameter; but our conclusion, $R = r_0$, shows that this opacity is effectively infinite in all cases examined. It seems far more likely that the second parameter is $N \simeq N_e$, the mean density in the bright part of the nebula. Thus the classification of nebular spectra is probably analogous to the classification of stellar spectra, the objects of excitation "8 pec" (showing both the high-excitation feature λ 4686 of *He* II and the low-excitation feature λ 3727 of [*O* II]) being those of low N_e, such as NGC 6720.

c) Although the turbulent state of the nebular material is well attested by the variety of shapes and the delicate filaments photographed in these objects, a satisfactory explanation of their crude forms (rings versus disks) is still lacking. It has been suggested[4] that ring forms might result in a spherically symmetrical nebula if the ejection from the nucleus were cut off. Aside from the fact that the resulting void near the nucleus is observed to be filled with higher-excitation lines in many ring nebulae, this assumption

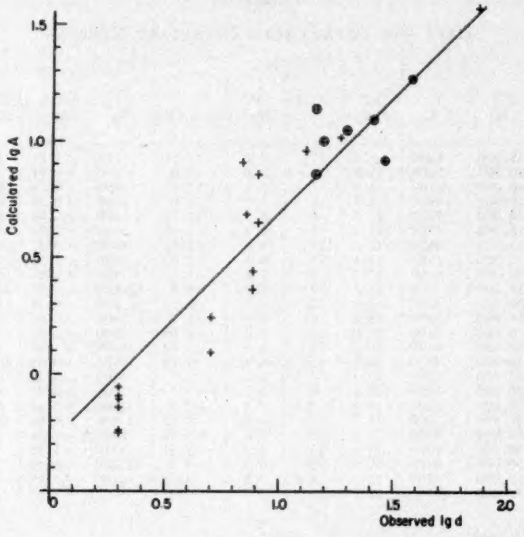

FIG. 1.—Relative dimensions of planetary nebulae and *H* II regions

would lead to rapid increase in dimensions of the visible nebula with time; in 20,000 years the *H* II region would expand to $r_0 = 3$ psc, owing to the 100-fold decrease in N as expansion progresses without ejection.

There is no good evidence that the form is influenced by T_e, by M_{SB}, by R, by N_e, or by the excitation;[12] in Table 2 there are seven definite rings and six definite disks or "amorphous types," with the values of these parameters summarized in Table 3.

Although the data are far from exact and the nebulae listed may not be a fair sample, there is almost complete overlapping of the values of T_e, M_{SB}, R, N_e, and the excitation between the two forms; it seems safe to say that the same values of these parameters occur in both rings and disks. Since $R = r_0$ for both types, the Lyman opacity is effectively infinite for both types.

It is readily shown[13] that if the ring nebulae are spherically symmetric, the luminosity in the emission lines at $R - \Delta R$ from the nucleus must drop to a value less than 10^{-1} of

[12] Contrary to a statement by Wilson, *op. cit.*, p. 297.

[13] Page, unpublished, based on microphotometer tracings across wide-slit spectra.

its maximum value. ΔR is the thickness of the ring. For hydrogen this would be the case if T_e increased from the value near 10,000° K observed in the luminous ring to over 50,000° K inside the ring.[14] If *O* II, *O* III, *N* II, *Ne* III, and other ions which cool the electron gas by the emission of forbidden lines were not present, such a high value of T_e might be expected. However, this explanation of ring forms would imply high T_e and/or high L_{SB} in ring nebulae, in contradiction to Table 3.

It has also been suggested, by Curtis[15] and more recently by Minkowski,[5] that the planetary nebulae are not spherically symmetric, even in the gross, and that apparent ring forms are actual rings in space, or other forms of revolution. This would imply that N, and probably the velocity of expansion as well, are symmetrical about an axis rather than about a point (the central star). The physical meaning of such an axis might be connected with rotation of, or magnetic fields in, the central star. The rotation, at least, should be studied further.

TABLE 3

COMPARISON BETWEEN RING AND DISK NEBULAE

	7 Rings	6 Disks
T_e	30,000°–70,000° K; mean, 49,000° K	30,000°–95,000° K; mean, 49,000° K
M_{SB}	−1.8 to −3.1 mag.; mean, −2.3 mag.	−1.6 to −2.5 mag.; mean, −2.2 mag.
R	18,000–55,000* A.U.; mean,* 35,000 A.U.	14,000–54,000 A.U.; mean, 33,000 A.U.
N_e	410–6800 cm^{-3}; mean, 2600 cm^{-3}	1100–4400 cm^{-3}; mean, 3100 cm^{-3}
Excit.†	1–8	2–7

* Omitting NGC 6720, R = 120,000 A.U.

† Page, *Ap. J.*, **96**, 78, 1942.

Even if the forms are nonspherical, our conclusion that $R = r_0$ would still be valid, since the ratio between maximum and minimum apparent diameters is not large and the correction for foreshortening would be small compared with errors in the data. If N were low over the two polar caps, owing possibly to higher velocities of the nebular material in those directions, the *H* II region would extend farther in those directions, also, and with lower surface brightness. Such a model would explain many of the faint outer loops of these nebulae.

In following papers[8,9] the data listed above will be utilized to calculate H^- emission and opacity in the planetary nebulae, and our conclusion that $R = r_0$ will be examined in connection with various determinations of T_e.

[14] G. C. Cillié, *M.N.*, **92**, 820, 1932.

[15] *Pub. Lick Obs.*, **13**, 57, 1918.

NEGATIVE HYDROGEN IONS IN PLANETARY NEBULAE

JESSE L. GREENSTEIN AND THORNTON PAGE
Mount Wilson and Palomar Observatories
Carnegie Institution of Washington
California Institute of Technology
and
Yerkes Observatory

Received February 12, 1951

ABSTRACT

Continuous emission has been observed in the spectra of planetary nebulae which is apparently not due to hydrogen recombination. The transition zone between ionized and neutral hydrogen is a favorable region for the existence of H^-. The computed concentration of H^- relative to H is higher in planetary nebulae than in the sun. However, the capture continuum of H^- is too weak to account for the observed continuous spectrum of planetary nebulae. The bright regions of the nebulae are found to be transparent in H^-.

The so-called "visual continuum," V_c, which is prominent in slitless and wide-slit spectra of the planetary nebulae, was first measured[1] quantitatively in the spectra of NGC 7662, 7027, and 6572 and later[2] in the spectra of twenty-six other planetary nebulae.

The intensity of the V_c per angstrom unit is roughly constant between λ 5000 and λ 3900 and is about 0.01 that of the $H\delta$ emission line. The V_c cannot be due to captures on the third level of the hydrogen atom (below the Paschen limit at λ 8206) or to free-free transitions of hydrogen, both of which would decrease rapidly with λ and would together produce less than 5 per cent of the observed continuum near λ 3900. Swings and Struve[3] believe that faint, unresolved emission lines could not account for the V_c. The possibility that it results from scattering of nuclear starlight by dust in the nebulae has also been eliminated.[4]

At the edge of the region where hydrogen is ionized in a planetary nebula there should be a region where N_H, the number of hydrogen atoms per cubic centimeter, and N_e, the number of electrons per cubic centimeter, are both large enough to produce a significant concentration of the negative hydrogen ion, H^-. We therefore calculate the emission at frequency ν, $I_\nu d\nu$, in erg/cm³ sec, resulting from

$$H + e \rightarrow H^- + h\nu\,, \tag{1}$$

by means of the relation between capture probability $F(v)$ and continuous absorption coefficient, k_ν. The details of the method are given by E. A. Milne.[5] In the case of H^- the statistical-weight factor is $\frac{1}{4}$, and

$$F(v) = \frac{\pi (h\nu)^2 k_\nu}{(2\pi m c)^2 v^2}\,. \tag{2}$$

[1] T. L. Page, *M.N.*, **96**, 604, 1936. The electron temperatures derived in this paper were later revised upward to about 10,000° K.

[2] T. L. Page, *Ap. J.*, **96**, 78, 1942.

[3] *Ap. J.*, **96**, 310, 1942.

[4] H. Zanstra, *Observatory*, **59**, 314, 1936.

[5] *Phil. Mag.*, **47**, 209, 1924.

The bound-free absorption coefficient, k_ν, is given by S. Chandrasekhar;[6] the emission arising from free-free transitions of H^- computed from the matrix elements given by Chandrasekhar and Breen,[7] proves to be negligible.

The H^- emission in erg/cm³ sec can be computed from the above equation when N_e and N_H are known. If N is the total number of protons and neutral hydrogen atoms per cubic centimeter and if the electrons come dominantly from hydrogen, then $N_e = xN$, $N_H = (1 - x)N$, and

$$I_\lambda d\lambda = 10^{-19.82} k_\nu T_e^{-3/2} \lambda^{-5} \exp\left\{-\frac{1.439}{T_e}\left(\frac{1}{\lambda}-\frac{1}{\lambda_0}\right)\right\} N^2 x(1-x)\, d\lambda\,, \qquad (3)$$
$$= A(\lambda, T_e)\, N^2 x(1-x)\, d\lambda\,.$$

The dissociation limit of H^- is at λ_0. Values of $A(\lambda, T_e)$ are given in Table 1, for bound-free transitions only.

TABLE 1

$\log_{10} A(\lambda, T_e)$

λ	1000° K	5000° K	10,000° K	20,000° K
3000	−35.3	−22.86	−21.62	−21.23
4000	−30.65	−22.30	−21.58	−21.44
5000	−27.92	−22.07	−21.65	−21.66
6000	−26.20	−21.92	−21.77	−21.89
7000	−24.98	−21.97	−21.92	−22.11

In the brighter parts of planetary nebulae, T_e has been found to be near 10,000° K; at this value, $A(\lambda, T_e)$, which measures the predicted intensity distribution, is almost independent of λ. The constancy of I_λ is an outstanding characteristic of the observed visual continuum.

The flux of the H^- continuum, $S_V(H^-)d\lambda$ in erg/cm² sec, can be readily calculated if we neglect absorption in the nebula, an approximation which will be justified below. Then, in a homogeneous nebula,

$$4\pi R^2 S_V(H^-)\, d\lambda = 4\pi d\lambda \int_0^R I_\lambda(r)\, r^2 dr\,, \qquad (4)$$

where r is the distance from the nucleus and R the radius of the nebula; the nebula is assumed to be spherically symmetrical. In another paper in this issue of the *Journal* we have shown[8] that the apparent radius of the nebula R is equal to r_0, the radius of the H II region around the nuclear star, as determined by Strömgren. The largest contribution to the integral in equation (4) occurs where hydrogen is about half-ionized, in a thin layer near $r = r_0$. We therefore neglect any change of N and T_e with r, set $r/R = 1$, retain the variation of $x(1 - x)$ with r, and obtain

$$S_V(H^-)\, d\lambda \approx A(\lambda, T_e)\, N^2 d\lambda \int_0^\infty x(1-x)\, dr\,. \qquad (5)$$

The run of the ionization x with r has been determined by B. Strömgren;[9] he gives one approximation for x when $r \approx r_0$ and another when $1 - x \ll 1$. Figure 1 shows the com-

[6] *Ap. J.*, **102**, 395, 1945.

[7] *Ap. J.*, **104**, 430, 1946.

[8] Page and Greenstein, *Ap. J.*, **114**, 98, 1951.

[9] *Ap. J.*, **89**, 531, 1939.

puted variation of x and of $x(1-x)$ near r_0 in a nebula for which $N = 5000$ cm^{-3}. The integral in equation (5) has been evaluated numerically as

$$\int_0^\infty x(1-x)\,dr = \frac{1.43 \times 10^{18}}{N}; \tag{6}$$

hence, finally, we obtain

$$S_\nu(H^-)\,d\lambda = 1.43 \times 10^{18} A(\lambda, T_e)\,N d\lambda\,. \tag{7}$$

The size of the H II region is given by

$$r_0 = f(T_S) R_S^{2/3} N^{-2/3}\,, \tag{8}$$

where R_S and T_S are the radius and temperature of the nuclear star in solar units and degrees Kelvin; $f(T_S)$ is 4.2 parsecs for $T_S = 20{,}000°$, 29 parsecs for $T_S = 50{,}000°$, and 54 parsecs for $T_S = 79{,}000°$. A more exact computation shows that the constant in

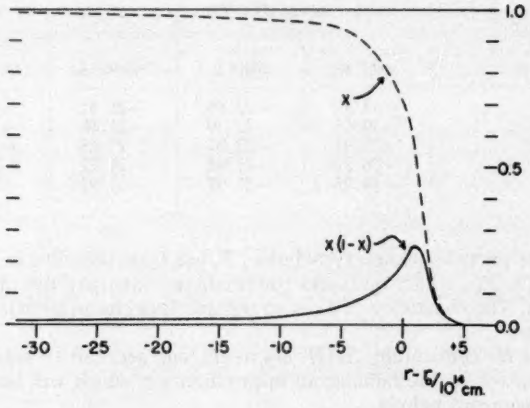

FIG. 1.—The ionization, x, and the measure of H^- emission, $x(1-x)$, near the edge of a planetary nebula. The distance, $r - r_0$, from the boundary of the Strömgren sphere is given in units of 10^{14} cm.

equation (6) varies slowly with r_0, from 1.23×10^{18} to 1.45×10^{18} for the nine nebulae we have considered in detail.[8] Although the concentration of H^- is highest at r_0, over 30 per cent of the integral in equation (6) comes from regions where hydrogen is more than 99 per cent ionized.

With these data on $x(1-x)$ it is possible to compute the concentration of, and absorption by, H^- in the nebulae. The maximum concentration of H^-, $x(1-x) = 0.25$, occurs near $r - r_0 = 5 \times 10^{17}/N$ cm. The dissociative equilibrium for H^- is not affected by the exhaustion of far-ultraviolet radiation and can be obtained approximately from

$$\frac{N_{H^-}}{N_H N_e} = \frac{h^3}{(2\pi m k T_S)^{3/2}} \frac{g_{H^-}}{g_H g_e} \frac{e^{hc/kT\lambda_0}}{W}\,, \tag{9}$$

where the dilution $W = R_S^2/4r^2$. We have neglected the difference between T_S and T_e. The values of N_{H^-} range from 10^{-3} to 1.5×10^{-2} cm^{-3}. The maximum relative concentration N_{H^-}/N_H lies between 2×10^{-7} and 3×10^{-6}, which is between ten and one hundred times larger than in the solar atmosphere. The great dilution of radiation favors the appearance of H^- at the boundary of a Strömgren H II sphere.

If we combine equations (6) and (9), we obtain n_{H^-}, the total abundance of H^- in a square centimeter column from $r = 0$ to $r = \infty$. The optical thickness is then obtained from

$$\tau_\nu = k_\nu n_{H^-} = k_\nu \int_0^\infty N(H^-)\, dr = 10^{-18.91} k_\nu r_0^2 N 10^{3770/T_S} T_S^{-3/2} R_S^{-2}. \quad (10)$$

In equation (10), R_S is in solar units and r_0 in centimeters. The values of n_{H^-} obtained range up to 10^{13} cm^{-2} (NGC 7662). Since the absorption cross-section per H^- ion is about 3×10^{-17} cm^2, $\tau_\nu(H^-)$ in the nebulae can be computed. It never exceeds 10^{-4} and can be neglected.

A comparison of columns 14 and 15 in Table 1 of our first paper[8] shows that H^- fails to account for the visual continuum. The ratio of the predicted $S_V(H^-)$ to the observed V_c ranges from 6×10^{-4} to 2×10^{-6}. Although several simplifying assumptions have been made in the above analysis, it is unlikely that physical conditions can be so extreme as to increase $S_V(H^-)$ by a factor of 10^4. For instance, density fluctuations of the type observed as filaments in high-resolution photographs can conceivably increase the number of "edges" of ionized regions through which we look, near the projected edge of a planetary nebula. From this we would expect the H^- continuum to be enhanced near the edge of each nebula, and it is, in fact, true that the observed[1] V_c has less central condensation than the Balmer continuum. But the recombination continuum, Ba_c, is proportional to N^2x^2 and the H^- continuum to $N^2x(1-x)$. The region where the H^- continuum is favored relative to the Ba_c is thus extremely limited (see Fig. 1). Unless density fluctuations, which are nearly opaque in the Lyman region, prove to be very common, such ionization edges could not increase the H^- continuum to near-equality with the Ba_c.

Another approximation is involved in taking $N_e = N_i = xN$, which is true only for a nebula of pure hydrogen. An admixture of 0.2 per cent of other ions, such as C II, is possible and could provide electrons outside r_0, where $N_H = N$. If these other ions provide one electron apiece, then $N_eN_H = 0.002N^2$ from $r = r_0$ to, say, $r = 2r_0$. Let us add the surface brightness S_V' of this large outer shell to that previously found from equation (5). Taking T_e, as an upper limit, to be the same as for $r < r_0$, the additional contribution is

$$S_V' d\lambda = \frac{d\lambda}{4r_0^2} \int_{r_0}^{2r_0} A(\lambda, T_e)\, 0.002 N^2 r^2 dr. \quad (11)$$

Since $Nr_0 \approx 10^{21}$, we find that $S_V' d\lambda \approx 1.2 \times 10^{18} A(\lambda, T_e) N d\lambda$. Comparing S_V' with $S_V(H^-)$ in equation (7), we see that the H^- emission can be increased in this manner only by a factor of 2. Outside r_0 it is very probable that T_e will decrease; when $r \gg r_0$, T_e will be low, as it is in the H I regions of interstellar space. An outer cool envelope maintained at a reasonably high density by continuous ejection of material from the nebula[10] would have no detectable emission by H^-.

This investigation was undertaken while one of the authors (Page) was on a visit to the Mount Wilson Observatory, on a contract with the Office of Naval Research. We wish to express our gratitude to Dr. S. Chandrasekhar for his interest and advice.

[10] O. C. Wilson, *Ap. J.*, 111, 279, 1950.

THE THEORY OF THE FLUCTUATIONS IN BRIGHTNESS OF THE MILKY WAY. III

S. CHANDRASEKHAR AND G. MÜNCH
Yerkes Observatory
Received January 23, 1951

ABSTRACT

In this paper the integral equation (derived in Paper I) governing the fluctuations in brightness of the Milky Way is explicitly solved for the case in which the system extends to a finite distance in the direction of the line of sight and when all the clouds are equally transparent. The derived theoretical distributions are illustrated.

1. *Introduction.*—In the two earlier papers[1] of this series we pointed out that the theory of the fluctuations in brightness of the Milky Way leads one to consider the probability distribution of the quantity

$$u = \int_0^{\xi} \prod_{i=1}^{i=n(r)} q_i \, dr \,, \tag{1}$$

where $q_i \leqslant 1$ is a chance variable occurring with a known frequency $\psi(q)$ and the number of factors—"clouds"—$n(r)$ is also a chance variable governed by the Poisson distribution

$$\frac{e^{-r}}{n!} r^n \qquad (n = 0, 1, \ldots) \,. \tag{2}$$

Further, in equation (1), ξ is some fixed positive constant. If $f(u, \xi)$ denotes the probability that u exceeds the specified value, then, as we have shown in Paper I, $f(u, \xi)$ as a function of the two variables u and ξ satisfies the partial integrodifferential equation

$$f + \frac{\partial f}{\partial u} + \frac{\partial f}{\partial \xi} = \int_0^1 f\left(\frac{u}{q'}, \xi\right) \psi(q') \, dq' \,. \tag{3}$$

From the definition of u as an integral over a quantity which must always be less than 1, it follows that u can never exceed the value ξ. But it can take the value ξ itself with *exactly* the probability $e^{-\xi}$ (cf. the remarks in Paper I following eq. [18]). The conditions on f resulting from this fact are

$$f(u, \xi) = 0 \qquad (u > \xi)$$

and

$$\lim_{u \to \xi - 0} f(u, \xi) = e^{-\xi} \,. \tag{4}$$

Equation (3) should therefore be strictly written in the form

$$f + \frac{\partial f}{\partial u} + \frac{\partial f}{\partial \xi} = \int_{u/\xi}^1 f\left(\frac{u}{q'}, \xi\right) \psi(q') \, dq' \,. \tag{5}$$

Further, the definition of f as a probability distribution requires that

$$f(0, \xi) \equiv 1 \,. \tag{6}$$

This is the normalization condition.

[1] *Ap. J.*, **112**, 380 and 393, 1950. These papers will be referred to as "Paper I" and "Paper II," respectively.

If, as in Paper I, $g(u, \xi)$ describes the frequency distribution of u, then, in accordance with conditions (4), we should define

$$f(u,\xi) = \int_u^\xi g(u,\xi)\, du. \tag{7}$$

The discontinuity of f at $u = \xi$ now implies that $g(u, \xi)$ has at this point a singularity of the nature of a δ-function (with "amplitude" $e^{-\xi}$).

The solution of equation (5) with boundary conditions (4) and (6) presents a problem of considerable mathematical interest. In this paper we shall show how the complete distribution of u can be obtained for the case when all the clouds are equally transparent, i.e., when

$$\psi(q') = \delta(q - q') \qquad (q = \text{constant} < 1). \tag{8}$$

In this case the equation governing f reduces to

$$f + \frac{\partial f}{\partial u} + \frac{\partial f}{\partial \xi} = f\left(\frac{u}{q}, \xi\right). \tag{9}$$

2. *Preliminary remarks on the structure of equation* (9).—Since u/q exceeds ξ when $q\xi < u \leqslant \xi$ and $f = 0$ for $u > \xi$, we conclude from equation (9) that

$$f + \frac{\partial f}{\partial u} + \frac{\partial f}{\partial \xi} = 0 \qquad (q\xi < u \leqslant \xi). \tag{10}$$

The general solution of this equation is

$$f(u,\xi) = e^{-\xi}\phi(\xi - u), \tag{11}$$

where ϕ is an arbitrary function of the argument. If ϕ can be specified in some way, then the solution can be continued into the region $q^2\xi < u \leqslant q\xi$; for the left-hand side of equation (9) in the domain $q^2\xi < u \leqslant q\xi$ depends only on f in the domain $q\xi < u \leqslant \xi$. And if the solution can be extended to the domain $q^2\xi < u \leqslant q\xi$, then it can also be extended to the next domain $q^3\xi < u \leqslant q^2\xi$, and so on. It thus appears that we must consider equation (9), successively, in the domains

$$q^n\xi < u \leqslant q^{n-1}\xi \qquad (n = 1, 2, \ldots). \tag{12}$$

The completion of the solution of equation (9) in the manner we have indicated requires that we know the solution in the first of the domains (12), namely,

$$q\xi < u \leqslant \xi. \tag{13}$$

And, to obtain the solution in this first domain, we must go back to the original definitions and appeal to the problem which gave rise to equation (9).

A further consequence which may be derived directly from equation (9) may be noted here. Since $f(0, \xi) \equiv 1$ for all ξ, it follows, successively, that all the derivatives of f with respect to u must vanish at $u = 0$:

$$\left(\frac{\partial^n f}{\partial u^n}\right) \equiv 0 \quad \text{for} \quad u = 0 \quad \text{and} \quad n = 1, 2, \ldots. \tag{14}$$

3. *The determination of $f(u, \xi)$ and $g(u, \xi)$ in the domain $q\xi < u \leqslant \xi$ and the enumeration of all their discontinuities.*—We inferred that $f(u, \xi) \to e^{-\xi}$ as $u \to \xi - 0$ and that $f(u, \xi) = 0$ for $u > \xi$ by appealing to the physical problem, in particular, to the fact that the probability that no cloud occurs in the interval $(0, \xi)$, is $e^{-\xi}$. The question now arises

whether further information concerning $f(u, \xi)$ cannot be similarly obtained by considering situations in which one or more specified numbers of clouds occur in the interval $(0, \xi)$. Actually, we shall see that this provides the key to the entire problem. Let

$$f_n(u, \xi) \quad \text{and} \quad g_n(u, \xi) \qquad (n = 0, 1, \ldots) \tag{15}$$

govern the absolute probability distribution of u when it is known that there are n clouds in the interval $(0, \xi)$ (but it is not known *where* they occur in the interval). More precisely, for every $n = 0, 1, 2, \ldots$, $f_n(u, \xi)$ represents the probability that there will be exactly n clouds in the interval $(0, \xi)$ and that the random variable u will exceed the preassigned quantity u. Further, let $g_n(u, \xi)$ represent the probability density of u, i.e., the derivative of $f_n(u, \xi)$ with respect to u at such points where this derivative exists. The results concerning f and g obtained from the consideration of the case when there are no clouds in $(0, \xi)$ can now be expressed in the form

$$f_0(u, \xi) = e^{-\xi} \quad \text{and} \quad g_0(u, \xi) = e^{-\xi}\delta(\xi - u). \tag{16}$$

With f_n and g_n defined in the foregoing manner, we can write

$$f(u, \xi) = \sum_{n=0}^{\infty} f_n(u, \xi) \quad \text{and} \quad g(u, \xi) = \sum_{n=0}^{\infty} g_n(u, \xi). \tag{17}$$

Now the probability that there are n clouds somewhere in the interval $(0, \xi)$ is $e^{-\xi}\xi^n/n!$. Therefore, the probability that there are n clouds in this interval and that they occur between $(\xi_1, \xi_1 + d\xi_1)$, $(\xi_2, \xi_2 + d\xi_2)$, . . . , and $(\xi_n, \xi_n + d\xi_n)$, where

$$0 \leqslant \xi_1 \leqslant \xi_2 \leqslant \xi_3 \ldots \leqslant \xi_{n-1} \leqslant \xi_n \leqslant \xi\,, \tag{18}$$

is

$$e^{-\xi} d\xi_1 d\xi_2 \ldots d\xi_n\,. \tag{19}$$

The inequalities (18) define a simplex[2] in the n-dimensional Euclidean space $(\xi_1, \xi_2, \ldots, \xi_n)$, whose vertices are at

$$\begin{gathered}(\xi, \xi, \ldots, \xi, \xi), (0, \xi, \ldots, \xi, \xi), \ldots, (0, 0, \ldots, 0, \xi, \xi), \\ (0, 0, \ldots, 0, \xi), \quad \text{and} \quad (0, 0, \ldots, 0, 0).\end{gathered} \tag{20}$$

We shall call this the "fundamental simplex." Its volume is $\xi^n/n!$.

Since the total probability of occurrence of n clouds in the interval $(0, \xi)$ is $e^{-\xi}\xi^n/n!$, it follows that in the $(\xi_1, \xi_2, \ldots, \xi_n)$-space we have a uniform distribution of a priori probability in the fundamental simplex with weight $e^{-\xi}$. This is, of course, in accordance with (19).

The value of u which would result from a distribution of n clouds specified by inequality (18), is

$$u = \xi_1 + q(\xi_2 - \xi_1) + q^2(\xi_3 - \xi_2) + \ldots + q^{n-1}(\xi_n - \xi_{n-1}) + q^n(\xi - \xi_n). \tag{21}$$

According to this equation, the smallest value which u can take, when it is known that there are n clouds in the interval $(0, \xi)$, is $q^n\xi$; this happens when $\xi_1 = \xi_2 = \ldots = \xi_n = 0$. And the largest value which u can take is ξ; this happens when $\xi_1 = \xi_2 = \ldots = \xi_n = \xi$. It therefore follows that $f_n(u, \xi)$ is defined only in the domain $q^n\xi \leqslant u \leqslant \xi$ and that

$$\begin{aligned} f_n(u, \xi) &= 0 \quad \text{for} \quad u > \xi \\ &= e^{-\xi}\xi^n/n! \quad \text{for} \quad u \leqslant q^n\xi\,. \end{aligned} \tag{22}$$

Since the total probability that n clouds occur in the interval $(0, \xi)$ is $e^{-\xi}\xi^n/n!$, we must also have

$$\int_{q^n\xi}^{\xi} g_n(u, \xi)\, du = \frac{e^{-\xi}}{n!}\xi^n. \tag{23}$$

[2] A simplex is the n-dimensional analogue of the three-dimensional tetrahedron.

From our earlier remark concerning the distribution of a priori probability in the $(\xi_1, \xi_2, \ldots, \xi_n)$-space, it follows that *the probability that u exceeds a specified value, when it is known that n clouds occur in the interval $(0, \xi)$ is $e^{-\xi}$ times the volume of the space in which inequalities* (18) *and the further inequality,*

$$\xi_1 + q(\xi_2 - \xi_1) + q^2(\xi_3 - \xi_2) + \ldots + q^n(\xi - \xi_n) \geqslant u\,, \tag{24}$$

are simultaneously satisfied.

Now the shape of the solid into which the fundamental simplex is truncated by hyperplane (21) depends on the specified value of u. In fact, we must distinguish the n cases

$$q^l\xi < u \leqslant q^{l-1}\xi \qquad (l = 1, \ldots, n)\,. \tag{25}$$

Except in the two cases

$$q\xi < u \leqslant \xi \tag{26}$$

and

$$q^n\xi < u \leqslant q^{n-1}\xi\,, \tag{27}$$

it is not simple to evaluate the volume of the truncated solid. But in the two cases (26) and (27), one of the two solids into which the hyperplane (21) cuts the fundamental simplex is again a simplex. Hence in these two cases the volume of the required solid may be found simply.

Considering, first, case (26), we observe that the volume delimited by inequalities (18) and (24) is a simplex, the co-ordinates of whose vertices are given by

$$\xi_1 = \xi_2 = \ldots = \xi_l\,, \qquad \xi_{l+1} = \xi_{l+2} = \ldots = \xi_n = \xi \qquad (l = 1, \ldots, n) \tag{28}$$

and

$$\xi_1 = \xi_2 = \xi_3 = \ldots = \xi_n = \xi \tag{29}$$

Using equation (21), we readily find that the n vertices defined by equations (28) have the co-ordinates

$$\xi_1 = \xi_2 = \ldots = \xi_l = \frac{u - q^l\xi}{1 - q^l}\,, \qquad \xi_{l+1} = \xi_{l+2} = \ldots = \xi_n = \xi\,. \tag{30}$$

The volume of the simplex whose vertices are given by equations (29) and (30) is[3]

$$\frac{1}{n!}\begin{vmatrix} 1 & 1 & \ldots & 1 & 1 & 1 \\ \dfrac{u-q^n\xi}{1-q^n} & \xi & \ldots & \xi & \xi & \xi \\ \dfrac{u-q^n\xi}{1-q^n} & \dfrac{u-q^{n-1}\xi}{1-q^{n-1}} & \ldots & \xi & \xi & \xi \\ \cdot & \cdot & \ldots & \cdot & \cdot & \cdot \\ \dfrac{u-q^n\xi}{1-q^n} & \dfrac{u-q^{n-1}\xi}{1-q^{n-1}} & \ldots & \dfrac{u-q^2\xi}{1-q^2} & \xi & \xi \\ \dfrac{u-q^n\xi}{1-q^n} & \dfrac{u-q^{n-1}\xi}{1-q^{n-1}} & \ldots & \dfrac{u-q^2\xi}{1-q^2} & \dfrac{u-q\xi}{1-q} & \xi \end{vmatrix} \tag{31}$$

[3] Cf. D. M. Y. Sommerville, *Geometry of n Dimensions* (London: Methuen, 1929), p. 124.

By subtracting from each column of this determinant the column immediately preceding it, we can make all the elements above the principal diagonal zero and leave along the principal diagonal the elements

$$1\,,\ \frac{\xi-u}{1-q^n}\,,\qquad \frac{\xi-u}{1-q^{n-1}}\,,\ \ldots\,,\ \frac{\xi-u}{1-q^2}\,,\qquad \text{and}\qquad \frac{\xi-u}{1-q}\,. \tag{32}$$

The volume of the simplex is, therefore,

$$\frac{1}{n!}\,\frac{(\xi-u)^n}{\prod_{j=1}^{n}(1-q^j)}\,. \tag{33}$$

The probability that u exceeds a specified value in the interval $q\xi \leqslant u \leqslant \xi$ when it is known that there are n clouds in $(0, \xi)$ is therefore given by

$$f_n(u, \xi) = \frac{e^{-\xi}}{n!}\,\frac{(\xi-u)^n}{\prod_{j=1}^{n}(1-q^j)} \qquad (q\xi \leqslant u \leqslant \xi;\quad n = 1, 2, \ldots). \tag{34}$$

The corresponding expression for $g_n(u, \xi)$ is

$$g_n(u, \xi) = \frac{e^{-\xi}}{(n-1)!}\,\frac{(\xi-u)^{n-1}}{\prod_{j=1}^{n}(1-q^j)} \qquad (q\xi < u < \xi;\quad n = 1, 2, \ldots); \tag{35}$$

in particular,

$$g_1(u, \xi) = \frac{e^{-\xi}}{1-q} \qquad (q\xi < u < \xi) \tag{36}$$[4]

and

$$g_2(u, \xi) = \frac{e^{-\xi}(\xi-u)}{(1-q)\,(1-q^2)} \qquad (q\xi < u \leqslant \xi)\,. \tag{37}$$

Considering, next, case (27), we observe that now the solid cut *off* from the fundamental simplex is a simplex. The co-ordinates of its $(n+1)$ vertices are given by

$$\xi_1 = \xi_2 = \ldots = \xi_l = 0 \quad \text{and} \quad \xi_{l+1} = \xi_{l+2} = \ldots = \xi_n \quad (l = 0, 1\,, \ldots, n-1) \tag{38}$$

and

$$(0, 0, \ldots, 0, 0)\,. \tag{39}$$

From equations (21) and (38) we readily find that the co-ordinates of the n vertices defined by equations (38) are

$$\xi_1 = \xi_2 = \ldots = \xi_l = 0 \quad \text{and} \quad \xi_{l+1} = \xi_{l+2} = \ldots = \xi_n = \frac{u - q^n\xi}{q^l\,(1-q^{n-l})} \qquad (l = 0, \ldots, n-1)\,. \tag{40}$$

[4] Actually, in this case, $g_1(u, \xi) = 0$ for $u < q\xi$.

The volume of this simplex is clearly

$$\frac{1}{n!}\frac{(u-q^n\xi)^n}{\prod_{l=0}^{n-1} q^l(1-q^{n-l})} = \frac{(u-q^n\xi)^n}{n!\,q^{n(n-1)/2}\prod_{j=1}^{n}(1-q^j)}. \tag{41}$$

The probability that u exceeds a specified value in the interval $q^n\xi \leqslant u \leqslant q^{n-1}\xi$ is therefore given by

$$f_n(u,\xi) = \frac{e^{-\xi}}{n!}\left[\xi^n - \frac{(u-q^n\xi)^n}{q^{n(n-1)/2}\prod_{j=1}^{n}(1-q^j)}\right] \qquad (q^n\xi \leqslant u \leqslant q^{n-1}\xi;\ \ n=1,\ldots). \tag{42}$$

The corresponding expression for $g_n(u,\xi)$ is

$$g_n(u,\xi) = \frac{e^{-\xi}}{(n-1)!}\frac{(u-q^n\xi)^{n-1}}{q^{n(n-1)/2}\prod_{j=1}^{n}(1-q^j)} \qquad (q^n\xi < u < q^{n-1}\xi;\ \ n=1,\ldots). \tag{43}$$

In particular,

$$g_2(u,\xi) = e^{-\xi}\frac{u-q^2\xi}{q(1-q)(1-q^2)} \qquad (q^2\xi \leqslant u \leqslant q\xi). \tag{44}[5]$$

According to equation (43),

$$\frac{\partial^{n-1}}{\partial u^{n-1}}g_n(u,\xi) = \frac{e^{-\xi}}{q^{n(n-1)/2}\prod_{j=1}^{n}(1-q^j)} = \text{constant} \qquad (q^n\xi < u < q^{n-1}\xi;\ \ n=1,\ldots). \tag{45}$$

It follows from this last equation that at $u = q^n\xi (n = 1, 2, \ldots)$ the complete frequency function $g(u, \xi)$ must have a jump in its $(n-1)$th derivative of amount given by the right-hand side of equation (45); the function and all its lower-order derivatives (if they exist) must, however, be continuous at $u = q^n\xi$. Thus, at $u = q\xi$, the function itself suffers a jump of amount $e^{-\xi}/(1-q)$; at $u = q^2\xi$ there is a jump in the first derivative of amount $e^{-\xi}/q(1-q)(1-q^2)$, but the function itself is continuous here; at $u = q^3\xi$ there occurs a discontinuity in the second derivative, but the function and its first derivative are continuous, and so on.

Returning to equation (34), we can now write down, in accordance with equations (17), the complete probability distribution of u in the domain (13). Thus, combining the results expressed by equations (16) and (34), we have

$$f(u,\xi) = e^{-\xi}\left[1 + \sum_{n=1}^{\infty}\frac{(\xi-u)^n}{n!\prod_{j=1}^{n}(1-q^j)}\right] \tag{46}$$

[5] It is readily verified that the solutions given by eqs. (37) and (44) are continuous at $u = q\xi$; but there is sudden change of slope. Also, in this case, $g_3(u, \xi) = 0$ for $u < q^2\xi$.

and

$$g(u,\xi) = e^{-\xi}\left[\delta(\xi-u) + \sum_{n=1}^{\infty} \frac{(\xi-u)^{n-1}}{(n-1)!\prod_{j=1}^{n}(1-q^j)}\right], \tag{47}$$

for $q\xi < u \leqslant \xi$.

4. *An alternative form of $f(u,\xi)$ in the domain $q\xi < u \leqslant \xi$.*—Solution (46) for $f(u,\xi)$ in the domain included between the straight lines $u = \xi$ and $u = q\xi$ in the (u,ξ)-plane can be rewritten in the form

$$f(u,\xi) = Ke^{-\xi}\sum_{n=0}^{\infty}\frac{(\xi-u)^n}{n!}\prod_{j=1}^{\infty}(1-q^{j+n}) \qquad (q\xi \leqslant u < \xi), \tag{48}$$

where

$$\frac{1}{K} = \prod_{j=1}^{\infty}(1-q^j). \tag{49}$$

Equation (48) can be transformed into a more convenient form by making use of the identity

$$\prod_{j=1}^{\infty}(1-q^{n+j}) = \sum_{k=0}^{\infty}(-1)^k\prod_{j=1}^{k}\frac{q^{j+n}}{1-q^j}, \tag{50}$$

established in Paper II (eq. [18]). Letting

$$Q_0 = 1, \qquad Q_k = -\frac{q^k}{1-q^k}Q_{k-1} = (-1)^k\prod_{j=1}^{k}\frac{q^j}{1-q^j} \qquad (k = 1, \ldots), \tag{51}$$

we can rewrite identity (50) in the form

$$\prod_{j=1}^{\infty}(1-q^{n+j}) = \sum_{k=0}^{\infty}Q_k q^{kn}. \tag{52}$$

Two particular results which follow from equation (52) and which we shall find useful in the subsequent work are

$$\sum_{k=0}^{\infty}Q_k = \frac{1}{K} \qquad \text{and} \qquad \sum_{k=0}^{\infty}\frac{Q_k}{q^{lk}} = 0 \qquad (l = 1, 2, \ldots). \tag{53}$$

Combining equations (48) and (52), we can now write

$$f(u,\xi) = Ke^{-\xi}\sum_{n=0}^{\infty}\frac{(\xi-u)^n}{n!}\sum_{k=0}^{\infty}Q_k q^{kn}; \tag{54}$$

or, inverting the order of the summations, we have

$$f(u,\xi) = Ke^{-\xi}\sum_{k=0}^{\infty}Q_k\sum_{n=0}^{\infty}\frac{1}{n!}[(\xi-u)q^k]^n. \tag{55}$$

Hence

$$f(u, \xi) = Ke^{-\xi} \sum_{k=0}^{\infty} Q_k \exp\,[q^k(\xi - u)] \qquad (q\xi \leqslant u < \xi). \quad (56)$$

This is the required form of the solution.

5. *The completion of the solution for f.*—With $f(u, \xi)$ now known in the domain $q\xi \leqslant u < \xi$, the solution of equation (9) can be completed in the manner suggested in § 2.

First, it is convenient to use

$$F(u, \xi) = e^{\xi} f(u, \xi), \quad (57)$$

instead of f. The equation satisfied by F is

$$\frac{\partial F}{\partial u} + \frac{\partial F}{\partial \xi} = F\left(\frac{u}{q}, \xi\right). \quad (58)$$

As we have already explained in § 2, the solution of equation (58) must be carried out, successively, in the domains

$$q^n\xi \leqslant u < q^{n-1}\xi \qquad (n = 1, 2, \ldots). \quad (59)$$

We shall refer to the region included between the straight lines $u = q^{n-1}\xi$ and $u = q^n\xi$ as the nth domain; let $F_n(u, \xi)$ denote the required solution of equation (9) in this domain.

According to equation (58), the equation governing F_{n+1} in the $(n + 1)$th domain is

$$\left(\frac{\partial}{\partial u} + \frac{\partial}{\partial \xi}\right) F_{n+1}(u, \xi) = F_n\left(\frac{u}{q}, \xi\right); \quad (60)$$

for, when (u, ξ) lies in the $(n + 1)$th domain, $(u/q, \xi)$ lies in the nth domain.

Now, in the first domain included between the straight lines $u = \xi$ and $u = q\xi$ (see Fig. 1), the solution is (cf. eq. [56])

$$F_1(u, \xi) = K \sum_{k=0}^{\infty} Q_k \exp\,[q^k(\xi - u)]\,. \quad (61)$$

We shall now show in detail how this knowledge of the solution in the first domain can be used to extend the solution into the second domain included between the straight lines $u = q\xi$ and $u = q^2\xi$.

Consider a point P, $(u = q\xi_0;\ \xi = \xi_0)$, on the straight line $u = q\xi$. Since $(\partial/\partial u + \partial/\partial\xi)$ is proportional to the directional derivative along a straight line of unit (positive) slope, we draw through P a line PP' inclined at 45° to the co-ordinate axes. The co-ordinates (u, ξ) of a point S on PP', which is at a distance s from P, are

$$u = q\xi_0 - \frac{s}{\sqrt{2}} \quad \text{and} \quad \xi = \xi_0 - \frac{s}{\sqrt{2}}. \quad (62)$$

Conversely,

$$\left(\frac{1}{q} - 1\right)\frac{s}{\sqrt{2}} = \xi - \frac{u}{q} \quad \text{and} \quad \xi_0(1 - q) = \xi - u\,. \quad (63)$$

In terms of the variable s, the equation governing F_2 can be expressed in the form

$$\sqrt{2}\,\frac{dF_2}{ds} = -F_1\left(\xi_0 - \frac{s}{q\sqrt{2}}, \quad \xi_0 - \frac{s}{\sqrt{2}}\right); \quad (64)$$

or, substituting for F_1 according to equations (61), we have

$$\sqrt{2}\,\frac{dF_2}{ds} = -K\sum_{k=0}^{\infty} Q_k \exp\left[q^k\left(\frac{1}{q}-1\right)\frac{s}{\sqrt{2}}\right]. \tag{65}$$

Integrating this equation from 0 to s and remembering that the solution must be continuous along the lines $u = q^n\xi$, $(n = 1, 2, \ldots)$, we obtain

$$F_2(s;\,\xi_0) = F_1(q\xi_0,\,\xi_0) - K\,\frac{q}{1-q}\sum_{k=0}^{\infty}\frac{Q_k}{q^k}\left\{\exp\left[q^k\left(\frac{1}{q}-1\right)\frac{s}{\sqrt{2}}\right]-1\right\}. \tag{66}$$

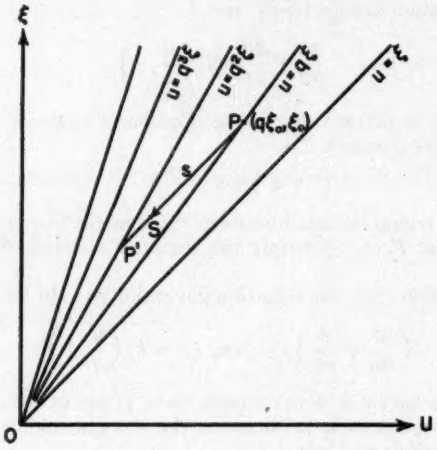

FIG. 1.—Illustrating the manner of integrating equation (60), successively, in the domains $q^n\xi \leqslant u \leqslant q^{n-1}\xi (n = 1, 2, \ldots)$.

The term

$$K\,\frac{q}{1-q}\sum_{k=0}^{\infty}\frac{Q_k}{q^k}, \tag{67}$$

which occurs on the right-hand side of equation (66), vanishes in virtue of the second of the identities in (53). Equation (66), therefore, reduces to (cf. eqs. [51])

$$F_2(s\,;\,\xi_0) = K\left\{Q_0\sum_{k=0}^{\infty}Q_k\exp\left[q^k\xi_0(1-q)\right] + Q_1\sum_{k=0}^{\infty}\frac{Q_k}{q^k}\exp\left[q^k\left(\frac{1}{q}-1\right)\frac{s}{\sqrt{2}}\right]\right\}. \tag{68}$$

Reverting to the variables (u, ξ) in accordance with equations (63), we can rewrite the foregoing solution in the form

$$F_2(u,\,\xi) = K\left\{Q_0\sum_{k=0}^{\infty}Q_k\exp\left[q^k(\xi-u)\right] + Q_1\sum_{k=0}^{\infty}\frac{Q_k}{q^k}\exp\left[q^k\left(\xi-\frac{u}{q}\right)\right]\right\}. \tag{69}$$

This is the required solution for F in the second domain.

We shall now complete the solution by proving by induction that, quite generally, the solution $F_n(u, \xi)$ in the domain included between the straight lines $u = q^n\xi$ and $u = q^{n-1}\xi$ is given by

$$F_n(u, \xi) = K\sum_{l=0}^{n-1} Q_l \sum_{k=0}^{\infty} \frac{Q_k}{q^{lk}} \exp\left[q^k\left(\xi - \frac{u}{q^l}\right)\right] \quad (n = 1, 2, \ldots). \tag{70}$$

Solutions (61) and (69), valid in domains 1 and 2, verify the truth of equation (70) for $n = 1$ and $n = 2$; to establish its general validity, we must prove that if the truth of equation (70) be assumed for a general value of n, then its truth for $(n + 1)$ can be derived. For this latter purpose, we shall integrate equation (60) along a straight line of unit slope in the domain $(n + 1)$ and passing through a given point $(q^n\xi_0, \xi_0)$ on the line $u = q^n\xi$. The co-ordinates (u, ξ) of a point on the line of unit slope distant s from $(q^n\xi_0, \xi_0)$ are

$$u = q^n\xi_0 - \frac{s}{\sqrt{2}} \quad \text{and} \quad \xi = \xi_0 - \frac{s}{\sqrt{2}}. \tag{71}$$

In terms of s, equation (60) becomes

$$\sqrt{2}\frac{dF_{n+1}}{ds} = -F_n\left(q^{n-1}\xi_0 - \frac{s}{q\sqrt{2}}, \quad \xi_0 - \frac{s}{\sqrt{2}}\right). \tag{72}$$

Substituting for F_n according to equation (70), we have

$$\sqrt{2}\,\frac{dF_{n+1}}{ds} = -K\sum_{l=0}^{n-1} Q_l \sum_{k=0}^{\infty} \frac{Q_k}{q^{lk}} \exp\left[q^k\left\{\xi_0(1 - q^{n-l-1}) + \frac{s}{\sqrt{2}}\left(\frac{1}{q^{l+1}} - 1\right)\right\}\right]. \tag{73}$$

Integrating this last equation from 0 to s and remembering that $F_{n+1}(0; s) = F_n(u = q^n\xi_0; \xi = \xi_0)$, we obtain

$$\begin{aligned} F_{n+1}(s\,;\,\xi_0) = {} & K\sum_{l=0}^{n-1} Q_l \sum_{k=0}^{\infty} \frac{Q_k}{q^{lk}} \exp\left[q^k\xi_0(1 - q^{n-l})\right] \\ & - K\sum_{l=0}^{n-1} \frac{q^{l+1}Q_l}{1 - q^{l+1}} \sum_{k=0}^{\infty} \frac{Q_k}{q^{(l+1)k}} \left\{\exp\left[q^k\xi_0(1 - q^{n-l-1})\right]\right. \\ & \left. - \exp\left[q^k\xi_0(1 - q^{n-l-1}) + \frac{s}{\sqrt{2}}\,q^k\left(\frac{1}{q^{l+1}} - 1\right)\right]\right\}. \end{aligned} \tag{74}$$

After some further reductions, in which we make use of equations (51) and (53), we find that we can simplify equation (74) to the form

$$F_{n+1}(s\,;\,\xi_0) = K\sum_{l=0}^{n} Q_l \sum_{k=0}^{\infty} \frac{Q_k}{q^{lk}} \exp\left[q^k\left\{\xi_0(1 - q^{n-l}) + \frac{s}{\sqrt{2}}\left(\frac{1}{q^l} - 1\right)\right\}\right]. \tag{75}$$

Now, reverting to the variables (u, ξ) in accordance with the transformation formulae (71), we have

$$F_{n+1}(u\,,\,\xi) = K\sum_{l=0}^{n} Q_l \sum_{k=0}^{\infty} \frac{Q_k}{q^{lk}} \exp\left[q^k\left(\xi - \frac{u}{q^l}\right)\right]. \tag{76}$$

This agrees with equation (70) for $(n + 1)$. This completes the proof of equation (70).

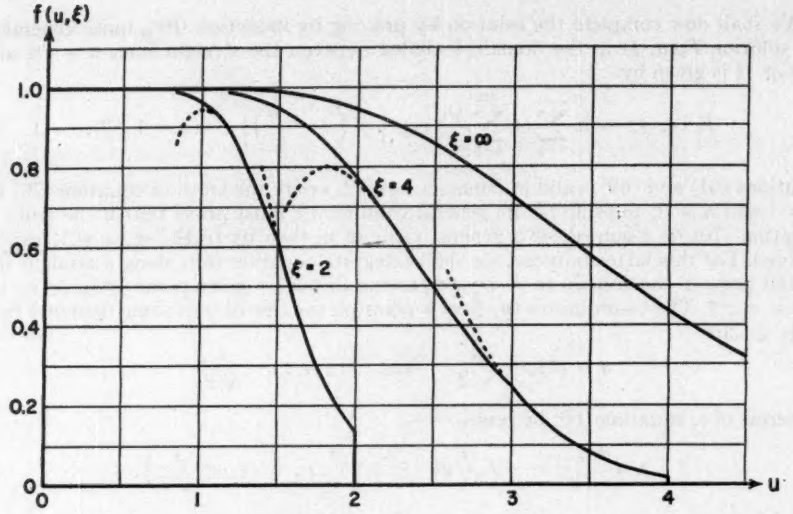

FIG. 2.—The probability distribution $f(u, \xi)$ for $q = 0.75$ and $\xi = 2$, 4, and ∞ (*full-line curves*). The solution for $f(u, \xi)$ in domains $q^n\xi \leqslant u < q^{n-1}\xi$ $(n = 1, 2, \ldots)$ has been extended to $u < q^n\xi$ (*dashed curves*) to illustrate the discontinuities of the function and/or its derivatives at $u = q^n\xi$.

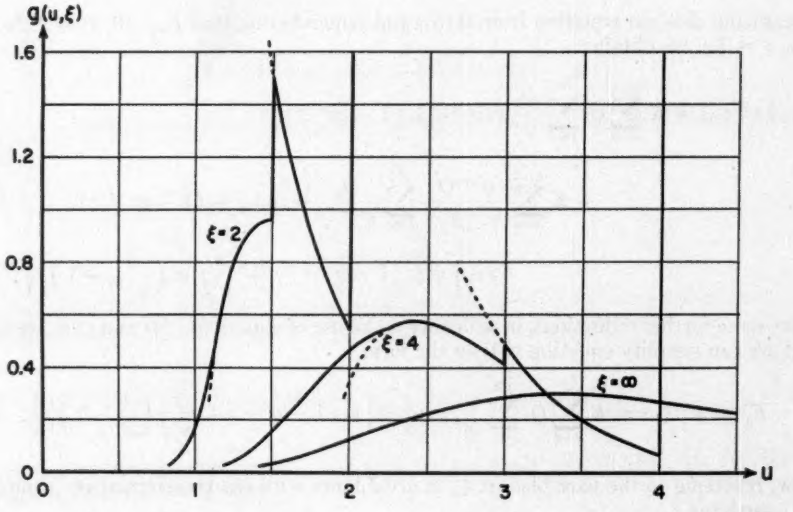

FIG. 3.—The frequency function $g(u, \xi)$ for $q = 0.75$ and $\xi = 2$, 4, and ∞ (*full-line curves*). The solution for $f(u, \xi)$ in domains $q^n\xi < u \leqslant q^{n-1}\xi$ $(n = 1, 2, \ldots)$ has been extended to $u < q^n\xi$ (*dashed curves*) to illustrate the discontinuities of the function and/or its derivatives at $u = q^n\xi$.

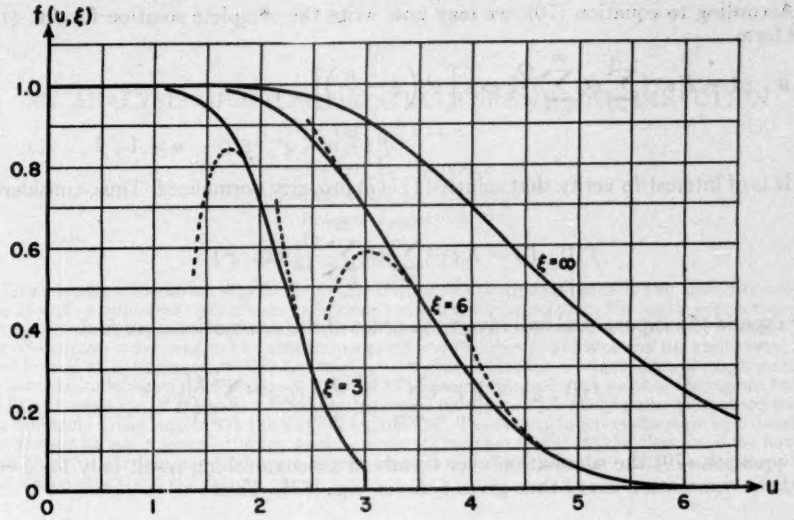

FIG. 4.—The probability distribution $f(u, \xi)$ for $q = 0.80$ and $\xi = 3$, 6, and ∞ (*full-line curves*). The solution for $f(u, \xi)$ in domains $q^n\xi \leqslant u < q^{n-1}\xi$ $(n = 1, 2, \ldots)$ has been extended to $u < q^n\xi$ (*dashed curves*) to illustrate the discontinuities of the function and/or its derivatives at $u = q^n\xi$.

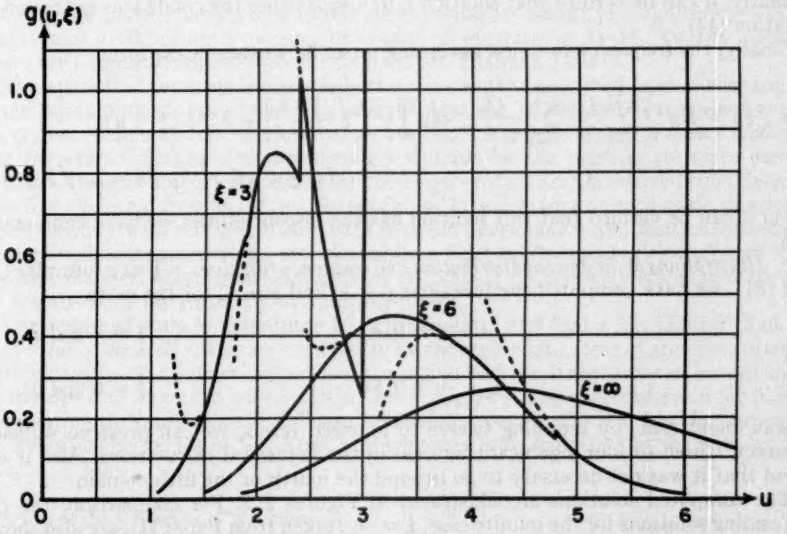

FIG. 5.—The frequency function $g(u, \xi)$ for $q = 0.80$ and $\xi = 3$, 6, and ∞ (*full-line curves*). The solution for $g(u, \xi)$ in domains $q^n\xi < u \leqslant q^{n-1}\xi$ $(n = 1, 2, \ldots)$ has been extended to $u < q^n\xi$ (*dashed curves*) to illustrate the discontinuities of the function and/or its derivatives at $u = q^n\xi$.

According to equation (70), we may now write the complete solution for $f(u, \xi)$ in the form

$$f(u, \xi) = Ke^{-\xi} \sum_{l=0}^{n-1} Q_l \sum_{k=0}^{\infty} \frac{Q_k}{q^{lk}} \exp\left[q^k\left(\xi - \frac{u}{q^l}\right)\right] \tag{77}$$

$$(q^n\xi \leqslant u < q^{n-1}\xi\,; \quad n = 1, 2, \ldots).$$

It is of interest to verify that solution (77) is properly normalized. Thus, considering

$$f(0, \xi) = Ke^{-\xi} \sum_{l=0}^{\infty} Q_l \sum_{k=0}^{\infty} \frac{Q_k}{q^{lk}} \exp\, q^k\xi\,, \tag{78}$$

we expand the exponential and invert the order of the summations; we find

$$f(0, \xi) = Ke^{-\xi} \sum_{m=0}^{\infty} \frac{\xi^m}{m!} \sum_{k=0}^{\infty} Q_k q^{km} \sum_{l=0}^{\infty} \frac{Q_l}{q^{lk}}. \tag{79}$$

In equation (79) the summation over l leads to a nonvanishing result only for $k = 0$, and the summation over l then gives $1/K$ (cf. eqs. [53]). Thus

$$f(0, \xi) = e^{-\xi} \sum_{m=0}^{\infty} \frac{\xi^m}{m!} = 1\,. \tag{80}$$

Similarly, it can be verified that solution (70) also satisfies the conditions expressed by equation (14).

Finally, the frequency function governing u can be written in the form

$$g(u, \xi) = Ke^{-\xi} \sum_{l=0}^{n-1} \frac{Q_l}{q^l} \sum_{k=0}^{\infty} \frac{Q_k}{q^{(l-1)k}} \exp\left[q^k\left(\xi - \frac{u}{q^l}\right)\right] + e^{-\xi}\delta(\xi - u) \tag{81}$$

$$(q^n\xi < u \leqslant q^{n-1}\xi\,; n = 1, \ldots).$$

Again it can be verified that this solution has the discontinuities we have enumerated in § 3.

6. *Illustrations of the derived distribution and frequency functions.*—Using formulae (77) and (81), we have computed the functions $f(u, \xi)$ and $g(u, \xi)$ for the cases

$$q = 0.75 \qquad \xi = 4 \text{ and } 2\,,$$

and (82)

$$q = 0.80\,, \qquad \xi = 6 \text{ and } 3\,.$$

It was found that, by retaining twelve to fourteen terms, we can preserve sufficient accuracy (three to four significant figures) in the numerical calculations. Also it was found that it was not necessary to go beyond the fourth or the fifth domain.

The computed solutions are illustrated in Figures 2-5. For comparison, the corresponding solutions for the infinite case, $\xi = \infty$ (taken from Paper II), are also shown. This comparison confirms the danger (to which we have already drawn attention in a different connection[6]) of applying the theory valid for $\xi = \infty$ even to relatively low galactic latitudes.

[6] S. Chandrasekhar and G. Münch, *Ap. J.*, **113**, 150, 1951.

AN ANALYSIS OF GALACTIC STRUCTURE IN THE DIRECTION OF AQUILA

RALPH L. CALVERT
University of Illinois Observatory*
Received August 5, 1950

ABSTRACT

This analysis of the Milky Way in the Aquila-Hercules-Lyra region is based on star counts to magnitude 15 and on published color excesses and counts of extragalactic nebulae. The region covers approximately 650 square degrees between galactic longitudes 5° and 33° and between latitudes −3° and +29°. The obscuration is ascribed to two clouds: one cloud at 500 parsecs, which covers the entire area; the second cloud at 1250 parsecs, which accounts for the greater amount of obscuration through most of the lower-latitude region. Obscuration as close as 200 parsecs is found in two parts of the region: one in the Rift at longitude 16°, the other at longitude 12° and latitude +7°.5. The greatest total obscuration, approximately 5 mag., appears in the Rift at longitude 24°. The density functions decrease with distance from the sun except in lower latitudes, where a moderate increase appears at the distance of the farther cloud. Surfaces of equal star density are nearly plane-parallel above latitude +12°.5 to a distance of at least 400 parsecs above the galactic plane.

THE STAR COUNTS

All plates were taken at the University of Illinois Observatory with the 4-inch Ross-Fecker camera, 28 inches in focal length. The scale of the plates is 290″/mm, or approximately 2°/inch. The plates are taken in pairs on twenty-six centers, from 3° to 5° apart. Each pair of plates consists of a 10-minute exposure for counts of magnitudes 9–13 inclusive and a 60-minute exposure for counts of magnitudes 11–15. Twenty pairs of plates are Cramer Hi-Speed Special; six pairs are Eastman 103*a*-O.

The method of counting is essentially the same as that described in an earlier paper.[1] Magnitude standards are available in Selected Areas 62, 63, 86, and 87 contained within the region. Standards for the fainter stars are taken from the *Mount Wilson Catalogue*.[2] The *Bergedorfer Spektral-Durchmusterung* standards for the brighter stars are used in Selected Areas 62 and 63. Standards for the brighter stars are transferred from Selected Area 62 to Selected Area 86 by two plates of equal exposure (one on each area), developed simultaneously with acetic acid stop bath between development and fixation. Standards for the brighter magnitudes are transferred from Selected Area 63 to Selected Area 87 in the same manner. Magnitude standards for calibrating the reference scale are carried to the remainder of the region by overlapping plates.

The counts of stars of magnitude 15 (approximate) and Plates 12, 13, and 15 of the Ross *Atlas of the Milky Way* are used to divide the region into areas of uniform apparent surface density. The higher latitudes of the region and the larger areas in low latitudes are divided into zones 2°.5 wide, as indicated in Figure 1. The values of mean log $N(m)$,[3] representing the counts for the different divisions, appear in Table 1. For the purpose of the analysis the values of log $N(m)$ are converted into log $A(m)$ at magnitudes 9.5, 10.5, . . . , 14.5.

* Now at the University of Wyoming.

[1] R. H. Baker, *Harvard Circ.*, No. 424, 1939.

[2] *Pub. Carnegie Inst. Washington*, No. 402, 1930.

[3] $N(m)$ is the number of stars per square degree as bright as, or brighter than, photographic magnitude m; and $A(m)$ is the number of stars per square degree with magnitudes between $m - \frac{1}{2}$ and $m + \frac{1}{2}$.

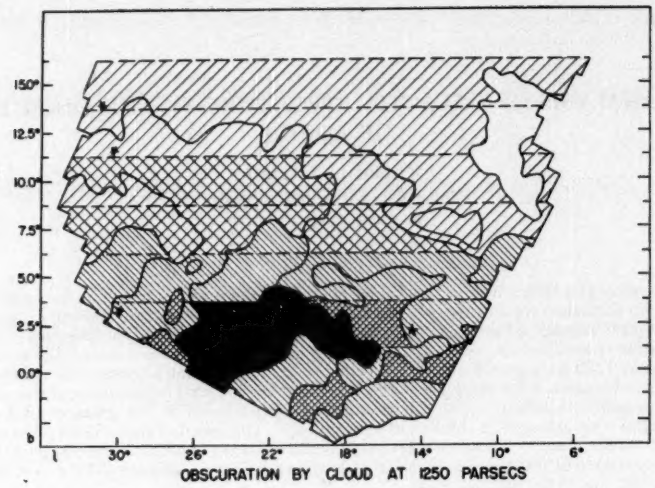

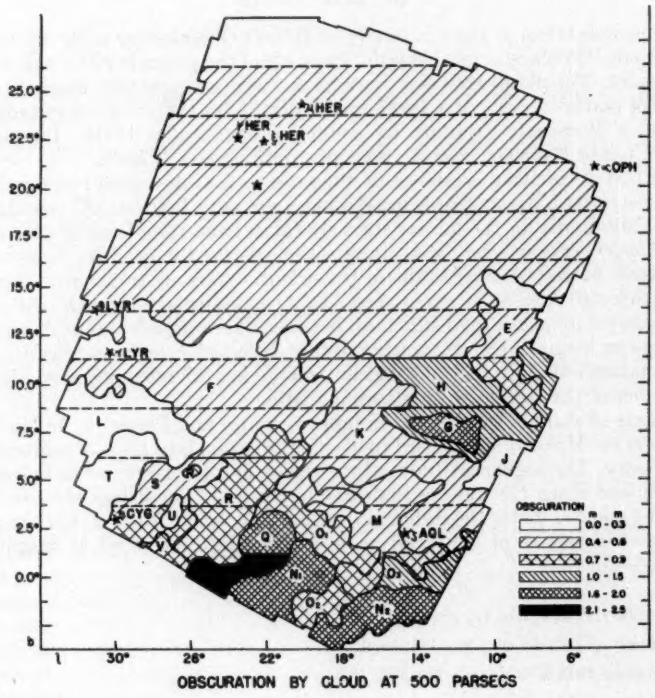

FIG. 1.—The divisions of the Aquila-Hercules-Lyra region with amounts of obscuration for each cloud.

TABLE 1

MEAN LOG $N(m)$ FOR EACH DIVISION

AREA AND ZONE	LONGITUDE OF CENTER*	AREA (SQ. DEG.)	LIMITING MAGNITUDE							OBSCURATION (MAG.)	
			9	10	11	12	13	14	15	At 500 Parsecs	At 1250 Parsecs
+27°5....	21°	30	0.35	0.77	1.18	1.55	1.85	2.11	2.41	0.3	0.0
+25.0....	18	44	.43	0.79	1.13	1.53	1.86	2.19	2.46	0.4	0.0
+22.5....	17	48	.47	0.82	1.19	1.58	1.91	2.24	2.52	0.4	0.0
+20.0....	17	58	.41	0.78	1.18	1.58	1.93	2.29	2.58	0.4	0.1
+17.5....	17	63	.36	0.74	1.13	1.55	1.94	2.30	2.63	0.6	0.2
+15.0....	19	60	.47	0.84	1.23	1.62	1.97	2.35	2.65	0.6	0.4
E +15.0....	9	4	.52	0.95	1.31	1.70	2.06	2.44	2.76	0.3	0.3
+12.5....	17	33	.43	0.83	1.20	1.58	1.96	2.36	2.65	0.6	0.5
E +12.5....	9	7	.49	0.86	1.22	1.63	2.04	2.39	2.72	0.5	0.3
F +12.5....	26	18	.55	0.97	1.35	1.68	2.03	2.48	2.79	0.3	0.4
K +12.5....	19	2	.56	0.90	1.24	1.59	1.98	2.36	2.70	0.5	0.5
E +10.0....	9	6	.34	0.74	1.13	1.58	1.92	2.34	2.63	0.7	0.3
F +10.0....	24	27	.52	0.91	1.27	1.64	2.00	2.46	2.79	0.4	0.7
H +10.0....	12	15	.44	0.74	1.08	1.52	1.87	2.28	2.62	1.0†	0.4
K +10.0....	17	10	.34	0.72	1.11	1.55	1.96	2.36	2.74	0.6	0.6
L +10.0....	30	5	.58	1.04	1.38	1.74	2.09	2.58	2.89	0.1	0.6
F + 7.5....	24	11	.60	0.94	1.27	1.61	1.95	2.43	2.77	0.6	0.8
G + 7.5....	12	4	.31	0.50	0.82	1.18	1.54	1.97	2.44	2.0†	0.4
H + 7.5....	11	10	.43	0.69	1.00	1.43	1.79	2.24	2.55	1.5†	0.4
K + 7.5....	17	14	.40	0.71	1.17	1.60	1.98	2.40	2.79	0.6	0.7
L + 7.5....	29	12	.64	1.02	1.41	1.76	2.07	2.54	2.86	0.2	0.9
R + 7.5....	22	5	.46	0.87	1.20	1.50	1.86	2.30	2.61	0.8	1.2
T + 7.5....	29	4	.46	1.00	1.38	1.74	2.06	2.54	2.88	0.1	1.0
J + 5.0....	10	4	.66	1.03	1.35	1.75	2.11	2.53	2.81	0.3	1.1
K + 5.0....	15	17	.50	0.92	1.28	1.64	2.01	2.42	2.76	0.5	1.1
M+ 5.0....	15	7	.51	0.85	1.25	1.60	1.94	2.32	2.63	0.6	1.4
R + 5.0....	23	11	.42	0.80	1.21	1.51	1.85	2.20	2.50	0.9	1.5
S + 5.0....	27	8	.57	0.96	1.29	1.64	1.95	2.34	2.71	0.6	1.1
T + 5.0....	31	8	.57	1.03	1.45	1.78	2.10	2.52	2.91	0.1	1.1
K + 2.5....	13	5	.55	0.96	1.40	1.75	2.11	2.44	2.80	0.5	1.5
M+ 2.5....	16	8	.51	0.88	1.28	1.65	1.98	2.35	2.69	0.6	1.6
O_1+ 2.5....	19	10	.61	0.91	1.27	1.59	1.94	2.21	2.50	0.8	2.2
Q + 2.5....	22	5	.55	0.77	1.16	1.47	1.78	1.99	2.22	1.7	2.3
R + 2.5....	25	10	.58	0.94	1.34	1.62	1.90	2.18	2.44	0.9	2.1
S + 2.5....	28	7	.51	0.85	1.31	1.62	1.94	2.35	2.70	0.7	1.4
U + 2.5....	27	1	.64	1.01	1.45	1.77	2.12	2.41	2.81	0.3	1.6
V + 2.5....	27	2	.46	0.94	1.35	1.66	1.99	2.30	2.62	0.7	1.7
M 0.0....	15	5	.62	0.88	1.29	1.68	2.02	2.40	2.75	0.8	1.5
N_1 0.0....	21	11	.40	0.76	1.20	1.54	1.86	2.14	2.41	2.0	1.4
O_3 0.0....	14	6	.56	0.91	1.25	1.60	1.92	2.26	2.58	1.2†	1.7
Q 0.0....	24	6	.68	0.94	1.29	1.51	1.77	2.00	2.21	2.2	2.5
N_2− 2.5....	16	12	.53	0.79	1.04	1.38	1.72	2.03	2.37	2.0†	1.2
O_2− 2.5....	19	5	0.62	0.93	1.25	1.61	1.95	2.28	2.56	0.9†	1.8

* Galactic co-ordinates used herein are referred to the conventional pole at R.A. 12^h40^m, dec. +28°.

† See Table 7.

RELIABILITY OF COUNTS

A measure of the reliability of the counts used herein is obtained by a comparison with those published for the Selected Areas; for the brighter magnitudes counts are taken from an area of 81 réseau squares to correspond as closely as possible to the Bergedorf Selected Areas, which are 3°5 to the side. Since the Bergedorf data do not include Selected Areas 86 and 87, two plates are used on each of Selected Areas 62 and 63. These individual comparisons are tabulated in Table 2. The Selected Areas of the *Mount Wilson Catalogue* are

TABLE 2

COMPARISON WITH BERGEDORF AND MOUNT WILSON COUNTS
(Calvert *minus* Berg. or Mt. W.)
$\Delta \log N(m)$

MAGNITUDE	SA 62		SA 63		SA 86	SA 87	MEAN
	Bergedorf						
9.0	+0.11	+0.05	+0.03	+0.10	.....	.....	+0.07
10.0	+ .05	+ .01	+ .07	+ .05	.....	.....	+ .04
11.0	− .01	− .04	+ .04	+ .02	.....	.....	.00
12.0	− .02	.00	− .02	− .09	.....	.....	− .03
13.0	+0.02	+0.05	−0.07	−0.13	.....	.....	−0.03
	Mount Wilson						
13.0	−0.23		−0.03		+0.10	+0.13	−0.01
14.0	− .11		− .04		− .16	+ .04	− .07
15.0	−0.13		+0.08		−0.15	+0.07	−0.03

TABLE 3

PROBABLE ERRORS OF LOG $N(m)$ FROM OVERLAPPING PLATES

P.E.	MAGNITUDE						
	9.0	10.0	11.0	12.0	13.0	14.0	15.0
In log $N(m)$	±0.03	±0.02	±0.03	±0.02	±0.02	±0.02	±0.03
In magnitude	±0.08	±0.06	±0.09	±0.05	±0.06	±0.06	±0.08

smaller than one réseau square. For these comparisons four squares are taken, with the area approximately centered therein. The Mount Wilson counts used are the Selected Area counts tabulated by van Rhijn.[4] These comparisons appear in Table 2.

A measure of the internal consistency of the counts is obtained by comparing counts of star fields common to pairs of plates overlapping the field. At least fifteen squares are used in each overlap. In each case the overlap is confined to an area of Figure 1, but not necessarily to a zone. With two exceptions, every pair of plates counted by the writer is involved in at least one overlap. The analysis of these comparisons appears in Table 3.

[4] *Groningen Pub.*, Vol. **43**, Table 1, 1929.

Eleven plates were counted by Professor Robert H. Baker. Residuals of spot counts made on three pairs of these eleven plates appear in Table 4. Professor Baker's counts contributed a comparatively small weight to the log $N(m)$ for any area.

No corrections are made to any of the counts.

THE ANALYSIS

For the analysis the obscuration is ascribed to two clouds: one at 500 parsecs and the other at 1250 parsecs. The two-cloud interpretation is used because it presents a physical picture, because it is suggested by the only detailed color studies from within the area analyzed, and because it allows a satisfactory fit to the star counts.

Color excesses in area M, determined by R. H. Baker,[5] fix the distance to the nearer cloud at 500 parsecs. His color excesses on the opposite side of the Rift indicate an obscuring cloud at 500 parsecs.

W. Becker's[6] treatment of C. E. Smith's[7] data on the latter's Area A2 (near Area O_3 + 0°.0 of this analysis) shows distinct increases in absorption at the distances adopted herein. Becker's treatment of Smith's data on the latter's Area A4 indicates absorption at shorter distances. However, the data on A4 are less reliable.

S. W. McCuskey and C. K. Seyfert[8] have published color excesses for an area near Area T + 5°.0 of this analysis. They use a factor of 2.6 to convert color excesses to absorption and find negligible obscuration to 700 parsecs. A factor of 3, indicated by the λ^{-1} law, reduces this distance about 100 parsecs.

TABLE 4

SPOT COUNTS: CALVERT *minus* BAKER
Mean Δ log $N(m)$

Magnitude	+9.0	+10.0	+11.0	+12.0	+13.0	+14.0	+15.0
Residual	+0.12	+ 0.02	− 0.03	− 0.01	− 0.06	− 0.06	− 0.07

F. D. Miller's[9] analysis of the Cygnus region indicates a decrease in distance to the obscuring cloud at the northern limits of the Aquila region. Along the Rift he finds obscuration at about 500 and 630 parsecs at longitudes 24° and 30°, respectively. Also he finds evidence of further obscuration at distances of 1000–1500 parsecs in some of the areas studied.

R. S. Zug's[10] color studies of two clusters at longitude 27° show no appreciable increase in obscuration at distances from 2000 to 4000 parsecs.

The analysis is made with the usual (m, log π) tables.[11] These tables are based on the van Rhijn luminosity function,[12] with account taken for both his corrections and those of Oort[13] for the change of luminosity with distance from the galactic plane.

Density functions are derived by entering the (m, log π) table with the amount of obscuration known from independent sources and finding a set of factors which produce the most satisfactory fit of computed to observed $A(m)$'s for the division involved.

[5] *Ap. J.*, **94**, 493, 1941.

[6] *Zs. f. Ap.*, **17**, 285, 1938.

[7] *Lick Obs. Bull.*, **18**, 39, 1937.

[8] *Ap. J.*, **106**, 1, 1947.

[9] *Harvard Ann.*, **105**, 297, 1937.

[10] *Lick Obs. Bull.*, **16**, 119, 1933.

[11] B. J. Bok, *The Distribution of the Stars in Space* (Chicago: University of Chicago Press, 1937).

[12] *Groningen Pub.*, No. 47, Table 6, 1936.

[13] *B.A.N.*, No. 290, 1936.

Density functions, $D(r)$, are derived on three assumptions: the region of unit density includes the stars at 125 parsecs, the change in density with change in latitude is approximately smooth, and the stellar distribution is symmetrical with respect to the galactic plane. The last assumption is applied only in determining the density function for the $-2°.5$ zone.

Hubble's nebulae counts[14] in Area E $+15°.0$ and in the $+20°.0$ and $+25°.0$ zones are used to guide the choice of density functions for these three zones. For this purpose his $\log N = 1.90$ is used to represent no obscuration. A combination of Hubble's nebulae

TABLE 5

ADOPTED DENSITY FUNCTIONS, $D(r)$

Zone	Distance (Parsecs)								
	125	200	300	500	800	1250	2000	3000	5000
0°.0	1.00	1.00	0.80	0.60	0.50	0.70	0.50	0.20	0.10
± 2.5	1.00	1.00	.70	.50	.45	.70	.50	.20	.10
+ 5.0	1.00	0.90	.70	.50	.40	.60	.45	.15	.07
+ 7.5	1.00	0.90	.70	.50	.40	.50	.40	.10	.05
+10.0	1.00	0.80	.70	.50	.40	.40	.30	.10	.05
+12.5	1.00	0.80	.70	.50	.40	.30	.20	.08	.04
+15.0	1.00	0.80	.70	.50	.40	.30	.20	.05	.....
+17.5	1.00	0.80	.70	.50	.40	.25	.15	.05	.....
+20.0	1.00	0.80	.70	.50	.30	.15	.10	.05	.....
+22.5	1.00	0.80	.60	.50	.30	.10	.06	0.03	.....
+25.0	1.00	0.80	.60	.40	.30	.10	.05	.....	.....
+27.5	1.00	0.70	0.60	0.40	0.20	0.10	0.05	.....	.....

ADOPTED DENSITY FUNCTIONS, $D(z)$

Zone	z (Parsecs)										
	10	16	25	40	63	100	158	251	400	630	1000
+15°.0	1.0	1.0	1.0	1.0	1.0	1.0	1.0	1.1	1.1	1.0	1.0
+17.5	1.0	1.0	1.0	1.0	1.0	1.0	1.1	1.1	1.1	1.1	1.0
+20.0	1.0	1.0	1.0	1.0	1.0	1.0	1.1	1.1	1.1	1.1	1.1
+22.5	1.0	1.0	1.0	1.0	1.0	1.0	1.1	1.1	1.1	1.0	0.8
+25.0	1.0	1.0	1.0	1.0	1.0	1.0	1.1	1.1	1.1	0.8	0.5
+27.5	1.0	1.0	1.0	1.0	1.0	1.1	1.2	1.1	1.0	0.7	0.4

counts and of Stebbins, Huffer, and Whitford's color excesses[15] in Area F $+10°.0$ guides the choice of density factors for the $+10°.0$ zone. In Area M, Baker's color excesses[5] determine the amount of absorption in the nearer cloud. This determination serves as the basis for the choice of density functions for the $+2°.5$ and $+5°.0$ zones. Density functions are extrapolated for the $0°.0$ and $+27°.5$ zones and interpolated for the $+7°.5$, $+12°.5$, $+17°.5$, and $+22°.5$ zones. Table 5 gives the adopted densities, $D(r)$.

Adopted values of the unobscured $\log A(m)$ appear in Table 6.

[14] *Mt. W. Contr.*, No. 485; *Ap. J.*, **79**, 8, 1934.

[15] *Mt. W. Contr.*, No. 621; *Ap. J.*, **91**, 20, 1940.

The analysis of the obscured divisions (other than those used in deriving the density functions) is accomplished by entering the zone (m, log π) table with the adopted density function for that zone. A trial-and-error adjustment to obtain the most satisfactory fit of computed to observed $A(m)$'s determines the amount of obscuration assigned to each cloud. A general outline of the obscuration attributed to each cloud appears in Figure 1. The amounts of obscuration found for each cloud are given in Table 1. As noted in Table

TABLE 6

ADOPTED UNOBSCURED LOG $A(m)$

Zone	Magnitude					
	9.5	10.5	11.5	12.5	13.5	14.5
0°0	1.22	1.67	2.14	2.58	2.96	3.27
± 2.5	0.99	1.47	2.00	2.48	2.86	3.18
+ 5.0	0.89	1.37	1.87	2.35	2.72	3.06
+ 7.5	0.83	1.30	1.79	2.25	2.62	2.94
+10.0	0.80	1.24	1.70	2.14	2.53	2.87
+12.5	0.75	1.19	1.64	2.04	2.42	2.74
+15.0	0.74	1.17	1.60	2.02	2.37	2.66
+17.5	0.72	1.11	1.57	1.95	2.31	2.60
+20.0	0.68	1.08	1.46	1.84	2.18	2.48
+22.5	0.64	1.05	1.42	1.76	2.08	2.34
+25.0	0.61	1.03	1.38	1.71	2.00	2.22
+27.5	0.59	0.96	1.31	1.66	1.93	2.15

TABLE 7

OBSCURATION AT DISTANCES LESS THAN 500 PARSECS

Area and Zone	Distance (Parsecs)		
	200	300	500 (Total)
H +10°0	0.0 mag.	0.6 mag.	1.0 mag.
G + 7.5	.5	1.2	2.0
H + 7.5	.0	0.9	1.5
O_3 0.0	.0	0.2	1.2
N_2 − 2.5	.4	0.7	1.8
O_2 − 2.5	0.0	0.2	0.9

7, it is necessary to allow for obscuration at distances less than 500 parsecs in two parts of the region in order to account for observed data. Area G is the dark area near the center of the left edge of Plate 13 of the Ross *Atlas of the Northern Milky Way*. Area N_2 lies in the Rift and appears about one-third the distance up from bottom-center on Plate 13.

Areas E, H, G, J, K, M, N, and O correspond to Baker's[5] areas of the same designation.

COMPARISON WITH RELATED DATA

Color excesses determined at the University of Illinois Observatory are for λλ 4250–6300. These color excesses have been multiplied by the factor 3 to obtain photographic absorption. In the following discussion the color excesses of other observers are multiplied by a factor determined on the basis of the λ^{-1} law.

Table 8 contains comparisons with related data from within the region analyzed. Close agreement is to be expected in Areas M, F +10°.0, E +15°.0, and in zones +20°.0 and +25°.0 (the first six entries in the table), since obscuration tabulated for these divisions is used to guide the choice of density functions. The adopted obscuration

TABLE 8

ADOPTED OBSCURATION COMPARED WITH OTHER SOURCES
(Obscuration in Magnitudes)

Area and Zone	Obscuration (Adopted at Pcs.)		Obscuration (Other Sources)	Distance (Parsecs)	Source*	Remarks
	500	1250 Total				
+25°.0	0.4	0.4	0.4	.....	H	3 counts
+20.0	0.4	0.5	0.5	.....	H	3 counts
E +15.0	0.3	0.6	0.9	.....	H	1 count
F +10.0	0.4	1.1	1.2	.....	H	3 counts
			0.3	430	SHW	7 stars
M + 5.0	0.6	2.0	0.6	500	RHB	Color excesses
M + 2.5	0.6	2.2	.....	.....	.....	.....
+17.5	0.6	0.8	<0.1	280	SHW	3 stars
+15.0	0.6	1.0	0.5	.....	H	3 counts
			<0.1	520	SHW	11 stars
+12.5	0.6	1.1	1.1	.....	H	2 counts
E +12.5	0.5	0.8	1.2	.....	H	2 counts
H + 7.5	1.5	1.9	>3.0	.....	H	1 count
R + 7.5	0.8	2.0	1.1	280	SHW	3 stars
K + 5.0	0.5	1.6	>3.0	.....	H	2 counts
J + 5.0	0.3	1.4	1.7	.....	H	1 count
S + 5.0	0.6	1.7	0.6	450	SHW	3 stars
T + 5.0	0.1	1.2	2.7	.....	H	1 count
O + 2.5	0.8	3.0	>3.0	.....	H	1 count
R + 2.5	0.9	3.0	0.6	500	SHW	5 stars

* Sources are as follows:
H = Hubble's nebulae counts (*Mt. W. Contr.*, No. 485; *Ap. J.*, **79**, 8, 1934).
SHW = Stebbins, Huffer, and Whitford's colors of B stars (*Mt. W. Contr.*, No. 621; *Ap. J.*, **91**, 20, 1940).
RHB = R. H. Baker's color excesses (*Ap. J.*, **94**, 493, 1941).

tabulated in the third column is the total for the two clouds. The Stebbins-Huffer-Whitford color excesses are multiplied by 8 to produce photographic absorption.

In an area of approximately 15 square degrees in the Rift at longitude 9°.9 and latitude −0°.9, Weaver[16] finds obscuration as close as 110 parsecs. His results, extrapolated to include stars at 1250 parsecs, indicate obscuration about 1.0 mag. greater than that found in this analysis for area N_2 in the Rift near by.

Smith's[7] investigations include six sample areas, B, four of which lie in the area discussed by Weaver. Smith's color excesses (through spectral class F5) multiplied by 3 give photographic absorption varying from 0 at 240 parsecs to 1.8 mag. at 540 parsecs in close agreement with the analysis of area N_2.

[16] *Ap. J.*, **110**, 190, 1949.

Mrs. P. Th. Shajn[17] has investigated selective absorption in a region of the Rift partially overlapping the areas of Smith and Weaver. She finds obscuration indicated as close as 150 parsecs. Her color excesses (graphical data) multiplied by 5 produce an absorption of 1.1 mag. at 500 parsecs.

McCuskey and Seyfert[8] have investigated a small area at longitude 33°, latitude +3° near Area T of this analysis. They find obscuration negligible at 700 parsecs but increasing beyond to 1.0 mag. at 2000 parsecs. These values are in substantial agreement with the analysis of Area T.

DENSITY FUNCTIONS

Densities throughout this region decrease with increasing distance from the sun, except near the galactic plane, where a moderate increase is found at the distance of the farther cloud. A retrial of the analysis indicates that this increase can be reduced by decreasing the obscuration of the farther cloud, but a poorer fit of observed to computed $A(m)$'s will result. Baker's analysis along the low-longitude side of this region shows an increase to unit density at 2000–3000 parsecs. His provisional estimate of the distance to the second cloud was 2000 parsecs. Above latitude +10°.0 the densities found in these two investigations are effectively the same. Since the Illinois counts do not go beyond magnitude 15, density factors for distances beyond 2000 parsecs are, at best, provisional. McCuskey and Seyfert find an increase in density at 2000–2500 parsecs.

For the higher latitudes, density functions, $D(z)$, in Table 5 are derived by methods outlined by Bok and MacRae.[18] These densities are expressed in terms of unit density at the same height, z, above the galactic plane at latitude 90°. The star distribution in the higher latitudes appears to be nearly plane-parallel. These results are in substantial agreement to a height of 250 parsecs with those of Baker and Kiefer[19] in positive latitudes in the Ophiuchus region. Bok and MacRae's analysis of Baker's Aquila star counts shows an increase in density, $D(z)$, which is not found herein at greater distances.

The writer wishes to express his appreciation to Professor R. H. Baker for suggesting the problem and for his helpful discussions throughout this investigation. Also the writer is grateful for the joint support of the University of Illinois Observatory and the University of Wyoming Research Council in the cost of publication of this article.

[17] *Bull. Abastumani Ap. Obs.*, **7**, 189, 1943.

[18] *Ann. New York Acad. Sci.*, **42**, 219, 1941.

[19] *Ap. J.*, **96**, 224, 1941.

AN ANALYSIS OF THE MILKY WAY IN PERSEUS

DAVID S. HEESCHEN
University of Illinois Observatory
Received November 11, 1950

ABSTRACT

The analysis of this region of the Milky Way is based on star counts to magnitude 15, color excesses of stars determined here, published color excesses of stars, and published counts of extragalactic nebulae. The obscuration is ascribed to two clouds; one cloud at the distance of 200–300 parsecs and the other at the distance of 800 parsecs from the sun. The nearer cloud accounts for most of the patchiness of the region, while the cloud at 800 parsecs is nearly uniform in density. A positive star-density gradient was found in one division of the region; in the rest of the region the star-density functions decrease with increasing distance from the sun.

The region of the Milky Way to be considered in this paper consists of about 1200 square degrees, lying roughly between galactic latitudes $+20°$ and $-20°$ and between galactic longitudes 100° and 120° in the northern latitudes and 100° and 140° in the southern latitudes. It covers the region between Cassiopeia and Auriga and extends south of Auriga into Taurus. In Figure 1 the positions of the brighter stars of the constellation Perseus are indicated. The large star in area C is α Persei.

THE STAR COUNTS

All the plates used were taken with the 4-inch Ross-Fecker camera of the University of Illinois Observatory. The scale of the plates is 290″ per millimeter. The counting was done by A. R. Sandage and T. J. McNamara.

The region is covered with forty-four pairs of plates, each pair consisting of a 10-minute and a 60-minute exposure. The pairs are taken on centers about 4° apart. The usable area of the plate is a roughly circular area of about 4° radius in the middle of the plate. All counting and calibrating of the magnitude scales is done in this area.

The method of counting the stars is the same as that described by Baker in a previous paper of this series.[1] Magnitude standards for calibrating the reference scale are available on plates containing Selected Areas 3, 9, 20, 21, 22, and 23. These are carried by overlapping plates to the remainder of the region. Magnitudes for the brighter stars are taken from the *Bergedorfer Spektral-Durchmusterung* and for the fainter stars from the *Mount Wilson Catalogue*.[2]

As a check on the consistency of the counts, comparisons were made of counts of the same area on each of eighteen pairs of overlapping plates at centers scattered throughout the region. On the basis of these comparisons, the results of which are summarized in Table 1, the corrections shown in Table 1 have been applied to the log $N(m)$ of the late Cramer plates. The designation *late* Cramer refers to Cramer Hi-Speed Special plates taken after 1946. *Early* Cramer plates were taken prior to 1943. The reason for the large $\Delta \log N(m)$ between the late Cramer and early Cramer plates has not been determined. No difference was found between the counts of different observers in the same region.

A measure of the consistency of the magnitude system is obtained by comparing the Illinois counts in the Selected Areas with those published in the Bergedorf catalogue for the brighter stars and with the Mount Wilson counts of the fainter stars tabulated by van Rhijn.[3] The mean differences, in Table 2, are considered to be satisfactorily small.

[1] *Harvard Circ.*, No. 424, 1939.

[2] *Pub. Carnegie Inst. Washington*, No. 402, 1930.

[3] *Groningen Pub.*, Vol. **43**, Table 1, 1929.

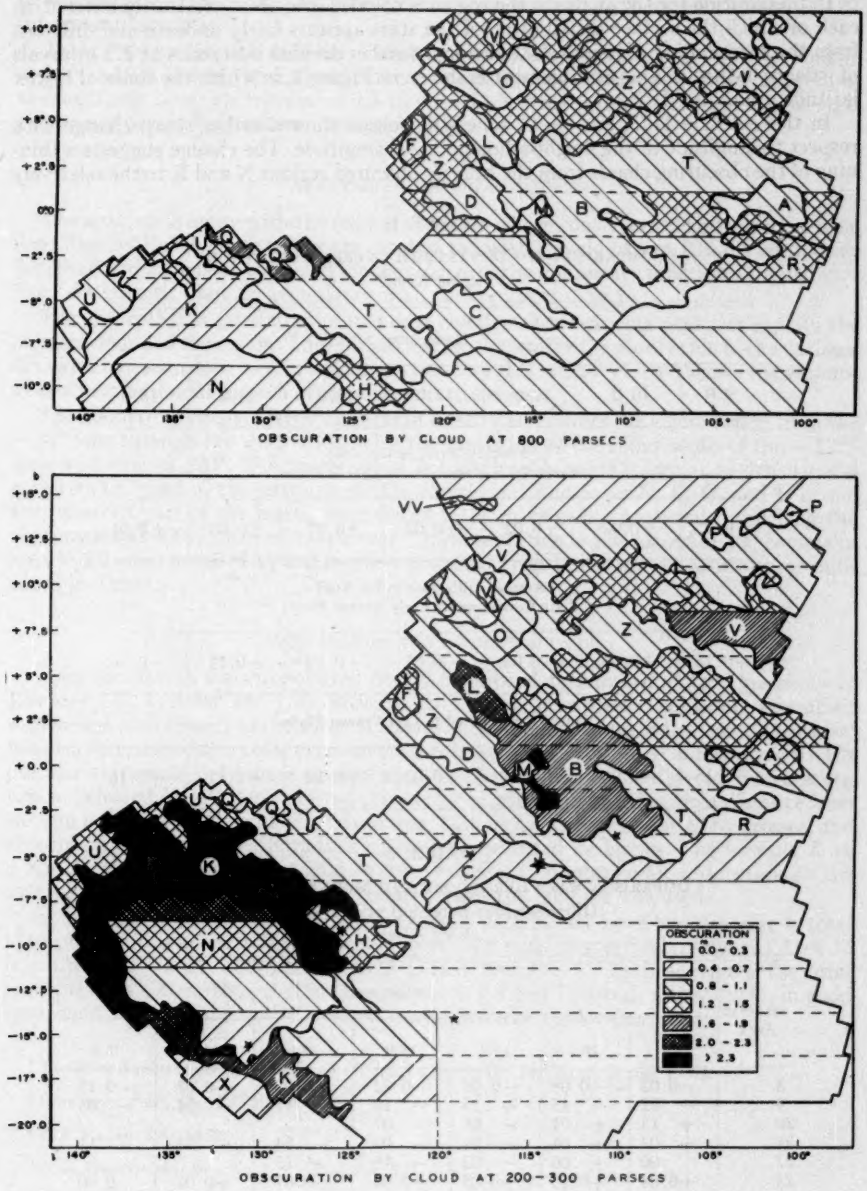

FIG. 1.—Divisions of the Perseus region, showing obscuration at 200–300 and 800 parsecs

In preparation for the analysis, the region is divided into areas arbitrarily lettered, in each of which the surface distribution of the stars appears fairly uniform and different from the surrounding divisions. The region is further divided into zones at 2°.5 intervals of galactic latitude. This arrangement is shown in Figure 1, in which the zones of higher latitude are omitted.

In the −15°, −17°.5, and −20° zones the counts show a rather sharp change with respect to longitude in the neighborhood of 120° longitude. The change suggests a thinning of the obscuring clouds from the heavily obscured regions N and K to the relatively

TABLE 1

COMPARISON OF COUNTS FROM OVERLAPPING PLATES
$\Delta \log N(m)$

Magnitude						
9.0	10.0	11.0	12.0	13.0	14.0	15.0
Probable Error in log $N(m)$ Early Cramer *minus* Early Cramer Plates						
±0.05	±0.02	±0.02	±0.02	±0.07	±0.03	±0.01
Average Difference in log $N(m)$ Late Cramer *minus* Early Cramer Plates						
+0.15	+0.06	−0.03	−0.07	−0.10	−0.11	−0.16
Corrections Applied to Late Cramer Plates						
−0.15	−0.06	+0.03	+0.07	+0.10	+0.11	+0.16

TABLE 2

COMPARISON WITH BERGEDORF AND MOUNT WILSON COUNTS
(Illinois *minus* Bergedorf or Mt. Wilson)
$\Delta \log N(m)$

Selected Area	Magnitude						
	9.0	10.0	11.0	12.0	13.0	14.0	15.0
3.....	−0.02	−0.08	−0.04	−0.02	−0.07	+0.02	−0.15
9.....	− .02	− .13	− .15	− .10	− .11	− .04	− .03
20.....	+ .13	+ .04	− .05	− .07	.....	.....	.....
21.....	+ .03	+ .04	− .04	− .09	− .04	− .04	− .11
22.....	.00	+ .06	− .02	− .10	− .13	.....	.....
23.....	+0.04	+0.10	+0.05	+0.04	+0.07	+0.07	0.00
Mean.	+0.04	+0.01	−0.04	−0.06	−0.06	0.00	−0.07

unobscured region west of 120°. These zones have accordingly been subdivided at 120° for separate analysis.

Table 3 shows for each division of the region the values of mean log $N(m)$ for magnitudes 9.0–15.0. Before the analysis of the counts is made, these are converted to log $A(m)$ at magnitude intervals from $m = 9.5$ to $m = 14.5$, where $A(m)$ is the number of stars per square degree between $m - \frac{1}{2}$ and $m + \frac{1}{2}$.

ANALYSIS OF THE STAR COUNTS

The analysis is made with the (m, log π) tables whose construction and use have been described by Bok.[4] These tables are constructed with the aid of van Rhijn's luminosity function[5] and have been corrected for the change in the luminosity function with distance from the galactic plane in accordance with the results of Oort.[6]

The absorption is attributed to two dust clouds, whose varying densities explain the patterns found in the region. The method used to determine the absorption in the various divisions has been described in a previous paper of this series.[1] Table 3 shows the amount of obscuration found in each of the different divisions.

The 800-parsec cloud is fairly uniform in density and covers the entire region from the −20° zone through the +15° zone, with the exception of the zones south of the −12°.5 zone and west of 120°. The nearer cloud is considerably more irregular in density and accounts for most of the patterns seen in the region. The areas N, K, Q, and U in the southeastern part of the region were found to be more easily analyzed by placing the obscuration at 300 instead of 200 parsecs. The obscuration is also placed at 300 parsecs in area V, all areas north of V, and in a few scattered areas in the middle latitudes, as indicated in Table 3.

COMPARISONS WITH RELATED DATA

Color excesses of stars in Selected Area 9 have been determined at the University of Illinois by T. P. Alton and J. C. Stewart. In Table 4 these color excesses are assembled into means with respect to the spectral classes and red magnitudes of the stars. Kharadse[7] has also determined the color excesses of stars in Selected Area 9. In conformity with the practice at Illinois, only those stars of spectral class B8–F0 are considered. The absorption in Selected Area 9, derived from these color excesses, is plotted against distance from the sun in Figure 2. Absorption derived from Illinois colors is represented by crosses, and absorption derived from Kharadse's colors is represented by circles. The formula $K = 3 \times$ C.E. was used to convert Illinois color excesses to photographic absorption on the International scale. For Kharadse's color excesses the factor 4 was used.

In Selected Areas 22[8] and 23[9] color excesses determined by Kharadse give a total absorption out to about 1000 parsecs of 0.6 and 1.6 mag., respectively. Selected Area 22 is in the −12°.5 zone, and Selected Area 23 is in area C −5°. In these regions the total absorption at 800 parsecs used in the analysis is 0.4 and 1.5 mag., respectively, in good agreement with the absorption derived from Kharadse's color excesses.

[4] *The Distribution of the Stars in Space* (Chicago: University of Chicago Press, 1937).

[5] *Groningen Pub.*, **47**, 17, Table 6, 1936.

[6] *B.A.N.*, No. 290, 1936.

[7] *Bull Abastumani Obs.*, No. 6, p. 29, Table VII, 1942.

[8] *Ibid.*, No. 8, 1945.

[9] *Ibid.*, No. 7, 1943.

TABLE 3

MEAN LOG $N(m)$ FOR THE DIFFERENT DIVISIONS

AREA	ZONE	LONGITUDE OF CENTER*	LIMITING MAGNITUDE							OBSCURATION (MAG.)		
			9.0	10.0	11.0	12.0	13.0	14.0	15.0	At 200 Parsecs	At 300 Parsecs	Additional at 800 Parsecs
A	0°0	102°	0.40	0.71	1.12	1.52	1.82	2.16	2.38	.....	1.5	1.1
B	− 2.5	112	.13	.52	1.02	1.37	1.68	2.02	2.41	.....	1.6	1.1
B	0.0	113	.27	.64	0.98	1.36	1.72	2.02	2.30	.....	1.8	1.0
B	+ 2.5	114	.34	.66	1.04	1.42	1.72	2.06	2.35	.....	1.6	0.9
C	− 5.0	117	.62	.93	1.36	1.68	1.98	2.27	2.69	0.5	.....	1.0
D	0.0	117	.45	.91	1.30	1.70	2.00	2.34	2.70	.....	0.9	0.8
F	+ 5.0	122	.46	.86	1.18	1.44	1.75	2.05	2.30	.....	1.3	1.5
H	−12.5	125	.42	.65	1.03	1.31	1.63	1.83	2.33	1.1	.....	1.0
H	−10.0	125	.30	.70	1.02	1.31	1.60	1.81	2.36	1.2	.....	1.3
K	−17.5	128	.22	.53	0.86	1.10	1.40	1.63	2.01	.....	1.8	0.2
K	−15.0	135	.....	.26	0.73	0.98	1.35	1.67	2.06	2.0	.....	0.1
K	−12.5	138	.16	.30	0.56	0.81	1.12	1.54	2.06	2.5	.....	0.0
K	−10.0	134	.28	.61	0.80	1.10	1.34	1.59	2.02	.....	2.5	0.7
K	− 7.5	134	.20	.54	0.89	1.17	1.46	1.66	2.04	.....	2.5	0.7
K	− 5.0	134	.33	.55	0.93	1.20	1.51	1.77	2.18	.....	2.5	0.6
K	− 2.5	134	.42	.52	0.98	1.25	1.50	1.73	2.21	.....	2.5	0.6
L	+ 2.5	117	.14	.49	0.91	1.24	1.55	1.84	2.20	.....	2.2	0.9
M	0.0	115	.26	.54	0.73	1.11	1.48	1.85	2.23	2.4	.....	0.8
N	−15.0	131	.50	.76	1.16	1.44	1.75	2.05	2.52	.....	0.7	0.3
N	−12.5	132	.44	.76	1.17	1.50	1.81	2.08	2.54	.....	0.8	0.3
N	−10.0	133	.48	.74	1.08	1.39	1.72	1.99	2.50	.....	1.2	0.6
N	− 7.5	133	.49	.61	0.94	1.26	1.64	1.87	2.39	.....	2.0	0.3
O	+ 7.5	118	.28	.70	1.14	1.53	1.84	2.16	2.46	0.9	.....	1.1
P	+12.5	103	.34	.63	0.98	1.29	1.57	1.92	2.20	1.0	.....	1.1
Q	− 2.5	130	.50	.96	1.32	1.61	1.94	2.16	2.58	.....	0.5	1.9
R	− 2.5	101	.67	.98	1.39	1.76	2.16	2.45	2.76	0.2	.....	1.3
T	− 7.5	123	.59	.81	1.22	1.54	1.87	2.14	2.56	0.8	.....	0.9
T	− 5.0	120	.51	.75	1.17	1.48	1.80	2.11	2.55	1.0	.....	0.8
T	− 2.5	115	.46	.75	1.18	1.52	1.84	2.17	2.55	1.0	.....	1.1
T	0.0	109	.50	.84	1.27	1.63	1.98	2.30	2.60	0.9	.....	1.3
T	+ 2.5	109	.47	.86	1.23	1.60	1.95	2.27	2.57	1.4	.....	0.8
T	+ 5.0	109	.37	.73	1.21	1.60	1.91	2.22	2.50	1.3	.....	1.2
U	− 2.5	134	.30	.73	1.06	1.32	1.58	1.87	2.37	.....	1.5	1.4
U	− 5.0	138	.32	.66	1.00	1.23	1.66	1.93	2.42	.....	1.5	1.1
U	− 7.5	140	.34	.70	1.09	1.29	1.63	1.90	2.38	.....	1.5	1.0
V	+ 7.5	105	.13	.55	0.97	1.29	1.53	1.87	2.13	.....	1.8	1.5
V	+10.0	110	.13	.51	0.95	1.34	1.65	1.94	2.20	.....	1.3	1.4
V	+12.5	116	.30	.65	1.14	1.48	1.79	2.06	2.30	.....	0.5	1.7
VV	+15.0	118	.16	.46	0.92	1.38	1.68	2.07	2.38	.....	1.3	0.0
X	−17.5	128	.33	.61	1.09	1.42	1.75	2.08	2.39	0.4	.....	0.2
Z	+ 2.5	120	.24	.74	1.08	1.48	1.79	2.19	2.47	1.0	.....	1.4
Z	+ 5.0	116	.22	.63	1.07	1.45	1.79	2.11	2.41	1.0	.....	1.3
Z	+ 7.5	112	.41	.75	1.17	1.50	1.79	2.11	2.38	0.9	.....	1.3
Z	+10.0	115	.20	.48	1.03	1.44	1.77	2.05	2.34	0.9	.....	1.2
	+10.0	105	.22	.55	1.12	1.47	1.78	2.10	2.41	.....	0.8	1.0
	+12.5	110	.18	.66	1.09	1.49	1.79	2.14	2.43	.....	0.8	0.6
	+15.0	110	.19	.65	1.10	1.51	1.85	2.21	2.56	.....	0.7	0.0
	+17.5	110	.18	.66	1.08	1.52	1.88	2.24	2.58	.....	0.4	0.0
	+20.0	110	.18	.62	1.06	1.48	1.84	2.19	2.54	.....	0.3	0.0
	− 5.0	104	.38	.80	1.24	1.64	2.05	2.40	2.82	0.7	.....	0.3
	− 7.5	106	.45	.83	1.31	1.68	2.03	2.32	2.76	0.3	.....	0.8
	−10.0	110	.56	.93	1.30	1.65	1.98	2.33	2.73	0.2	.....	0.8
	−12.5	110	.41	.82	1.24	1.61	1.96	2.33	2.68	0.3	.....	0.1
	−15.0	109	.45	.87	1.25	1.63	1.96	2.33	2.62	0.2	.....	0.0
	−15.0	123	.35	.63	1.02	1.37	1.67	2.02	2.43	0.9	.....	0.1
	−17.5	109	.37	.79	1.20	1.59	1.93	2.25	2.58	0.0	.....	0.0
	−17.5	123	.33	.61	1.09	1.42	1.75	2.08	2.39	0.4	.....	0.2
	−20.0	115	.36	.77	1.17	1.54	1.89	2.23	2.53	0.0	.....	0.0
	−20.0	123	0.56	0.72	1.10	1.37	1.68	2.04	2.31	0.0	.....	0.9

* All galactic co-ordinates in this paper are referred to the conventional pole at right ascension 12^h40^m, dec. +28°.

TABLE 4

ABSORPTION DETERMINED FROM COLORS

Spectral Class	No. of Stars	Mean Red Mag.	Color Excess (Mag.)	Distance (Parsecs)
B8–B9	15	9.7	0.45	600
	22	10.5	.61	690
	16	11.2	.73	790
A0–A1	14	9.5	.20	480
	29	10.3	.45	480
	42	11.2	.65	550
A2	18	10.3	.43	320
	24	11.3	.53	440
A3–A7	19	10.4	.44	210
	39	11.3	.47	300
A8–F0	7	8.8	.09	120
	18	10.5	.46	170
	21	11.3	0.50	230

ADOPTED NORMAL COLOR INDICES AND MEAN ABSOLUTE MAGNITUDES FOR SPECTRAL CLASSES

Spectral Class	Normal Color Index (Mag.)	Mean Abs. Mag.
B8–B9	−0.2	−0.5
A0–A1	− .1	+0.5
A2	.0	+1.5
A3–A7	+ .2	+2.5
A8–F0	+0.3	+3.0

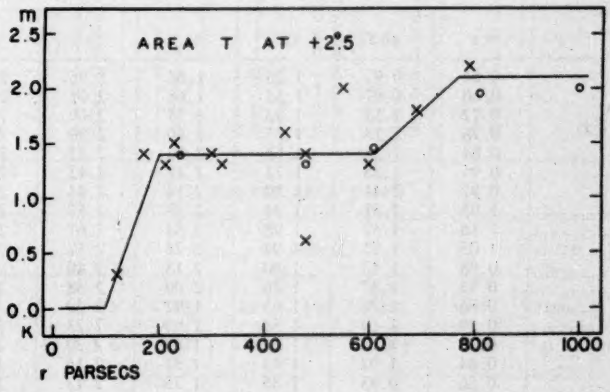

FIG. 2.—Photographic absorption in Selected Area 9, determined from color excesses

TABLE 5

OBSCURATIONS FROM STAR COLORS, CLUSTER COLORS, AND NEBULA COUNTS COMPARED WITH ADOPTED OBSCURATIONS

AREA AND ZONE	FROM SHW COLOR EXCESSES			FROM ZUG'S COLOR EXCESSES			FROM HUBBLE'S NEBULA COUNTS (TOTAL OBSCURATION)	ADOPTED IN ANALYSIS	
	No. of Stars	Mean Obscuration	Mean Distance (Parsecs)	N.G.C.	Obscuration	Distance (Parsecs)		At 200–300 Parsecs	Additional at 800 Parsecs
B 0°0	4	1.6	350	.....	.....	.....	.....	1.8	1.0
C −5.0	7	0.2	150	.....	.....	.....	.....	0.5	1.0
D 0.0	3	0.7	520	.....	.....	.....	.....	0.9	0.8
N −12.5	5	0.7	260	.....	.....	.....	.....	0.8	0.3
N −15.0	3	0.9	250	.....	.....	.....	1.2	0.7	0.3
R − 2.5	25	1.4	810	663	1.8	1750	.....	0.2	1.3
T − 5.0	6	0.5	330	.....	.....	.....	2.6	1.0	0.8
T − 2.5	8	1.6	310	.....	.....	.....	.....	1.0	1.1
T + 2.5	7	1.6	430	.....	.....	.....	.....	1.4	0.8
T + 5.0	.....	.....	.....	1502	2.4	1450	.....	1.3	1.2
Z + 5.0	3	1.6	580	.....	.....	.....	.....	1.0	1.3
Z + 7.5	4	1.8	400	.....	.....	.....	.....	0.9	1.3
− 5.0	6	0.7	1150	869	1.1	1330	2.2	0.7	0.3
−10.0	4	0.5	410	.....	.....	.....	1.0	0.2	0.8
(l=109°) −15.0	.....	.....	.....	.....	.....	.....	0.2	0.2	0.0
(l=123°) −15.0	3	0.8	220	.....	.....	.....	1.2	0.9	0.0
−17.5	.....	.....	.....	1039	0.0	450	.....	0.0	0.0
−20.0	.....	.....	.....	.....	.....	.....	0.2	0.0	0.0
+15.0	.....	.....	.....	.....	.....	.....	1.3	0.7	0.0
+20.0	.....	.....	.....	.....	.....	.....	0.2	0.3	0.0

TABLE 6

ADOPTED VALUES OF UNOBSCURED LOG $A(m)$

ZONE	MAGNITUDE					
	9.5	10.5	11.5	12.5	13.5	14.5
−20°0	0.54	0.92	1.28	1.63	1.95	2.23
−17.5	0.60	0.97	1.33	1.68	2.01	2.29
−15.0	0.72	1.13	1.43	1.77	2.09	2.35
−12.5	0.78	1.18	1.55	1.89	2.20	2.46
−10.0	0.84	1.28	1.68	2.02	2.32	2.59
− 7.5	0.95	1.38	1.77	2.12	2.42	2.66
− 5.0	0.97	1.41	1.80	2.14	2.44	2.67
− 2.5	1.05	1.51	1.94	2.28	2.57	2.80
0.0	1.16	1.57	1.98	2.33	2.61	2.82
+ 2.5	1.05	1.51	1.94	2.28	2.57	2.80
+ 5.0	0.98	1.42	1.80	2.13	2.40	2.64
+ 7.5	0.95	1.37	1.76	2.09	2.38	2.63
+10.0	0.86	1.26	1.65	1.97	2.29	2.55
+12.5	0.79	1.19	1.58	1.92	2.23	2.51
+15.0	0.73	1.12	1.51	1.88	2.20	2.48
+17.5	0.64	1.02	1.43	1.81	2.16	2.43
+20.0	0.56	0.93	1.35	1.75	2.13	2.38

Other information on the absorption in this region is obtained from the following sources:

1. Stebbins, Huffer, and Whitford's color excesses of B stars.[10] These have been converted to photographic absorption by the formula $K = 7 \times$ C.E.

2. Zug[11] has determined the color excesses of four open clusters in this region. The factor 3 has been used to convert these to photographic absorption.

3. Hubble's[12] counts of extragalactic nebulae. The value of log N for no absorption has been taken as 1.90.

TABLE 7

$D(r)$ NEAR THE EQUATOR

Zone	r (Parsecs)							
	125	200	300	500	800	1250	2000	3000
−10°.0	1.0	0.9	0.8	0.6	0.5	0.3	0.10	0.03
− 7.5	1.0	1.0	.9	.8	.6	.3	.15	.03
− 5.0	1.0	1.0	.9	.8	.6	.3	.15	.03
− 2.5	1.0	1.0	.9	.9	.7	.4	.20	.04
± 0.0	1.0	1.0	.9	.9	.7	.4	.20	.04
+ 2.5	1.0	1.0	.9	.9	.7	.4	.20	.04
+ 5.0	1.0	1.0	.9	.9	.6	.3	.10	.03
+ 7.5	1.0	1.0	.9	.8	.6	.3	.10	.03
+10.0	1.0	1.0	0.8	0.7	0.5	0.2	0.10	0.03

$D(z)$ FOR HIGHER LATITUDES

Zone	z (Parsecs)						
	40	63	100	158	250	400	630
−20°.0	1.0	1.0	0.9	0.8	0.7	0.5	0.5
−17.5	1.0	1.1	0.9	0.6	.7	.4	.5
−15.0	1.0	1.3	1.4	0.8	.4	.3	.2
−12.5	1.0	1.3	1.2	0.7	.3	.2	.2
−10.0	1.0	1.3	1.1	0.7	.3	.2	.2
+10.0	1.0	1.3	1.1	0.6	.3	.2	.2
+12.5	1.0	1.3	1.2	0.8	.6	.5	.5
+15.0	1.0	1.1	1.3	1.0	.8	.6	.5
+17.5	1.0	1.0	1.0	0.8	.9	.8	.7
+20.0	1.0	1.0	0.9	0.8	0.9	0.9	0.9

$D(r)$ FOR AREA T +2°.5

r (Parsecs)									
50	80	125	200	300	500	800	1250	2000	3000
1.0	1.4	1.6	2.0	1.8	1.3	0.8	0.3	0.1	0.02

[10] *Mt. W. Contr.*, No. 621, 1940; *Ap. J.*, 91, 20, 1940.

[11] *Lick Obs. Bull.*, No. 454, 1933.

[12] *Mt. W. Contr.*, No. 485, 1934; *Ap. J.*, 79, 8, 1934.

In Table 5 absorption derived from the above three sources is compared with that used in the analysis. In general, the agreement is quite satisfactory.

THE DENSITY GRADIENTS

Table 6 shows the true values of log $A(m)$ for the different zones, while Table 7 shows the density factors, provided that the correct amounts of absorption have been used in the analysis. The factors $D(r)$ in the upper part of Table 7 show the star densities near the equator at distances r from the sun relative to unit density in the sun's vicinity. The factors $D(z)$ appearing in the lower part of the table represent the star densities at higher latitudes relative to the density at the same distance z above the galactic plane for latitude 90°. The method given by Bok and MacRae[13] has been used in determining the $D(z)$.

In area T +2°.5 a positive density gradient was found. The density increases rapidly to a maximum of 2.0 at a distance of 200 parsecs from the sun. It then decreases somewhat less rapidly out to about 1000 parsecs, where the density is about the same as in the rest of the +2°.5 zone. The density factors for this star cloud are shown at the bottom of Table 7. The extent of the star cloud could not be determined from inspection of the plates and counts. The density factors above +10° are found to be somewhat higher than those in the corresponding southern latitudes.

It is a pleasure to express my appreciation to Dr. R. H. Baker for his invaluable advice and guidance throughout the course of this investigation.

[13] *Ann. New York Acad. Sci.*, **42**, 219, 1941.

PHOTOELECTRIC STUDIES. VIII. POSITIONAL EFFECT IN PHOTOMULTIPLIERS AND SOME REVISED MAGNITUDES IN THE NORTH POLAR SEQUENCE AND HARVARD REGION C 12*

OLIN J. EGGEN
Lick Observatory, University of California
Received March 15, 1951

ABSTRACT

It has been found that the 1P21 photomultiplier varies in sensitivity, depending on its orientation in the earth's magnetic field. This "positional effect" has been eliminated by shielding the photomultiplier with demagnetized strap-iron.

The only magnitudes in the previous seven papers of this series that are seriously affected by the positional effect are those in Paper I for the North Polar Sequence. New magnitudes for some of these polar stars have been determined (Table 2). Otherwise no change is required in all other magnitudes in Papers I–VII, which are uniformly on a consistent system referred to Harvard Standard Region C 12. A standard radium light-source has been used to control the observations of stars in widely different parts of the sky.

Improved magnitudes and colors, Pg_p and C_p, for the stars in Region C 12 differ at most by 0.02 or 0.03 mag. from the values used in previous papers (Table 1). Equations (1) and (2) give the conversion of Pg_p and C_p to the system of Stebbins, Whitford, and Johnson, which is based on nine stars of the North Polar Sequence. The change of the zero point in this conversion would make all apparent and absolute magnitudes in Papers I–VII fainter by 0.14 mag.

The small size of the random errors in measures of stellar brightness made with the photomultiplier tube suggested a closer examination of some possible systematic sources of error. These may be divided into two categories: (1) atmospheric and (2) instrumental. The effect of the atmosphere is that of a filter of variable thickness and color transmission, and it introduces errors into photoelectric and photographic photometry alike. Methods of correcting for both the thickness and the color transmission of the atmosphere have previously been discussed.[1] It should be mentioned, however, that, if standard magnitudes are to be transferred over large hour angles, the extinction factors and their dependence upon stellar colors should be determined on both sides of the meridian. Even with the relatively good "photoelectric sky" at Mount Hamilton, differences in the extinction amounting to 0.1 mag. have been found between stars at polar altitude in the Western and Eastern Hemispheres. This fact is, of course, a potent argument against the use of the North Polar Sequence for precise magnitude standards.

The purpose of this note is to point out one of the sources of instrumental error peculiar to the photomultiplier tube. We might designate this as the "positional effect." The positional effect, which was first encountered soon after observations had begun in 1948 with the Lick Observatory 12-inch refractor, consists of a variation of the sensitivity of the photomultiplier with position of the telescope. This sensitivity variation was detected by the use of a standard light-source made of radium paint, which has become standard equipment on all the Lick Observatory photometers. A check on the constancy of the standard light-source was made by the use of the brightness ratio between two such sources.

The photometer is mounted on the 12-inch telescope in such a manner that when the telescope is vertical the photomultiplier is horizontal, with its base-plug pointing north or south. Translation of the photomultiplier to the east or west has no appreciable effect on its sensitivity. Large rotations of the telescope about its declination axis, however,

* *Contributions from the Lick Observatory*, Ser. II, No. 37.

[1] O. J. Eggen, *Ap. J.*, 111, 65, 1950; *Lick Obs. Contr.*, Ser. II, No. 25.

which tend to bring the photomultiplier to a vertical position, cause sensitivity changes in the photomultiplier that, in extreme cases, amount to 10 or 15 per cent. When first noticed, the positional effect was corrected for by liberal use of a standard light-source. It was suggested by Kron, and independently by Whitford, that the effect might result from a defocusing of the electron stream in the photomultiplier, caused by the earth's magnetic field. A test with a small magnet showed that large changes in sensitivity could be caused by a weak magnetic field. The photomultiplier was then inclosed with a shield of demagnetized strap-iron, and the positional effect all but disappeared.

The positional effect is illustrated in Figure 1, *a*, which contains (*1*) a deflection on a standard light-source with the photomultiplier horizontal and oriented with its base-plug pointing south (telescope directed to the zenith); (*2*) photomultiplier nearly vertical, with base-plug pointing upward (telescope directed to H.A. = 0^h, $\delta = +90°$); and (*3*) photomultiplier with base-plug pointing downward (telescope directed to H.A. = 0^h, $\delta = +15°$). The change in sensitivity shown in Figure 1, *a*, corresponds to a difference of 0.12 mag. between $\delta = +90°$ and $\delta = +15°$. In Figure 1, *b*, Nos. *1*, *2*, and *3* show the corresponding deflections with the telescope in the same positions as in Figure 1, *a*,

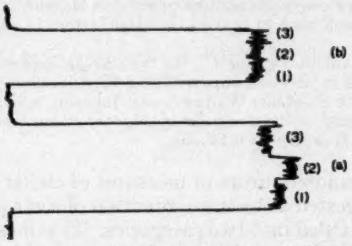

FIG. 1.—*a*, *1*, a deflection on a standard light-source with the photomultiplier horizontal and oriented with its base-plug pointing south; *2*, photomultiplier nearly vertical with base-plug pointing upward; and *3*, photomultiplier nearly vertical with base-plug pointing downward. *b*, *1*, *2*, and *3*, show the corresponding deflections with the telescope in the same positions as in *a*, but with a magnetic shield in place about the photomultiplier.

but with the magnetic shield in place about the photomultiplier. No appreciable sensitivity change can be seen in Figure 1, *b*. Fortunately, the color sensitivity of the photomultiplier does not appear to be altered by the positional effect. Also, no appreciable positional effect has been noted in photomultipliers mounted on the Crossley reflector. The lack of the effect with the reflector may be due to the fact that (1) the photomultiplier is mounted at the Newtonian focus and in ordinary practice does not suffer nearly complete rotation from base-plug up to base-plug down and (2) the reflector is mounted in an iron dome, while the refractor is housed in a copper dome.

The only magnitudes published from the Lick Observatory that are seriously affected by the positional effect are those of the brightest stars in the North Polar Sequence given in Paper I of this series.[1] The photoelectric magnitudes and colors of the Hyades stars determined with the 12-inch refractor, given in the same paper, were referred to the color and magnitude systems defined by stars in the Polar Sequence. Subsequently, the Hyades stars were intercompared with the stars in Harvard Standard Region C 12, and the resulting magnitudes for the C 12 stars were given in Paper IV of this series[2] and are repeated here in column *d* of Table 1. These magnitudes of the C 12 stars have since been used as standards for all the magnitudes determined with the 12-inch refractor. The magnitudes and colors in column *d* of Table 1 were derived with our 1P21-c, operated, unrefrigerated, at 90 volts per stage with standard optical thicknesses of Cor-

[2] *Ap. J.*, 112, 141, 1950; *Lick Obs. Contr.*, Ser. II, No. 30.

ning filters Nos. 5330 and 3385. These stars have also been observed with other combinations of two telescopes, three filters, and two multipliers, as indicated in the notes to Table 1.

Since the positional effect has been corrected for by the use of the standard source, or eliminated by the use of the magnetic shield, for all observations made subsequent to the intercomparison of the Hyades and the Polar stars listed in Paper I, we can either (1)

TABLE 1*

MAGNITUDES AND COLORS OF STARS IN HARVARD STANDARD REGION C 12

STAR	(a)			(b)			(c)			(d)			MEANS		MEANS	
	P_{gp}	C_p	n	P_{gp}	C_p	n	P_{gp}	C_p	n	P_{gp}	C_p	n	P_{gp}	C_p	P	$P-V$
A	6m54	−0m06	...	6m50	−0m05	...	6m54	−0m05	...	6m54	−0m04	...	6m53	−0m05	6m67	−0m155
C	7.30	+0.06	2	.....	.....	...	7.30	+0.07	1	7.34	+0.06	3	7.31	+0.06	7.45	−0.03
D	7.55	+1.14	...	7.56	+1.12	...	7.58	+1.12	...	7.60	+1.12	...	7.57	+1.12	7.71	+1.13
E	7.84	+0.86	2	7.84	+0.87	2	7.84	+0.86	1	7.88	+0.865	4	7.85	+0.865	7.99	+0.85
F	8.32	+0.25	3	8.30	+0.24	2	8.30	+0.25	1	8.26	+0.24	4	8.30	+0.245	8.44	+0.17
G	8.37	+0.23	2	8.36	+0.24	2	.....	.....	...	8.33	+0.23	2	8.35	+0.23	8.49	+0.15
H	8.43	0.00	2	8.40	−0.01	2	8.44	0.00	1	8.41	−0.01	4	8.42	−0.005	8.56	−0.105
I	9.06	+1.16	2	9.10	+1.16	2	9.10	+1.16	2	9.08	+1.16	3	9.08	+1.16	9.22	+1.18
K	.....	.....	...	9.13	+0.395	2	.....	.....	...	9.13	+0.40	1	9.13	+0.40	9.27	+0.34
L	9.42	+0.39	3	9.39	+0.39	2	9.39	+0.35	1	9.38	+0.36	3	9.40	+0.38	9.54	+0.32
M	9.62	+1.20	2	9.68	+1.205	2	9.66	+1.21	2	9.64	+1.20	3	9.65	+1.20	9.79	+1.22
N	9.97	+0.395	2	9.94	+0.40	2	9.97	+0.38	2	9.93	+0.40	3	9.95	+0.39	10.09	+0.33
O	10.00	+0.99	2	10.00	+0.99	2	.....	.....	...	9.97	+0.955	3	9.99	+0.98	10.13	+0.98
P	.....	.....	...	10.14	+1.10	2	.....	.....	...	10.10	+1.10	2	10.12	+1.10	10.26	+1.11
Q	.....	.....	...	10.58	+1.33	2	.....	.....	...	.....	.....	...	10.58	+1.33	10.72	+1.36

* The meaning of columns *a*, *b*, etc., is as follows:

a. 12-inch refractor, 1P21-c, 110 volt/stage, unrefrigerated, Corning filters Nos. 5562 and 3385.
b. Crossley, 7073B-110, 110 volt/stage, refrigerated, Corning filters Nos. 5562 and 3385.
c. Crossley, 7073B-109, unrefrigerated, 90 volt/stage, Corning filters Nos. 5530 and 3385.
d. 12-inch refractor, 1P21-c, unrefrigerated, 90 volt/stage, Corning filters Nos. 5530 and 3385.

TABLE 2

MAGNITUDES AND COLORS OF STANDARD STARS IN THE NORTH POLAR SEQUENCE

NPS	EGGEN		STEBBINS, WHITFORD, AND JOHNSON			EGGEN	
	P_{gp}	C_p	n	P	$P-V$	P	$P-V$
6	7m00	+0m13	1	7m15	+0m06	7m14	+0m04
2r	7.75	+1.51	1	7.90	+1.56	7.89	+1.56
10	9.00	+0.205	5	9.17	+0.12	9.14	+0.12
4r	9.11	+1.01	1	9.24	+1.02	9.25	+1.02
8r	11.32	+1.01	3	11.43	+1.02	11.46	+1.02
16	11.41	+0.40	2	11.56	+0.32	11.55	+0.34
19	12.55	+0.47	1	12.66	+0.41	12.69	+0.42

correct all magnitudes in Papers I–VII to those of the Polar stars given in Paper I or (2) abandon the magnitudes given in Paper I for the stars in the North Polar Sequence. The second alternative has been adopted as the simplest. The magnitudes in Papers I–VII are then on a homogeneous system defined by the magnitudes, in column *d* of Table 1, for the stars in C 12. Table 2 contains new observations of Polar stars obtained with a magnetically shielded photomultiplier mounted on the 12-inch refractor and on the

Crossley reflector. A direct comparison was made between the C 12 region and the polar stars.

In July, 1950, an informal meeting[3] held in Pasadena led to the adoption of the magnitudes derived by Stebbins, Whitford, and Johnson[4] for the nine stars NPS 6, 2r, 10, 4r, 13, 8r, 16, 19, and 12r, as standards for future photoelectric work at these observatories. Following Kron,[5] we shall adopt the symbols P and $P - V$ to designate the magnitudes and colors on this new system. Seven of the nine stars that define the P and $P - V$ systems are contained in Table 2. To strengthen the conversion factors from Pg_p and C_p to P and $P - V$, observations, on one night only, were made of seven stars in Selected Area 61; they are listed in Table 3. The values of P and $P - V$ assigned by

TABLE 3

MAGNITUDES AND COLORS OF STARS IN SELECTED AREA 61

Star	Eggen		Stebbins, Whitford, and Johnson			Eggen	
	Pg_p	C_p	n	P	$P-V$	P	$P-V$
61-80	9^{m}13	+0^{m}37	1	9^{m}27	+0^{m}29	9^{m}27	+0^{m}30
61-45	9.91	+0.36	1	10.07	+0.27	10.05	+0.29
61-1235	11.82	+0.52	1	11.97	+0.47	11.96	+0.47
61-19	11.87	+0.94	1	12.02	+0.93	12.01	+0.93
61-1295	12.87	+1.47	1	13.00	+1.54	13.01	+1.52
61-32	13.76	+0.71	1	13.96	+0.74	13.90	+0.68
61-100	14.33	+0.56	1	14.43	+0.50	14.47	+0.51

Stebbins, Whitford, and Johnson to these stars are also listed in Tables 2 and 3. A comparison of Pg_p and C_p with P and $P - V$ leads to the relations:

$$P = Pg_p + 0^m14\,, \tag{1}$$

$$P - V = -0^m10 + 1.10\,C_p\,. \tag{2}$$

These conversion formulae have been applied to the values of Pg_p and C_p for the stars in Harvard Standard Region C 12, and the resulting values of P and $P - V$ are given in the last two columns of Table 1.

To summarize: Except for the polar stars in Paper I, the magnitudes and colors in Papers I–VII are on the system of Pg_p and C_p in Tables 1, 2, and 3 of the present paper; to convert to the system P and $P - V$ of Stebbins, Whitford, and Johnson would involve a change of zero point of 0.14 mag., which would make both apparent and absolute magnitudes fainter.

[3] Attended by Messrs. Bowen, Baade, Pettit, Minkowski, and Baum, of the Mount Wilson and Palomar Observatories; Whitford and Johnson, of the Washburn Observatory; and Kron, Weaver, and Eggen, of the Lick Observatory.

[4] *Ap. J.*, **112**, 469, 1950.

[5] *Ap. J.*, **113**, 324, 1951.

THE STRUCTURE OF THE SOLAR ATMOSPHERE AS DEDUCED FROM LIMB-DARKENING MEASURES*

A. KEITH PIERCE AND LAWRENCE H. ALLER
McMath-Hulbert Observatory, University of Michigan, Pontiac, Michigan
Received January 23, 1951

ABSTRACT

From solar limb-darkening measurements made at the McMath-Hulbert Observatory and from the intensity distribution at the center of the disk the temperature at optical depth, τ_λ, is derived for a number of wave lengths. The theoretical k_λ, based on the negative hydrogen ion as the main source of opacity, appears to give an adequate interpretation of the solar limb-darkening measurements in the visual and infrared region of the solar spectrum. The boundary temperature of the sun is about 4500°.

I. INTRODUCTION

The intensity $I_\lambda(0, \theta)$ of a ray emergent from the disk of the sun and making an angle θ with respect to the outward directed normal is given by the well-known formula[1]

$$I_\lambda(0, \theta) = \int_0^\infty B_\lambda(\tau_\lambda)\, e^{-\tau_\lambda \sec\theta} \sec\theta\, d\tau_\lambda . \tag{1}$$

The optical depth τ_λ is related to the coefficient of continuous absorption at wave length λ by

$$d\tau_\lambda = k_\lambda \rho\, dx . \tag{2}$$

If the material obeys Kirchhoff's law at each point, the emission and absorption coefficients are defined by

$$j_\lambda = 4\pi k_\lambda B_\lambda(T) , \tag{3}$$

where j_λ is the total emission of the stellar material per gram per second, $B_\lambda(T)$ is the Planckian function, and T depends on τ_λ. In principle T is determined by an integration of τ_λ over λ.

From observations of the limb darkening, $I_\lambda(0, \theta)/I_\lambda(0, 0)$, and of the intensity distribution at the center of the disk, $I_\lambda(0, 0)$, it is possible in principle to find for a fixed temperature the run of the optical depth τ_λ with λ and to obtain some data on the variation of k_λ with wave length.

The most detailed analysis of this type is that carried out by D. Chalonge and V. Kourganoff[2] with the aid of Abbot's[3] measurements of solar limb darkening and of the intensity distribution at the center of the disk as compiled by Mulders.[4]

Our present discussion is based on the same principles but employs new measurements of limb darkening in the sun.[5] In our first reconnaissance we shall employ the $I_\lambda(0, 0)$ values given by Mulders. We shall find, however, that the values of $I_\lambda(0, 0)$ in the near infrared are uncertain and are in need of revision.

* Supported in part by Contract N6onr-232-V with ONR.

[1] See, e.g., A. Unsöld, *Physik der Sternatomosphären* (Berlin: J. Springer, 1938), chap. v; or L. H. Aller, *Astrophysics* (Philadelphia: Blakiston Co., 1951), chap. vii.

[2] *Ann. d'ap.*, **9**, 69, 1946.

[3] *Ann. Ap. Obs. Smithsonian Inst.*, **3**, 157, 1913; **4**, 721, 1922.

[4] *Zs. f. Ap.*, **11**, 143, 1936.

[5] K. Pierce, R. R. McMath, L. Goldberg, and O. Mohler, *Ap. J.*, **112**, 289, 1950.

From equation (1) we write the limb-darkening expression as

$$\phi_\lambda(\theta) = \frac{I_\lambda(0, \theta)}{I_\lambda(0, 0)} = \int_0^\infty b_\lambda(\tau_\lambda)\, e^{-\tau_\lambda \sec\theta} \sec\theta\, d\tau_\lambda , \tag{4}$$

where

$$b_\lambda(\tau_\lambda) = \frac{B(\tau_\lambda)}{I_\lambda(0, 0)} . \tag{5}$$

In their discussion, Chalonge and Kourganoff supposed that $\phi_\lambda(\tau_\lambda)$ could be represented by an empirical formula of the form

$$\phi_\lambda(\theta) = \alpha_\lambda + \beta_\lambda \cos\theta + \gamma_\lambda \cos^2\theta , \tag{6}$$

which implies an expression for $b_\lambda(\tau_\lambda)$ of the form

$$b_\lambda(\tau_\lambda) = \alpha_\lambda + \beta_\lambda \tau_\lambda + \tfrac{1}{2}\gamma_\lambda \tau_\lambda^2 . \tag{7}$$

At each wave length for which limb-darkening measurements are available, one may determine the coefficients α_λ, β_λ, and γ_λ by least squares. On general grounds we would expect that this representation does not hold for very small τ, because of the singular character of the integral equation of radiative equilibrium. It can be used as an interpolation formula but will fail for small τ_λ. The Planckian function B may be computed as a function of temperature for a given wave length, and, since $I_\lambda(0, 0)$ is assumed to be known, b_λ may also be found as a function of temperature. By comparison of this $b_\lambda(T)$ with the right-hand side of equation (7), we may obtain T as a function of τ_λ.

The difficulty with this procedure is that the representation of $b_\lambda(\tau_\lambda)$ by a truncated power series of the form of equation (6) is inadequate. Theoretically, one should include higher powers of $\cos\theta$ and determine the coefficients by least squares; however, no matter how many powers of $\cos\theta$ are included, equation (6) remains an interpolation formula. In practice, the inclusion of higher-order terms introduces spurious small fluctuations in the representation, because of the imperfect accuracy of the observational results. Hence, although the derived $b_\lambda(\tau_\lambda)$'s represent the limb-darkening measurements with sufficient accuracy, they will show fictitious fluctuations at large optical depths.

The source function for the integrated radiation may be represented very well by an empirical expression of the form

$$B(\tau) = A_0 + A_1\tau + A_2 E_2(\tau) + A_3 E_3(\tau) + \ldots , \tag{8}$$

which suggests that, at any particular wave length, one may write an expansion of the type

$$b_\lambda(\tau_\lambda) = A_\lambda + B\tau_\lambda + C_\lambda E_2(\tau_\lambda) + D E_3(\tau_\lambda) + \ldots . \tag{9}$$

Here A, B, C, and D are empirical constants to be determined from the observations, and the E's are the exponential integral functions defined by

$$E_n(x) = \int_{y=1}^\infty y^{-n} e^{-xy} dy . \tag{10}$$

If expression (9) is substituted in equation (4), there results[6]

$$\phi_\lambda(\theta) = A_\lambda + B_\lambda\mu + C_\lambda\left[1 - \mu \log_e\left(1 + \frac{1}{\mu}\right)\right] + D_\lambda\left[\tfrac{1}{2} - \mu + \mu^2 \ln\left(1 + \frac{1}{\mu}\right)\right] , \tag{11}$$

where

$$\mu = \cos\theta . \tag{12}$$

[6] V. Kourganoff, *C.R.*, 228, 2011, 1949.

II. REPRESENTATION OF LIMB-DARKENING OBSERVATIONS

The first step was to derive the coefficients in expansions of types (6) and (11) by the method of least squares. Each observed value of $I_\lambda(0, \theta_i)/I_\lambda(0, 0)$ gave a single observational equation, to which a weight was assigned, depending on the precision of the measurement. Normal equations were derived and solved in the usual way to yield the coefficients α, β, and γ for equation (6) or the coefficients A, B, C, and D in equation (11). Table 1 gives the least-squares coefficients A, B, and C for the various wave lengths at which limb darkening has been measured; $A + C$ is the limb intensity for center equal to unity. In Figure 1 we present the limb-darkening observations for λ 22870 and the representation by a three-term equation of type (11).

TABLE 1

COEFFICIENTS FOR REPRESENTATION OF LIMB-DARKENING OBSERVATIONS

λ (A)	A	B	C	$A+C$
5485	0.7088	+0.4499	−0.5173	0.1915
6151	0.7751	+ .3922	− .5453	.2298
6980	0.8432	+ .3269	− .5543	.2889
8384	0.8665	+ .2769	− .4676	.3989
9920	0.9559	+ .2089	− .5372	.4187
11973	1.0298	+ .1484	− .5809	.4489
15397	1.1583	+ .0427	− .6549	.5034
17093	1.1757	+ .0199	− .6375	.5382
20664	1.1224	+ .0363	− .5170	.6054
22870	1.1381	+ .0266	− .5370	.6011
35000	1.0154	+ .0575	− .2376	.7778
83000	1.0740	− .0021	− .2343	.8397
102000	1.0446	+0.0063	−0.1659	0.8787

The representation in terms of exponential functions was very much superior to the power-series representation. Furthermore, the four-term exponential gave no great improvement over the three-term exponential. The observations at λ 22870, for example, gave the sums of squares of residuals $[vv]$ (arbitrary units) shown in the accompanying tabulation.

	$[vv]$
Three-term exponential	529
Four-term exponential	535
Three-term exponential (observation near limb, weighted 5)	617
Three-term power series	2607
Four-term power series	1118

The superiority of the exponential representation is obvious. One of the quantities that we can obtain from the limb-darkening measurements is the intensity distribution $I_\lambda(0, \pi/2)$ at the extreme limb and hence the boundary temperature of the sun. Actually, it has not been possible, outside an eclipse, to observe $I_\lambda(0, \theta)$ for values of $\sin\theta$ greater than 0.997. Hence we must extrapolate equations of types (6) and (11) to $\mu = 0.0$. The observations nearest the limb are the most critical for the determination of the boundary temperature. Unfortunately, they are also the observations of lowest weight.

Figure 2 shows the $I_\lambda(0, \pi/2)$-curve obtained by extrapolating $\phi_\lambda(\theta)$ to $\theta = \pi/2$ and employing Mulders' $I_\lambda(0, 0)$. Notice that the data fit a black-body-curve for a temperature of 4500° K reasonably well except in the region beyond λ 12500. In this article we shall adopt a boundary temperature of 4500° K.

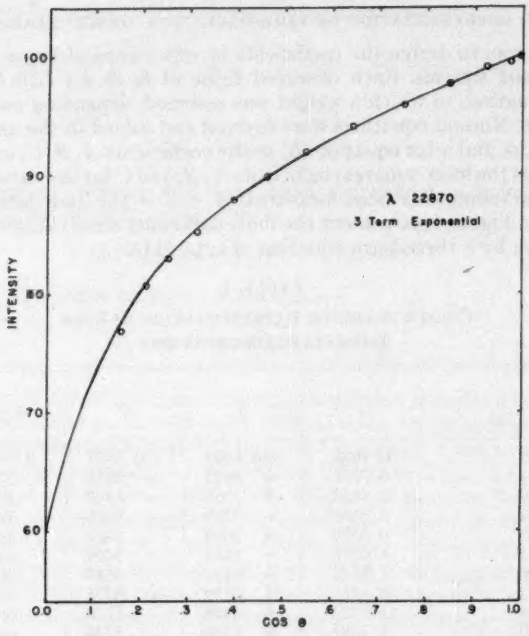

FIG. 1.—Representation of limb-darkening data with a source function of the type $A_\lambda + B_\lambda \tau_\lambda + C_\lambda E_2(\tau_\lambda)$.

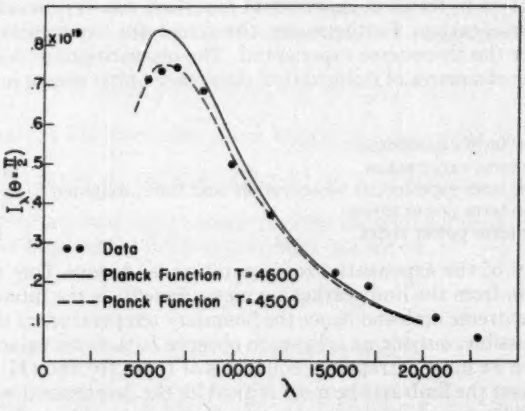

FIG. 2.—Extrapolated energy distribution $I_\lambda(0, \pi/2)$ at the boundary of the sun. The limb-darkening curves expressed on an absolute intensity scale are extrapolated to the solar boundary $\theta = \pi/2$ to obtain $I_\lambda(0, \pi/2)$. The points thus obtained for each observed wave length are compared with black-body-curves for 4500° and 4600° K.

The analyses of the limb-darkening measures for the far infrared, at wave lengths 3.5, 8.3, and 10.2μ present a special problem. No measures of the energy distribution in this region of the solar spectrum are at present available. When equation (11) was used to represent the data, we found the coefficient B to be very small, and at 8.3μ was actually negative, -0.0021, a physically impossible result. Calculation of the probable error of the least-squares coefficient shows the error in B to be greater than B itself. Thus in the far infrared the present limb-darkening measures can give no information on the temperature gradient, except perhaps in the outermost layers, where the influence of the coefficient C of the "transient" term, $E_2(\tau_\lambda)$, is important.

III. THE TEMPERATURE DISTRIBUTION

Once the coefficients A, B, and C have been determined for each wave length, we may compute $b_\lambda(\tau_\lambda)$ as a function of τ_λ with the aid of equation (9). Since $I_\lambda(0, 0)$ is known, the Planckian function $B_\lambda(\tau_\lambda)$ is determined. The left-hand side of equation (9) is a constant for a fixed temperature and wave length. When we choose a fixed temperature, we are choosing a fixed depth in the atmosphere of the sun. Hence we may take a particular temperature, compute b_λ for each wave length, and find the corresponding τ_λ's. Figure 3, *a*, *b*, shows, by means of crosses and a dotted line, the empirical τ_λ-curves obtained from the Mulders' $I_\lambda(0, 0)$ compilation and our limb-darkening measures.

To derive an empirical k_λ from these τ_λ-curves for comparison with the theoretical k_λ as given by Chandrasekhar,[7] we follow the procedure of Chalonge and Kourganoff. Let us write

$$\tau_\lambda = \int k_\lambda \left[\rho \frac{dx}{dT}\right] dT = \int a_T k_\lambda dT , \tag{13}$$

where

$$a_T = \rho \frac{dx}{dT} \tag{14}$$

is a factor that depends only on the depth in the atmosphere and therefore only on the temperature—not on the wave length. Differentiating this expression, we obtain

$$\frac{d\tau_\lambda}{dT} = a_T k_\lambda(T) . \tag{15}$$

At each wave length, we plot τ_λ against T and determine $d\tau_\lambda/dT$ by numerical differentiation for a series of different values of T. Then, for each of these selected temperatures, we compute $k_\lambda(T)$ and plot $d\tau_\lambda/dT$ against $k_\lambda(T)$. If the negative hydrogen ion is the principal cause of the opacity, the points should fall along a straight line whose slope will be a_T. In practice, the uncertainties in the observations produce a certain amount of scatter. We have estimated the best values of a_T and have calculated $\tau_\lambda(T)$ with the aid of equation (13) and the theoretical absorption coefficients due to Chandrasekhar. The computed synthetic curves are shown by crosses and a dotted line in Figure 3, *c*, *d*. The comparison between the "synthetic" and the empirical τ_λ-curves confirms the earlier results of Chalonge and Kourganoff that the negative hydrogen ion is the principal source of opacity in the solar atmosphere.

A detailed comparison proves disappointing. The empirical τ_λ-curves tend to rise to steeper maxima near λ 9000 and to sink to deeper minima near 1.9μ than do the synthetic curves calculated from an integration of equation (15). Beyond 2.1μ the empirical τ_λ-curve rises with incredible steepness.

The behavior of the empirical τ_λ-curves beyond about 1.5μ is probably to be accounted for by the fact that the measured intensity distribution in the near infrared

[7] *Ap. J.*, **104**, 430, 1946.

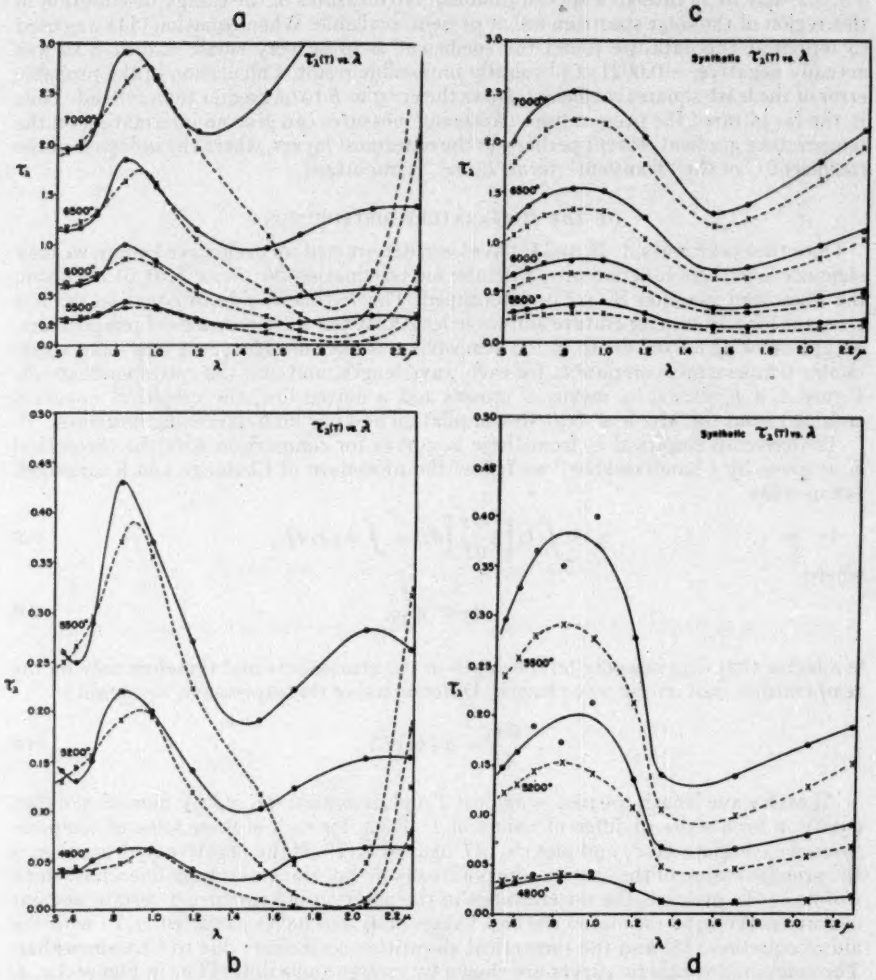

FIG. 3.—Comparison of empirical and synthetic τ_λ's for a few typical temperatures. *a*, *b*, ***dotted lines***, empirical τ_λ's computed from the observed limb darkening and Mulders' intensity distribution for the center of the sun's disk, $I_\lambda(0, 0)$; ***solid lines***, empirical τ_λ's computed from the observed limb darkening and from $I_\lambda(0, 0)$ as derived from the limb-darkening curves with the intensity at the limb, $I_\lambda(0, \pi/2)$ taken as appropriate to 4500° K. *c*, *d*, ***dotted lines***, synthetic τ_λ's obtained from integration of equation (15) (these are based on Chandrasekhar's absorption coefficient for H^- and Mulders' intensity distribution); ***solid lines***, synthetic τ_λ's obtained from integration of equation (15). These are based on Chandrasekhar's absorption coefficient for H^- and $I_\lambda(0, 0)$ as derived from the boundary temperature of 4500° K.

utilized by Mulders to form his definitive energy distribution is actually rather poor. Accordingly, in lieu of more accurate observations, we have attempted the following procedure: We suppose that the boundary temperature of the sun is 4500° K and use the limb-darkening measures to construct the $I_\lambda(0, 0)$ from $I_\lambda(0, \pi/2)$. A repetition of the analysis gives a new empirical $\tau_\lambda(T)$, and the Chalonge-Kourganoff type of analysis gives the synthetic τ_λ's calculated with the Chandrasekhar absorption coefficients and the temperature gradient derived from the limb-darkening data. Figure 3, *a*, *b*, *c*, *d*, circles and solid curves, shows the comparison of results. The agreement between theory and observation is much improved. It would appear that, until improved measurements of the energy distribution in the center of the solar disk are available, further discussion is not worth while and that the theoretical k_λ gives an adequate interpretation of the solar limb-darkening measurements in the visual and infrared regions of the solar spectrum.

It is of interest that the boundary temperature of near 4500° K is substantiated by an investigation by P. ten Bruggencate, H. Gollnow, and F. W. Jager,[8] in which a partial solar eclipse was used to determine the intensity distribution in the outermost part of the solar disk.

In our next paper we shall derive an improved model for the solar atmosphere with the aid of the new temperature distribution.

Thanks are due to Mr. William Potter for assistance in some of the computations and to Dr. Guido Münch, who read the manuscript and made helpful suggestions.

[8] *Zs. f. Ap.*, **27**, 223, 1950.

A ROTATIONAL ANALYSIS OF THE γ-SYSTEM OF THE *TiO* MOLECULE

JOHN G. PHILLIPS
Berkeley Astronomical Department, University of California
Received February 16, 1951

ABSTRACT

Rotational analyses have been carried out on the (1–0), (0–0), and (0–1) bands of the γ-system of the *TiO* molecule, at 6651, 7054, and 7590 A, respectively. In addition to providing the molecular constants presented in Table 4, the analysis showed that the system was produced by a $^3\Delta - {}^3\Pi$ transition, and not by a $^3\Sigma - {}^3\Pi$ transition, as has been formerly assumed.

A. INTRODUCTION

The γ-system of the *TiO* molecule is composed of a number of bands in the spectral region between 5860 and 8000 A. The most prominent of the bands form three sequences, at 6651, 7054, and 7590 A, respectively. The locations of the band heads have been studied by several investigators. The most recent laboratory measurements are those by Lowater[1] and Kiess.[2] A vibrational analysis by Lowater showed that the lower state of the γ-system is the same as the lower state of the α-system ($B^3\Pi - X^3\Pi$) as analyzed by Christy.[3] From the fact that the bands of the γ-system possessed intense *Q* branches and on the theory that there would be general similarity between the energy-level diagrams of the *TiO* molecule and the *Ca* atom, Lowater concluded that the γ-system was produced by an $A^3\Sigma - X^3\Pi$ transition.

As is well known, these infrared bands are prominent in the spectra of M-type stars.[4] On high dispersion, certain of the stellar absorption bands show regular progressions of lines which prove to be resolved rotational lines. This is particularly true of the region between 7054 and 7088 A, where the rotational structure of the band forming the 7054 A head is fairly well resolved. There is thus the possibility of using the intensities of the rotational lines to determine the rotational temperatures of the molecules in the stellar atmosphere. However, this requires the existence of rotational analyses of the corresponding bands. Since the early study by Lowater did not include such rotational analyses, the present investigation was undertaken to provide the necessary data.

On high dispersion, the bands of the γ-system are quite complex. An inspection of the spectrum showed that the (1–0), (0–0), and (0–1) bands at 6651, 7054, and 7590 A, respectively, were the only bands of the system which showed any promise of being analyzable. Accordingly, the discussion was limited to these three bands.

B. EXPERIMENTAL

The source used to obtain the spectrum of *TiO* has been described in a previous paper.[5] The region between 6600 and 8000 A was photographed in the second order of the 21-foot grating spectrograph of the Yerkes Observatory, with a dispersion of 1.25 A/mm. Eastman Kodak I-N plates were used, sensitized with ammonia. Exposure times ranged from 20 minutes at 6600 A to 60 minutes at 8000 A.

[1] *Proc. Phys. Soc. London, A*, **41**, 557, 1929.

[2] Paper read before the American Astronomical Society, Pasadena, California, 1948.

[3] *Phys. Rev.*, **33**, 701, 1929.

[4] See, e.g., C. D. Shane, *Lick Obs. Bull.*, **10**, No. 335, 131, 1922; N. T. Bobrovnikoff, *Ap. J.*, **78**, 211 1933; Dorothy N. Davis, *Ap. J.*, **106**, 28, 1947.

[5] John G. Phillips, *Ap. J.*, **111**, 314, 1950.

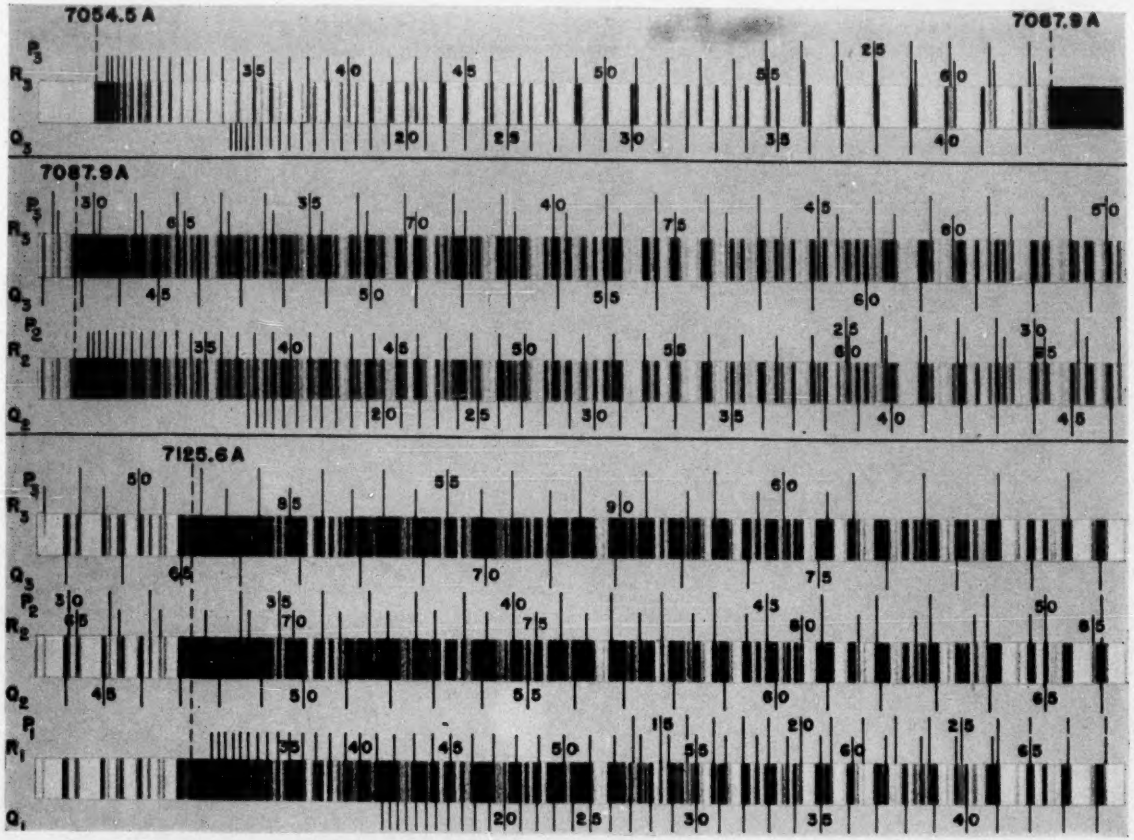

FIG. 1.—The rotational analysis of part of the (0–0) band of the γ-system of *TiO* at 7054 A

C. EMPIRICAL ROTATIONAL ANALYSIS

As was first shown by Lowater, each vibrational transition of the γ-system results in three well-separated sub-bands, corresponding to the three triplet components of the transition. Part of the (0–0) band is shown in Figure 1. The heads of the three sub-bands are at 7054, 7088, and 7125 A. In the following discussion these will be called the "violet," "central," and "red" sub-bands, respectively. Each sub-band consists of three branches —P, Q, and R. Satellite branches, which theoretically should also be present if the transition is $A^3\Sigma - X^3\Pi$, are not observed. The heads of the (1–1) band, at 7125, 7159, and 7197 A, are also present on the plates, but this band is so much less intense than the (0–0) band, that no complications were introduced into the positive identification of the branches of the latter.

The method of identification of branches can be illustrated by taking the (0–0) band as an example. As can be seen in Figure 1, the violet sub-band is unblended with any other band system in the interval between its head at 7054 A and the head of the central sub-band at 7088 A. Thus no difficulty was experienced in assigning each line in this wave-length interval to the three series forming its P, Q, and R branches. The rotational quantum numbers, J, of the individual lines were not known at this stage of the analysis, so that provisional running-numbers, m, were assigned to successive lines of each series.

These three short series were then extended to longer wave lengths by applying the graphical method of Loomis and Wood.[6] It was found that it was possible to trace the series completely through the crowded spectral regions occupied by the central and red sub-bands, there being no noticeable rotational perturbations. Hence all lines belonging to the three branches of the violet sub-band could be identified.

Upon turning to the central sub-band of the (0–0) band, it can be seen in Figure 1 that all lines in the interval between 7088 and 7125 A which had not been identified as members of the violet sub-band must be members of the central sub-band. Furthermore, abnormally large intensities of a number of the lines of the violet sub-band in this wave-length interval indicated that they were blended with lines of the central sub-band. Three series, with constant second difference between the wave numbers of successive lines, were formed of these unidentified and blended lines. The three series were readily identified as the P, Q, and R branches of the central sub-band. As before, application of the method of Loomis and Wood made possible the extension of these branches to longer wave lengths. A similar procedure was followed in identifying the lines comprising the three branches of the red sub-band. Table 1 lists the lines of the nine branches of the band. Also included in Table 1 are the lines of the (1–0) and (0–1) bands, which were analyzed in exactly the same way.

D. DETERMINATION OF THE ROTATIONAL CONSTANTS

The assignments of the rotational quantum numbers, J, to the lines of the twenty-seven branches included in the three bands were greatly facilitated by the fact that the lower state of the system is the same as the lower state of the α-system. The (1–0), (0–0), and (0–1) bands of this latter system have been analyzed by Christy.[3] The notation used by Christy has been converted by Budó[7] to the currently accepted notation. Budó also published partial lists of the combination differences, $\Delta_2F_1(J+1)$, $\Delta_2F_2(J)$, and $\Delta_2F_3(J-1)$ of the three electronic substates $X^3\Pi_0$, $X^3\Pi_1$, and $X^3\Pi_2$ for the vibrational level with $v'' = 0$. These lists were readily extended through the use of Christy's measurements of the (0–0) band and the equation $\Delta_2F''(J) = R(J-1) - P(J+1)$. Christy's measurements of the (0–1) band made possible the computation of similar lists for the $v'' = 1$ vibrational level.

[6] *Phys. Rev.*, **32**, 223, 1928.

[7] *Zs. f. Phys.*, **98**, 437, 1936.

TABLE 1

WAVE NUMBERS OF THE LINES OF THE (1–0) BAND

$\nu_0 = 14952.70\ \mathrm{Cm}^{-1}$

J	$^1\Delta_1 - {}^3\Pi_0$			$^3\Delta_2 - {}^3\Pi_1$			$^1\Delta_2 - {}^3\Pi_2$		
	$R_1(J)$	$Q_1(J)$	$P_1(J)$	$R_2(J)$	$Q_2(J)$	$P_2(J)$	$R_2(J)$	$Q_2(J)$	$P_2(J)$
	Cm^{-1}	Cm^{-1}	Cm^{-1}	Cm^{-1}	Cm^{-1}	Cm^{-1}	Cm^{-1}	Cm^{-1}	Cm^{-1}
7..									15013.60
8..									012.17
9..									010.50
10..									008.75
11..								15017.72	006.88
12..								017.19	005.10
13..								016.37	003.21
14..								015.38	001.28
15..								014.60	14999.21
16..								013.31	997.15
17..							15030.56	012.17	995.00
18..							030.16	010.92	992.78
19..	14889.10	14869.29	14850.38				029.88	009.63	990.46
20..	888.91	868.04	848.07		14942.15		029.54	008.25	988.00
21..	888.70	866.75	845.84		940.85	14919.83	029.15	006.88	985.59
22..	888.42	865.49	843.48	14962.61	939.55	917.62	028.64	005.40	983.20
23..	888.15	864.26	841.43	962.25	938.21	915.19	028.06	003.81	980.52
24..	887.76	862.82	838.95	961.75	936.68	912.59	027.45	002.22	977.98
25..	887.31	861.38	836.40	961.15	935.08	910.04	026.74	000.57	975.29
26..	886.82	859.91	834.01	960.50	933.46	907.49	025.97	14998.72	972.46
27..	886.28	858.30	831.40	959.77	931.74	904.70	025.16	996.90	969.65
28..	885.62	856.74	828.84	959.02	929.96	901.85	024.27	995.00	966.87
29..	884.97	855.09	826.14	958.14	928.12	898.99	023.28	993.04	963.76
30..	884.27	853.36	823.35	957.27	926.25	896.22	022.25	990.99	960.75
31..	883.49	851.56	820.64	956.28	924.24	893.17	021.14	988.89	957.68
32..	882.63	849.73	817.84	955.25	922.23	890.14	020.05	986.72	954.52
33..	881.51	847.82	814.88	954.17	920.13	887.03	018.74	984.48	951.25
34..	880.67	845.84	812.07	953.06	917.95	883.98	017.45	982.21	948.03
35..	879.76	843.83	808.93	951.77	915.73	880.67	016.04	979.79	944.62
36..	878.64	841.77	805.79	950.47	913.45	877.42	014.60	977.34	941.06
37..	877.42	839.62	802.72	949.08	911.10	874.23	013.12	974.85	937.76
38..	876.20	837.45	799.62	947.71	908.68	870.61	011.57	972.27	934.02
39..	874.99	835.11	796.38	946.10	906.19	867.14	009.91	969.65	930.42
40..	873.69	832.84	792.97	944.62	903.63	863.51	008.25	966.87	926.77
41..	872.15	830.45	789.70	943.01	901.05	859.91	006.43	964.13	922.94
42..	870.77	828.02	786.22	941.33	898.46	856.34	004.53	961.36	919.13
43..	869.29	825.51	782.79	939.55	895.63	852.61	002.62	958.43	915.19
44..	867.71	822.94	779.26	937.76	892.81	848.82	000.57	955.44	911.10
45..	866.04	820.35	775.49	935.90	889.93	844.92	14998.58	952.40	907.18
46..	864.26	817.60	771.95	934.02	887.03	841.01	996.43	949.27	903.10
47..	862.63	814.88	768.19	931.95	883.98	837.07	994.26	946.10	898.99
48..	860.75	812.07	764.40	929.96	880.97	833.01	991.99	942.83	894.65
49..	858.81	809.20	760.46	927.69	877.81	828.84	989.62	939.55	890.35
50..	857.03	806.28	756.68	925.53	874.65	824.71	987.23	936.14	885.90
51..	854.82	803.29	752.72	923.20	871.31	820.35	984.78	932.67	881.51
52..	852.78	800.21	748.57	920.88	868.04	816.12	982.21	929.16	877.09
53..	850.64	797.11	744.49	918.46	864.63	811.73	979.63	925.53	872.44
54..	848.51	793.89	740.30	915.99	861.17	807.36	976.97	921.91	867.71
55..	846.13	790.66	736.11	913.45	857.66	802.72	974.21	918.19	863.06
56..	843.83	787.30	731.87	910.83	854.05	798.29	971.40	914.38	858.30
57..	841.43	783.96	727.39	908.16	850.38	793.60	968.52	910.51	853.36
58..	838.95	780.50	722.93	905.38	846.67	788.90	965.58	906.57	848.51
59..	836.40	776.96	718.56	902.58	842.88	784.10	962.61	902.58	843.48
60..	833.76	773.44	714.00	899.72	838.95	779.26	959.47	898.46	838.36
61..	831.10	769.76	709.37	896.75	835.11	774.43	956.28	894.37	833.34
62..	828.37	766.07	704.71	893.73	831.10	769.48	953.06	890.14	828.37
63..	825.51	762.30	699.92	890.62	827.04	764.40	949.84	885.90	822.94
64..	822.69	758.46	695.18	887.49	822.94	759.42	946.45	881.51	817.60
65..	819.75	754.57	690.44	884.27	818.74	754.17	943.01	877.09	812.22
66..	816.68	750.61	685.37	880.97	814.48	748.94	939.55	872.65	806.88

TABLE 1—*Continued*

J	$^2\Delta_1$—$^3\Pi_0$			$^2\Delta_2$—$^3\Pi_1$			$^2\Delta_3$—$^3\Pi_2$		
	$R_1(J)$	$Q_1(J)$	$P_1(J)$	$R_2(J)$	$Q_2(J)$	$P_2(J)$	$R_3(J)$	$Q_3(J)$	$P_3(J)$
	Cm^{-1}	Cm^{-1}	Cm^{-1}	Cm^{-1}	Cm^{-1}	Cm^{-1}	Cm^{-1}	Cm^{-1}	Cm^{-1}
67..	14813.69	14746.57	14680.42	14877.81	14810.17	14743.66	14935.90	14868.04	14801.27
68..	810.53	742.44	675.35	874.23	805.79	738.27	932.25	863.51	795.61
69..	807.36	738.27	670.16	870.77	801.27	732.90	928.55	858.81	790.12
70..	804.14	734.09	665.01	867.14	796.78	727.39	924.78	854.05	784.26
71..	800.68	729.75	659.76	863.51	792.19	721.81	920.88	849.19	778.48
72..	779.11	725.35	654.47	859.91	787.54	716.19	916.97	844.31	772.61
73..	793.89	720.96	649.07	856.12	782.79	710.51	912.97	839.30	766.67
74..	790.30	716.47	643.67	852.16	778.03	704.71	908.91	834.30	760.67
75..	786.67	711.98	638.05	848.36	773.17	699.01	904.70	829.18	754.57
76..	783.02	707.24	632.48	844.31	768.19	692.99	900.54	824.01	748.57
77..	779.26	702.59	626.81	840.27	763.20	687.15	896.22	818.74	742.44
78..	775.49	697.86	621.14	836.10	758.11	681.11	891.93	813.47	736.11
79..	771.56	692.99	615.39	831.97	752.97	674.96	887.49	808.10	729.75
80..	767.55	688.07	609.49	827.69	747.77	668.75	882.96	802.72	723.39
81..	763.54	683.07	603.63	823.35	742.44	662.50	878.26	797.11	716.74
82..	759.42	678.03	597.55	818.74	737.08	656.26	873.69	791.55	710.51
83..	755.34	672.95	591.53	814.48	731.69	649.90	869.06	785.87	703.63
84..	751.05	667.78	585.32	810.17	726.18	643.44	864.26	780.07	696.91
85..	746.73	662.50	579.17	805.31	720.64	636.97	859.41	774.43	690.20
86..	742.44			800.68	714.99	630.35	854.46		
87..	737.90			796.12	709.37	623.71	849.45		
88..	733.36			791.23	703.63	617.06	844.31		
89..					697.86	610.47	839.30		
90..						603.63			
91..									
92..									

TABLE 1—*Continued*

WAVE NUMBERS OF THE LINES OF THE (0–0) BAND
($\nu_0 = 14092.87\ Cm^{-1}$)

J	$^2\Delta_1$—$^3\Pi_0$			$^2\Delta_2$—$^3\Pi_1$			$^2\Delta_3$—$^3\Pi_2$		
	$R_1(J)$	$Q_1(J)$	$P_1(J)$	$R_2(J)$	$Q_2(J)$	$P_2(J)$	$R_3(J)$	$Q_3(J)$	$P_3(J)$
	Cm^{-1}	Cm^{-1}	Cm^{-1}	Cm^{-1}	Cm^{-1}	Cm^{-1}	Cm^{-1}	Cm^{-1}	Cm^{-1}
6..					14094.68			14161.70	14155.62
7..					094.28			161.28	154.16
8..					093.81			160.80	152.71
9..		14017.43			093.28			160.27	151.07
10..		016.94			092.82			159.61	149.44
11..		016.38			092.08			158.99	147.75
12..		015.79	14003.69		091.46			158.30	146.03
13..		015.12	002.00		090.86			157.43	144.18
14..		014.44	000.36		089.90			156.56	142.29
15..		013.66	13998.55		088.97			155.62	140.35
16..		012.79	996.75		088.12			154.66	138.34
17..		012.00	994.98		087.16			153.60	136.29
18..		011.06	992.94		086.09		14171.89	152.71	134.14
19..		010.11	991.23		085.02		171.67	151.34	131.95
20..		009.09	989.04		083.91		171.46	150.10	129.70
21..	14030.18	008.04	987.01		082.68		171.17	148.83	127.35
22..	030.18	006.89	984.84		081.37	14058.70	170.82	147.47	125.16
23..	029.76	005.73	982.67		080.14	056.51	170.42	146.03	122.73
24..	029.76	004.52	980.39		078.75	054.41	169.96	144.58	120.26
25..	029.43	003.36	978.21	14103.64	077.32	052.11	169.44	143.05	117.53
26..	029.16	002.00	975.79	103.13	075.85	049.59	168.85	141.46	115.15
27..	028.63	000.61	973.57	102.60	074.31	046.98	168.21	139.81	112.43
28..	028.27	13999.20	971.04	102.01	072.70	044.48	167.49	138.08	109.70
29..	027.77	997.73	968.77	101.35	071.04	041.81	166.73	136.29	106.91
30..	027.31	996.13	966.05	100.67	069.33	039.06	165.89	134.47	104.05

TABLE 1—*Continued*

J	$^1\Delta_1$—$^3\Pi_0$			$^1\Delta_2$—$^3\Pi_1$			$^1\Delta_2$—$^3\Pi_2$		
	$R_1(J)$	$Q_1(J)$	$P_1(J)$	$R_2(J)$	$Q_2(J)$	$P_2(J)$	$R_2(J)$	$Q_2(J)$	$P_2(J)$
	Cm^{-1}	Cm^{-1}	Cm^{-1}	Cm^{-1}	Cm^{-1}	Cm^{-1}	Cm^{-1}	Cm^{-1}	Cm^{-1}
31..	14026.72	13994.57	13963.48	14099.87	14067.60	14036.29	14165.00	14132.57	14101.13
32..	026.01	992.94	960.88	099.03	065.75	033.48	164.04	130.60	098.17
33..	025.34	991.23	958.14	098.17	063.80	030.56	163.03	128.58	095.14
34..	024.61	989.48	955.41	097.21	061.90	027.77	161.95	126.50	092.08
35..	023.86	987.74	952.46	096.20	059.90	024.61	160.80	124.36	088.97
36..	022.91	985.84	949.77	095.14	057.80	021.66	159.61	122.15	085.64
37..	022.02	983.94	946.83	094.02	055.72	018.44	158.30	119.92	082.37
38..	021.07	982.02	943.94	092.82	053.55	015.34	157.00	117.53	079.03
39..	019.97	980.01	940.86	091.62	051.31	012.00	155.62	115.15	075.66
40..	018.99	977.89	937.86	090.32	049.03	008.63	154.16	112.71	072.16
41..	017.64	975.79	934.72	088.97	046.70	005.39	152.71	110.19	068.53
42..	016.62	973.57	931.50	087.56	044.27	002.00	151.07	107.62	065.07
43..	015.34	971.35	928.32	086.09	041.81	13998.55	149.44	105.00	061.53
44..	014.08	969.07	925.04	084.53	039.29	994.98	147.75	102.30	058.01
45..	012.79	966.74	921.63	082.95	036.69	991.43	146.03	099.53	053.98
46..	011.31	964.32	918.28	081.37	034.06	987.74	144.18	096.70	050.16
47..	009.83	961.90	914.90	079.58	031.35	984.09	142.29	093.81	046.28
48..	008.30	959.35	911.45	077.82	028.63	980.39	140.35	090.86	042.32
49..	006.71	956.82	907.98	075.98	025.76	976.54	138.34	087.85	038.33
50..	005.08	954.22	904.22	074.09	022.91	972.60	136.29	084.79	034.29
51..	003.36	951.51	900.54	072.16	019.97	968.77	134.14	081.67	030.18
52..	001.70	948.74	896.85	070.14	016.94	964.82	131.95	078.45	026.01
53..	13999.90	945.98	893.04	068.07	013.89	960.88	129.70	075.20	021.66
54..	998.02	943.14	889.18	065.94	010.77	956.64	127.35	071.90	017.43
55..	996.13	940.22	885.35	063.80	007.58	952.46	124.98	068.53	013.06
56..	994.11	937.28	881.37	061.53	004.34	948.23	122.54	065.07	008.63
57..	992.00	934.26	877.39	059.20	001.12	943.94	119.92	061.53	004.13
58..	989.96	931.17	873.34	056.86	13997.73	939.64	117.53	058.01	13999.60
59..	987.74	928.04	869.21	054.41	994.32	935.25	114.83	054.41	994.98
60..	985.57	924.85	865.06	051.90	990.85	930.76	112.14	050.72	990.30
61..	983.31	921.63	860.84	049.35	987.30	926.25	109.38	046.98	985.57
62..	980.96	918.28	856.55	046.70	983.71	921.63	106.55	043.17	980.76
63..	978.57	914.90	852.20	044.07	980.01	917.08	103.64	039.29	975.79
64..	976.13	911.45	847.80	041.33	976.35	912.35	100.67	035.37	971.04
65..	973.57	907.98	843.34	038.54	972.60	907.61	097.70	031.35	966.05
66..	971.04	904.45	838.90	035.68	968.77	902.82	094.62	027.31	960.88
67..	968.39	900.83	834.23	032.76	964.82	897.93	091.46	023.20	955.91
68..	965.71	897.16	829.61	029.76	960.88	893.04	088.25	018.99	950.75
69..	962.96	893.45	824.92	026.72	956.82	888.03	085.02	014.75	945.52
70..	960.10	889.65	820.13	023.62	952.79	882.95	081.67	010.47	940.22
71..	957.24	885.78	815.34	020.44	948.74	877.91	078.22	006.05	934.93
72..	954.22	881.88	810.46	017.18	944.46	872.58	074.80	001.70	929.50
73..	951.28	877.91	805.55	013.89	940.22	867.44	071.27	13997.17	924.15
74..	948.23	873.90	800.34	010.47	935.87	862.16	067.60	992.62	918.52
75..	945.08	869.80	795.50	007.10	931.50	856.81	064.01	987.97	912.91
76..	941.90	865.67	790.38	003.69	927.05	851.26	060.30	983.31	907.28
77..	938.65	861.44	785.19	000.08	922.50	845.88	056.51	978.57	901.57
78..	935.25	857.15	779.97	13996.45	917.94	840.35	052.67	973.57	895.78
79..	931.92	852.80	774.74	992.94	913.31	834.83	048.77	968.77	890.00
80..	928.48	848.42	769.33	989.04	908.60	829.12	044.78	963.92	884.11
81..	924.85	843.94	763.84	985.23	903.82	823.42	040.77	958.94	877.91
82..	921.63	839.41	758.34	981.37	899.01	817.65	036.69	953.88	872.08
83..	917.94	834.83	752.84	977.41	894.11	811.75	032.46	948.74	865.97
84..	914.09	830.19	747.28	973.57	889.18	805.94	028.27	943.56	859.86
85..	910.28	825.47	741.61	969.40	884.11		023.86	938.33	853.63
86..	906.43	820.69	735.88	965.20	879.06		019.57	932.98	847.26
87..	902.56	815.83	730.07	960.88	873.90		015.12	927.62	840.99
88..	898.57	810.93	724.22	956.64	868.70		010.77	922.15	834.59
89..	894.48	805.94	718.32		863.42		006.05	916.64	828.16
90..	890.41	800.91	712.32		858.10		001.41	911.05	821.60
91..	886.32	795.82	706.28		852.80		13996.75	905.41	815.02
92..	882.19	790.66	700.17		847.26		992.00	899.69	808.37
93..	877.91	785.46	693.99		841.72		987.30	893.88	801.63

TABLE 1—*Continued*

J	$^3\Delta_1 - {}^3\Pi_0$			$^3\Delta_2 - {}^3\Pi_1$			$^3\Delta_3 - {}^3\Pi_2$		
	$R_1(J)$	$Q_1(J)$	$P_1(J)$	$R_2(J)$	$Q_2(J)$	$P_2(J)$	$R_3(J)$	$Q_3(J)$	$P_3(J)$
	Cm^{-1}	Cm^{-1}	Cm^{-1}	Cm^{-1}	Cm^{-1}	Cm^{-1}	Cm^{-1}	Cm^{-1}	Cm^{-1}
94..	13873.34	13780.14	13687.76		13836.06			13888.03	13794.95
95..	868.95	774.74	681.50		830.44			882.19	
96..	864.50	769.33	675.10		824.67			876.17	
97..	859.86	763.84	668.68		818.92			870.14	
98..		758.34	662.19		813.01			864.04	
99..		752.84			807.08			857.87	
100..					801.07			851.64	
101..					794.95			845.34	
102..					788.91			838.90	
103..					782.72			832.55	
104..					776.45			826.01	
105..					770.13			819.41	
106..					763.84			812.73	
107..					757.22			805.94	
108..					750.73			799.27	
109..					744.11			792.46	
110..					737.42				
111..					730.69				
112..					723.87				
113..					716.96				
114..					710.06				
115..					703.05				
116..					695.92				
117..					688.71				
118..					681.50				
119..					674.23				

TABLE 1—*Continued*

WAVE NUMBERS OF THE LINES OF THE (0–1) BAND

($\nu_0 = 13092.86$ Cm^{-1})

J	$^3\Delta_1 - {}^3\Pi_0$			$^3\Delta_2 - {}^3\Pi_1$			$^3\Delta_3 - {}^3\Pi_2$		
	$R_1(J)$	$Q_1(J)$	$P_1(J)$	$R_2(J)$	$Q_2(J)$	$P_2(J)$	$R_3(J)$	$Q_3(J)$	$P_3(J)$
	Cm^{-1}	Cm^{-1}	Cm^{-1}	Cm^{-1}	Cm^{-1}	Cm^{-1}	Cm^{-1}	Cm^{-1}	Cm^{-1}
8..					13094.17			13160.94	
9..					093.51			160.47	
10..					093.02			159.94	
11..		13017.00			092.47			159.27	
12..		016.31			091.85			158.68	
13..		015.71			091.15			157.98	13144.83
14..		015.02	13000.80		090.54			157.19	142.98
15..		014.36	12999.30		089.82			156.38	141.13
16..		013.68	997.51		088.92			155.49	139.20
17..		012.89	995.63		088.06			154.55	137.31
18..		012.17	993.97		087.15			153.55	135.30
19..		011.35	992.16		086.18			152.46	133.17
20..		010.39	990.27		085.16			151.40	131.14
21..		009.43	988.50		084.07		13172.61	150.25	128.94
22..		008.46	986.36		082.96		172.41	149.02	126.69
23..		007.47	984.30		081.80		172.14	147.75	124.40
24..		006.33	982.24	13105.89	080.54		171.83	146.44	122.09
25..		005.19	980.11	105.59	079.28		171.48	145.04	119.66
26..	13031.19	004.13	977.92	105.26	078.04	13051.64	171.05	143.62	117.20
27..	030.97	002.82	975.72	104.85	076.59	049.33	170.54	142.11	114.72
28..	030.66	001.54	973.42	104.42	075.17	046.91	170.02	140.59	112.15
29..	030.41	000.23	971.13	103.94	073.68	044.41	169.40	138.98	109.56
30..	030.08	12998.89	968.79	103.40	072.15	041.90	168.76	137.31	106.84
31..	029.60	997.51	966.36	102.83	070.59	039.26	168.06	135.61	104.19
32..	029.16	996.03	963.79	102.22	068.93	036.66	167.30	133.86	101.52
33..	028.67	994.59	961.45	101.52	067.27	033.96	166.50	132.03	098.74
34..	028.05	992.96	958.91	100.78	065.50	031.19	165.62	130.19	095.72

TABLE 1—*Continued*

J	$^2\Delta_1$—$^2\Pi_0$			$^2\Delta_2$—$^2\Pi_1$			$^2\Delta_3$—$^2\Pi_2$		
	$R_1(J)$	$Q_1(J)$	$P_1(J)$	$R_2(J)$	$Q_2(J)$	$P_2(J)$	$R_3(J)$	$Q_3(J)$	$P_3(J)$
	Cm^{-1}	Cm^{-1}	Cm^{-1}	Cm^{-1}	Cm^{-1}	Cm^{-1}	Cm^{-1}	Cm^{-1}	Cm^{-1}
35..	13027.51	12991.41	12956.27	13100.00	13063.72	13028.43	13164.70	13128.22	13092.70
36..	026.89	989.79	953.76	099.17	061.87	025.61	163.71	126.24	089.82
37..	026.20	988.12	950.98	098.27	060.00	022.63	162.69	124.20	086.71
38..	025.36	986.36	948.32	097.33	058.05	019.81	161.58	122.09	083.59
39..	024.64	984.60	945.46	096.34	056.06	016.77	160.47	119.96	080.54
40..	023.83	982.78	942.74	095.29	054.03	013.68	159.27	117.74	077.26
41..	022.95	980.87	939.84	094.17	051.85	010.69	157.98	115.49	073.97
42..	022.00	978.96	936.95	093.02	049.74	007.47	156.67	113.17	070.59
43..	021.07	976.99	933.95	091.85	047.54	004.13	155.30	110.79	067.27
44..	020.01	975.01	930.95	090.54	045.30	001.01	153.87	108.34	063.89
45..	018.99	972.88	927.88	089.23	042.86	12997.75	152.46	105.89	060.39
46..	017.70	970.76	924.78	087.87	040.60	994.33	150.86	103.40	056.91
47..	016.59	968.55	921.62	086.45	038.20	990.96	149.27	100.78	053.27
48..	015.34	966.36	918.40	084.95	035.72	987.52	147.62	098.14	049.74
49..	014.03	964.08	915.15	083.44	033.24	984.00	145.91	095.44	045.94
50..	012.73	961.81	911.81	081.80	030.66	980.41	144.15	092.70	042.19
51..	011.18	959.41	908.47	080.24	028.05	976.99	142.34	089.82	038.39
52..	009.87	956.96	905.11	078.52	025.36	973.12	140.47	086.99	034.49
53..	008.46	954.52	901.81	076.80	022.63	969.38	138.52	084.07	030.66
54..	006.89	952.00	898.01	074.99	019.81	965.73	136.55	081.09	026.60
55..	005.19	949.42	894.54	073.15	017.00	961.81	134.52	078.04	022.63
56..	003.65	946.79	890.93	071.25	014.03	957.94	132.40	074.99	018.49
57..	001.98	944.13	887.28	069.28	011.18	954.01	130.19	071.83	014.36
58..	000.23	941.37	883.57	067.27	008.17	950.12	128.05	068.63	010.39
59..	12998.41	938.62	879.87	065.20	005.19	946.01	125.78	065.37	005.93
60..	996.53	935.78	876.03	063.08	001.98	941.89	123.45	062.06	001.54
61..	994.59	932.90	872.15	060.91	12998.89	937.73	121.07	058.68	12997.25
62..	992.68	929.98	868.26	058.68	995.63	933.67	118.63	055.28	992.98
63..	990.62	926.98	864.28	056.37	992.38	929.36	116.13	051.85	988.50
64..	988.50	923.93	860.28	054.03	989.02	925.05	113.58	048.28	984.00
65..	986.36	920.84	856.17	051.64	985.66	920.64	110.97	044.68	979.27
66..	984.30	917.69	852.12	049.17	982.24	916.26	108.34	041.03	974.70
67..	982.04	914.47	847.92	046.67	978.75	911.81	105.59	037.34	970.06
68..	979.76	911.22	843.65	044.09	975.22	907.30	102.83	033.58	965.29
69..	977.41	907.91	839.36	041.47	971.60	902.71	100.00	029.79	960.50
70..	975.01	904.55	835.03	038.77	967.96	898.01	097.10	025.88	955.71
71..	972.55	901.13	830.68	036.09	964.26	893.44	094.17	022.00	950.77
72..	970.06	897.67	826.26	033.24	960.50	888.69	091.15	018.01	945.81
73..	967.49	894.18	821.76	030.41	956.68		088.06	014.03	940.90
74..	964.82	890.61	817.22	027.51	952.84		084.95	009.87	935.78
75..	962.19	886.94	812.65	024.64	948.88		081.80	005.67	930.64
76..	959.41	883.19	807.95	021.55	944.95		078.52	001.54	925.35
77..	956.68	879.51	803.21	018.49	940.90		075.17	12997.25	920.23
78..	953.76	875.70	798.49	015.34	936.78		071.83	992.96	914.92
79..	950.98	871.90	793.67	012.17	932.64		068.42	988.50	909.64
80..	948.11	867.95	788.81	008.89	928.44		064.96	984.00	904.15
81..	944.95	863.96	783.83	005.67	924.17		061.41	979.58	898.55
82..	941.89	859.93	778.73	002.45	919.85		057.81	975.01	893.16
83..		855.84		12999.30	915.88		054.17	970.41	887.62
84..		851.74		995.63	911.22		050.45	965.73	882.12
85..		847.49		992.16	906.53		046.67	961.05	876.40
86..		843.13		988.50	901.81		042.86	956.27	870.68
87..		839.07		985.15	897.41		038.95	951.51	864.88
88..				981.64	892.65		035.02	946.45	858.88
89..				977.92	887.98		030.97	941.57	852.93
90..				974.14	883.19		026.89	936.54	
91..				970.41	878.39			931.46	
92..				966.55	873.47			926.33	
93..				962.60				921.13	
94..				958.55				915.88	
95..				954.52				910.61	
96..									
97..									
98..									
99..									
100..									
101..									

The procedure used to determine the J-values of the R and P branches was to find, by trial and error, those particular numberings which yielded the same combination differences as did the α-system for the same lower vibrational level. After numerous attempts, numberings of the R and P branches of the violet, central, and red sub-bands were found for which the combination differences agreed with the differences $\Delta_2F_2''(J)$, $\Delta_2F_2''(J)$, and $\Delta_2F_1''(J)$, respectively. The nature of the agreement found is illustrated in Table 2,

TABLE 2

COMPARISON OF COMBINATION DIFFERENCES $\Delta_2F''(J)$ OF THE (0-0) BANDS OF THE ($^3\Delta-{}^3\Pi$) AND ($^3\Pi-{}^3\Pi$) SYSTEMS

J	$^3\Delta-{}^3\Pi$			$^3\Pi-{}^3\Pi$		
	Red Sub-band	Central Sub-band	Violet Sub-band	$\Delta_2F_1''(J)$	$\Delta_2F_2''(J)$	$\Delta_2F_3''(J)$
	Cm^{-1}	Cm^{-1}	Cm^{-1}	Cm^{-1}	Cm^{-1}	Cm^{-1}
30.....	64.29	65.06	65.60	64.38	64.96	65.65
31.....	66.43	67.19	67.72	66.39	67.09	67.80
32.....	68.58	69.31	69.86	68.46	69.24	69.94
33.....	70.60	71.26	71.96	70.32	71.55	72.15
34.....	72.88	73.56	74.06	72.73	73.43	73.86
35.....	74.84	75.55	76.31	74.76	75.72	76.19
36.....	77.03	77.76	78.43	76.95	77.84	78.66
37.....	78.97	79.80	80.58	79.08	79.90	80.66
38.....	81.16	82.02	82.64	81.20	81.96	82.79
39.....	83.21	84.19	84.84	83.18	83.91	84.82
40.....	85.25	86.23	87.09	85.36	86.05	86.90
41.....	87.49	88.32	89.09	87.46	88.36	89.16
42.....	89.32	90.42	91.18	89.53	90.37	91.27
43.....	91.58	92.58	93.06	91.54	92.52	93.40
44.....	93.71	94.66	95.46	93.66	94.62	95.52
45.....	95.80	96.79	97.59	96.02	96.61	97.68
46.....	97.89	98.86	99.75	98.03	98.72	99.86
47.....	99.86	100.98	101.86	100.18	100.88	101.90
48.....	101.85	103.04	103.96	102.30	102.96	103.88
49.....	104.08	105.22	106.06	104.16	105.02	106.01
50.....	106.17	107.21	108.16	106.20	107.24	108.52

which presents a section of the data for the (0-0) band.

The J-values of the Q branches were found through the use of the equation

$$R(J)-Q(J)=Q(J+1)-P(J+1).$$

Since $R(J)$ and $P(J+1)$ were known, numberings of the Q branches were easily found which satisfied this relationship.

The fact that the violet sub-bands had the combination differences $\Delta_2F_3''(J)$, etc., had an important implication when the nature of the upper electronic state was considered. According to the suggestion of Lowater, this was a $^3\Sigma$ state. Such a state is single for a nonrotating molecule, so that the fact that the violet sub-bands had combination differences $\Delta_2F_3''(J)$ would have meant that the triplet components of the $X^3\Pi$ state with rotational terms $F_3(J)$ were lower than the components with terms $F_2(J)$ and $F_1(J)$. However, the equations of Budó[8] for the terms of a $^3\Pi$ state showed that the opposite was actually the case, i.e., the terms $F_3(J)$ were highest, followed by $F_2(J)$ and $F_1(J)$. Thus the upper electronic state must have a greater triplet splitting than the $X^3\Pi$ state.

[8] *Ibid.*, **96**, 219, 1935.

Therefore, it could not be a $^3\Sigma$ state. The only alternative was that the upper state was actually a $^3\Delta$ state, since the presence of a strong Q branch in each of the sub-bands required that $\Delta\Lambda = \pm 1$.

According to Budó, the $X^3\Pi$ state of *TiO* was regular, i.e., the $X^3\Pi_0$ substate lay lowest. Thus the violet, central, and red sub-bands were produced by the transitions $A^3\Delta_3 - X^3\Pi_2$, $A^3\Delta_2 - X^3\Pi_1$, and $A^3\Delta_1 - X^3\Pi_0$, respectively. These are the designations given the sub-bands in Table 1.

After the rotational quantum numbers had been found for all the lines in the three bands, the method of Budó[7] was used to derive the approximate rotational constants

TABLE 3

ROTATIONAL CONSTANTS IN WAVE NUMBERS OF THE BANDS OF THE γ-SYSTEM

Constants	(1–0)	(0–0)	(0–1)
$\bar{B}'_v$	0.5026	0.5057	0.5058
$\bar{B}''_v$	0.5338	0.5340	0.5306
$\bar{D}'_v$	0.70×10^{-6}	0.68×10^{-6}	0.71×10^{-6}
$\bar{D}''_v$	0.60×10^{-6}	0.61×10^{-6}	0.59×10^{-6}
$(B'_v - B''_v)$	-0.0312_9	-0.0281_1	-0.0250_8
$(D'_v - D''_v)$	$0.09_0\times10^{-6}$	$0.08_9\times10^{-6}$	$0.08_8\times10^{-6}$
ν_0	14952.70	14092.87	13092.86

TABLE 4

MOLECULAR CONSTANTS OF THE $A^3\Delta$ AND $X^3\Pi$ STATES

Electronic State	$A^3\Delta$	$X^3\Pi$
B_0	0.5058_4 cm^{-1}	0.5339_5 cm^{-1}
B_1	0.5026_6 cm^{-1}	0.5309_2 cm^{-1}
D_0	$0.69_9\times10^{-6}$ cm^{-1}	0.61×10^{-6} cm^{-1}
D_1	$0.70_0\times10^{-6}$ cm^{-1}	$0.61_4\times10^{-6}$ cm^{-1}
B_e	0.5074_3 cm^{-1}	0.5354_7 cm^{-1}
D_e	$0.69_8\times10^{-6}$ cm^{-1}	0.61×10^{-6} cm^{-1}
α_e	0.0031_8 cm^{-1}	0.0030_3 cm^{-1}
β_e	0.00	0.00
r_e	1.6641 A	1.6200 A
ω_e	867.71 cm^{-1}	1008.26 cm^{-1}
$\omega_e x_e$	3.94 cm^{-1}	4.13 cm^{-1}
ν_{00}	14092.87 cm^{-1}	.....
ν_e	14163.10 cm^{-1}	.....

$\bar{B}_v$ and $\bar{D}_v$ from the mean combination differences. The usual procedures[9] were followed in obtaining the band origins, ν_0, and the improved constants B_v and D_v from the differences $(B'_v - B''_v)$ and $(D'_v - D''_v)$. Since these procedures are well known, they will not be discussed in detail here. The pertinent quantities are tabulated in Table 3. Since the approximate constants $\bar{B}''_v$ and $\bar{D}''_v$ derived for the $X^3\Pi$ state were necessarily very close to being the same as those derived by Budó, for the sake of consistency his values were adopted for B_0 and D_0 of that state appearing in Table 4. The constants of the $A^3\Delta$ state in Table 4 were then derived from the differences $(B'_v - B''_v)$ and $(D'_v - D''_v)$ of Table 3,

[9] See, e.g., G. Herzberg, *Spectra of Diatomic Molecules* (2d ed.; New York: D. Van Nostrand Co., Inc., 1950).

B_0 and D_0 being the averages of the constants obtained from the (0–1) and the (0–0) bands.

The usual equilibrium rotational constants B_e, D_e, α_e, and β_e were readily obtained from B_v and D_v through the use of the equations

$$B_v = B_e - \alpha_e(v+\tfrac{1}{2}) \text{ and } D_v = D_e + \beta_e(v+\tfrac{1}{2}).$$

They are included in Table 4.

E. VIBRATIONAL CONSTANTS OF THE $A^3\Delta$ AND $X^3\Pi$ STATES

The difference of the band origins, ν_0, of the (0–0) and (0–1) bands gave the vibrational quantum difference, $\Delta G_{1/2}$, of the $^3\Delta$ state as 859.83 cm^{-1}. In order to derive the equilibrium vibrational constants, ω_e and $\omega_e x_e$, directly from the vibrational quanta, at least two differences, $\Delta G_{v+1/2}$, must be available. Since only $\Delta G_{1/2}$ was known, indirect methods had to be used to find the constants.

According to the quantum mechanical theory of the vibrationless nonrigid rotator, the following relationship holds between the equilibrium constants D_e, B_e, and ω_e:

$$D_e = \frac{4B_e^3}{\omega_e^2}.$$

Since D_e and B_e were known, ω_e could be derived. In the case of the $^3\Delta$ state, it was 865.27 cm^{-1}. This could be considered only an approximation to ω_e, since the constant D_e was only approximately known. A corresponding value for $\omega_e x_e$ could be derived from the usual equation:

$$2\omega_e x_e = \omega_e - \Delta G_{1/2}.$$

The resultant value for $\omega_e x_e$ was 2.72 cm^{-1}.

More accurate determinations of ω_e and $\omega_e x_e$ could be carried out if it was assumed that the Morse function represented the potential curve of the $A^3\Delta$ state. Pekeris[10] has shown that in this case the following equation can be derived:

$$\alpha_e = \frac{6\sqrt{\omega_e x_e B_e^3}}{\omega_e} - \frac{6B_e^2}{\omega_e}.$$

This equation was rewritten as

$$\omega_e x_e = B_e\left[\frac{\alpha_e\omega_e}{6B_e^2} + 1\right]^2$$

and was used to compute $\omega_e x_e$ from the known values of B_e and α_e and the approximate ω_e found above. This new value for $\omega_e x_e$ could be used, in turn, to compute an improved ω_e from $\Delta G_{1/2}$, and the process repeated. Since $\omega_e x_e$ was much smaller than ω_e and varied more rapidly, the process was rapidly convergent. The final values for ω_e and $\omega_e x_e$ were 867.71 cm^{-1} and 3.94 cm^{-1}, respectively.

As a check on the internal consistency of the constants, the first equation of this section was used to compute a D_e corresponding to this final computed ω_e. The computed value, 0.694×10^{-6} cm^{-1}, compared favorably with the value derived from the rotational lines, 0.698×10^{-6} cm^{-1}.

Exactly the same procedure was followed in computing the constants ω_e and $\omega_e x_e$ of the $X^3\Pi$ state. The computed value of D_e for this state was 0.604×10^{-6} cm^{-1}, while the observed value was 0.61×10^{-6} cm^{-1}.

[10] *Phys. Rev.*, **45**, 98, 1934.

F. THE TRIPLET SPLITTINGS OF THE $A^3\Delta$ AND $X^3\Pi$ STATES

The band origins, ν_0, given in Table 3, were derived from the means of lines with the same J in the Q branches of the three sub-bands. Hence the effects of the triplet splittings had been eliminated. The origins of the individual sub-bands were determined by extrapolating each Q branch. They are given in Table 5 and can be represented within

TABLE 5

ORIGINS OF THE SUB-BANDS OF THE γ-SYSTEM

v', v''	$\nu_{0(3)}$ (Cm^{-1})	$\nu_{0(2)}$ (Cm^{-1})	$\nu_{0(1)}$ (Cm^{-1})
(1–0).....	15022.42	14955.55	14880.06
(0–0).....	14162.96	14095.85	14019.74
(0–1).....	13162.98	13095.82	13019.90

the error of observation by the equation

$$\nu = \left\{\begin{matrix}14233.08\\14166.03\\14090.19\end{matrix}\right\} + 867.71\,(v'+\tfrac{1}{2}) - 3.94\,(v'+\tfrac{1}{2})^2 - 1008.26\,(v''+\tfrac{1}{2}) + 4.13\,(v''+\tfrac{1}{2})^2\ \mathrm{cm}^{-1}.$$

In Table 5 the origins $\nu_{0(3)}$, $\nu_{0(2)}$, and $\nu_{0(1)}$ refer to the origins of the transitions $A^3\Delta_3 - X^3\Pi_2$, $A^3\Delta_2 - X^3\Pi_1$, and $A^3\Delta_1 - X^3\Pi_0$, respectively.

Since both the upper and the lower electronic states exhibited strong triplet splitting, the method of Budó[7] was used to compute the coupling constants, A, from the combination differences $\Delta_2F(J)$. The resulting coupling constants were $A = 105$ cm^{-1} for both the $A^3\Delta$ and the $X^3\Pi$ states.

A difficulty arose when these coupling constants were introduced into Budó's equations for the rotational quanta, $F_1(J)$, $F_2(J)$, and $F_3(J)$ to compute the resulting separations of the origins of the sub-bands. For example, the computed separations for the (0-0) band were: $\nu_{0(3)} - \nu_{0(2)} = 106.31$ cm^{-1}; $\nu_{0(2)} - \nu_{0(1)} = 106.19$ cm^{-1}. The corresponding observed separations were 67.11 cm^{-1} and 76.11 cm^{-1}. In addition to being much smaller, the two observed separations differed by 9.00 cm^{-1}. Apparently, the only explanation for the erroneous results, if the equations of Budó were valid in the case of a $^3\Delta - {}^3\Pi$ transition, was that one or both of the electronic states were experiencing a vibrational perturbation. It could be shown, on the basis of the equations of Budó, that, for any pair of constants A for the two electronic states that resulted in a triplet separation of, say, 70 cm^{-1}, the difference of the separations $(\nu_{0(3)} - \nu_{0(2)})$ and $(\nu_{0(2)} - \nu_{0(1)})$ was, at most, 0.2 cm^{-1}.

The possibility that vibrational perturbations were present was strengthened somewhat when it was found that the coupling constants derived by Budó for the $B^3\Pi$ state ($A = 88$ cm^{-1}) and the $X^3\Pi$ state ($A = 100$ cm^{-1}) did not yield the observed separations of the sub-bands of the a-system. For example, the measurements by Christy of the heads of the sub-bands of the (0-0) band of the a-system gave: $\text{head}_3 - \text{head}_2 = -9.13$ cm^{-1}; $\text{head}_2 - \text{head}_1 = +1.90$ cm^{-1}. The computed separations of the corresponding origins were -12.29 cm^{-1} and -12.49 cm^{-1}. Here again, computation showed that no possible selection of the constants A would yield the observed separations.

At present it is impossible to ascertain which of the electronic states is being perturbed. Until the reason for the differences between the observed and calculated triplet splittings has been definitely established, the computed constants A must be used with caution. Hence, they have not been included in Table 4.

NOTES

A NOTE ON THE SPECTRUM OF RR TELESCOPII

The light-variations of RR Telescopii were discussed recently by Mrs. Mayall.[1] For several years prior to 1944 the star varied from photographic magnitude 12.5 to fainter than 16, in a period of approximately 387 days. About JD 2431000 (November, 1944) it rose suddenly to seventh magnitude, where it remained fairly constant through 1948. Overexposed spectra were described as showing no bright lines, but strong H and K absorption lines were present, and numerous other dark lines in the violet showed a resemblance to class F. Observations by A. D. Thackeray[2] in the blue-violet show a change from an absorption spectrum of about class F in June, 1949, to a bright-line spectrum of hydrogen and *Fe* II in September of the same year. This was accompanied by a fading of the star that began in July.

The star was observed September 6, 1950, at the Lamont Hussey Observatory with the 10-inch camera and 15° objective prism. Eastman 103*a*-E emulsion was used. The spectrum was recorded from *Hα* to *Hβ*, but wave lengths shorter than λ 5200 are in poor focus. The dispersions are 450 A/mm at *Hα* and 370 A/mm at the D lines. The continuous spectrum was recorded from *Hα* to the cutoff of the filter, near *Hβ*. Comparison with several neighboring stars ranging in spectral class from A0 to K5 indicates an energy distribution similar to that of class A5 or F0. The estimated magnitude of the continuum in the red region is 8.7. This estimate disregards completely the effect of bright lines.

Hα was an extremely strong and unsymmetrically widened bright line, with a wing extending considerably on the side of shorter wave length. Possibly λ 6516 *Fe* II contributed to this feature. A number of other emissions were present. Table 1 gives measured wave lengths and suggested identifications for all the bright lines observed. Eye estimates of intensities and widths are also tabulated. Both the wave lengths and the widths may be subject to an uncertainty of ± 10 A. Owing to the asymmetry of *Hα*, it was not considered reliable as a fiducial line, and λ 6300 was used instead. On the whole, the spectrum resembled that of a fading nova 2–3 mag. below maximum. In particular, there was a fair resemblance to the spectrum of Nova Scorpii 1950 II, as observed with the same instrument[3] on August 15–19 at about 2 mag. below maximum. However, the spectrum of RR Tel was definitely in a more advanced stage of development than that of Nova Scorpii on the dates named. The differences are shown by three criteria: (1) λ 5755 [*N* II] was stronger in RR Tel; (2) λ 5876 *He* I was strong in RR Tel, while *Na* I was dominant in Nova Scorpii;[4] (3) λλ 6300, 6363 [*O* I] were a little stronger, relative to *Fe* II, in RR Tel.

The slow changes of RR Tel since its nova-like outburst indicate membership in the RT Serpentis type. Comparison with other RT Ser stars is therefore of interest. Three others have been observed spectroscopically: RT Ser, DO Aquilae, and FU Orionis. Although the observed spectral regions were almost mutually exclusive, it can be said that in general composition the spectrum of RR Tel in 1950 probably resembled that of DO Aql as observed at Mount Wilson in August, 1926, at about 2 mag. below its maximum.[5] The latter star showed numerous permitted and forbidden lines of *Fe* II and weak lines of [*O* III]. RT Ser at a corresponding stage in 1928 had a similar spectrum but lacked [*O* III], which was first observed in 1931.[6] During their

[1] *Harvard Bull.*, No. 919, p. 15, 1949.

[2] *M.N.*, **110**, 46, 1950.

[3] Henize and McLaughlin, *A.J.* (in press).

[4] The different origin of the yellow lines in the two spectra is confirmed by direct comparison that shows a discordance of wave length.

[5] Merrill, *Pub. A.S.P.*, **38**, 387, 1926; Vorontsov-Velyaminov, *Ap. J.*, **92**, 283, 1940.

[6] Adams and Joy, *Pub. A.S.P.*, **40**, 252, 1928; Joy, *Pub. A.S.P.*, **43**, 353, 1931.

maxima of light, both DO Aql[7] and RT Ser lacked conspicuous emission lines, as did RR Tel, according to Mrs. Mayall. FU Ori, still at its maximum in 1950, eleven years after its brightening, showed an absorption spectrum of class cF5 on recent Michigan spectrograms.

Although the spectrum was not observed before the outburst, the character of the light-variation of RR Tel before 1944 is almost surely that of a long-period variable, presumably of class M. The star, therefore, is probably to be included in the "symbiotic" category. Among class M stars with known or probable nova-like companions, T Coronae Borealis, Z Andromedae, CI Cygni, AX Persei, and R Aquarii are outstanding. The last-named is particularly noteworthy as a long-period variable with a hot companion that has been observed in the act of mild nova-like variation.[8] Perhaps it is even allowable to add to the list *o* Ceti, a long-period variable with a peculiar hot bright-line companion, though the latter has not been observed to vary through a large range.

TABLE 1

EMISSION LINES IN THE SPECTRUM OF RR TELESCOPII

λ	Int.	Width (A)	Identification
4860	3	.....	4861 *Hβ*
5005	1	.....	4995, 5005 *N* II; 5007 [*O* III]
5165	1	.....	5169 *Fe* II; (5158 [*Fe* II]?)
5245	1	10:	5235 *Fe* II
5282	2	10:	5276 *Fe* II; 5273 [*Fe* II]
5320	6	10:	5317 *Fe* II
5535	2	12:	5535 *Fe* II
5680	1	20	5667, 5676, 5680, 5686 *N* II
5750	10	8	5755 [*N* II]
5880	10	10	5876 He I
5985	1	40	5991 *Fe* II
6058	1	15	6046 *O* I?
6177	1	40	6148 *Fe* II; 6157 *O* I; 6167, 6173 *N* II
6245	3	10	6238, 6248 Fe II
6298	5	10	6300 [*O* I]
6370	3	25	6364 [*O* I]
6450	3	10	6455 *O* I; 6456 *Fe* II
6550±	500	70	6563 *Hα*; 6516 *Fe* II

All the observations are in harmony with an interpretation of RR Tel as a double star composed of a long-period variable and a typical RT Ser nova. However, an increase of amplitude of the long-period variation as the outburst was approached suggests a possibility that we are dealing with a single variable star.

We are indebted to Dr. I. S. Bowen, director of Mount Wilson and Palomar Observatories, for the loan of the 10-inch telescope and objective prism. The establishment of the instrument at the Lamont-Hussey Observatory and its operation there were made possible by a grant from the Horace H. Rackham Fund of the University of Michigan, which is gratefully acknowledged.

KARL G. HENIZE
DEAN B. MCLAUGHLIN

OBSERVATORY, UNIVERSITY OF MICHIGAN
March 17, 1951

[7] A. J. Cannon, *Harvard Bull.*, No. 826, 1925; M. Beyer, *A.N.*, **235**, 428, 1929.
[8] Merrill, *Ap. J.*, **81**, 312, 1935.

LIDES

servatory of
has been re-
transparen-
astronomical
Bay.

ionally 4⅜
call for small
lecture pur-
tion of a list
a catalogue of
upon request to
Press, 5750

be furnished,
window trans-

information write
Chicago Press
Chicago, Ill.

POP
AST
A
Publ
sept July
Yearly
Domestic
$4.25; For
dollars).
POPULAR
MOUNTFIELD,

OBSERVA
FOUNDED 1877
* * *
presenting current developments in Astro
correspondence, Notes on discoveries and
Critical books. The papers read at the Meet
of the Royal Astronomical Society are
also fully reported.
* * *
Annual subscription for 6 issues, post free
should be sent to
ROYAL GREENWICH OBS
Hoathly Hill, Sussex, Eng

ASTROPHYSICAL MONOGRAPHS

Recommended by the Editors of the *Astrophysical Journal*

PRINCIPLES OF STELLAR DYNAMICS

By S. CHANDRASEKHAR

[illegible] monograph the dynamical problems of interpreting the [illegible] stellar systems, and their clusters are developed from a [illegible] These results should exert a profound influence on the future [illegible] of galactic dynamics. I can recommend its study [illegible] and to those who already have a passing acquaintance with [illegible] one profit from reading it."—Harry J. Reed, in *Science*, [illegible]

SPECTRA OF LONG-PERIOD VARIABLES

By PAUL W. MERRILL

This monograph is devoted largely to the observational side of the [illegible] discussion of the physical significance of various spectral [illegible] introduction and a historical chapter are inserted for the [illegible] not a specialist in stellar spectra. "To one wishing an [illegible] knowledge of the spectra of long-period variable stars, [illegible] astronomer, physicist, or chemist, the present monograph is [illegible] Meeting of the *Astronomical Society of the Pacific*, 1940, *Popular Astronomy*, [illegible]

THE MASSES OF THE STARS, WITH A CATALOGUE OF DYNAMICAL PARALLAXES

By HENRY NORRIS RUSSELL and CHARLOTTE E. MOORE

"Astrophysicists will be grateful to the authors for an [illegible] all available knowledge. . . . We may be permitted to congratulate [illegible] the magnificent outgrowth from an idea which germinated in [illegible]"—Professor A. S. Eddington, *The Observatory* (December, [illegible]

THE DISTRIBUTION OF THE STARS IN SPACE

By BART J. BOK

"[illegible] an extremely important contribution to the field of [illegible] will be both students and research workers in the field. [illegible] and variety of researches carried out in this field during the [illegible] treated critically in this study with clarity and dignity. [illegible]

THE UNIVERSITY OF CHICAGO